Downloaded from orbit.dtu.dk on: Apr 10, 2024

DTU Library

Ab-initio and comparative analysis of single-atom metal–nitrogen–carbon systems for CO reduction

Tsang, Sze-Chun

Publication date:
2023

Document Version
Publisher's PDF, also known as Version of record

Link back to DTU Orbit

Citation (APA):
Tsang, S-C. (2023). Ab-initio and comparative analysis of single-atom metal–nitrogen–carbon systems for CO *reduction*. Department of Physics, Technical University of Denmark.

General rights
Copyright and moral rights for the publications made accessible in the public portal are retained by the authors and/or other copyright owners and it is a condition of accessing publications that users recognise and abide by the legal requirements associated with these rights.

- Users may download and print one copy of any publication from the public portal for the purpose of private study or research.
- You may not further distribute the material or use it for any profit-making activity or commercial gain
- You may freely distribute the URL identifying the publication in the public portal

If you believe that this document breaches copyright please contact us providing details, and we will remove access to the work immediately and investigate your claim.

Ab-initio and comparative analysis of single-atom metal–nitrogen–carbon systems for CO_2 reduction

PhD Thesis
August 2023

Author

Sze-Chun Tsang
stsang@dtu.dk

Supervisor

Professor Thomas Bligaard
Section for Atomic Scale Materials Modeling, Department of Energy Conversion and Storage, Technical University of Denmark
tbli@dtu.dk

Co-supervisor

Assistant Professor Georg Kastlunger
Catalysis Theory Center, Department of Physics, Technical University of Denmark
geokast@dtu.dk

Copyright: Reproduction of this publication in whole or in part must include the customary bibliographic citation, including author attribution, report title, etc.

Cover photo: Digital illustration by Sze-Chun Tsang

Published by: Catalysis Theory Center, Department of Physics,
Technical University of Denmark
Fysikvej, Building 311, 2800 Kongens Lyngby, Denmark
https://www.fysik.dtu.dk/english/research/cattheory

Abstract

Metal–nitrogen–carbon (MNC) systems are seeing an explosion of research interest in recent years for their potential role in diverse energetically- and environmentally-relevant catalytic applications, for example the electrochemical CO_2 reduction reaction (CO_2RR). Their varied morphologies promise high tunability towards specific reactions, and their compositions represent a way-out from the commonplace use of precious metals in thermo- and electro-catalysis. Naturally, the catalytic activities of these systems are dictated by their interactions with the reactive species and the environment, which are underpinned by their structural and electronic properties.

In this thesis, the current state of the ongoing collaborative work on MNCs in which I have taken part is first summarized. Then, in view of the mixed experimental and theoretical results, I set out to further our understanding of the aforementioned fundamental properties from an *ab-initio* approach. This is done by the comparative characterization of the electronic structures of both molecular and extended MNCs – specifically, metal–cyclic-tetrapyrrole complexes and graphene-embedded MNC centers; such comparative analysis is then extended to the adsorption energetics on these sites. Attempts are made to construct and identify consistent trends across the various motifs, whilst "traditional" electronic-structure descriptors are illustrated to be insufficient in describing the adsorption energetics. This complexity of chemisorption on MNCs, which sets them apart from transition-metal catalysts, is summarized and discussed. The knowledge compiled and generated in the thesis is envisioned to facilitate the future search and engineering of these materials as catalysts for CO_2RR and adjacent reactions.

Resumé

Metal-nitrogen-karbon (MNC) systemer har oplevet en eksplosion i forskningsinteresse i de seneste år på grund af deres potentielle rolle i diverse energetiske og miljømæssige relevante katalytiske anvendelser, f.eks. den elektrokemiske CO_2 reduktionsreaktion (CO_2RR). Deres varierende morfologier lover høj justerbarhed mod specifikke reaktioner, og deres sammensætninger repræsenterer en udvej fra den almindelig brug af ædelmetaller i termo- og elektrokatalyse. Naturligvis er de katalytiske aktiviteter for disse systemer dikteret af deres interaktioner med de reaktanter og omgivelser, hvilket er underbygget af deres strukturelle og elektroniske egenskaber.

I denne afhandling er det igangværende samarbejde om MNC, som jeg har været en del af, først opsummeret. Derefter, i lyset af de kombinerede eksperimentelle og teoretiske resultater, sætter jeg mig ud for at fremme vores forståelse af de førnævnte fundamentale egenskaber fra en *ab-initio* tilgang. Dette er opnået ved den komparative karakterisering af de elektroniske strukturer af både molekylære og udvidede MNC'er – specifikt metal-cykliske-tetrapyrrol-komplekser og grafen-indlejrede MNC-centre; en sådan komparativ analyse er derefter udvidet til adsorptionsenergetik på disse centre. Forsøg er blevet gjort på at konstruere og identificere konsistente tendenser på tværs af de varierende motiver, mens det er illustreret at "traditionelle" elektroniske strukturdeskriptorer er utilstrækkelige til at beskrive adsorptionsenergetikken. Kompleksiteten af kemisorption på MNC'er, som adskiller dem fra overgangsmetalkatalysatorer, er opsummeret og diskuteret. Den kompilerede og genererede viden fra afhandlingen er etableret med henblik på at muliggøre den fremtidige søgning og design af disse materialer som katalysatorer for CO_2RR og lignende reaktioner.

Preface

This thesis is submitted in August 2023 to the Department of Physics, Technical University of Denmark (DTU), in fulfillment of the requirements of the PhD Program in Physics.

The research resulting in the thesis has been primarily conducted in the Catalysis Theory Center (CatTheory), DTU, from Fall 2020 to Fall 2023 under three supervisors:

- Karen Chan, Associate Professor
    - Initial and former main supervisor, initiator of project
    - Retired from role circa Winter 2021
    - Expertise: theoretical (electro-)catalysis
- Thomas Bligaard, Professor
    - Current main supervisor
    - Then-co-supervisor
    - Expertise: data-driven and machine-learning methods
- Georg Kastlunger, Assistant Professor
    - Current co-supervisor
    - Took over Chan's duties gradually, formally assuming co-supervisor role in Spring 2023
    - Expertise: method development for the interface

The research presented has been partially funded by the European Union's Horizon 2020 program under the grant agreement SelectCO2 (no. 851441), and the Villum Fonden's VILLUM Centre for the Science of Sustainable Fuels and Chemicals (grant no. 9455).

The thesis is primarily divided into two parts. The Chapters "Introduction" to "Electrocatalytic CO_2 reduction" serve as a walkthrough for what is already known, and what is to be done. This is then followed by the Chapters "Computational details" to "Outlook", which discuss the methods behind my study and the broader research that I have been a part of; the results generated; and what can be further done in view of the discoveries and limitations of the present work.

Acknowledgments

Looking back, the past three years have been frightfully short and eventful, at times difficult, and yet always fruitful – and all these would not have been possible if not for the combined support I have received from many, many a person. Before we proceed, I would therefore like to make use of this space to express my gratitude to these people.

To start with, I owe my thanks to my former supervisor Karen Chan, who initiated the project, introduced me to the world of catalysis, and gave me the chance to meet with most of the people mentioned hereafter. While much of the research effort presented is relatively new, her tenure certainly laid the very foundation to it all.

The guidance and assistance of my current supervisors, Professor Thomas Bligaard and Assistant Professor Georg Kastlunger, are of course indispensable. I would like to thank them for always being there, available for consultations, advice, and insights, while also being flexible and allowing me immense freedom in how to approach the research problem.

I would like to also thank my collaborators over the course of the research for pleasant collaborations and for being way more knowledgeable, prolific, and industrious than I have been: our former and current colleagues Sudarshan Vijay, Sihang Liu, and Naiwrit Karmodak; and external collaborators the ECEMS Group, Technical University of Berlin, especially Prof. Dr. Peter Strasser and Wen Ju.

My colleagues here at the Catalysis Theory Center (CatTheory) must also be acknowledged for their role in maintaining an excellent work environment and research atmosphere. Special thanks to these former and current colleagues: Ang Cao, Mikael Valter-Lithander, and Megha Anand, for their assistance with the science and with technicalities; Lone Jensen Coe, Kathrine Bjerregaard Nielsen, and Martin Vendel Nielsen, for ensuring the smooth running of all administrative affairs; and last but not the least Center Director Prof. Jens Kehlet Nørskov, for uniting all these outstanding people under his leadership and vision.

A very special shoutout to Andreas Lynge Vishart for helping with the translation of the thesis abstract into Danish; and to him, Mikael, and Mianle Xu for proofreading the draft version.

Thanks to the Fritz Haber Institute, Max Planck Society, in particular Hendrik Helge Heenen and his team, for being amazing hosts to my external research stay, during which we worked on the machine-learning-based modelling of metal–nitrogen–carbon centers on graphene surfaces. Though the work remained at a preliminary stage at my return, the experience has nonetheless been exceedingly enjoyable, rewarding, and eye-opening.

Most of the computational work presented in the thesis has been conducted on the Niflheim supercomputing cluster, DTU Physics. I would like to thank especially Ole Holm Nielsen for incessantly working to keep the cluster running in top shape, despite the constant ongoing construction work in and around the Department.

List of publications

Ref.[1]

Unified mechanistic understanding of CO_2 reduction to CO on transition metal and single-atom catalysts[*]
Sudarshan Vijay, Wen Ju, Sven Brückner, Sze-Chun Tsang, Peter Strasser, and Karen Chan
Nature Catalysis **4**(12), 1024–1031 (2021)
© The Author(s), under exclusive licence to Springer Nature Limited 2021

Ref.[2]

Covalent organic framework (COF) derived Ni-N-C catalysts for electrochemical CO_2 reduction: unraveling fundamental kinetic and structural parameters of the active sites[†]
Changxia Li, Wen Ju, Sudarshan Vijay, Janis Timoshenko, Kaiwen Mou, David A. Cullen, Jin Yang, Xingli Wang, Pradip Pachfule, Sven Brückner, Hyo Sang Jeon, Felix T. Haase, Sze-Chun Tsang, Clara Rettenmaier, Karen Chan, Beatriz Roldan Cuenya, Arne Thomas, and Peter Strasser
Angewandte Chemie (International Edition) **61**(15), e202114707 (2022)
© 2022 The Authors. Angewandte Chemie International Edition published by Wiley-VCH GmbH. This is an open access article under the terms of the Creative Commons Attribution License, which permits use, distribution and reproduction in any medium, provided the original work is properly cited.

Ref.[3]

Rationalization and deconvolution of trends in adsorption energetics on metal–nitrogen–carbon single-atom centers
Sze-Chun Tsang, Naiwrit Karmodak, Sihang Liu, and Georg Kastlunger
In preparation

---

[*] Included in "Appendices § II"

[†] Ditto

Glossaries

I. Elements and analogs

H	**H**ydrogen
C	**C**arbon
N	**N**itrogen
O	**O**xygen
M	**M**etal
V	**V**anadium
Mn	**M**a**n**ganese
Fe	Iron (***Fe****rrum*)
Co	**Co**balt
Ni	**Ni**ckel
Cu	Copper (***Cu****prum*)
Rh	**Rh**odium
Au	Gold (***Au****rum*)

II. Materials and substances

MNC	Metal–nitrogen–carbon system
G-MNC	Graphene-MNC
CTP	**C**yclic **t**etra**p**yrrole
MPc	**M**etal **p**hthalo**c**yanine
MPz	**M**etal **p**orphyra**z**ine
MPor	**M**etal **por**phyrin
NCP	Nitrogen-confused porphyrin
TM	Transition metal
CO	Carbon monoxide (gas)
CO_2	Carbon dioxide (gas)

III. Adsorbates

*H	Hydrogen/Proton
*CO	Carbon monoxide
*COOH	Carboxyl
*CO_2	Carbon dioxide/Carboxylate

IV. Theories and methods

DFT	Density-functional theory
GGA	Generalized-gradient approximation
RMSE	Root-mean-squared error

V. Reactions

CO_2RR	CO_2 reduction reaction ($CO_2 \rightarrow CO, HCOOH, C_xH_y, \ldots$)
HER	Hydrogen evolution reaction ($H_2O \rightarrow H_2$)
ORR	Oxygen reduction reaction ($O_2 \rightarrow H_2O_2, H_2O$)
OER	Oxygen evolution reaction ($H_2O \rightarrow O_2$)
NRR	Nitrogen reduction reaction ($N_2 \rightarrow NH_3$)

Table of Contents

Abstract ii

Resumé iii

Preface iv

Acknowledgments v

List of publications vii

Glossaries viii

- **I. Elements and analogs** viii
- **II. Materials and substances** viii
- **III. Adsorbates** ix
- **IV. Theories and methods** ix
- **V. Reactions** ix

Table of Contents x

Introduction 1

- **I. On the situation** 1
- **II. On catalysis** 2
- **III. On this thesis** 4

Metal–nitrogen–carbon single-atom catalysts 5

- **I. Cyclic tetrapyrroles** 6
  - I.1. (Nitrogen-confused) Porphyrins 6
  - I.2. Phthalocyanines 7
  - I.3. Porphyrazines 7
  - I.4. NCP derivatives 7
- **II. Graphene-MNCs** 8

Electrocatalytic CO_2 reduction 10

Computational details 11

- **I. A brief introduction to DFT** 11

II. Basic computational facts 12
III. Spin-state treatment protocol 13
IV. Single-point hybrid calculations 14
V. Bader charge partitions 15
VI. Charging the slab 16
Bridging the metal–SAC gap: one picture to rule them all 18
I. Background 18
II. Is electron transfer rate-limiting in MNCs? 20
III. RDS variation in MNCs 22
IV. *CO_2 dipole, the central quantity 23
V. The activity volcano 24
VI. Discussion 25
Reaching down to the fundamentals: an exercise in atomic precision 26
I. Background 27
II. Synthesis 28
III. Site characterization and identification 29
IV. e-CO_2RR activities 30
V. Discussion 32
The spin conundrum 33
I. Poor mapping from spin input to output 33
II. Different geometries stabilize different spin states 36
III. Energetic implications of the spin state 36
IV. Conclusions 37
Comparative characterization of MNCs 38
I. CTP–G-MNC correspondence and inter-CTP comparisons 40
I.1. d-state descriptors 40
I.2. Electronic density 42

II. Coordination and energetics 46
III. Conclusions 51
Scaling relations in MNCs 52
I. Inter-adsorbate scaling 53
II. Inter-quantity scaling 58
III. Conclusions 61
Rationalization of adsorption energetics 62
I. Divide-and-conquer: isolation of spin dependence 62
II. Does the d-band model work on MNCs? 65
III. Conclusions 70
Outlook 72
I. Electrochemical modelling of MNCs 72
II. ML-boosted thermodynamic surface simulations 74
Conclusions 78
References 79
Appendices 106
I. Additional figures 106
II. Included publications 120

Introduction

I. On the situation

The role of CO_2 in heat retention from incident sunlight has been noticed in the scientific community since the Mid-19th century,[4,5] and before the turn of the century it has already been linked to the global climate.[6] By a mix of real and willful ignorance[7] of the consequences of industrialization, our society has grown to its current scale; however, anthropogenic greenhouse-gas (GHG) emissions and climate change have also come to a critical point, where immediate mitigation is necessary for the warming to be limited to a manageable level of 2 °C year^{-1}.[8]

The overwhelming majority of global GHG emissions can be attributed to the industrial and energetic uses of fossil fuels.[8] Around 80% of the globe's energy is still powered by these fuels;[9] about a half of all energy and fuel consumption is tractable to the industries, of which about 16% is from the use of fuel as feedstocks instead of for energy.[10] This highlights three crucial technical aspects of economically- and socially-viable climate-change mitigation: (1) increase in the energetic efficiency of all sectors; (2) decoupling as far as possible from petrochemistry; and (3) full migration towards renewable sources of energy.

To the first point, we would like to highlight the unreasonable inefficiency at which industrial processes often operate. The Haber–Bosch process for the manufacturing of ammonia,[11,12] from which fertilizers are made, is often cited as the decisive factor behind modern population growth.[13,14] Yet this cornerstone of humanity, which alone accounts for 1% of global energy consumption and CO_2 emission[15] and 3–5% of natural gas use,[16] is merely 50% energy-efficient[15] – which, for the better or the worse, leaves much room for improvements.

To the second, the ubiquity of petroleum-based plastics in all aspects of the modern society is self-apparent; petrochemicals also appear in perhaps unexpected contexts like pharmaceuticals.[17][*] However, this is not to say that all hope is lost: the Fischer–Tropsch process[18,19] for example grows long hydrocarbon chains out of CO, a simple gas, potentially mitigating our existing dependence on fossil-fuel-derived carbon; as well as serving as a form of energy storage, where the energy invested into building the carbon chains can later be retrieved by using them as fuels.

II. On catalysis

One common theme unites the two aspects of the fossil-fuel problem named above: catalysis – the facilitation of a chemical reaction via providing it with an alternative pathway. By the reduction of elementary-step barriers and the (de-)stabilization of the various reaction intermediates, a catalyst changes the energetic landscapes of the reactions, thus steering the system towards the pathways made the most thermodynamically favorable. A catalyst is typically described by three metrics:

Activity	The rate at which the desired reaction(s) occur on the catalyst, depending on both intrinsic and extrinsic factors: the turnover frequency (TOF), measuring how facile/quick a single catalytic site sustains a reaction; and the site density, quantifying how many such sites exist per amount (mass, area, or volume) of the catalyst material.
Selectivity	The fraction of reactant going into the actual production of the desired products, instead of being lost to the surroundings, poisoning (passivating) the catalyst against further reactions, or wasted in reaction towards unwanted side products.
Stability	The degree to which the catalytic site retains its integrity in open-air and operando conditions, after e.g. a certain number of cycles or running duration.

---

[*] For a broad overview, see https://www.scimed.co.uk/education/what-products-are-made-from-petroleum/.

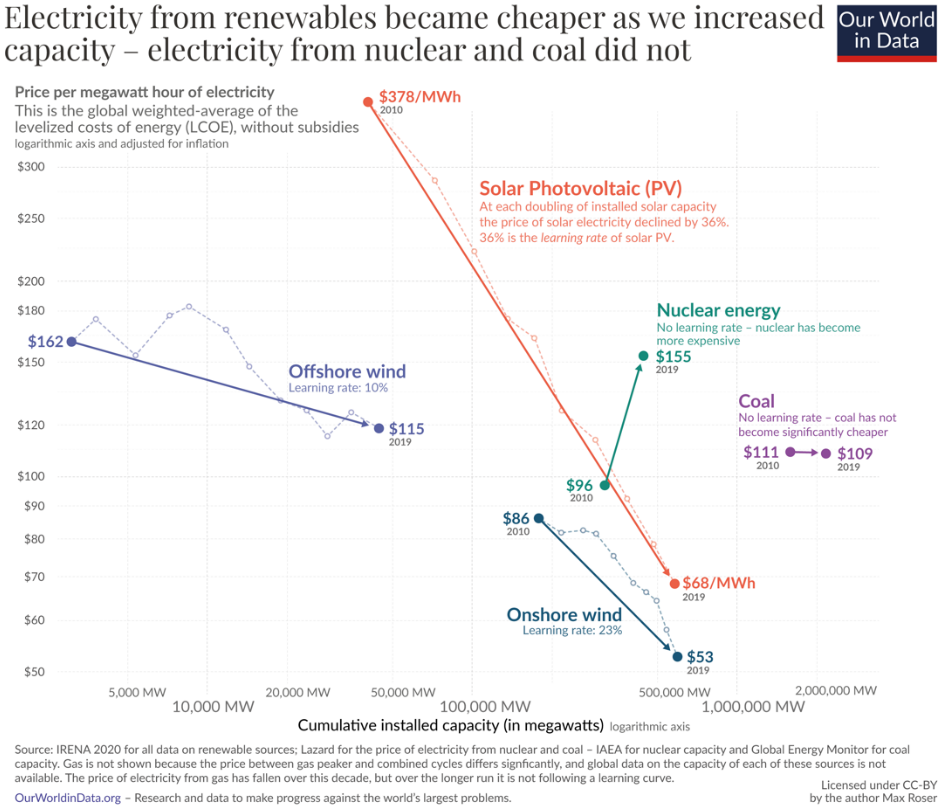

Electricity from renewables became cheaper as we increased capacity – electricity from nuclear and coal did not

Source: IRENA 2020 for all data on renewable sources; Lazard for the price of electricity from nuclear and coal – IAEA for nuclear capacity and Global Energy Monitor for coal capacity. Gas is not shown because the price between gas peaker and combined cycles differs signficantly, and global data on the capacity of each of these sources is not available. The price of electricity from gas has fallen over this decade, but over the longer run it is not following a learning curve.

OurWorldinData.org – Research and data to make progress against the world's largest problems.

Licensed under CC-BY by the author Max Roser

Figure 1. Illustration for the falling cost of renewables over the first two decade of the millennium. (Reproduced from Ref.[20] under a CC-BY license; the reference used data from Ref.[21–24])

In electrocatalysis,[*] reductive or oxidative reactions are respectively driven by the application of a negative or positive electric potential. Owing to the falling cost of renewable electricity (Figure 1), it is increasingly believed to be a potent solution to our environmental and energetic woes. One such application is the CO_2 reduction reaction (CO_2RR; see Chapter "Electrocatalytic CO_2 reduction" for more discussion), which this thesis is about: where CO_2 is reduced into various carbon-containing products, like CO, small alcohols, formate/-ic acid, or even multi-carbon products.[25,26] As the most-oxidized carbon species, often emitted after the use of carbon-based fuels for energy, CO_2 is captured, fixated, and converted into more usable forms of carbon by natural photosynthesis; however, as our energy use outstrips such natural carbon recycling, a deficit is formed in the carbon cycle, leading to CO_2 buildup in the atmosphere.[18] Employing renewables to drive electrochemical CO_2RR is thus a stone for multiple metaphorical birds, (1) contributing to the closure of the carbon cycle,[18] and (2) mitigating the intermittency issue of renewables by the production of either fuels (e.g. hydrocarbons and alcohols), value-added products (e.g. formic acid), or feedstock (i.e. CO) to the production thereof.

---

[*] Research interest in electrocatalysis has been exponentially growing over the past two decades, seeing more than 3000 publications per year for the past three years. (Based on Web of Science analytics on a search of the all-fields keyword "electrocatalysis".))

III. On this thesis

To that effect, metal–nitrogen–carbon single-atom catalysts (MNC-SACs) have emerged in recent years as a promising class of candidates for CO_2RR (and other reactions). [*] While traditional precious-metal-based electrocatalysts[25,27,28] are costly and prone to supporting side reactions like the hydrogen evolution reaction (HER), MNCs are based on relatively inexpensive materials and capable of suppressing such side reactions.[29–31] Though well-trodden both experimentally and theoretically, there still remains room for further research in the discipline simply due to its vastness.

Employing standard density-functional-theoretical (DFT) tools, [†] we comparatively examine the electronic structures of, electron distribution around, and the adsorption energetics on cyclic-tetrapyrrole- and graphene-MNC-based MNC centers, highlighting the similarities and differences between families of MNCs. Afterwards, we explore and evaluate the scaling relations on MNCs, as well as attempt to develop methods to rationalize the adsorption energetics on these systems.

---

[*] Catalysis on MNC systems is a burgeoning field seeing exponential growth of interest in the past two decades, and upwards of 200 publications per year in the past several years. (Based on Web of Science analytics on the following search: the union of the all-fields keywords “metal-nitrogen-carbon”, “M-N-C”, “MNC”, “MN4”, plus the mandatory in-topic keyword “catalyst”.) See also Ch. “Metal–nitrogen–carbon single-atom catalysts”.

[†] DFT is a mature and well-used tool resulting in upwards of 20000 publications per year in the past two years; interest therein has grown steadily from two decades ago (≈ 5000 publications per year). (Based on Web of Science analytics on a search of the all-fields keyword “density functional theory”.) See also “Computational details § I”.

Metal-nitrogen-carbon single-atom catalysts

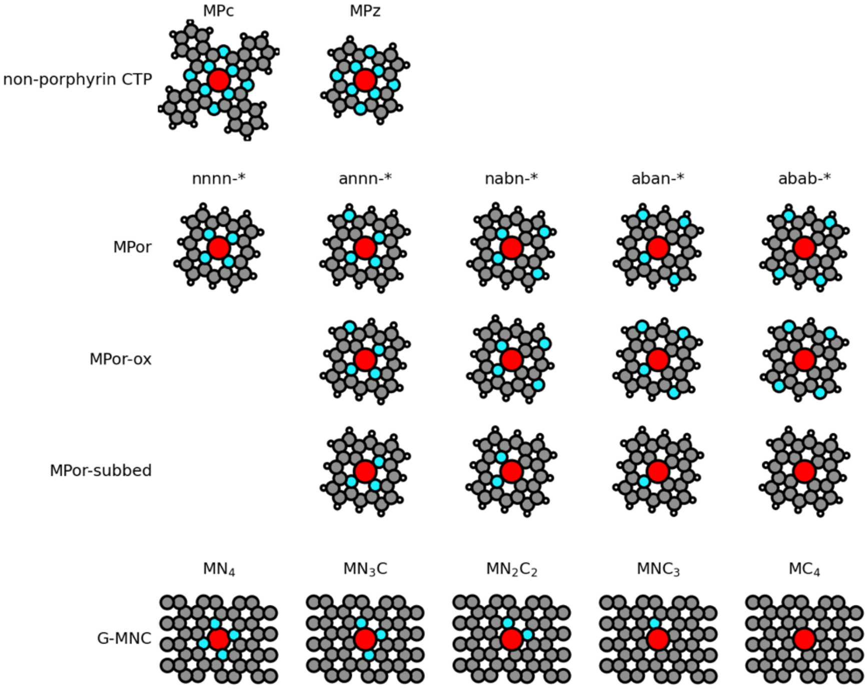

Schematic 1. MNC structures. Atom colors: red: metal (M); aqua: nitrogen (N); gray: carbon (C); white: hydrogen (H). Note that the N atoms are colored differently only in this Schematic for better visual contrast.

Falling under the umbrella of the metal–organic frameworks (MOFs), metal–nitrogen–carbon (MNC) single-atom catalysts (SACs) have seen almost a century of intense research interest – and are indeed found in nature in abundance. From a more modern perspective, they are atomically-dispersed – hence their designation as SACs – metal active sites on organic molecular skeletons or extended frameworks. SACs make for better catalytic-species economy, and may increase energy efficiency in electrochemical contexts depending on charge localization/distribution. For a schematic of the structures discussed here (and hereafter), see Schematic 1.

I. Cyclic tetrapyrroles

As the name indicates, metal cyclic tetrapyrroles (CTPs) are molecular complexes consisting of a cyclic organic skeleton chelating the central metal (M) atom with four pyrrolic nitrogen (N) atoms. They are often fully π-conjugated and even (partially) aromatic systems.[32] Pyrolysis into graphene-MNCs (G-MNCs; see § II) is possible and was one of the main pathways thereto;[33,34] such treatment risks altering the well-defined structure of the active site,[35] but that has also been disputed.[36] As such, they are often otherwise immobilized onto supports for use as heterogenous catalysts, with strategies ranging from simple adsorption, which may result in self-assembly into surface arrays;[37,38] polymerization/framework formation on top of the support;[39–42] anchoring on surface defects[35,43] via chained moieties;[44,45] to chemical fusion/conjugation to the graphene-sheet edge.[46] CTPs also find use in homogenous photocatalysis, where reactions happen in solution and are driven by light.[44]

In this study the following families of metalated CTPs are included:

I.1. (Nitrogen-confused) Porphyrins

Metal porphyrins (MPors) have been catalytically relevant before the history of catalysis itself. As examples, the heme group present in enzymes like the heme peroxidases is a (substituted) iron porphyrin with axial ligands; chlorophylls, the workhorse of photosynthesis, are magnesium porphyrins with side chains and a cyclic appendage. While the bare porphyrin (also called a "porphin") is best thought as a theoretical base-case, variants like the tetraphenylporphyrins (TPPs) are often encountered in catalysis literature.[36,46]

Of particular interest to this study are their isomers the metal nitrogen-confused porphyrins (NCPs), where the atom orders in one or more of the pyrrole rings are permutated during synthesis. One or more N atoms are thus on the periphery of porphyrin macrocycle instead of chelating the metal center. NCPs are thus in a sense direct molecular analogs of G-MNC centers which are only partially nitrogenated. Singly- and doubly-NC porphyrins, with respectively only three and two N atoms neighboring the metal, have been successfully synthesized.[47,48] These successes sparked the research field of the "porphyrinoid" molecules.[49]

Still, as a simplifying choice, in the present work we only explore the bare metal porphyrin and its N confusions, plus the derivatives named in § I.4. From here onwards, all such molecules will be referred to in the form `<configuration>-<metal>Por[-suffix]`, where `<configuration>` is a four-letter string indicating the N-atom positions (`a` for α-carbon, `b` for β-carbon, and `n` for nitrogen (i.e. the non-confused position)),* and the optional `[-suffix]` indicates the derivative class where applicable.

I.2. Phthalocyanines

Metal phthalocyanines (MPcs) have a long history as catalysts; their activities in decomposing hydrogen peroxide (H_2O_2) being attested as early as the 1930s.[50] Structurally it is four isoindoles (pyrrole rings with benzene rings fused to the opposite side to the nitrogen) chelating the metal, bridged together in a ring by N atoms ("aza-" groups). Being something of a large planar molecule, the MPc can be considered a step from the MPor core towards an MNC center embedded in a graphene flake,[51,52] then onwards to full extended G-MNC systems.

I.3. Porphyrazines

Metal porphyrazines (MPzs), also called tetraazaporphins, structurally resembles MPors with the bridging C–H ("methine") groups replaced by N atoms; alternatively, they can be viewed as MPcs with the fused benzene rings removed. Though isoelectronic to MPors when considering the macrocycle valences, the electronic structure of the metal and the strength of its ligand interactions in MPzs show differences from those of MPors and MPcs.[53]

I.4. NCP derivatives

In this theoretical work, two extra classes of metal NCP derivatives/analogs are also considered. The "oxidized" metal NCP ("MPor-ox" or "MPor (NH → N)") has the confused N atoms deprotonated as a probe to changing the oxidation state of the central M atom, while the "substituted" metal NCP ("MPor-subbed" or "MPor (NH → CH)") replaces the confused N atoms

---

[*] The nomenclature follows the scheme in Fig. 3 of Ref.[48] However, note the difference from the usual assignment of the α and β locant with respect to the N in the pyrrole ring.

with C atoms, which again changes the nominal oxidation state of the metal and the electronic properties of the molecule.

II. Graphene-MNCs

A G-MNC center is best described as a single M atom anchored in a vacancy of a graphene sheet with chelating N and/or C atoms. The common synthesis strategy is the thermal carbonization/pyrolysis of organic-molecular (e.g. CTPs[35,54,55]), -polymeric,[29] and/or -framework [e.g. zeolite imidazolate[56–58] and covalent-organic[59] frameworks (resp. ZIF and COF)] and metal-containing precursors: the C-rich bulk coalesces on the nanoscale into a graphitic matrix, the thermodynamic ground state of carbon;[60] while the metal embeds itself into the framework, often being stabilized by one or more chelating N atoms, the latter species being in pyrrolic or pyridinic configurations with their surrounding C atoms.[61] The case where four N atoms chelates a metal center in a square-planar configuration (commonly called MN_4) has been proposed be the most catalytically active for ORR,[62] the focus of the majority of the early literature. This configuration can be considered analogous to the aforementioned CTPs, having locally-similar stoichiometries at the active site.[*] By replacing the chelating nitrogen with carbon, one recovers structural analogs for the NCP (§ I.1) molecules. More recently, the community has found success in using the system in other reductive contexts like in CO_2RR[51,63–65] and NRR.[66]

After the formation of the metal-incorporating bulk structure, the elemental identity of the active site can be modified by displacement reactions.[38,52,63] While the atomic morphology of single-atom catalytic sites and their surroundings is largely observed to be similar[2,67] – or is at least so modeled[63] – mesoscopic factors like support conductivity and electrochemical surface area mean that the activity can nonetheless exhibit considerable variation based on the precursors, synthetic conditions, and post-processing treatments.[68,69]

---

[*] Yet another structural analog is the 14-member tetraaza macrocycles prevalent in early literature.[195] While the ring topology seems to more directly resemble the nitrogenated double vacancy in graphene, they are non-pi-conjugated and non-planar species.[196]

With the proper synthesis pathways, it is possible and well-attested that multi-metallic active sites (e.g. diatom catalysts (DACs)) can be formed, exhibiting atomic-scale synergy[70] and even permitting entirely new adsorption (and thus reaction) modes.[71] Such sites hold promises for enabling C–C coupling,[72] paving the road towards multi-carbon (C_n) products and energetic applications.

Electrocatalytic CO_2 reduction

The first step in CO_2RR is a two-electron ($2e^-$) process, with the CO_2 undergoing a change of −2 in its oxidation number, receiving two electrons from the cathode. Depending on the mechanism, the $2e^-$ product obtained at this stage can either be CO or HCOOH (formic acid). From this point on, the $2e^-$ product can (1) desorb and be yielded, (2) couple with another *CO in a step towards a C_2 product like ethanol, acetate, or ethylene,[73] or (3) be further reduced into e.g. formaldehyde.[74]

The main $2e^-$ product of the TM surface is found to be described by the competing adsorption energetics of *CO and *H: surfaces are shown mostly classifiable into the HCOOH-forming, CO-forming, and H_2-forming groups. Cu, being unique in binding *CO but not *H at 0 V against the reversible hydrogen electrode (RHE),[30] is alone in being active towards further-reduced and C-coupled products.[25,27,75,76]

Though various micro-structuring, nanofabrication, and alloying techniques seem to have created Cu catalysts of varying activities, even to the point of rivalling Au in CO production, it has been shown that Au remains the state-of-the-art in terms of intrinsic activity,[18,65,77] while all Cu-based catalysts ultimately falls on the same trend[18] – indeed, be it Cu or Au, intrinsic activity trends on the same metal rarely deviate from one another.[65,77]

However, as we have previously hinted at,[29–31] MNC-SACs have the potential of circumventing the woes of the TM surface by side-stepping the parasitic HER, which is attributed to the preclusion of the *H–*H coupling Tafel step by the single-atom geometry; it is also unfavorable for a single *H to bind due to the metal center's resemblance of the metal-surface atop site.[30] Beside the suppression of HER, these sites are shown to be rather energetically different from TM surfaces with their loss of *H–*CO[30] and *CO–*COOH[78] scaling between the adsorbate binding energies. This has especially in the case of the former interesting implications, given our prior discussion of *CO and *H being activity classifiers in CO_2RR: scaling relations would have related the energetics of "analogous" adsorbates[79] and allowed for a simplified model of the surface – but at the cost of more inflexible energetic (and thus reactivity) trends.

Computational details

This Chapter describes the computational approach, tools, parameters, and strategies used for generating the results presented from the Chapter “The spin conundrum” onwards.

I. A brief introduction to DFT

To recover a quantum-mechanical description of a multi-electron system, one typically has to solve the Schrödinger equation[80] to get the multi-electron *wavefunction*, which quickly becomes un-tractable for anything more than a few electrons. However, in Hohenberg and Kohn’s seminal paper,[81] the multi-electron *density* was proposed instead as the central quantity capable of describing the entirety of a system with a given number of electrons, exhibiting a one-to-one relationship with an electric potential to which it is the ground state solution of. A universal *functional* (i.e. a mathematical object mapping a function to a number) acting on the density was also shown to exist, capable of retrieving the energy of the system of electrons therefrom – and such is the dawn of the density-functional theory.

While immensely profound, this all-important density functional gave not so much as a hint as to its construction. Later, Kohn and Sham proposed the eponymous formalism,[82] under which the all-electron density can be self-consistently solved for in a single-electron equation, the eigenfunctions of which are then used to reconstruct said density. Such is the local-density approximation (LDA) forming the basis of the modern DFT methods, later extended into the generalized-gradient approximation (GGA) by Perdew and Burke,[83] including also semi-local effects via the gradient of the density.

Employing the Born–Oppenheimer approximation,[84] the atomic nuclei and electrons in a material can be separately considered, allowing the system ground state to be obtained iteratively in a self-consistent loop of the nuclear and electronic degrees of freedom, relaxing each alternatively while treating the effects of the other as a fixed external potential. Since the core electrons are largely irrelevant to the chemistry of materials, later simplifications abstract their effects away into numerically-convenient smooth forms (ultrasoft pseudopotentials)[85–87] or projectors on a plane-wave basis (projector-augmented wave).[88,89]

II. Basic computational facts

All DFT calculations presented from “The spin conundrum” onwards are staged and analyzed with the Atomic Simulation Environment (ASE);[90*] they are run with the Vienna ab-Initio Simulation Package (VASP),[†] a plane-wave DFT code.[91,92] Calculations are done with the Revised Perdew–Burke–Ernzerhof[93,94] (RPBE)[95] exchange–correlation functional at the generalized-gradient approximation (GGA) level using the projector-augmented-wave (PAW) formalism.[88,89] To sample the reciprocal space, uniform Monkhorst–Pack[96,97] k-point grids with an approximate line density of 35 points per $Å^{-1}$ are used along the periodic directions, while the aperiodic directions are sampled with a single k-point coplanar with the Γ-point;[‡] and wavefunctions are represented by plane-wave bases with the energy cutoff of 500 eV. Occupancy smearing are done with Gaussians of width 0.1 eV. Atomic and electronic structures are relaxed self-consistently: first, the self-consistent-field (SCF) relaxation of the electronic density is converged to within an energetic tolerance of 1 μeV between successive steps using a variational approach;[98–100 §] relaxation of the atomic structure then follows with a conjugate-gradient algorithm, and final convergence is considered attained when the forces on the atoms were smaller than 20 meV $Å^{-1}$. Single-point calculations making use of GGA-relaxed geometries are also run on the HSE06 functional (see § IV for more discussion).[101–103]

The formation energy $\Delta E_{\text{ads.}}$ of an adsorbate is calculated by referencing out the simulation-cell stoichiometry with that of the clean (or “slab”, i.e. no-adsorbate) cell and with an appropriate linear stoichiometric combination of the gas-phase references H_2, H_2O, and CO_2. An energy correction of 0.45 eV is added to the DFT energy of the GGA CO_2 reference to correct for

---

[*] Calculations in “Bridging the metal–SAC gap: one picture to rule them all” and “Reaching down to the fundamentals: an exercise in atomic precision” are largely run with the same parameters; see the methodology sections of the relevant publications for details.[1,2]

[†] Version 5.4.4.

[‡] Note that the plane-wave basis imposes a spurious periodicity to the system; however, such interaction between neighboring copies of the simulation cell can be (partially) compensated for, with e.g. multipole corrections as described in the next paragraph.

[§] See the entry of the `ALGO` parameter in the VASP Manual (https://www.vasp.at/wiki/index.php).

systematic errors in the functional. [*] Grimme's DFT-D3 dispersion correction,[104] calculated from the atomic positions, is added to the energy. A density-based dipole correction[105] is applied along the (primary) vacuum direction, helping in screening the electrostatic effects of any adsorbate (and of the catalyst in neighboring images) from the bottom side of the simulation cell, while also enabling the calculation of the cell dipole moment.

For G-MNC calculations, a $3\sqrt{3} \times 4$ orthonormalized graphene supercell with an average C–C bond length of 1.43 Å is used,[†] and over 10 Å of vacuum on each side of the sheet in the third dimension; a 3×4×1[‡] *k*-point grid is used, in accordance with the reciprocal-space-sampling criteria. For metal CTP calculations, each molecule is suspended in *in-vacuo* in a cubic simulation cell of sides 25 Å, ensuring even for the biggest molecule (MPc) a minimal distance of 12.9 Å between atoms in neighboring images. In line with the lack of periodicity inherent to the modeled molecule, only the Γ-point is sampled.

III. Spin-state treatment protocol

It has long been known – and indeed self-evident – that the spin state of the metal in an MNC system is energetically relevant,[106] directly affecting its adsorption[67] and thus catalytic properties. As such, in any investigation into these materials it is imperative to pay extra attention in the correctness of the metal spin state.

Motivated by the failure of calculations conducted towards the start of the project to reliably recover the spin ground state, the vacuum-GGA results presented in this thesis are prepared with the following workflow:

1. For each combination of metal, MNC morphology (MPc, annn-MPor, MN_2C_2, etc.; see Schematic 1), and surface state (clean or any of the adsorbate states), the starting structure is separately relaxed five times with a different initial magnetic moment on the metal site (0–4 μ_B) in

---

[*] See Supplementary Information, Ref.[197]

[†] The bond length (equivalently cell parameter) is chosen with reference to the cell-size relaxations of the pristine graphene sheet under similar computational setups.

[‡] This is prior to symmetry reductions; the same applies to other *k*-point grid size mentioned.

a linear scan. To hopefully steer the geometry – for example the adsorbate adsorption mode – into one compatible with the requisite spin state, the global (simulation-cell) magnetic moment is constrained to the same value via the `NUPDOWN` switch.[*]

2. After the geometric relaxation, the spin constraint is lifted and the calculation is again started from scratch, i.e. from `VASP`'s default atomic densities and random wavefunctions. Relaxation continues until convergence as defined in § II.

The necessity of these measures and their ramifications on the results are further discussed in "The spin conundrum".

IV. Single-point hybrid calculations

Hybrid functionals are density functionals (DFs) which mix a portion of the (nonlocal Hartree–Fock)[107–110] exact exchange functional with a lower-level (LDA or GGA) version thereof. Representing a higher level of theory on the "Jacob's ladder of DF approximations",[111] they are computationally more involved but are often better at e.g. accounting for the bandgap of materials.[112,113][†]

In a single-point calculation, only the SCF (inner, electronic) loop is run to convergence, with the geometry and atomic positions of the simulation cell frozen in place; such calculations thus represent the simple evaluation of the instantaneous electronic ground state at the given structure, without also equilibrating the atomic nuclei. Owing to the high computational cost[‡] of hybrid functionals, we decided to forgo full relaxation in hybrid-functional calculations, and instead only run single-point calculations therewith. In the present work, the 2006 revision[103] to the Heyd–Scuseria–Ernzerhof hybrid functional[101,102] (HSE06) is used.

---

[*] Being a code using an inherently nonlocal basis, stock `VASP` does not support more fine-grain control of the site occupancies.

[†] Still, as the referenced sources also indicate, going to the hybrid-functional level of theory does not necessarily entail an all-round improvement; the optimal functional ultimately depends on both the system and the property to be modelled.

[‡] Each hybrid SCF step takes about an order or magnitude longer than in a corresponding GGA step; owing to the risk of divergence, hybrid calculations also often have to be run at more conservative optimization parameters, further prolonging them.

In the standard workflow of a single-point hybrid calculation, the stored GGA-relaxed structure and atomic magnetizations (where applicable) are first used in a single-point GGA calculation to regenerate a set of wavefunctions, providing a more reasonable initial guess for the slow-converging hybrid calculation compared to `VASP`'s default behavior of starting "from scratch", i.e. from superposing atomic charges and from randomized wavefunctions.[*] The generated wavefunctions are then fed with the structure to a single-point hybrid-functional calculation, with a relaxed electronic convergence criterion of 10 μeV, again from practical considerations. On top of the high computational costs of hybrid functionals, electronic convergence with them is also notedly more difficult than with GGA functionals; diverging calculations are variously restarted with changes in the optimization algorithm[†] or its parameters.

V. Bader charge partitions

The Bader-charge partition scheme is used as a qualitative description of charge distribution and transfer. Within the Bader (or "atoms-in-molecules")[114,115] model, atomic boundaries are to be drawn with reference to the electron density: owing to the localization of the density around atom centers, the surfaces on which the density falls locally to a minimum can be considered their natural boundaries. In this work we use the implementation by Henkelman *et al.*[116–119] Volumetric partition of the simulation cell is done with respect to the reconstructed "all-electron density",[‡] then the volumes are used to partition the valence-electron density.

---

[*] See the entries of the `ICHARG`, `ISTART`, and `INIWAV` parameters in the VASP Manual (https://www.vasp.at/wiki/index.php).

[†] E.g. of the variational algorithms used,[98–100] the conjugate-gradient (`ALGO = All`) may catastrophically fail on a line search; while the damped-molecular-dynamics algorithm (`ALGO = Damped`) usually marches on with the iterative optimization anyhow, but may suffer from slow and non-monotonic convergence.

[‡] See the entry of the `LAECHG` parameter in the VASP manual.

VI. Charging the slab

The `VASPsol` plugin[120,121] for `VASP`, implementing implicit solvation, is used primarily to study the charging behavior of the MNC species, simulated by a series of calculations with the number of (valence) electrons adjusted incrementally in a scan. Owing to the use of the linearized Poisson–Boltzmann equation, with the Debye screening length λ_D set to 3 Å, and the negligence of the cavitation energy (effective surface tension τ set to zero) for better electronic convergence, the solvation is not expected to be adequately accounted for.[*] Rather, the major boon of the model is the distribution of the compensation charge to the change in the electron number; the compensation would have been merely treated as a homogenous background in stock `VASP`.

To single out the electronic effects and to avoid spurious desorption of the adsorbate[†] over the course of the charging process, single-point calculations are conducted on sensible geometries.[‡] Each SCF step in a solvated GGA calculations often take several times longer than the corresponding vacuum calculations to run; interestingly however, solvated hybrid calculations were comparable in per-SCF-step speed and convergence behavior to that in vacuum, and are sometimes slightly faster. Nonetheless, the scans over multiple charge levels (thus to run multiple single-point calculations) using a hybrid functional represent a significant computational effort, which is unfortunately still ongoing at the point of writing. Owing to technical limitations of the code, multipole corrections must also be deactivated for these charged calculations.[§]

---

[*] See however e.g. the recent work by Islam *et al.*,[198] which extends the `VASPsol` plugin to include nonlinear and solvent-size effects.

[†] This has happened repeatedly with adsorbates like $*CO$ and $*CO_2$ in preliminary calculations.

[‡] The geometries used here are mostly based on said preliminary calculations.

[§] See the entry "Monopole dipole and quadrupole corrections" in the VASP manual.

The following MNC candidates are examined in the charging calculations:

- A CoPc molecule adsorbed on a $6\sqrt{3} \times 8$ rectangular graphene sheet to simulate a carbon nanotube support; a *k*-point grid of 1×2×1 is used, again according to the criteria specified in § II.
- An MN_2C_2 (M = Fe, Ni) center embedded in the $3\sqrt{3} \times 4$ rectangular graphene sheet.
- An MN_2C_2 center embedded in a 4×4 graphene-sheet super cell; a 4×4×1 *k*-point grid is used. Note however that the MN_2C_2 center is arranged differently from the case shown in Schematic 1 – the N atoms are in a *trans* configuration here, as opposed to the *cis* configuration used elsewhere in this thesis.

Bridging the metal-SAC gap: one picture to rule them all

This Chapter is a summary of the work we have presented in Ref.[1*] Despite the apparent simplicity of CO_2-to-CO electroreduction, the rate-determining step thereof is still a source of much contest. Herein, we present a common framework under which the reaction can be analyzed across the examined active sites: G-MNCs (M = Fe, Ni), CoPc, and transition-metal (TM) surfaces. Firstly, we establish that the electron transfer to $^*CO_2$ does not impede the reaction even on G-MNCs. Afterwards, we show that both CO_2 adsorption ($CO_2 \rightarrow {}^*CO_2$) and protonation ($^*CO_2 \rightarrow {}^*COOH$) can become rate-limiting on MNCs; such variation is attributable to the electrostatic stabilization of the sizeable $^*CO_2$ dipole moment on these systems at reducing potentials, which in turn is caused by their narrower *d*-states compared with TM surfaces. We also present an activity volcano and a coverage map based on a microkinetic model of the surface, using these two adsorbate states as the key descriptors.

I. Background

On account of its potential in converting cheaply-available and renewable electricity into a myriad of value-added products,[122–124] electrochemical CO_2RR has seen immense research interest in recent years. Even its most simple product CO can be used, for example, in feeding the Fischer–Tropsch process,[18,19] which polymerizes single-carbon species into multi-carbon fuels as a form of energy storage. Conventional catalysts of the reaction are often based on the surface of noble metals; meanwhile, MNC systems based on the metal-doping of organic matrices are less expensive in material cost, and also less prone to hosting the hydrogen evolution reaction (HER),[30,31] parasitic to the desired reduction of carbon.

---

[*] Full text (in "Appendices § II") and figures reproduced with the permission of co-authors; authorial reuse of the article in this thesis is covered by Springer Nature's policies (https://www.nature.com/nature-portfolio/reprints-and-permissions/permissions-requests#Author%20reuse).

Still, a key piece of the deceptively simple reaction mechanism – its rate-determining step (RDS) – remains ill-understood and eludes scientific consensus:

- Identity: depending on the surface on which CO_2RR occurs, the RDS is variously proposed to be CO_2 adsorption,[31,125–127] protonation,[128,129] or even the formation of *CO from *COOH.[130]
- Nature: it is unclear whether the adsorbed *CO_2 exists merely as a polarized neutral adsorbate stabilized by the field, indicative of facile electron transfer between the surface and the adsorbate;[131,132] a single-electron-charged species;[27,133] or some middle ground between the two involving partial charge transfers.[78,127] In particular, the second option being the result of a proton-decoupled electron transfer, it would preclude the use of the usual computational-hydrogen-electrode methodologies.[134]

This study encompasses TM surfaces, the graphene-based MNC single-atom catalysts (SACs) G-FeNC and G-NiNC, and the supported Co phthalocyanine which can be considered a molecular analog to these G-MNC systems. We thus present in Ref.[1] our contribution towards the resolution of these issues by demonstrating that how electron transfer to CO_2 is unlikely to be rate-limiting even on MNCs, hence allowing us the use of the usual repertoire of theoretical electrochemical methods to describe these systems. Combining experiments and calculations, we show that for MNCs the RDS of CO_2RR can variously be CO_2 adsorption or protonation. We also propose the dipole–field stabilization of the CO_2 state as a common determining factor to these variations in behaviors, rationalizing it in view of the differing *d*-state electronic structures of the systems. Finally, we present a microkinetic model built on free-energetic considerations and make qualitative recommendations and interpretations therewith.

II. Is electron transfer rate-limiting in MNCs?

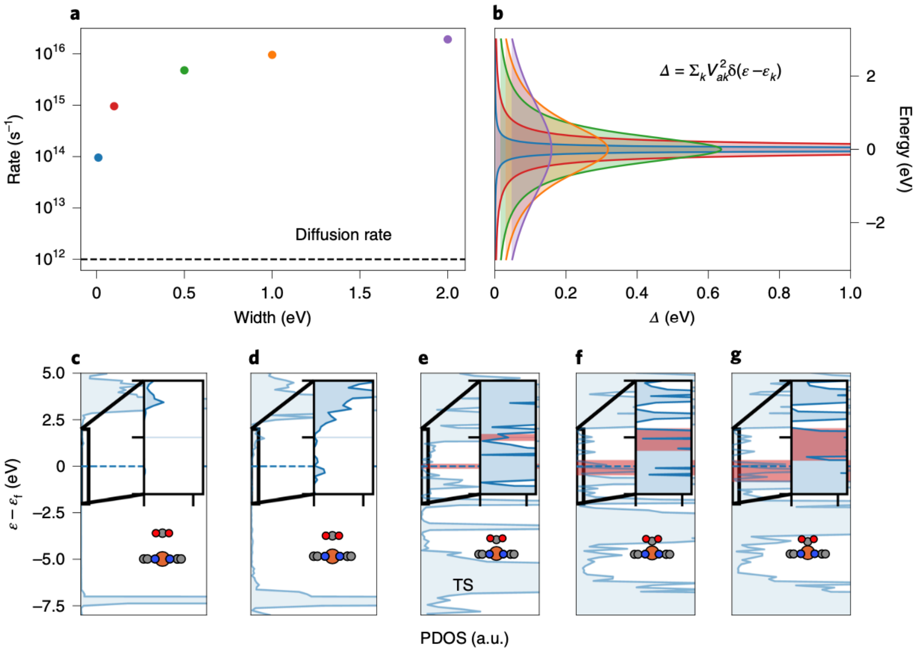

Figure 2. (a) Variation of the rate of electron hopping against the width of the idealized state peak straddling the Fermi level; the dashed line indicates a nominal rate[135] for species to diffuse to the surface. (b) Visualization of the Lorentzian peaks in (a) as given by the (c) CO_2-projected DOSes at various snapshots of the adsorption process; an estimation of its width is indicated by the red band. (Reproduced from Fig. 1 of Ref.[1])

We start by theoretically addressing the second issue named above: the nature of the RDS – or rather, whether it is the electron transfer to the adsorbed CO_2. The rate of electron hopping (transfer) can be estimated from Fermi's golden rule, which depends on the overlap between the relevant states and the density-of-states at the energy level – which can together be identified (via the Newns–Anderson model[136–138]) to be the density-of-states (DOS) projected onto the adsorbate. Even with an exceedingly small width of 0.1 eV, the hopping rate is estimated to be two orders of magnitude faster than the diffusion of solvated species to the catalyst surface (Figure 2a). Inspecting the DFT-calculated projected DOSes (pDOSes) along an adiabatic adsorption pathway as prepared by a climbing-image nudged-elastic-band algorithm,[139,140] we see at least for this sample G-FeNC system that the $^*CO_2$ state is more than wide enough to support the requisite electron transfer (Figure 2c).

It has been shown that the electron transfer rate can however indeed be insufficiently fast for CoPc, if it is merely adsorbed on pristine graphene.[141] However, in use the graphene is often doped, and N-doped graphene have been demonstrated to be useful in immobilizing and activating MPcs for various catalytic purposes.[43,142,143] Inspired by such findings, we have simulated the N-doping of the graphene support in DFT; it is shown that the adsorbate states are fairly responsive to the doping (Figure 3), hinting at well-hybridized states which assuages concerns about electron transfer – and ensures that the usual DFT toolbox continues being applicable to our problem.

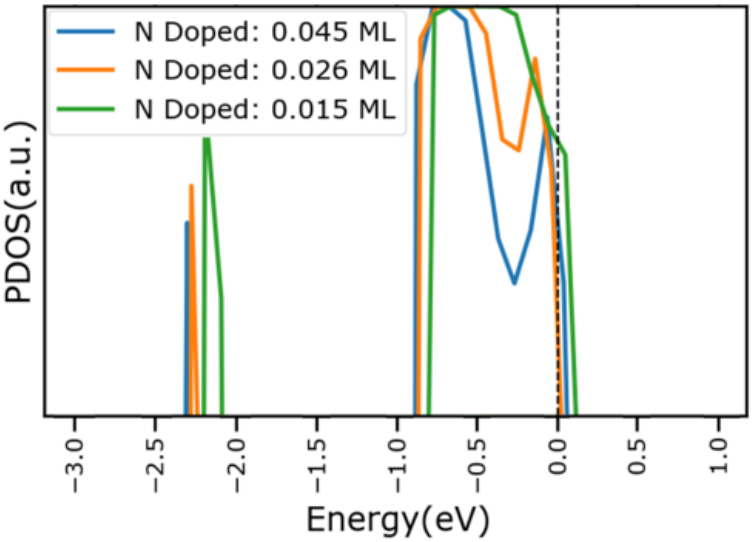

Figure 3. CO_2-projected pDOSes for *CO2 adsorbed on CoPc adsorbed on N-doped graphene. (Adapted from Supp. Fig. 6 of Ref.[1])

III. RDS variation in MNCs

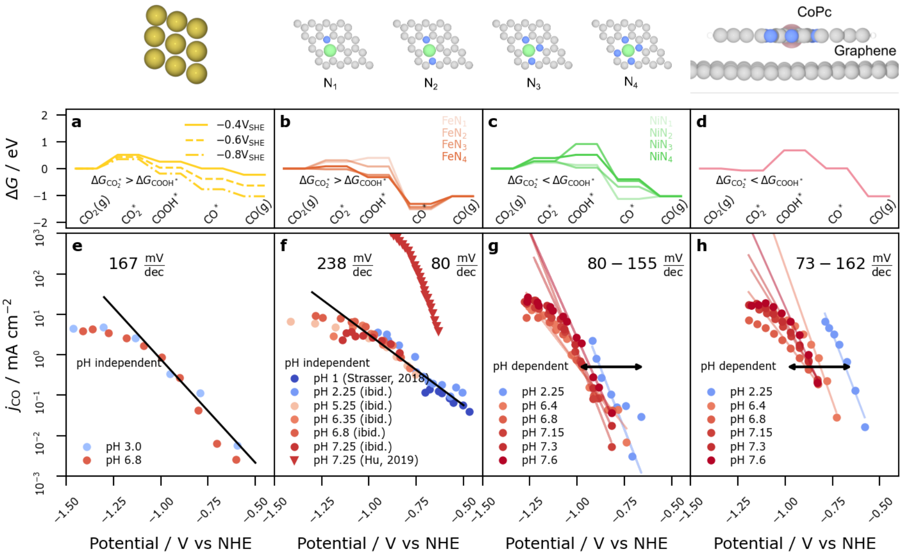

Figure 4. Free-energy diagrams for the CO_2-to-CO reaction on (a) Au(211), (b) G-FeNC, (c) G-NiNC, and (d) CoPc. The dashed lines in (a) shows the corresponding energetics at various potentials, and the differently shaded lines in (b–c) the energetics on the different G-MNC motifs. (Adapted from Fig. 2 of Ref.[1])

Following the synthesis of the MNC samples with standard/previously-used methods,[29,35,144] we are able to evaluate their performance using a three-electrode H-cell setup. Interestingly, the electrochemical current density on the G-FeNC sample showed independence from the pH on the normal hydrogen electrode (NHE) scale in a similar manner to Au, hinting at a chemical RDS; meanwhile both the G-NiNC and CoPc samples exhibited pH dependence, pointing towards an electrochemical one. Indeed, in our potential-dependent DFT calculations[145,146] we have recovered matching behaviors at the potential of interest: reasoning that the later barriers are not limiting due to the overwhelming energetic favorability of the *COOH to *CO step, we can model the chain of reaction by only examining the surface intermediates. As such, we conclude that in the above examples Au(211) and G-FeNC are CO_2-adsorption-limited, while G-NiNC and CoPc are protonation limited.

IV. *CO_2 dipole, the central quantity

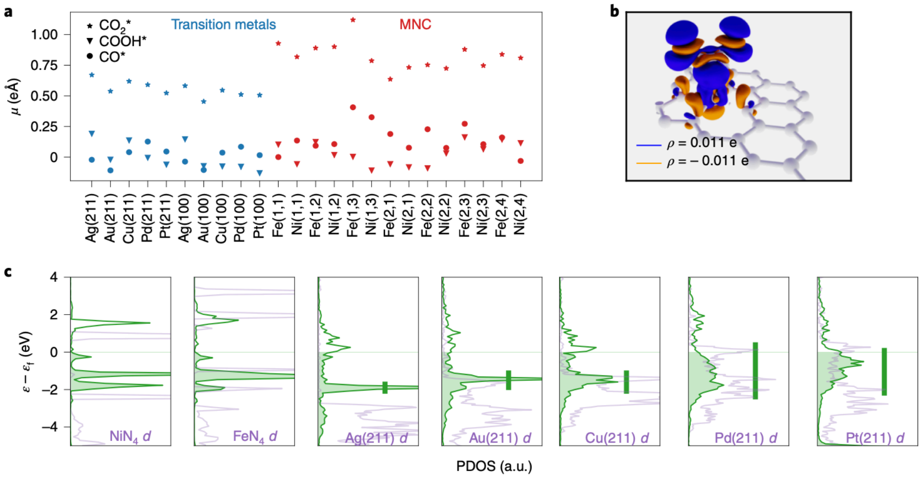

Figure 5. (a) Comparison of the adsorbate-induced dipole moments on various C_1 adsorbates on select TM facets and G-MNCs. (b) Visualization of the charge-density difference at the NiN_4 center upon CO_2 adsorption. (c) pDOS plots of the *CO_2 adsorbate state on various surfaces; the purple and green outlines denote the metal-*d* and CO_2 projections respectively. The green overlaid bar illustrates the "width" of the metal-*d* state. (Reproduced from Fig. 4 of Ref.[1])

We propose that the adsorbate-induced dipole moment is responsible for the observed differences between the TM and MNC energetics. From simple electrostatics[147] we expect adsorbates to be stabilized by a dipole moment parallel to the electric field; hence at reducing potentials *CO_2 with its relatively large dipole moment (Figure 5a, b)[*] is exceptionally stabilized on MNCs in comparison to TM surfaces. This can be rationalized through the Newns–Muscat model,[148] which links the electric dipole to the adsorbate-state width via the interaction between the adsorbate and the surface – on weakly-interacting surfaces (1) the adsorbate states remain unbroadened, and (2) the adsorbate charge polarization is not neutralized by the surface, hence the correlation, which we can also observe in action by comparing Figure 5a and c.

---

[*] Since the dipole moments are directly calculated by VASP which treats electrons as being positive, a positive dipole would be one which points into the surface. The rest of the thesis will follow this convention.

V. The activity volcano

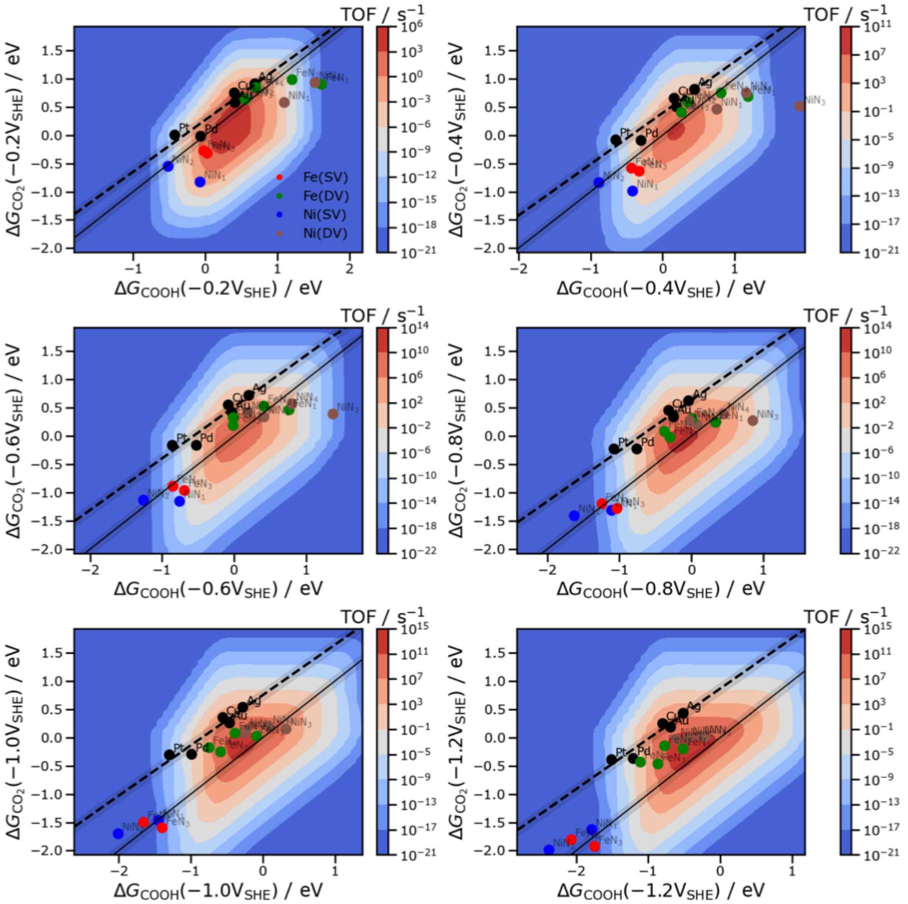

Figure 6. Activity volcano plots at various reducing potentials (−0.2 to −1.2 V relative to the SHE); the red, green, blue, and brown points denote respectively the single-vacancy- (SV-) embedded FeNC, double-vacancy- (DV-) embedded FeNC, SV-NiNC, and DV-NiNC; and the black points, TM surfaces. (Reproduced from Supp. Fig. 11 in Ref.[1])

Based on the TM scaling relations (see Supp. Fig. 10) and the energetics laid out in § III we have built a microkinetic model in `CatMAP`[149] (Figure 6). Using the free energy $\Delta G_{\text{ads.}}$ of the *CO_2 and *COOH, we have an expedient formation which places the summit of the activity volcano near the origin; the parity ($x = y$) line thus serves to delineate the *CO_2-adsorption-limited regime above, and the *CO_2-protonation-limited one below. While we have noted that *CO_2 is stabilized by a reducing potential (downward-pointing field), the electronic driving force means that *COOH and other reduced species will eventually win out. By the model we see that all the TM surfaces remain adsorption-limited throughout the potential range, and are joined by the MNCs at large overpotentials.

Inspecting the coverage plots (Figure 7), we see that the surface is expected to quickly become *CO-poisoned after a mere shift of the binding energies by some 0.5 eV. This firmly renders the single-vacancy MNCs inactive towards the reaction and highlights the subtlety required of the ideal catalyst: moderate binding towards $^*CO_2$ and *COOH, plus narrow *d*-states enabling electrostatic stabilization of the $^*CO_2$ dipole.

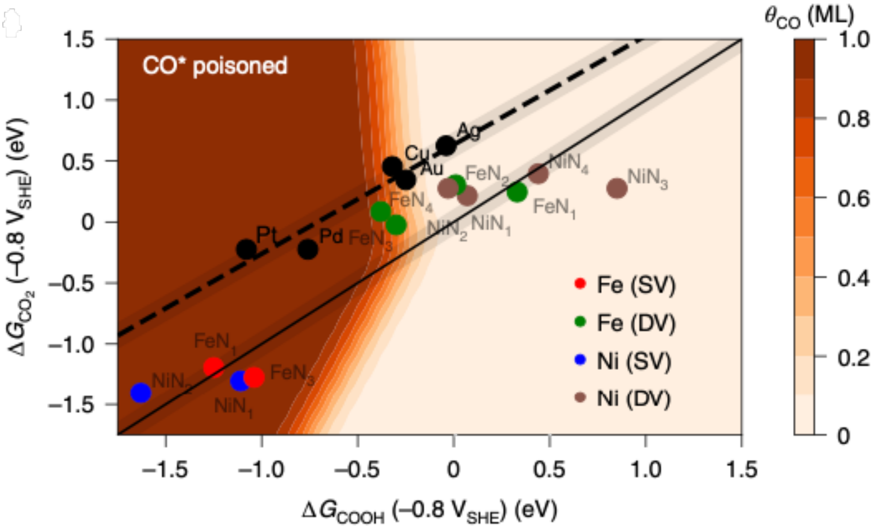

Figure 7. *CO coverage plot at −0.8 V vs. SHE, based on the same microkinetic model as used for Figure 6. (Adapted from Fig. 3b of Ref.[1])

VI. Discussion

In the present work we have examined the trends in activity for both TM facets and extended and molecular MNCs, showing that a common framework based on the adsorbate-induced electric dipole and the *d*-state interaction exists for the description thereof. However, our analysis has also shown the landscape around the activity peak to be rather precarious, thus requiring fine control of both the catalyst composition and operando conditions to maximize CO_2RR activity.

Reaching down to the fundamentals: an exercise in atomic precision

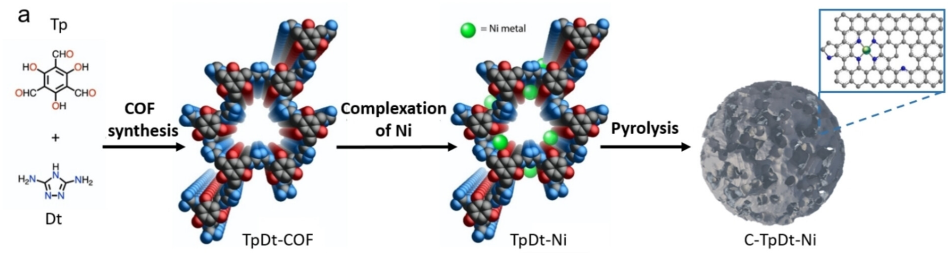

Schematic 2. Synthesis of C-TpDt-Ni catalysts. (Adapted from Fig. 1a in Ref.[2])

This Chapter summarizes the work we have presented in Ref.[2][*] While the Ni–N–C system has been known as a candidate for the electrochemical CO_2RR with the G-MNC-like single-atom NiN_x motifs touted as the catalytic center, fundamental descriptors for their performance remain obscure: the turnover frequency (TOF) measuring per-site intrinsic activity, and the site density (SD) describing their abundance on the electrode surface. Here a family of covalent-organic-framework- (COF) based electrocatalysts are prepared and characterized, featuring fabrication-temperature tunable NiN_x content. Atomically-dispersed Ni sites are identified with X-ray-absorption-spectroscopic and electron-microscopic techniques, and their densities estimated with photoemission. These experimental tools, combined with DFT-based microkinetics, allow for the characterization and modelling of the surface sites that are well-grounded in both reality and theory.

---

[*] Full text (in "Appendices § II") and figures reproduced with the permission of co-authors; the article is published under the CC-BY 4.0 license permitting attributed reuse.

I. Background

MNC catalysts are of interest and potential in electrochemical $CO_2RR^{51,54,59,63,150–152}$ owing to their capacity to suppress parasitic hydrogen evolution reaction (HER);[29,30,134,150,153] in particular, NiNC systems boast both high CO_2-to-CO (>90%) selectivity and operational current densities,[54,59,63,150,152,154,155] thought to be attributable to the weak *H and *CO bindings on their NiN_x single-atom catalytic (SAC) sites, preventing site depletion and poisoning.[63,152] Still, the experimental understanding of the actual catalytic surface is lacking: the identification of the active species, and the evaluation of the site TOF and surface SD, two fundamental quantities.

The catalytic activity of a material, being proportional to both the TOF and the SD, is maximized when high TOF sites are densely located on a porous matrix. To this effect, multiple pyrolytic pathways for MNC-SAC preparation have been proposed (see "Metal–nitrogen–carbon single-atom catalysts § II"); while high-TOF sites have been identified, it remains especially for the density of the generated sites to be systemically analyzed. In Ref.[2] we therefore present our analysis of a Ni-loaded nitrogen-enriched triazole-based covalent-organic-framework catalysts C-TpDt-Ni obtained at different conditions, decomposing their TOF and SD guided by both experimental and DFT techniques.

II. Synthesis

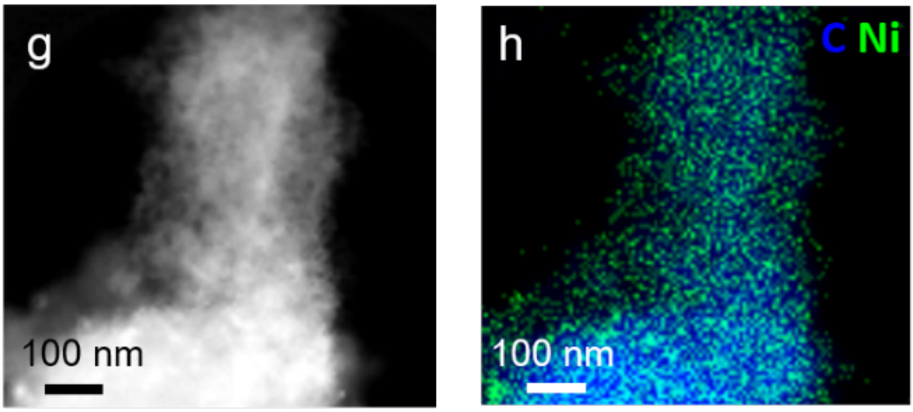

Figure 8. (g) High-angle annular dark-field scanning transmission electron microscopic (HAADF-STEM) and (h) energy-dispersive X-ray spectroscopic (EDS) images of the C-TpDt-Ni-900 catalyst. (Adapted from Fig. 1g–h in Ref.[2])

Opting for a nitrogen-rich precursor for the catalyst,[156] the triazole-based COF (TpDt-COF; see Schematic 2) is first synthesized from condensing its Tp and Dt precursors into a polymer. The COF is then metalated by immersion in a Ni(II) solution, which sees the coordination of Ni ions to the N atoms, forming TpDt-Ni; the Ni ions are shown to be well-dispersed in Figure 8. To improve the electric conductivity of the material, it is then thermally annealed (pyrolyzed) into the carbonized C-TpDt-Ni catalysts at temperatures ranging from 800 to 1000°C; these will then be referred to as C-TpDt-Ni-800, -900, and -1000 respectively.

Additional MNC systems are prepared for comparisons with C-TpDt-Ni. Following similar procedures but replacing the Dt precursor with the less nitrogenated Pa (see Fig. S6 of the article), the C-TpPa-Ni-900 catalyst is prepared. Carbon-nanotube-supported Ni phthalocyanine (NiPc/CNT) and the polyaniline-based PANI-Ni-900[29] are also prepared [see Supporting Information (SI) of the article].

III. Site characterization and identification

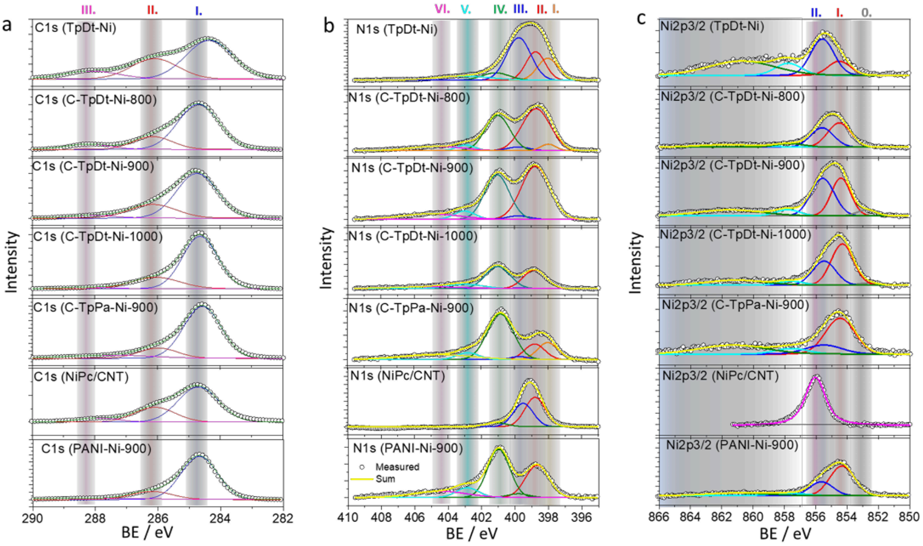

Figure 9. (a) XPS C 1s spectra, (b) XPS N 1s spectra, and (c) XPS Ni 2p spectra for TpDt-Ni, C-TpDt-Ni-800, C-TpDt-Ni-900, C-TpDt-Ni-1000, C-TpPa-Ni-900, NiPc/CNT, and PANI-Ni-900.[29] (Reproduced from Fig. S12 in Ref.[2])

Scanning and transmission electron microscopy reveal the post-pyrolysis structure of the catalyst, which is porous at the micro- and mesoscales (see Fig. 1b, c and S8 of the article) – the COF nanosheets having fused into particles. Metallic Ni particulates encrusted in 3 nm-thick carbonic shells are also observed, but they are expected to be passivated and catalytically inactive.[157,158]

The oxidation states of Ni species are identified by X-ray photoelectron spectroscopy (XPS; Figure 9). Though pyrolysis has slightly boosted the Ni(0) signal, consistent with the appearance of the aforementioned particulates, Ni(I) and Ni(II) remain the majority. Having removed non-immobilized Ni ions via acid-washing (see SI), these are concluded to be surface NiN$_x$ SAC sites; the SDs are calculated from the Brunauer–Emmett–Teller theory[159] and the Ni(I) and Ni(II) site fractions, and are listed in Fig. S13d of the article.

Via X-ray absorption near-edge structure (XANES) and extended X-ray absorption fine structure (EXAFS) spectroscopies, we can inspect the local geometry of the Ni centers. The untreated TpDt-Ni has a XANES spectrum resembling that of rock-salt NiO, suggesting octahedrally-coordinated Ni(II) species (see Fig. 2a in article); meanwhile, the pyrolyzed C-TpDt-Ni samples have similar spectra to NiPc, with the feature at circa 8337 eV being a hallmark of CTP-like motifs in graphene double vacancies.[158,160] Compared with C-TpDt-Ni, TpCt-Ni also sports an extra smaller peak at higher *R*-values in the wavelet-transformed EXAFS spectrum, which indicates disorder around the immediate vicinities of the Ni centers (see Fig. 2c in article).

IV. e-CO_2RR activities

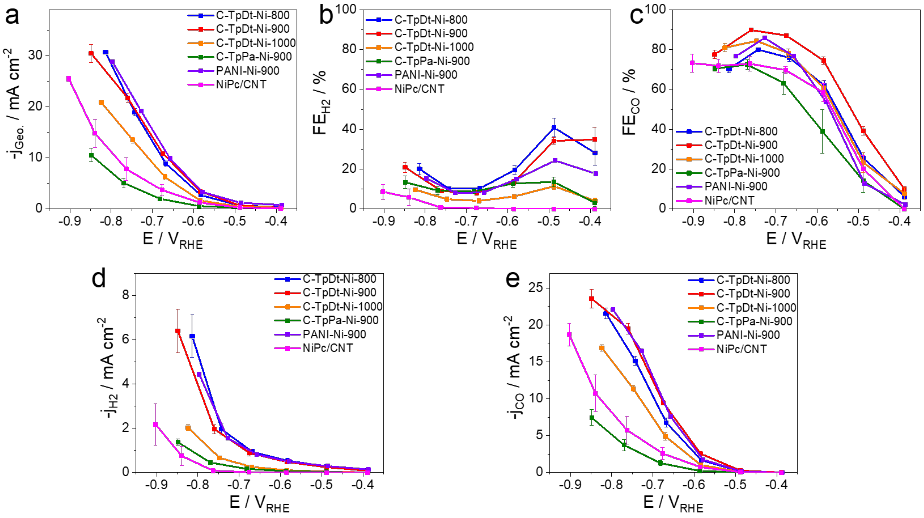

Figure 10. Electrochemical descriptors of CO2RR on the catalyst samples, as functions of the IR-corrected potential. (a) Geometric current densities; (b–c) Faradaic efficiencies; (d–e) partial current densities. (Reproduced from Fig. 3 in Ref.[2])

A liquid-based three-electrode H-cell is used to evaluate the activities of the prepared catalysts (C-TpDt-Ni and the reference samples) towards CO_2RR (Figure 10). Except for the non-pyrolyzed TpDt-Ni which shows negligible activity towards CO, CO and H_2 are the main products for all samples, and CO is invariably the dominant product at appropriate potentials (<-0.7 V). Still, while they behave similarly in terms of selectivity, their activities differ per mass of the catalysts. The C-TpDt-Ni-900 sample is the most performant, showing a 90% selectivity at such potentials and a 22 mA cm^{-2} partial current density towards CO. Excessive temperature is shown to deactivate the catalyst; the C-TpDt-Ni-1000 sample is only two-thirds as active as the 900˚C sample in both HER and CO_2RR. The N-poor analog C-TpPa-Ni-900 trails all other catalysts in performance.

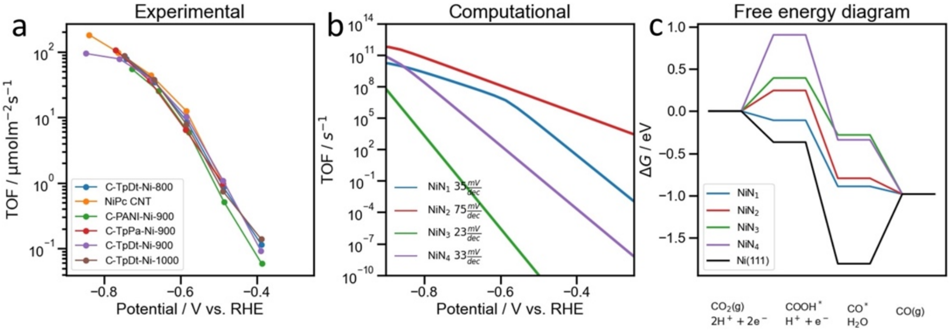

Figure 11. (a) Experimental and (b) microkinetic-model-based potential dependences of the catalyst TOFs; (c) DFT-calculated free-energy diagrams of the CO_2-to-CO reaction on the NiN_x centers and Ni(111) surface at −0.8 V_{SHE} at pH 4. (Reproduced from Fig. 4 in Ref.[2])

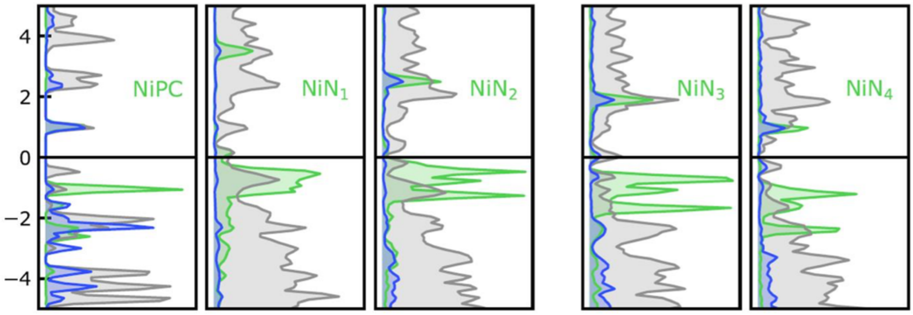

Figure 12. DFT-calculated projected densities-of-states (pDOSes) of Ni (green), N (blue), and C (gray) in NiPc and various double-vacancy-based G-NiNC centers. (Reproduced from Fig. S16 in Ref.[2])

Using the determined SDs to convert the current densities into TOFs, it is noticed that the intrinsic per-site activities of all the pyrolyzed samples (and NiPc) are immensely similar (Figure 11a), hinting towards (1) a common kinetic barrier at *COOH,[1] and (2) an identical dominant active site. A DFT-based microkinetic model shows that the TOFs and their potential responses on different NiN_x motifs are likely to be qualitatively different by orders of magnitude (Figure 11b); therefore, we conclude that all the observed TOFs are mainly rooted in the same NiN_4 motif, like the one in NiPc. From the DFT calculations, it is seen that the *d*-states of the NiN_x motifs are downshifted relative to the Fermi level as the N content increases (Figure 12), weakening the binding to the *COOH state (Figure 11c). It is also noted that the position of the *d*-states in NiPc is calculated to be similar to that in NiN_4; such similarities have motivated our comparative analysis of the extended and molecular MNCs, which is to be presented from the Chapter “Comparative characterization of MNCs” onwards.

V. Discussion

Having carefully devised a chain of experiments, our collaborators have succeeded in experimentally determining the electrochemically active surface areas of real MNC catalysts, decoupling and discerning their SDs and TOFs; leading to the insight that the examined catalysts all have largely identical intrinsic activities. Combined with theoretical input, we are able to conclude that the activities of the catalysts are likely to be uniformly dominated by the NiN_4 sites. The different synthesis processes thus only seem to make for a difference in site quantities, not qualities.

The spin conundrum

(Results presented in the thesis from this point onward are either to be reported in Ref.[3] or have been generated in its preparation.)

As stated in "Computational details § III", a correct picture of the metal spin state is essential towards an accurate description of the adsorption energetics; this short Chapter will demonstrate how so, and discuss some of the challenges we have encountered related to the magnetic moment of the MNCs.

I. Poor mapping from spin input to output

During preliminary research, we have noticed a tendency for the metal magnetic moment (MMM) in an MNC to assume one of the preferred values (which differs for each system). Thinking that it will simplify the analysis of spin state, calculations were initially often only submitted with a reasonable initial guess for the initial magnetic moments, or with a high-spin and a low-spin one, hoping that either will relax into the true minimum. However, the control afforded by such unsystematic method was limited. This difficulty, combined with the observation that the abrupt changes in spin states are often correlated with geometric changes (e.g. adsorbate desorption) during structural relaxation, prompted the design of the current protocol (Computational details § III).

Still we note the protocol to be far from perfect, and there remain occasions where the final output spin state deviates from monotonicity with respect to the input state – i.e. between two calculations, the one starting from a lower spin ends up relaxing into the higher-spin configuration. In Table 1 we have tabulated the results highlighting the offending rows. Such irregularities serve to highlight the need to more systematically sample the spin configuration, so as to increase the chance of covering the requisite ground in the configuration space and recovering the true minimum.

system	state	metal mag. mom. / μ_B			ΔE /eV	ads. geom.
		init.	const.	final		
CoNC$_3$	slab	0	0.052	1.493	0.000	
CoNC$_3$	slab	1	1.189	0.042	0.213	
CoNC$_3$	slab	2	1.501	1.495	0.000	
CoNC$_3$	slab	3	1.61	1.494	0.000	
CoNC$_3$	slab	4	1.752	1.493	0.000	
FeC$_4$	CO	0	0.829	2.356	0.094	M-C
FeC$_4$	CO	1	1.172	2.354	0.094	M-C
FeC$_4$	CO	2	1.444	1.411	0.000	M-C
FeC$_4$	CO	3	2.262	2.355	0.094	M-C
FeC$_4$	CO	4	2.497	2.353	0.095	M-C
abab-CoPor-ox	H	0	0.824	0.839	0.162	C-H
abab-CoPor-ox	H	1	1.373	1.504	0.003	C-H
abab-CoPor-ox	H	2	0.742	0.744	1.508	M-H
abab-CoPor-ox	H	3	1.672	1.505	0.000	C-H
abab-CoPor-ox	H	4	1.795	1.506	0.001	C-H
abab-FePor-ox	COOH	0	1.134	2.059	1.100	M-C
abab-FePor-ox	COOH	1	2.501	2.868	0.000	C-C
abab-FePor-ox	COOH	2	2.027	2.061	1.100	M-C
abab-FePor-ox	COOH	3	2.225	2.227	1.234	M-C
abab-FePor-ox	COOH	4	2.397	2.473	1.153	M-C
abab-VPor-subbed	slab	0	0.745	0.695	0.045	
abab-VPor-subbed	slab	1	0.157	0.157	0.002	
abab-VPor-subbed	slab	2	1.026	0.13	0.000	
abab-VPor-subbed	slab	3	1.238	0.628	0.051	

abab-VPor-subbed	slab	4	1.496	0.75	0.050	
aban-FePor-ox	COOH	0	1.64	2.432	1.026	M-C
aban-FePor-ox	COOH	1	1.94	2.432	1.028	M-C
aban-FePor-ox	COOH	2	2.553	2.939	0.000	C-C
aban-FePor-ox	COOH	3	2.275	2.429	1.026	M-C
aban-FePor-ox	COOH	4	2.433	2.431	1.026	M-C
nabn-CoPor-ox	H	0	0.032	0.943	0.848	M-H
nabn-CoPor-ox	H	1	0.605	1.582	0.003	C-H
nabn-CoPor-ox	H	2	0.933	0.933	0.849	M-H
nabn-CoPor-ox	H	3	1.764	1.583	0.000	C-H
nabn-CoPor-ox	H	4	2.133	1.578	0.000	C-H
nabn-CoPor-ox	slab	0	1.148	1.483	0.000	
nabn-CoPor-ox	slab	1	1.481	1.481	0.000	
nabn-CoPor-ox	slab	2	1.521	0.667	0.231	
nabn-CoPor-ox	slab	3	1.549	1.481	0.000	
nabn-CoPor-ox	slab	4	1.65	1.481	0.000	
nabn-CoPor-subbed	H	0	0.001	1.573	0.006	C-H
nabn-CoPor-subbed	H	1	1.303	1.562	0.000	C-H
nabn-CoPor-subbed	H	2	0.976	0.977	0.910	M-H
nabn-CoPor-subbed	H	3	1.751	1.569	0.004	C-H
nabn-CoPor-subbed	H	4	2.217	1.561	0.002	C-H

Table 1. Systems where the final output metal magnetic moments (MMMs) in the spin scans behaves erratically relative to the input magnetic moments. Δ*E* is the energy difference from the most-stable configuration. The "init.", "const." and "final" mean respectively the initially supplied, post-spin-constrained-relaxation, and final MMMs. Rows belonging to the same spin scan, the final MMMs of which are disordered relative to the initial MMMs, have the relevant MMMs highlighted in red. Spin scans where the final MMMs show a strong correlation with the final adsorbate geometry have the system name highlighted in blue.

II. Different geometries stabilize different spin states

As have been previously noted in § I, changes in magnetization during the relaxation are often correlated with changes in geometries; such occurrences are highlighted in blue in Table 1. In those calculations, an increase in the metal magnetization is directly linked to the "sliding off" of the adsorbate from the metal onto an adjacent C atom.

III. Energetic implications of the spin state

Moreover, sometimes the same (adsorption) geometry can support multiple spin states and see significant energetic changes. Here we tabulate several such adsorbate states for illustrative purposes, showing that we can see up to eV-level differences (Table 2):

system	state	ads. geom.	MMM / μ_B	ΔE / eV
MnPc	CO	M-C	1.135	0
MnPc	CO	M-C	2.986(1)	0.639
nabn-MnPor	CO	M-C	1.334	0
nabn-MnPor	CO	M-C	3.16(1)	0.588
FeN_4	H	M-H	0.99(4)	0.03(5)
FeN_4	H	M-H	3.306	1.168

Table 2. Selection of systems where different metal magnetic moments are supported on similar adsorbate geometries, and their energetic differences ΔE compared to the sampled most-stable configuration.

IV. Conclusions

Though our strategy has a good physical motivation, it was nonetheless sometimes insufficient for steering the system towards specific magnetization (occupation) configurations – which can be a daunting task given that `VASP` is a code using an inherently nonlocal basis. However, it is noted that methods exist for such manipulations, e.g. the Watson Group's (Trinity, Dublin) occupation matrix control plugin.[161]

Overall speaking, these difficulties speak to the complicated energetic landscapes that MNCs have – with a slightly off initial guess one can end up entirely in another local minimum. It is thus essential that care is taken to sample the parameter space to find the "true" energy minimum.

Comparative characterization of MNCs

Having established in "Bridging the metal–SAC gap: one picture to rule them all" how the binding energetics on TMs and MNC-SACs seem to permit a common rationalizing framework and highlighted some of its subtleties, it is useful to verify such a model against more MNC species in a screening study. In this Chapter, the results of said studies are visualized, described, and analyzed.

Herein, we limit ourselves to presenting mostly the hybrid-functional data. By comparing e.g. Figure 17 and App. Figure 5, we see that the formation energies of the adsorbates are overwhelmingly more negative on FeNCs and CoNCs (i.e. the binding is stronger; more so for the former), in GGA calculations compared to those in the hybrid calculations,[*] showing in some cases whole-eV differences. Since the excessively negative *CO formation energies would entail an uphill desorption to gaseous CO,[†] these MNCs will have become *CO poisoned and thus inactive towards further catalysis – which is however at odds with the catalytic activity that they have experimentally demonstrated.[38,151,162] Therefore, the rest of the Chapter shall focus on the hybrid-functional data; the corresponding GGA data may be referred to when appropriate and necessary, and such references are accompanied by corresponding App. Figures in "Appendices § I".

---

[*] While we note that the +0.45 eV correction to the energy of the gaseous CO_2 reference[199] have caused the formation energies to be shifted more negative by the same amount, it must be noted that the differences between the GGA and hybrid $\Delta E_{\mathrm{ads.}}$ are not uniform across all metal centers; particularly, said differences in FeNCs and CoNCs exceed the correction in magnitude.

[†] We estimate the *CO formation energy (relative to the gas references of CO_2, H_2O, and H_2) at which desorption becomes energetically free ($\Delta G = 0$) to be $\Delta E_{*\mathrm{CO}} \approx -0.34$ eV.

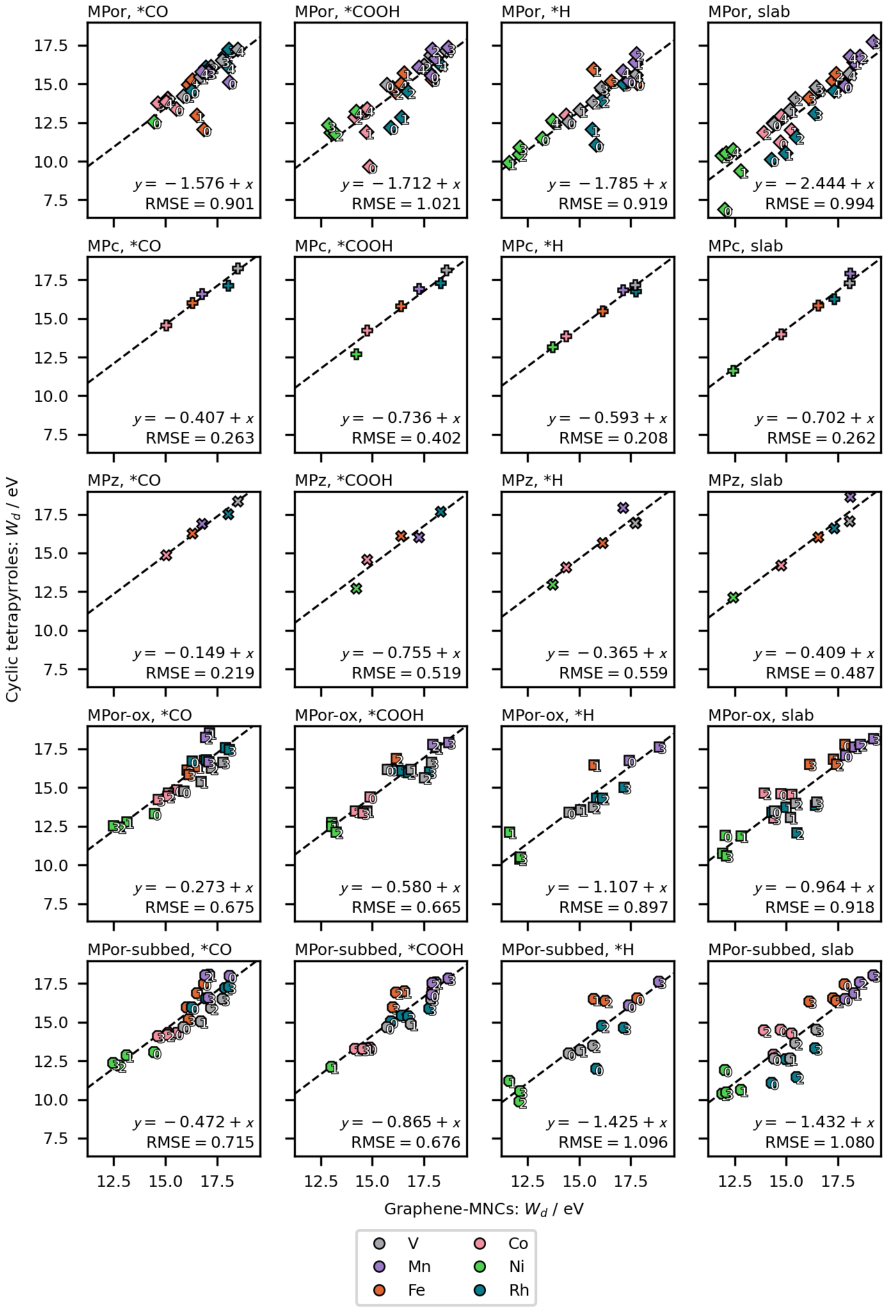

Figure 13. Plot of the hybrid *d*-band widths of the metal CTPs, against those of the G-MNCs of corresponding local stoichiometry. The dashed lines are fitting lines with a fixed slope of unity. Data points are split between subplots by the family of the CTP, and the adsorbate on the metal (if any); the numeric subscripts indicate the number of chelating N atoms in porphyrin derivatives and G-MNCs.

I. CTP-G-MNC correspondence and inter-CTP comparisons

In this Section, we directly address one of the leading questions posed towards the beginning of the thesis: whether the graphene-based, extended MNCs can be meaningfully compared with their molecular analogs (and at times precursors). The analysis will be divided into two parts: comparisons of metal-*d*-state descriptors (e.g. state width and center), followed by comparisons of electronic-density-related observables (e.g. local spin, cell dipole). Thus, we go from the fundamental to the applicational, culminating in § II where we start to examine the adsorbate energetics.

I.1. *d*-state descriptors

We begin by inspecting the metal-*d* states of the MNCs. Figure 13 demonstrates the approximate parity between the *d*-state widths W_d[*] in the molecular and graphene-based MNCs. It is also noted that the identity of the metal remains the dominant factor in the ordering, with

$$W_{d,\mathrm{Ni}} < W_{d,\mathrm{Co}} < W_{d,\mathrm{Fe}} < W_{d,\mathrm{Mn}}$$

being fixed in relative orders, and the V and Rh widths drifting up and down the line relative to the rest of the data points. Meanwhile, changes in the number of chelating N atoms in most cases only cause a relatively small spread in the descriptor values along the fitted line.

The consistently negative intercepts of the fitted lines in Figure 13[†] suggest that the *d*-states in the CTPs are narrower than in the G-MNCs: the MPor (NCP) molecules see the most constriction relative to the G-MNCs, and the MPz molecules the least.

---

[*] Note though, that W is defined as the base of the semielliptical distribution having the same first and second (centered) moments as the normalized pDOS – hence four times the standard deviation thereof. With the pDOS being a sum of projections over the entire energy range, W is not a direct measure of the width of any single state. Still, assuming all other states to be unperturbed at adsorption, and that the one state we are looking at only changes in width but not position, any change in its W is one-to-one to the W of the entire pDOS.

[†] See also App. Figure 1 for the GGA data set. We note that the outliers in the "MPor-subbed, *COOH" panel therein cause the intercept to become positive.

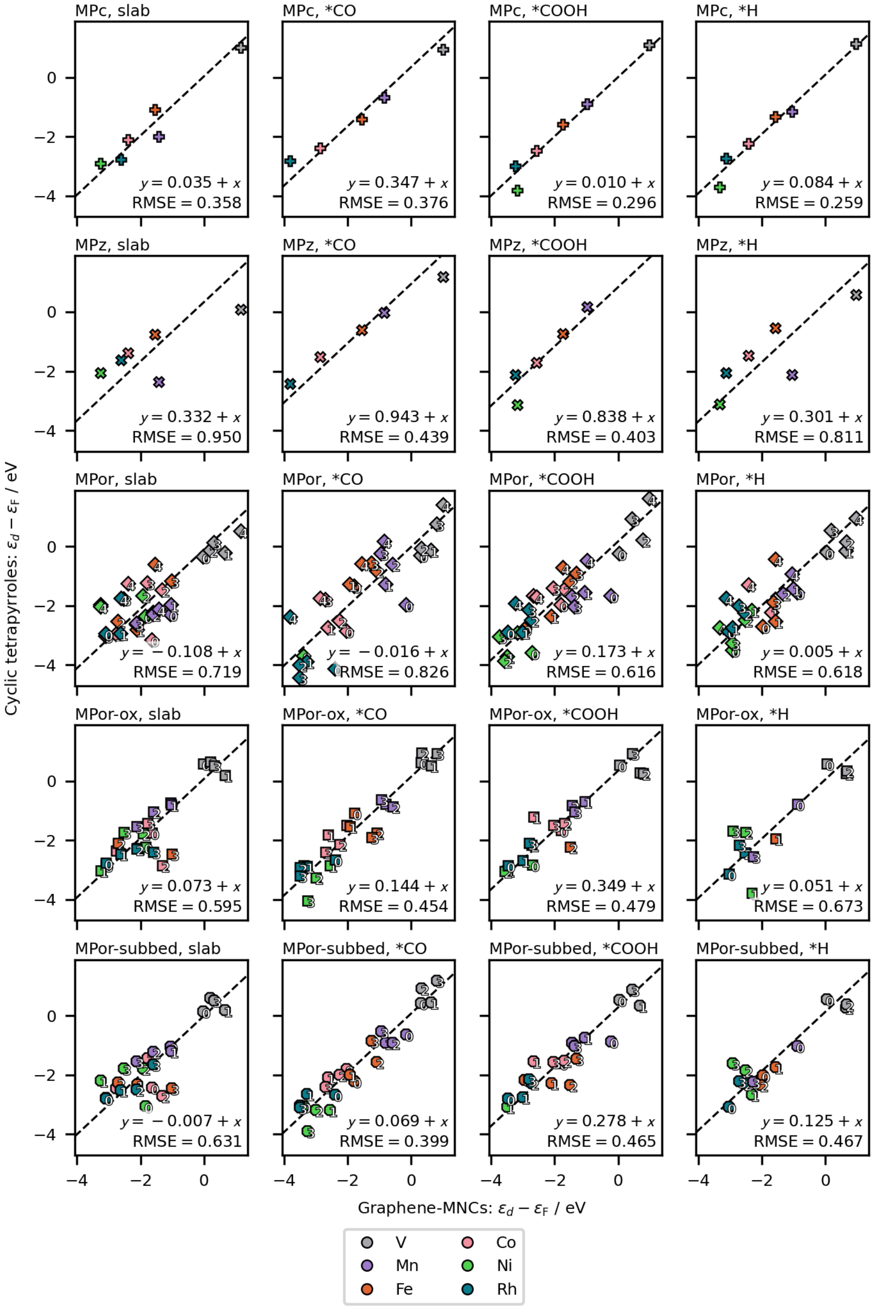

Figure 14. Plot of the hybrid *d*-band centers of the metal CTPs against those of the G-MNCs of corresponding local stoichiometry. The dashed lines are fitting lines with a fixed slope of unity. Data points are split between subplots by the family of the CTP, and the adsorbate on the metal (if any); the numeric subscripts indicate the number of chelating N atoms in porphyrin derivatives and G-MNCs.

In Figure 14,[*] we repeat the previous analysis but with the state center ε_d, defined to be the (p)DOS's mean. Though not without scattering and outliers, it is apparent that the *d*-state position is also consistent between CTPs and G-MNCs, with the metal identity again dictating the ordering, this time being

$$\varepsilon_{d,\mathrm{Rh}} \approx \varepsilon_{d,\mathrm{Ni}} \leq \varepsilon_{d,\mathrm{Co}} \leq \varepsilon_{d,\mathrm{Fe}} \leq \varepsilon_{d,\mathrm{Mn}} < \varepsilon_{d,\mathrm{V}},$$

while the effects of nitrogen content remain secondary.

The ordering is intuitive: Rh being a fifth-period metal, its *d*-projections would contain both the 3*d* and 4*d* states, the former being well beneath the Fermi level; meanwhile the 3*d* metals have their *d*-states increasingly filled, thus sinking below the Fermi level, as one goes left to right in the periodic table. Other than that, the trends are murkier here than for the state widths: there does not seem to be a consistent trend regarding how the state centers are shifted in the CTP molecules relative to the G-MNCs.

I.2. Electronic density

Having looked at descriptors related to the electronic structure and confirmed the approximate parity between the molecular and extended systems, we can climb one rung on the ladder and see if the observables from the electronic densities also align between the two.

---

[*] See also App. Figure 2 for the GGA data set. We note again outliers in the "MPor-subbed, *COOH" panel therein, massively inflating the RMSE.

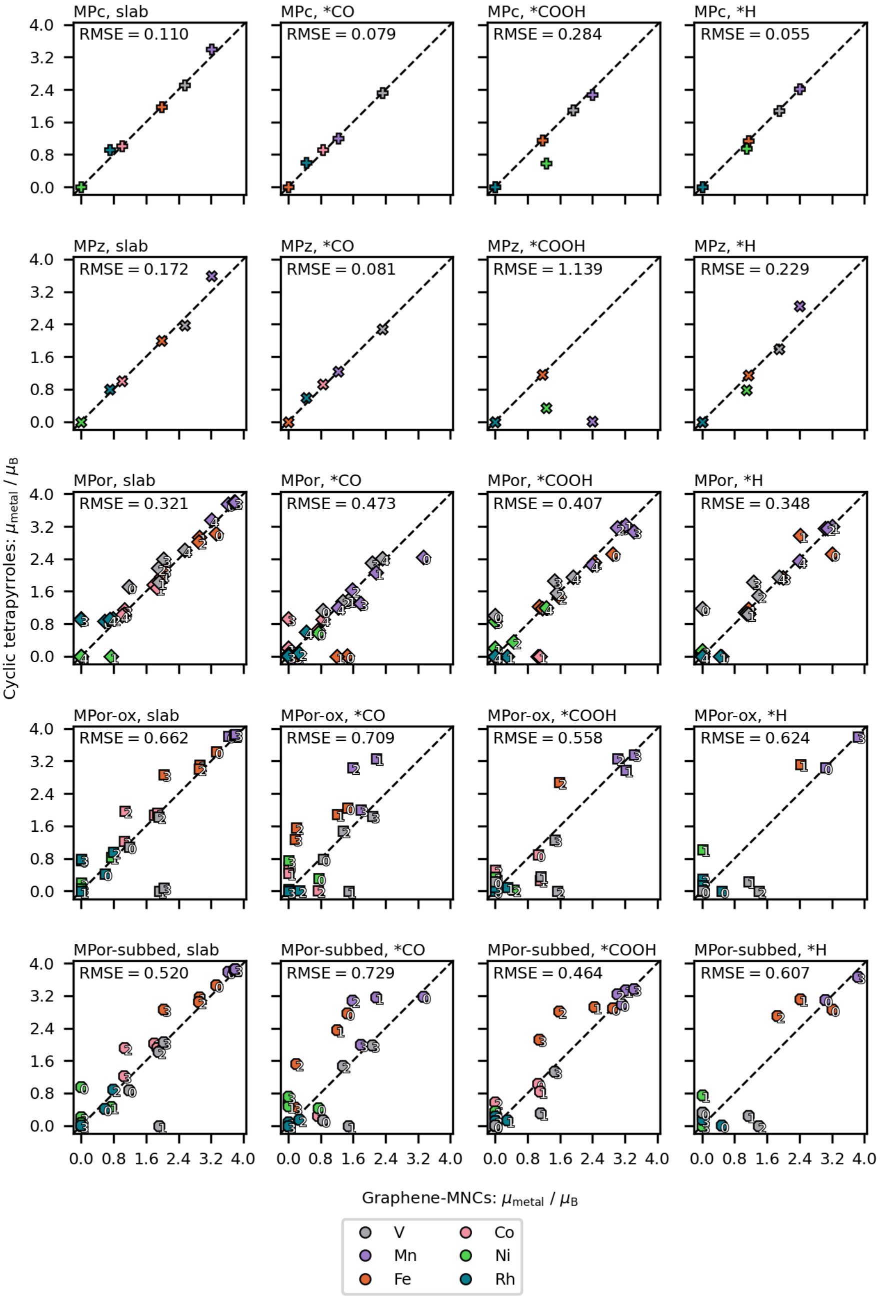

Figure 15. Plot of the hybrid metal magnetic moments of the metal CTPs against those of the G-MNCs of corresponding local stoichiometry. The dashed lines are parity lines. Data points are split between subplots by the family of the CTP, and the adsorbate on the metal (if any); the numeric subscripts indicate the number of chelating N atoms in porphyrin derivatives and G-MNCs.

The correspondence we see in the *d*-state descriptors is also observed in the electron-density distribution, albeit somewhat weaker. Figure 15[*] compares the metal magnetic moment of CTPs with G-MNCs. Again, the metal identity is mostly responsible for the spin value in the same way in both kinds of MNC systems, with Mn supporting higher spin states and Ni remaining in the low-spin state. Deviation from parity seems in comparison with the *d*-state descriptors more severe, which is understandable given the small range of viable values the magnetic moments can take.

Compared with the GGA data set (App. Figure 3), the deviations grow bigger for the hybrid data set, which may hint towards insufficiencies in the implicit assumption (see “Computational details § IV”) that the GGA most-energetically-favorable spin configuration (1) is preserved and (2) remains the most energetically favorable after the change in the functional.

---

[*] See also App. Figure 3 for the GGA data set, which is qualitatively similar in results.

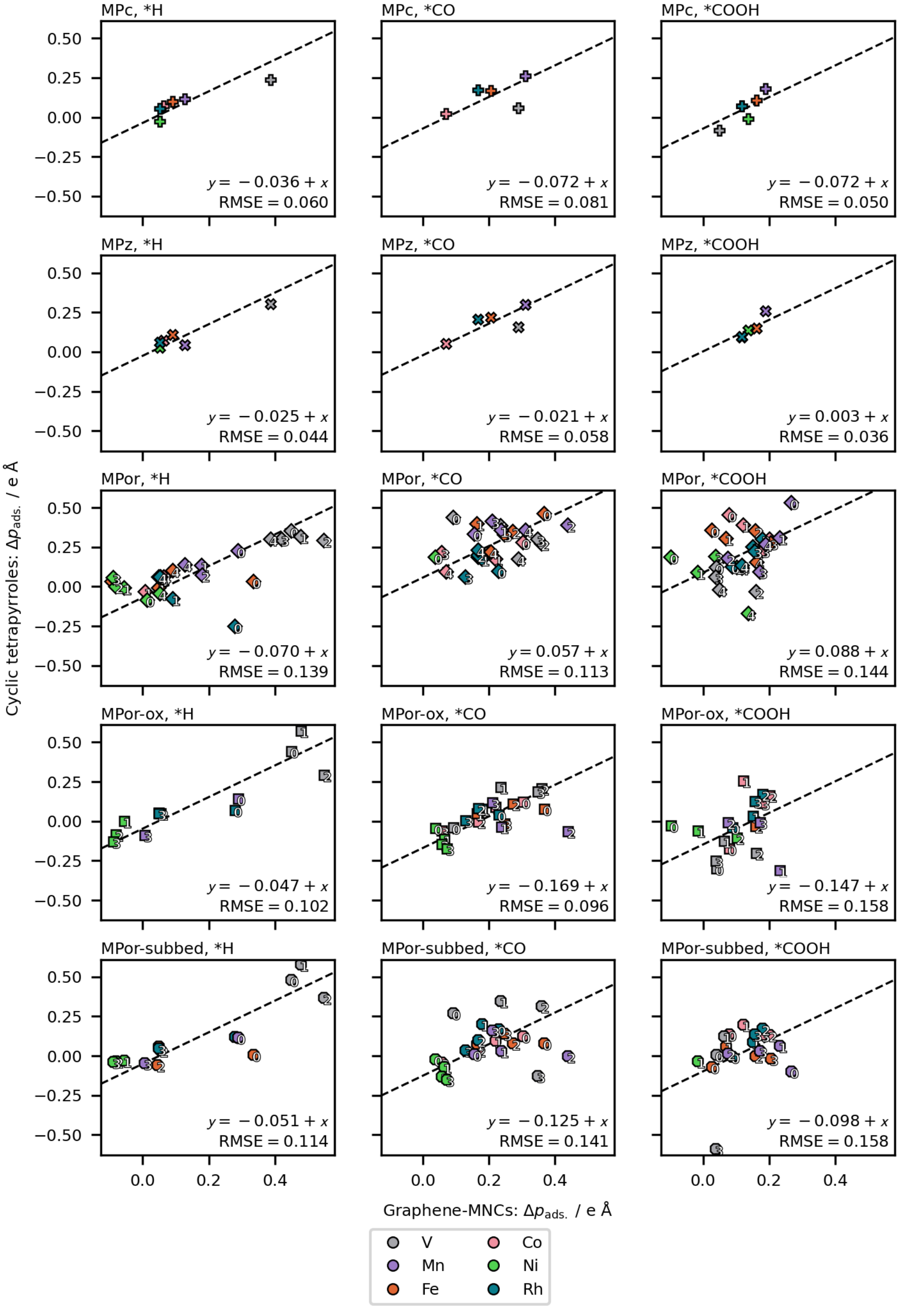

Figure 16. Plot of the hybrid adsorbate-induced dipole moments, on metal CTPs against those on the G-MNCs of corresponding local stoichiometry. The dashed lines are fitting lines with a fixed slope of unity. Data points are split between subplots by the family of the CTP, and the adsorbate on the metal; the numeric subscripts indicate the number of chelating N atoms in porphyrin derivatives and G-MNCs.

In Figure 16[*] the adsorbate-induced dipole moments are plotted. In contrast to the previous results which more or less exhibit parity between the CTP and G-MNC results, the correspondences between the dipoles values are shown to range from being excellent (e.g. *H and *COOH on MPc/G-MNC), moderate (e.g. *CO on MPor-ox/G-MNC), to nonexistent (e.g. *CO on MPor-subbed/G-MNC).

Despite the relative disorder, we still notice from the fits that the intercept is constantly negative, implying the dipoles on the CTPs to be on average slightly smaller than those on the corresponding G-MNCs, with the exceptions of *CO and *COOH on MPor.

II. Coordination and energetics

The trends and correspondences of the more fundamental quantities discussed in the previous Section are admittedly rather coarse-grained; the visible scatter in the data limits their predictive power, largely relegating them to being a descriptive tool for examining these materials. Nonetheless, we now look at the adsorption energetics on the metal center, and how the center's immediate chemical environment (i.e. coordination by N or C atoms) changes them.

In Figure 17[†] we show the approximate parity between the formation energies $\Delta E_{\text{ads.}}$ of C_1 adsorbates (*CO and *COOH) on the molecules and that on the corresponding G-MNC. For both GGA and hybrid calculations, we do find a reasonable parity between the results of molecular and extended systems in both the two- (MN_2, $\#N = 2$) and four-N-coordinated (MN_4, $\#N = 4$) cases. While the molecular backbones do influence the binding non-negligibly, especially in the case of MN_2, the overall trends still tend towards parity. For the MN_3 (in the GGA case) and MN_1 (in both cases) systems the equivalence reduces significantly; while for MN_0 systems no significant trends can be identified, with the VNCs and RhNCs contributing the most to the scattering.

---

[*] See also App. Figure 4 for the GGA data set, which is qualitatively similar in results.

[†] See also App. Figure 5 for the GGA data set, again showing approximate parity for $MN_{1\text{–}4}$ and disparity for MN_0.

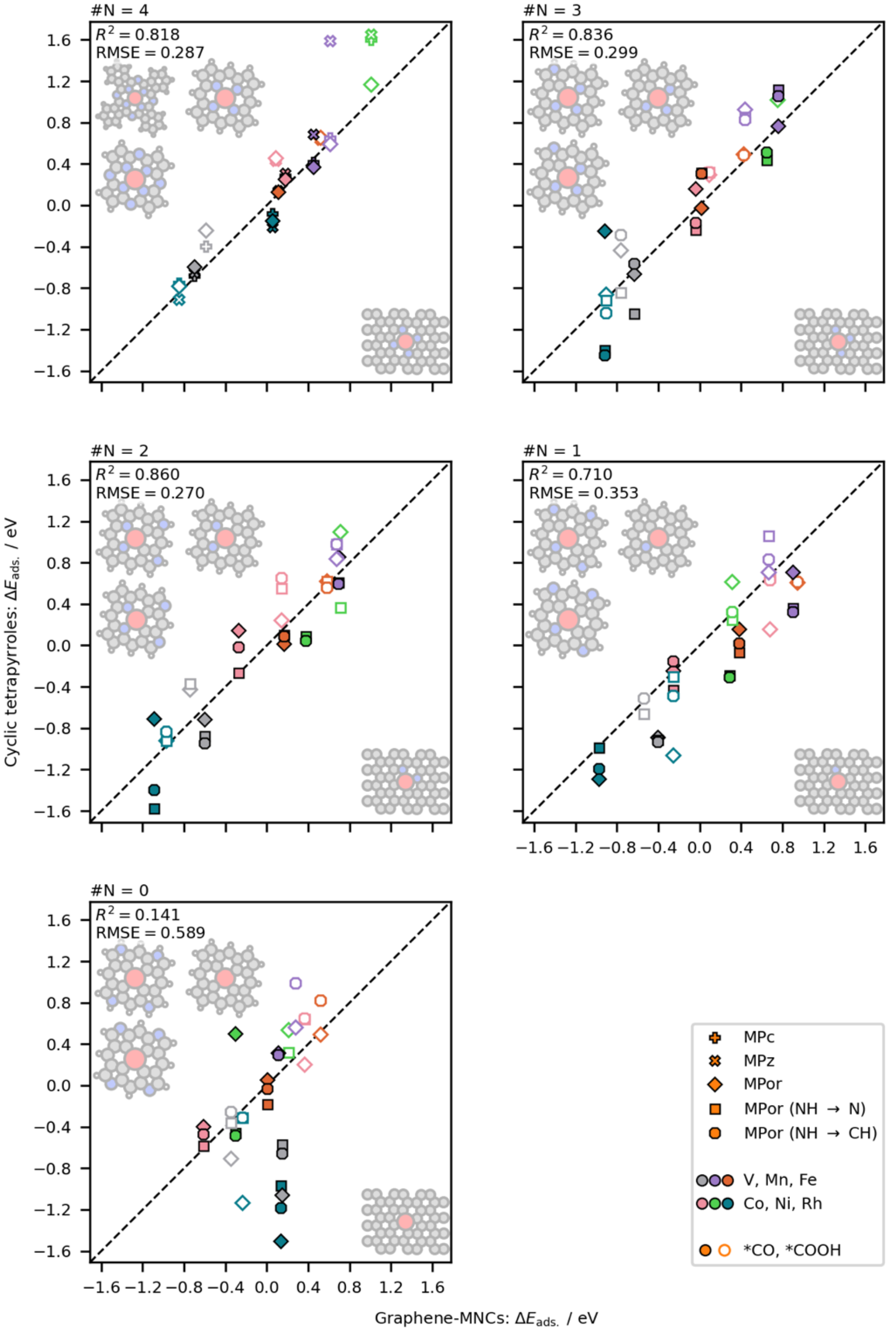

Figure 17. Plot of the hybrid formation energies of the *CO and *COOH adsorbate states on metal CTPs against the same quantities on G-MNCs of corresponding local stoichiometry. The dashed lines are parity lines. Data points are split between subplots by the number of N atoms chelating the metal center.

The deterioration and loss of parity between extended and molecular MNCs was first observed on MPors (CTPs), which was what initially prompted the investigation into the MPor-subbed derivatives; we reasoned that the higher N content in the periphery may have had a greater effect on the metal center than was initially suspected, and a more graphene-like pure-carbon skeleton may have more in common with the G-MNC. As shown in Table 3, while in some cases the MPor derivative classes (MPor-ox and MPor-subbed) do show a better correlation with the G-MNCs, such is not consistently the case.

Family (data set)	#N = 3	#N = 2	#N = 1	#N = 0
MPor (GGA)	0.583	0.830	0.590	0.117
MPor (hybrid)	0.763	0.863	0.718	0.026
MPor-ox (GGA)	0.671	0.799	0.784	0.100
MPor-ox (hybrid)	0.863	0.855	0.700	0.013
MPor-subbed (GGA)	0.717	0.763	0.793	0.224
MPor-subbed (hybrid)	0.844	0.861	0.708	0.306

Table 3. Separate R-squared values of the parity lines in Figure 17 and App. Figure 5 for the MPor, MPor-ox, and MPor-subbed families.

As with the *d*-state and electronic descriptors, adsorbate binding on the MNCs is largely dictated by the metal-center identity (Figure 17). For most levels of N-neighbor abundance (#*N*) except for the lowest, the *CO formation energy ΔE_{*CO} on Mn is consistently the most endothermic, followed by Ni, Fe, and Co, the order of which depending on #*N*. The severe exothermicity of ΔE_{*CO} on V and Rh metal centers will likely lead to a poisoning of the catalyst with *CO, rendering them unviable for CO_2RR. With *COOH (App. Figure 5), the formation energy ΔE_{*COOH} sees somewhat different behaviors: again V and Rh bind the strongest (most negative), and Fe generally weaker (more positive) than Co; however, other aspects of the ordering are not always consistent, which as we will discuss in the next Chapter make for poor scaling between *CO and *COOH binding.

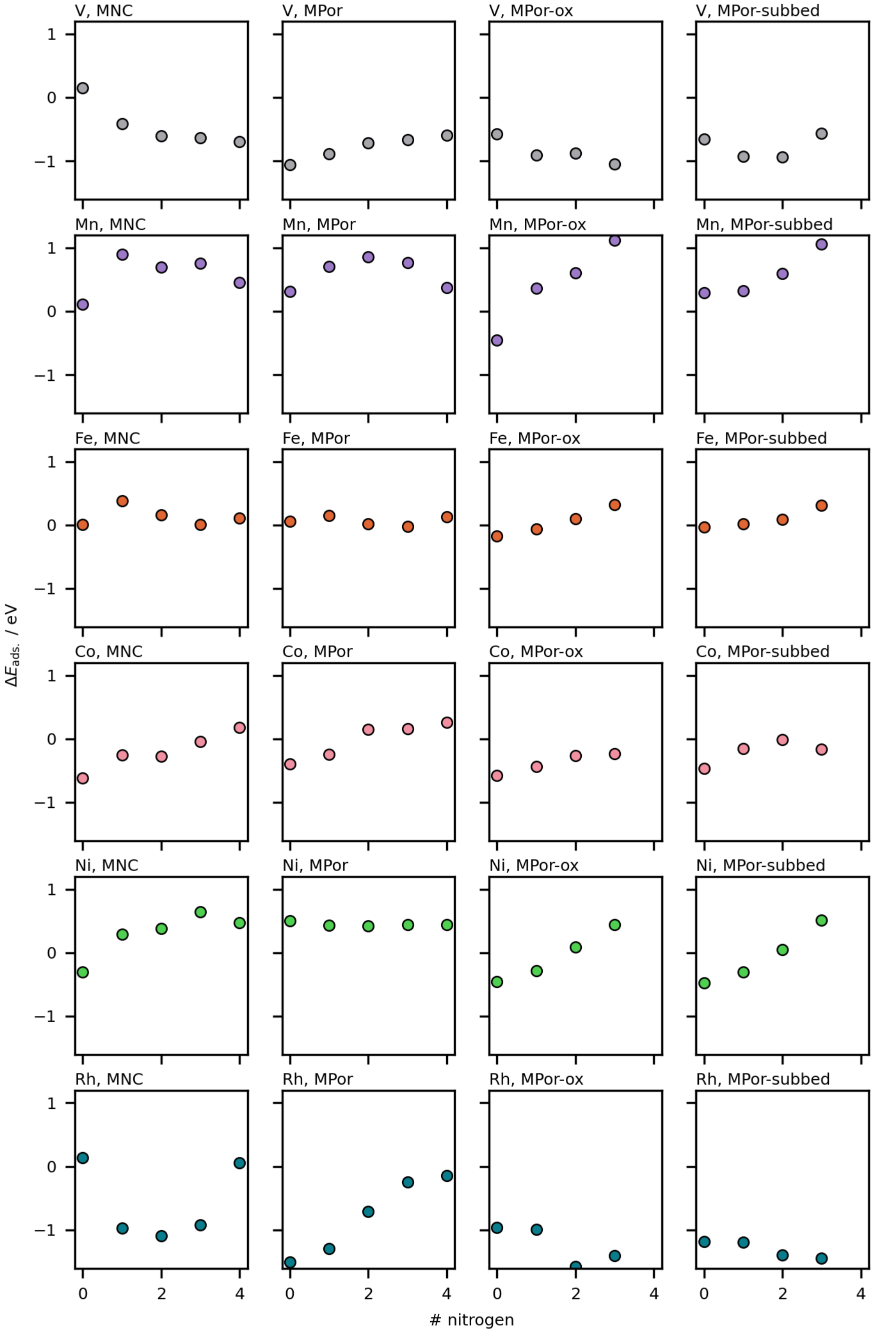

Figure 18. Plot of the hybrid formation energies of the *CO adsorbate state on various MNCs against the number of N atoms chelating the metal. Data points are split between subplots by the metal species and the family of MNC structures. Note that "MNC" here is to be understood as "G-MNC".

The effect of the nitrogen environment of the metal center is in most cases secondary in influencing the binding properties of molecular catalysts. As shown in Figure 18,[*] no general monotonous trend between $\Delta E_{\mathrm{ads.}}$ and $\#N$ is found upon by changing the $\#N$ on the same combination of metal identity and MNC family, except for individual catalyst candidates like G-NiNC.

III. Conclusions

Throughout the Chapter, we have examined the electronic structure, electronic distribution, and the adsorption energetics of the MNCs. Though not without considerable noise relative to exact parity, it is noticed that for most cases there is indeed a correspondence between the properties of a molecular MNC versus that of a G-MNC with a similar local coordination environment for the metal site. These MNC systems being single-atom catalysts, it is also intuitive that the variation of these quantities is mostly ordered according to the metal identity. While the coordination environment of the metal does also contribute to the variation, the effect is less pronounced, and the form of dependence thereon often not permitting the use of simplistic models.

---

[*] See also App. Figure 6 for the *COOH results, which is qualitatively similar in how no appreciable trends consistent across the metals can be identified.

Scaling relations in MNCs

One of the major successes in surface science is the discovery of ubiquitous scaling relations for adsorption energies, reaction barriers, and other quantities, allowing catalytic processes to be modeled and reasoned about with simplicity.[149] Scaling relations are well established for metal surfaces,[163–165] (including alloy-based SACs[166]), supported single atoms,[167] and molecular catalysts.[168,169] Even on G-MNCs, scaling behaviors like Brønsted–Evans–Polanyi scaling[170,171] and free-energy scaling for NRR[172] and ORR[170] intermediates have been reported. However, it remains for us to examine these relations in the context of the thesis: the energetics of CO_2RR intermediates and adjacent species, on both molecular and graphene-based MNCs.

I. Inter-adsorbate scaling

In

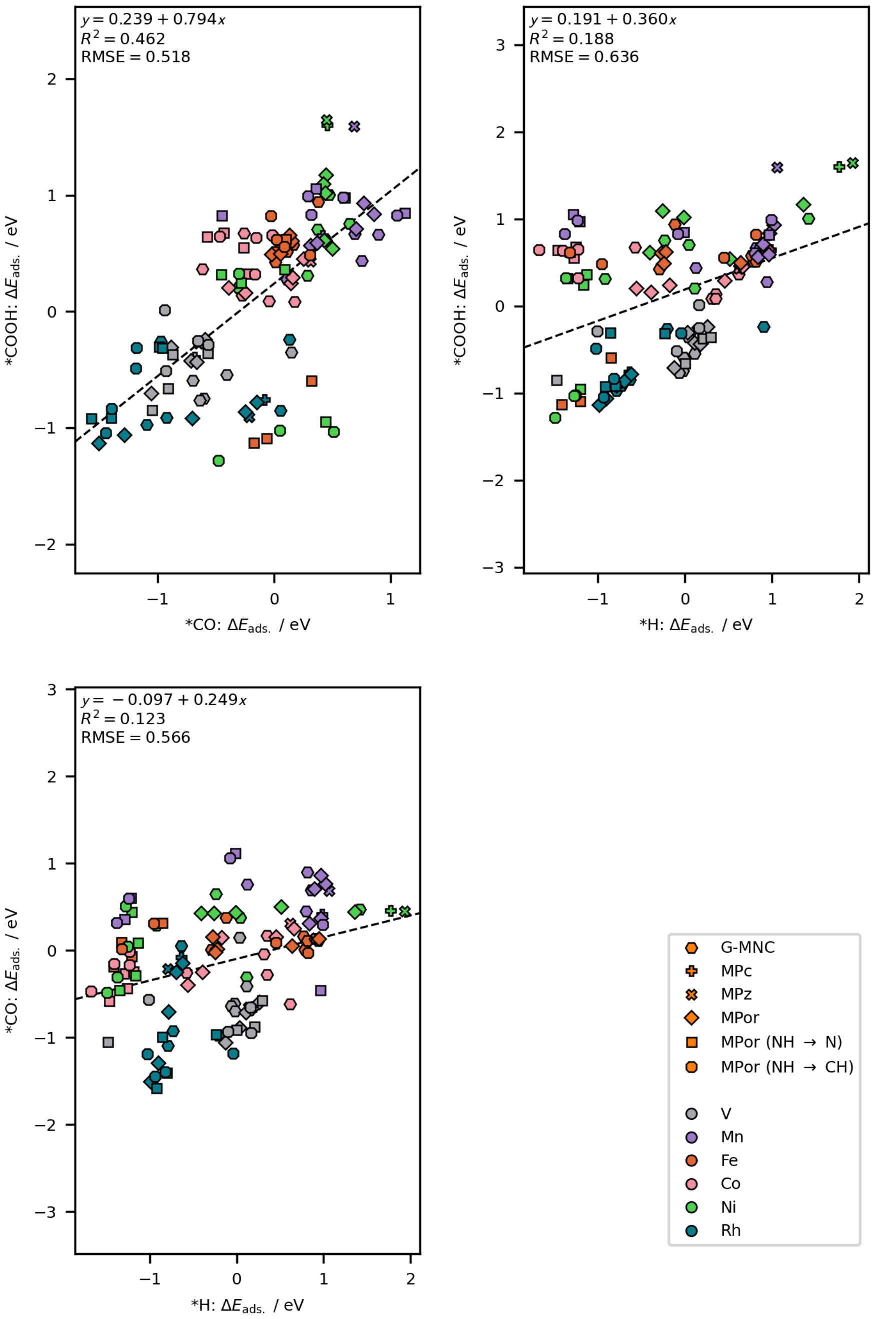

Figure 19[*] we have gathered all the adsorbate formation energies $\Delta E_{\text{ads.}}$ across all the MNC systems[†] in order to check for scaling among them. While there seems to be in general a weakly positive correlation between any pair of such energies, it is apparent that there is no global scaling across the MNCs for these energies – not even for relatively simple and (for other classes of materials) well-attested cases like *CO–*COOH,[1,129] echoing earlier reports of the loss of inter-adsorbate scaling on MNCs.[78,173] The lack of scaling behavior complicates analysis of a system of reactions (e.g. by microkinetic modelling), because the dimensionality of the problem can no longer be reduced.

---

[*] See also App. Figure 7 to App. Figure 9 for the GGA and/or non-spin-polarized data. It is noted that results vary quite significantly with these alternative data sets, but the fits are nonetheless all rather poor.

[†] For the purpose of this Section, we have only included data points where the C_1 adsorbate (resp. *H) adsorbs atop the metal on its C (resp. H) atom.

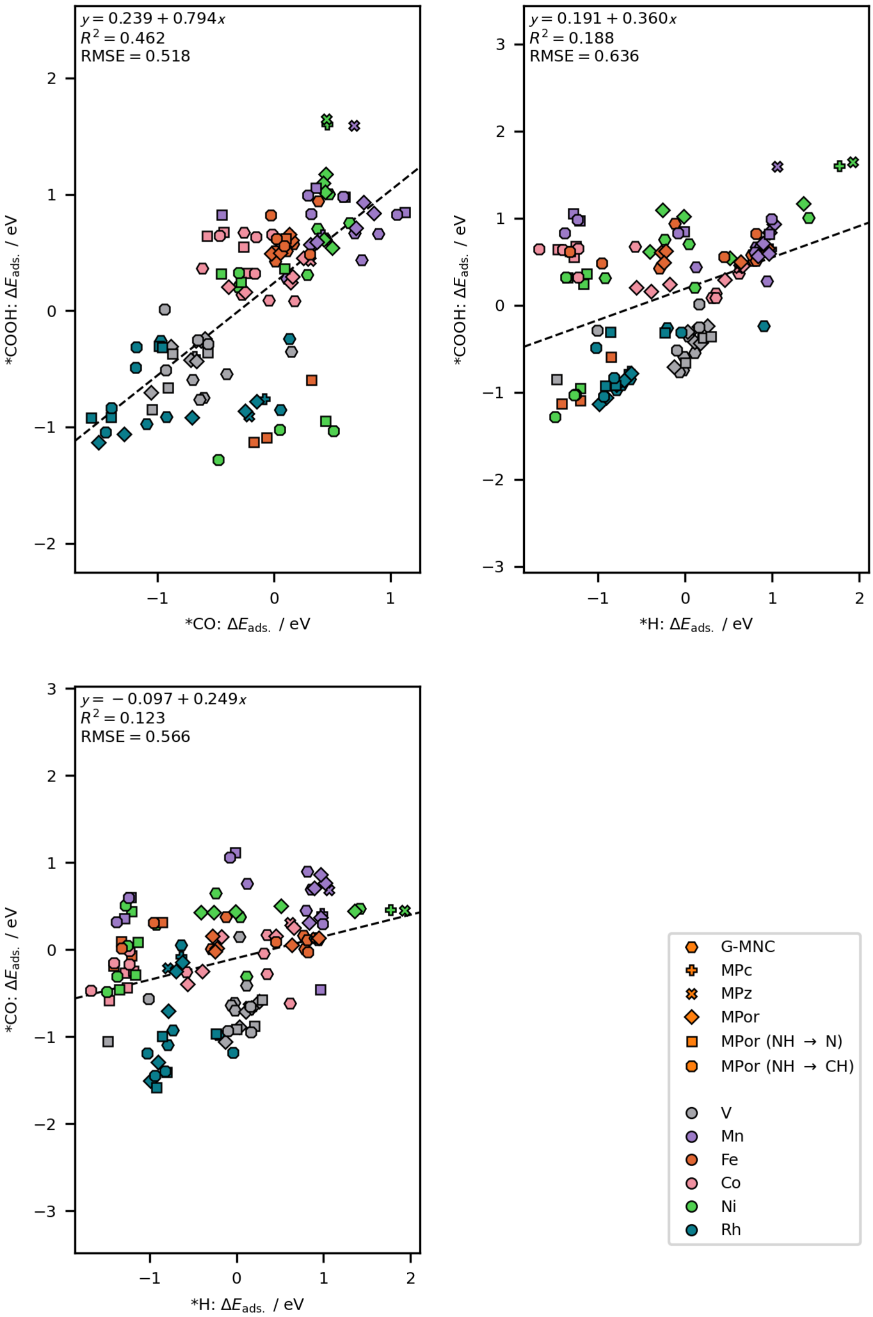

Figure 19. Inter-adsorbate "scaling lines" of their formation energies (spin-polarized hybrid calculations).

Since scaling across all MNCs may be too ambitious, we attempt to re-examine the scaling relations for individual MNC families (Table 4). Scaling lines of good quality (small RMSE, large R-squared) are indicated by green cells, and egregiously bad ones are in red. Interestingly, not even for relatively simple cases like MPc do we see *CO–*COOH and *H–*CO scaling. Still, the non-spin-polarized *H and *COOH energies do globally show better correlation than the other pairings of adsorbates; and we also note that these two adsorbates scale particularly well on MPc and MPz – almost perfectly linear. It is noticed that any scaling-line fit to these two families of MNCs also tend to have quantitatively similar slopes and qualitatively similar quality-of-fit (R-squared values and errors); meanwhile, out of all the MNC families, the MPor derivatives exhibit the worst scaling behavior.

Again, we note that the choice of density functional does not have any obvious general correlation with the quality of the fitted scaling lines. Surprisingly, despite the general difficulty we have had with the determination and convergence of magnetic moments (see "The spin conundrum"), and the removal of a degree-of-freedom effected by going to a non-spin-polarized (pure density) picture, for almost all cases (except for *H–*COOH) the non-spin-polarized scaling lines are not appreciably better fits than the corresponding spin-polarized lines – often even worse.

	Calculation	GGA		Hybrid	
		SP	Non-SP	SP	Non-SP
Ads.	MNC family	(App. Figure 7)	(App. Figure 9)	(Figure 19)	(App. Figure 8)
*CO–*COOH	G-MNC	0.745, 0.469, 0.322	0.640, 0.618, 0.337	0.824, 0.538, 0.400	0.603, 0.376, 0.576
	MPc	1.126, 0.440, 0.532	0.603, 0.395, 0.699	1.499, 0.574, 0.501	0.693, 0.141, 1.163
	MPz	1.242, 0.461, 0.543	0.632, 0.363, 0.738	1.753, 0.703, 0.503	0.630, 0.105, 1.210
	MPor	0.891, 0.638, 0.370	0.602, 0.576, 0.491	0.982, 0.772, 0.323	0.747, 0.342, 0.897
	MPor-ox	0.464, 0.204, 0.367	0.390, 0.268, 0.326	0.534, 0.225, 0.633	0.083, 0.010, 0.429
	MPor-subbed	0.291, 0.074, 0.394	0.176, 0.059, 0.343	0.648, 0.339, 0.588	−0.254, 0.102, 0.394
*H–*COOH	G-MNC	0.551, 0.302, 0.369	0.885, 0.558, 0.363	0.487, 0.236, 0.514	0.787, 0.523, 0.503
	MPc	0.955, 0.984, 0.091	0.946, 0.997, 0.048	1.010, 0.964, 0.146	0.911, 0.995, 0.086
	MPz	0.941, 0.995, 0.050	0.947, 0.998, 0.046	1.040, 0.891, 0.305	0.919, 0.996, 0.079
	MPor	0.950, 0.636, 0.371	1.202, 0.760, 0.369	0.698, 0.442, 0.506	1.102, 0.770, 0.530
	MPor-ox	−0.011, 0.000, 0.412	0.095, 0.013, 0.378	0.012, 0.000, 0.719	0.128, 0.036, 0.423
	MPor-subbed	0.170, 0.053, 0.399	0.331, 0.156, 0.325	0.191, 0.042, 0.708	0.393, 0.316, 0.344
*H–*CO	G-MNC	0.473, 0.263, 0.349	0.898, 0.381, 0.528	0.393, 0.193, 0.470	0.406, 0.135, 0.689
	MPc	0.332, 0.342, 0.340	0.583, 0.348, 0.757	0.337, 0.420, 0.296	0.161, 0.107, 0.642
	MPz	0.329, 0.408, 0.311	0.520, 0.332, 0.720	0.363, 0.474, 0.320	0.151, 0.101, 0.624
	MPor	0.584, 0.298, 0.462	1.043, 0.360, 0.761	0.608, 0.418, 0.462	0.351, 0.128, 0.809
	MPor-ox	0.006, 0.000, 0.400	0.098, 0.008, 0.504	−0.148, 0.021, 0.632	−0.133, 0.027, 0.513
	MPor-subbed	−0.038, 0.003, 0.382	−0.366, 0.100, 0.461	−0.018, 0.000, 0.650	−0.459, 0.274, 0.445

Table 4. Parameters for the fitted inter-adsorbate scaling line of their formation energies. Each cell value consists of the triplet: line slope (unitless), R-squared value (unitless), and RMSE (eV). Adsorbate pairs are given in the format (x)–(y). "SP" stands for "spin-polarized". Cells in green have an R-squared of ≥ 0.7 *and* an RMSE of ≤ 0.4 eV; cells in pink have an R-squared of ≤ 0.4 *or* an RMSE of ≥ 0.6 eV.

II. Inter-quantity scaling

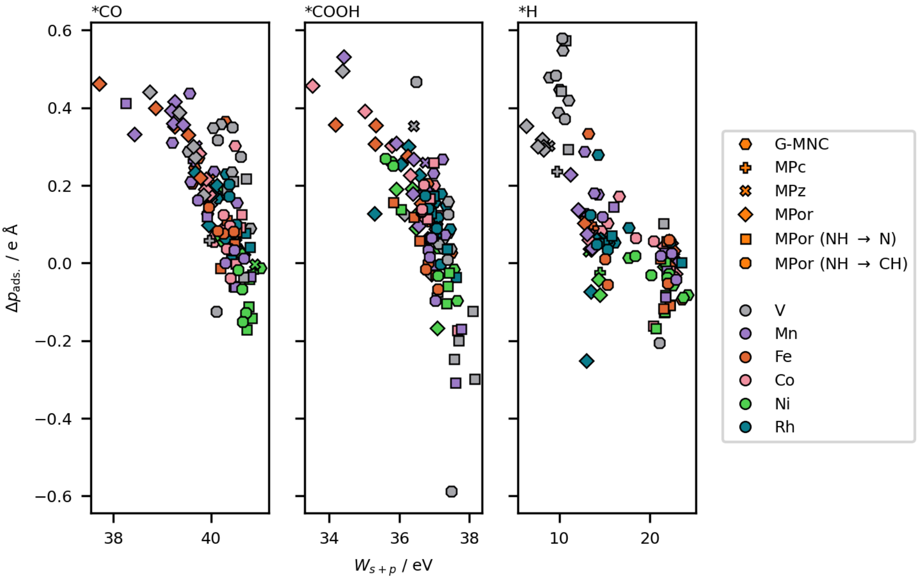

Figure 20. Plot of the adsorbate-induced dipole moment against the adsorbate-state “width” on various MNC systems.

Here we explore the correlation between two pairs of quantities in our MNC systems. As discussed in “Bridging the metal–SAC gap” (see esp. Supp. Note 7 in Ref.[1]), we in general expect the adsorbate state width to be negatively correlated with the adsorbate-induced dipole moment $\Delta p_{\text{ads.}}$ since both are dictated by the strength of the interaction with the catalyst surface.[137,148,174] In Figure 20 we have plotted $\Delta p_{\text{ads.}}$ against W_{s+p}, a metric of the actual width of the adsorbate states interacting with the catalyst, [*] and the previous conclusions are shown to still hold across MNCs as a whole – up to some scatter of course.[†]

---

[*] See the discussion of W in a footnote in “Comparative characterization of MNCs § I.1”.

[†] Scatter or not, here the functional form is not expected to be linear.[148]

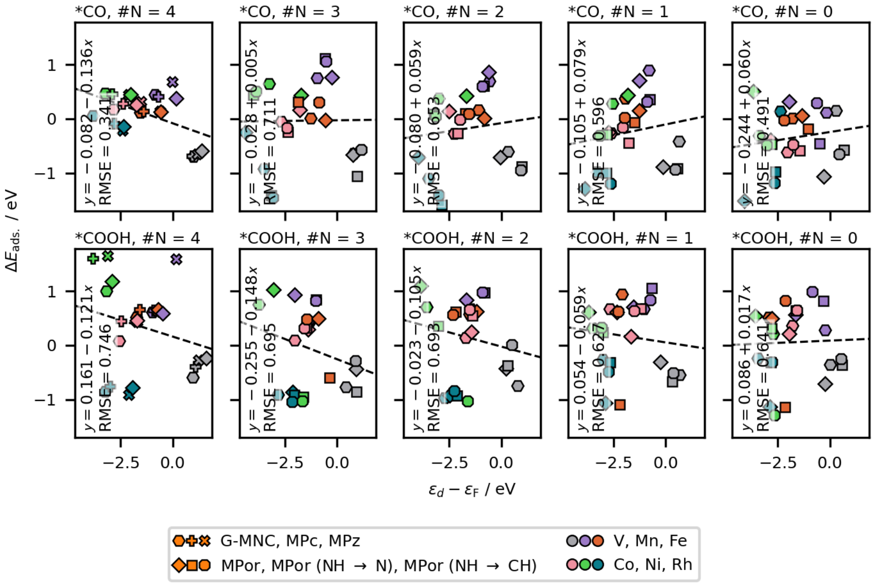

Figure 21. Plots of the hybrid-functional formation energies of *CO and *COOH on the various MNCs, against the *d*-band center of the clean-/"slab"-state MNCs. Data points are split between subplots by the adsorbate identity and the number of N atoms chelating the metal center.

Yet another important quantity is the *d*-band/-state center, which has been successfully used as a descriptor for adsorbate binding energies for decades since the debut of the Hammer–Nørskov (HN) model.[165,175,176] While we will also attempt the full treatment of the data therewith (in the next Chapter), we note that the *d*-band theory is constantly evolving and has spawned many different flavors in terms of both the descriptors and the functional dependence[164,177] – not necessarily restricted to the perturbation-theory-like energy expression in HN. Therefore, it will be instructive to first try a linear fit before further parametrizing the model – even if the linear fit itself fails, any sort of correlation between the quantities of interest should become apparent.

In Figure 21, we have plotted $\Delta E_{\text{ads.}}$ against the *d*-band (or more realistically, *d-state*) center of the bare catalyst $\varepsilon_{d,\text{ clean}}$. It is immediately obvious that there is no general correlation between the two quantities, except for a very narrow subset of the data (*CO on MN_4 catalysts) – or perhaps the correlation is again buried beneath scatter.

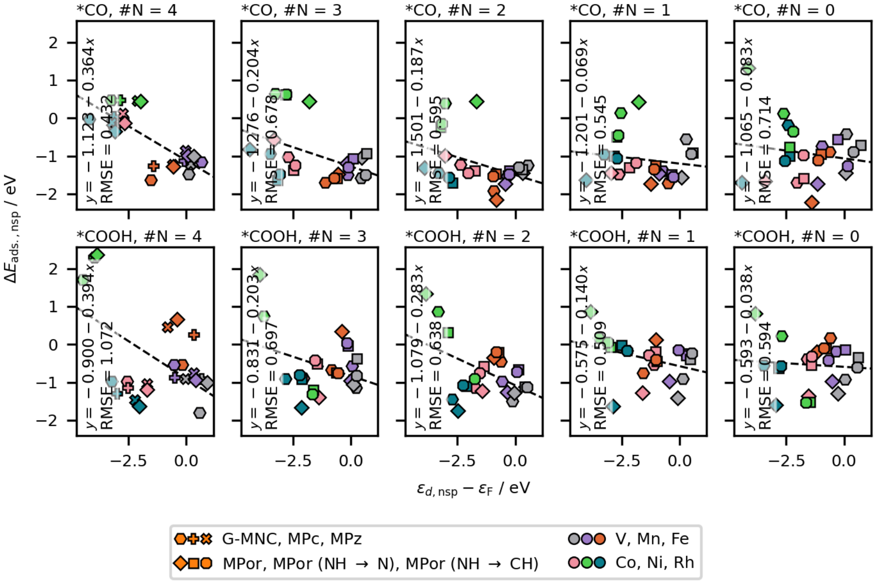

Figure 22. Plots of the non-spin-polarized hybrid-functional formation energies of *CO and *COOH on the various MNCs, against the *d*-band center of the clean-/"slab"-state MNCs. Data points are split between subplots by the adsorbate identity and the number of N atoms chelating the metal center.

Trying to remove complicating factors, we also inspect the corresponding plots in non-spin-polarized calculations (Figure 22). As with the spin-polarized case, there seem to be no overarching correlations across the MNCs. A remark that may be of interest though is how the one can also interpret the non-spin-polarized *CO on MN_3 and MN_4 cases as sporting a "flipped-checkmark" functional form: a long descending stroke from top left to the bottom, followed by a small, upturned hook at the end. Such a form is reminiscent of the chemisorption energy from a Newns–Anderson-based model[136–138] as described by Vijay *et al.*;[178][*] the degree to which linear scaling holds between any two adsorbates is thus determined by how well the features of their functional forms align with one another.

---

[*] Note though that in that work the chemisorption energy E_{chem} is shown to have a peak/kink at some rather negative ε_d, after which it sharply turns and starts decreasing w.r.t. more negative ε_d. In a sense the functional form more closely resembles a ladle, which may well also be the case here; perhaps the MNCs that are studied in this work do not have the requisite deep *d*-states, and we thus fail to capture that regime.

III. Conclusions

Overall speaking, the correlations between the examined adsorbate energetics are rather weak, with $\Delta E_{*\mathrm{H}}$ and $\Delta E_{*\mathrm{COOH}}$ being the sole exception – and only so for certain molecular MNCs. Such failing of adsorbates to scale, with one another and with *d*-state descriptors, may not be a failing of the *d*-band/-state model; rather, it may be precisely *due to* the subtleties thereof that we see such seemingly erratic behavior – or that we are violating key assumptions in the model. Still, we will among other tools also employ the original *d*-state model in the following Chapter to see whether we can rationalize adsorption on MNCs.

On the one hand, the loss of scaling does make the interpretation, modelling, and predictions of the energetics on these systems more difficult;[*] but on the other, we note that the *breaking* of scaling laws to achieve certain free-energy landscapes is often explicitly the goal in catalysis,[179,180] and may even be the motivation behind research into unconventional catalyst types.

---

[*] As an example, the microkinetic model used in Ref.[1] is contingent on the assumption that *CO and *COOH scale (see Supp. Fig. 10 in the reference).

Rationalization of adsorption energetics

In light of the absence of linear scaling between quantities and between adsorbates in MNCs, as described in the previous Chapter, we thus proceed to employ additional tools and models in trying to describe them. In this Chapter, I present two approaches taken: one by attempting to decompose the energetics into easier-handled components; and another trying to apply a fuller *d*-state model.

I. Divide-and-conquer: isolation of spin dependence

From the previous Chapter, we have seen that the CO_2RR intermediate energetics on MNCs are unfortunately not captured well by linear scaling relations. However, as was discussed in "The spin conundrum", the magnetization influences the energetics significantly, which poses additional challenges to the application of simplifying models. Being inspired by recent results, which made full use of the freedom afforded by DFT to toggle spin effects as needed,[181*] we have thus taken to try to decompose the adsorbate formation energy $\Delta E_{\text{ads.}}$ into two parts:

- The "electronic–electrostatic" component $\Delta E_{\text{ads., nsp.}}$, taken to be captured by a non-spin-polarized DFT calculation; and
- The "magnetic" component $\Delta\Delta E_{\text{ads.}} \coloneqq \Delta E_{\text{ads.}} - \Delta E_{\text{ads., nsp.}}$, taken to be the difference between the spin-polarized and non-spin-polarized energies.

---

[*] In the reference, the electrostatic (dipole-moment-and-field-based) stabilization of the N–N transition state by co-adsorbed promoter cations was found to be insufficient for describing the full stabilization; said remainder of the stabilizing effect was shown to be modelled by the difference in stabilizations between the full spin-polarized and the non-spin-polarized calculations.

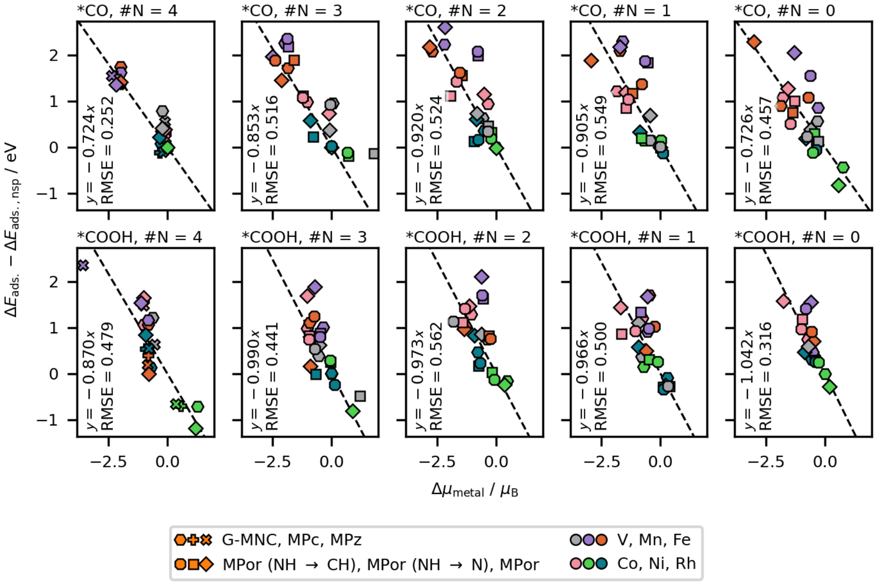

Figure 23. Plot of the "magnetic component" of the adsorbate formation energy against the change in metal magnetic moment upon adsorption. The fitting lines are constrained to pass through the origin.

In Figure 23, we start by plotting this magnetic component of the energy against the change in the metal magnetic moment (MMM). Here we see a decent correlation between the two quantities, which can be thus explained: the removal of the spin degree of freedom unphysically and energetically penalizes the system; as such, if an adsorbate state induces a higher MMM than in the clean state, $\Delta E_{\text{ads., nsp.}}$ will be penalized and thus $\Delta\Delta E_{\text{ads.}}$ is driven down.

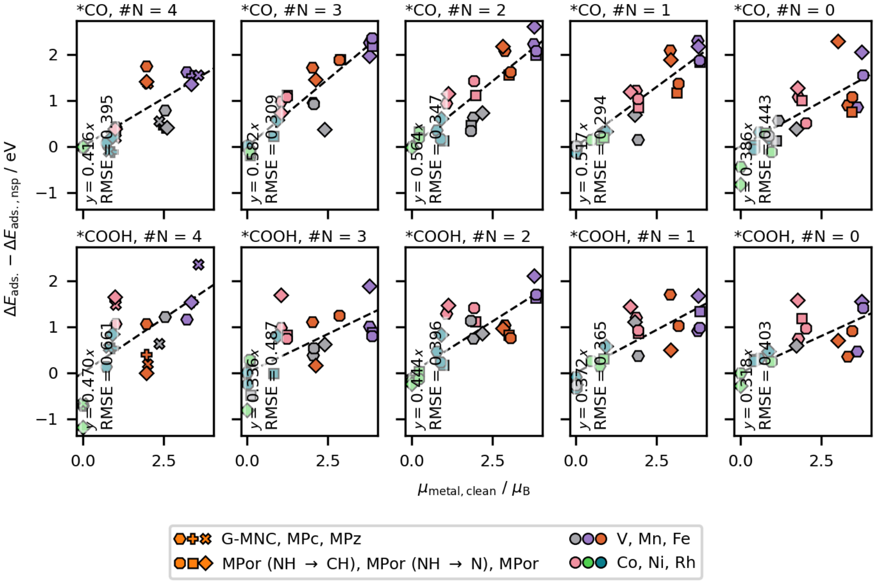

Figure 24. Plot of the "magnetic component" of the adsorbate formation energy against the metal magnetic moment. The fitting lines are constrained to pass through the origin.

More interestingly, it is of interest to note that the spin state of the clean metal site alone is already sufficient to describe the $\Delta\Delta E_{\text{ads.}}$ to a similar degree of accuracy (Figure 24; take note of the similar mean average error (MAE) values). This however is non-trivial, because the MMM is not uniformly quenched on adsorption unlike on TM surfaces (Figure 23),[182] and hence it is not immediately obvious that $\Delta\mu_{\text{metal}}$ and $\mu_{\text{metal, slab}}$ are somewhat interchangeable. This is also encouraging for the further development of such models in the future – having only to calculate the clean slab state with spin-polarized calculations to be able to capture the essential spin-dependent energetics makes for a simple descriptor, and will immensely cut down on the computational burden needed (see "Computational details § VI" and "The spin conundrum") for the proper screening and verification of MNC systems.

II. Does the d-band model work on MNCs?

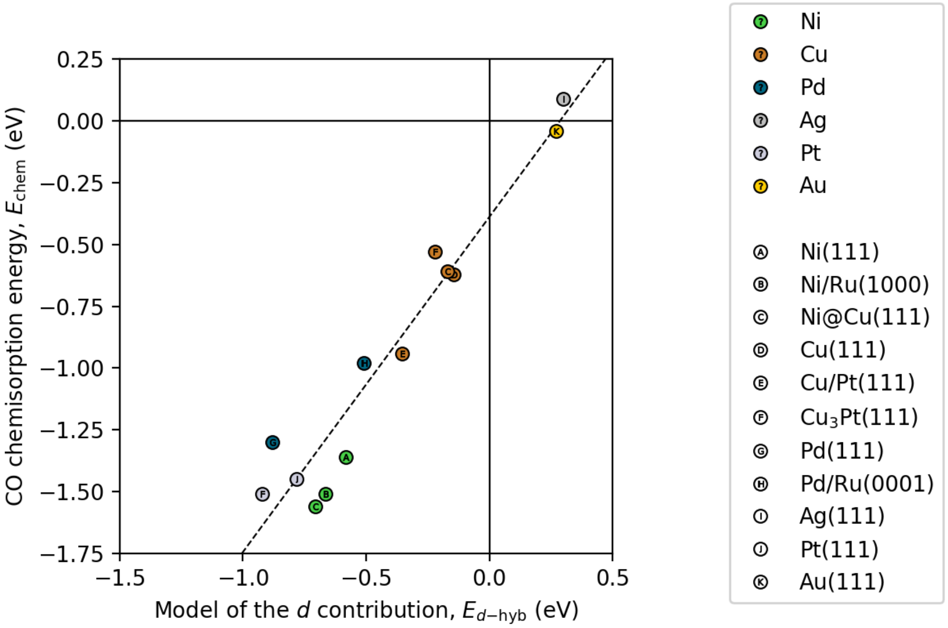

Figure 25. *d*-band model of *CO adsorption – a reconstruction of Ref.[165]'s Fig. 2. The values for the parameters are taken from Table I, ibid.

Motivated by the preceding Section, we then move onto the description of the electronic–electrostatic (i.e. non-spin-polarized) part of the energy $\Delta E_{\mathrm{nsp.}}$. The Hammer–Nørskov (HN) model[165,175,176] has enjoyed great success in describing the binding of gases on TMs, and has inspired the entire field of *d*-band theory.[164,174,177] Generalizing and reparametrizing from Hammer, Morikawa, and Nørskov's[165] formulation (hereafter HMN), we note that the formation energy $\Delta E_{*\mathrm{CO}}$ of the *CO state should follow a form of

$$\begin{aligned}\Delta E_{*\mathrm{CO}} = E_{\mathrm{offset}} \\ - V_{sd}^2 \sum_i \beta_i \left[4 \left(\frac{f_i}{\epsilon_{2\pi} - (\epsilon_d)_i} - f_i \alpha_i \right) \right. \\ \left. + 2 r_i^2 \left(\frac{1 - f_i}{(\epsilon_d)_i - \epsilon_{5\sigma}} - (1 + f_i) \alpha_i \right) \right].\end{aligned}$$

Here we have these parameters:

i	Index for *d*-states
$\epsilon_{2\pi}, \epsilon_{5\sigma}$	(Position of the) renormalized adsorbate states
V_{sd}	Dimensionless coupling integral, relative to the Cu value
α	$-\frac{\text{overlap integral}}{\text{coupling integral}}$
β	$\left(\frac{\text{coupling integral}}{\text{relative coupling integral}}\right)^2$
r	$\frac{\text{overlap integral }(\sigma)}{\text{overlap integral }(\pi)}$
ϵ_{d_i}	Center of the *i*-th *d*-state
f_i	Fractional filling of the *i*-th *d*-state

We note that the last two (sets of) parameters are easily available from DFT calculations – though the original work has opted to use the idealized filling $0.1(\text{valence} - 1)$ over integrating over the pDOS. V_{sd} has been tabulated in literature;[176] a and β are explicitly tunable/fitted parameters;[*][†] and $\varepsilon_{2\pi}$, $\varepsilon_{5\sigma}$, and r are parameters chosen in view of DFT results.[‡] Since the 2π and 5σ states owe their energetic position to the interaction with metal *s*- and *p*-bands, further broadening them for interaction with the *d*-bands, it is also expected that the $\varepsilon_{2\pi}$ and $\varepsilon_{5\sigma}$ will differ between our MNCs and the TM surfaces in the original work.

---

[*] HMN values:[165] $a = .063\ \text{eV}^{-1}$, $\beta = 1.5$ eV

[†] Naturally, E_{offset} is also a fitted parameter.

[‡] HMN values:[165] $\varepsilon_{2\pi} = +2.5$ eV, $\varepsilon_{5\sigma} = -7$ eV, $r = 1.3$

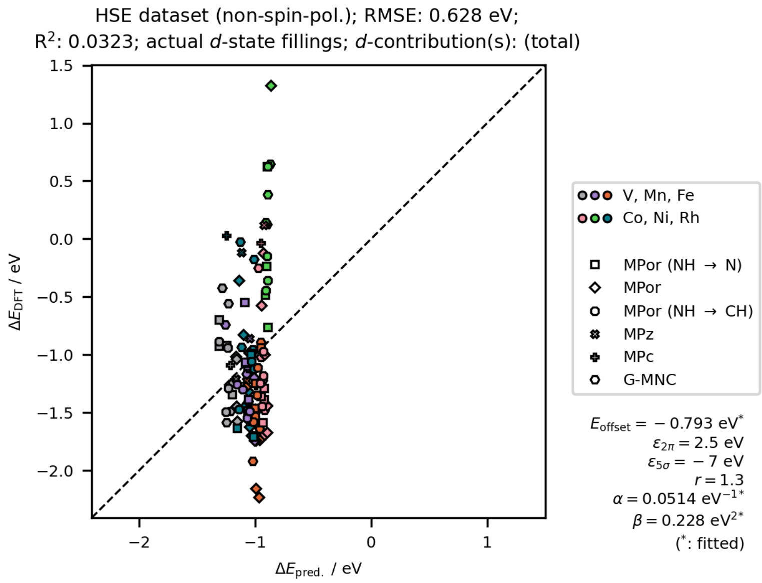

Figure 26. Parity plot of the hybrid non-spin-polarized $\Delta E_{*\mathrm{CO}}$ against the HMN predictions fitted on all data. The total d-band projection and its actual filling are used and the parameters α and β are fitted.

Replicating HMN's analysis, we start by fitting the entirety of the non-spin-polarized dataset[*] to the *d*-band model (Figure 26)[†] on all the total pDOS of all *d*-states. It is noted that the fit completely lacks any predictive power, given that the predictions only have a spread of about 0.5 eV while the DFT data have more than 3.5 eV; while less severe, the same is observed with the fit on the GGA data (App. Figure 10). This however is not surprising given that as mentioned, the adsorbate-state renormalization may have worked differently on MNCs, leading to the chosen values not being applicable. It is perhaps not appropriate either to start by fitting to the entire data set.

---

[*] Here only use the configurations binding atop the metal center ("M–C").

[†] See App. Figure 10 for the fit with the GGA dataset, with qualitative similar results (i.e. lack of correlation).

In trying to better understand the problem, we thus further filter the data set by the following criteria and work from there: (1) the V, Rh, and MN_0 data points are ignored due to their history of being outliers skewing the data;* (2) we also remove the MPor derivatives from consideration, noting that their the behavior can be at times problematic.† By doing so, we have arrived at a 33-point data set, which should be allowing the effects of various parameters and settings of the model to be more clearly seen, while also keeping the risk of overfitting manageable. In further tests, we have noticed the frequent failing of the optimization routine. Thus, we have also introduced constraints (Table 5) which aided in the convergence.

Parameter	Range	Reason
$\varepsilon_{2\pi}$	$(0.5, 10)$	Antibonding orbital
$\varepsilon_{5\sigma}$	$(-20, -0.5)$	Bonding orbital
a	$(0.005, 1)$	Orders of magnitude from HMN value
β	$(0.1, 20)$	Orders of magnitude from HMN value
r	$(1, \infty)$	σ-bonds by definition overlap more than π-bonds

Table 5. Table of constraints introduced for the extended-HMN model parameters and their justifications.

---

* See e.g. Figure 17 and Figure 21.

† See e.g. Table 3.

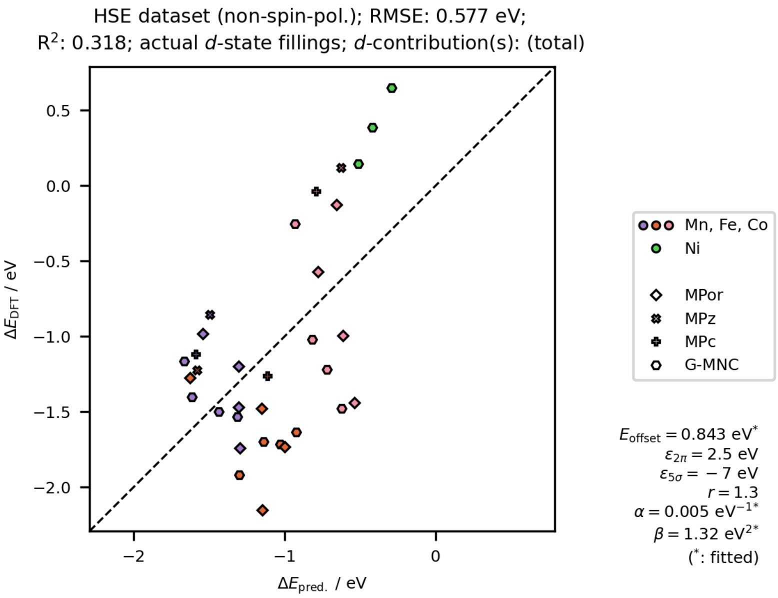

Figure 27. Parity plot of the hybrid non-spin-polarized ΔE_{*CO} against the HMN predictions fitted on the reduced set of data. The total *d*-band projection and its actual filling are used and the parameters *α* and *β* are fitted.

By these measures, we have recovered results that are more amenable to interpretation; in Figure 27 we have plotted the fit for the reduced data set. Though a correlation can now be seen, the errors in the order of 0.6 eV remain too high for the model to be considered usable. The corresponding fit for the GGA results has a more palatable error of 0.4 eV and a decent R-squared of > 0.7 (App. Figure 11), which however does not suffice either. Switching from the actual *d*-state fillings to the idealized ones causes a slight deterioration of the results (App. Figure 12 and App. Figure 13). Doing a full fit of the data with all the parametric degrees of freedom does not significantly improve the quality of predictions for either hybrid (App. Figure 14) or GGA (App. Figure 15) or. In particular for the former, the r, $\varepsilon_{2\pi}$, and $\varepsilon_{5\sigma}$ parameters all attained their extremal values as permitted by the constraints, indicative of a failure in searching for their optimal values.

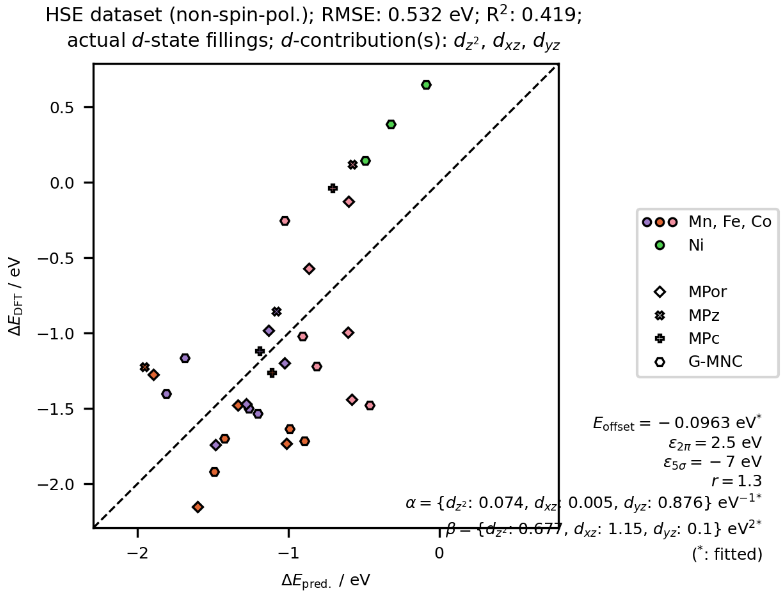

Figure 28. Parity plot of the hybrid non-spin-polarized ΔE_{*CO} against the HMN predictions fitted on the reduced set of data. The d_{z^2}, d_{xz}, and d_{yz} projections and their actual fillings are used, and the parameters α and β are fitted separately for each thereof.

Finally, we also look at the composition of several *d*-state terms, motivated by the desire to treat the separately the individual *d*-states, and in Figure 28[*] we have again plotted the DFT energies against the fitted model predictions. While the errors do show a qualitative improvement over the previous model (Figure 27), it is likely to be entirely attributable to the three-fold increase in parameters. The disparity between the coefficients of the d_{xz} and the d_{yz} orbitals may be indicative of projection errors.

III. Conclusions

We have demonstrated progress in the decomposition of the MNC adsorbate energetics via the extraction of the spin-dependent part. However, we still note the correspondence to be quite coarse-grained, and it will be also of interest to explain the values of the qualitatively similar slopes in Figure 23 (≈ −1eV μ_B^{-1}) and Figure 24 (≈ 0.4 eV μ_B^{-1}).

---

[*] See App. Figure 16 for the GGA version.

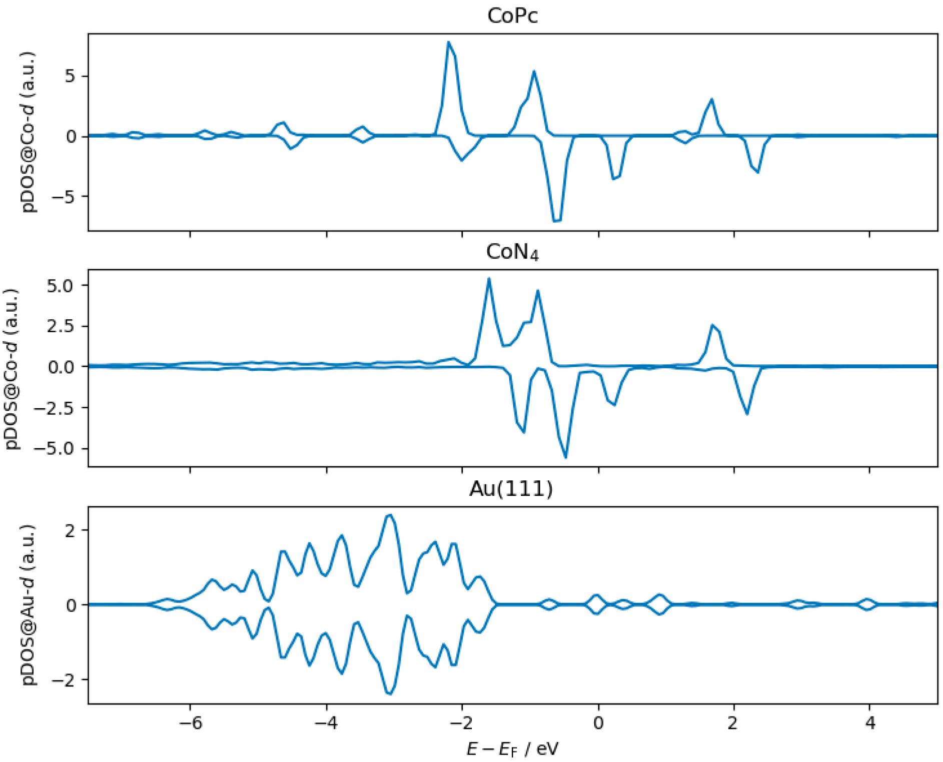

Figure 29. Surface-metal-*d* pDOS near the Fermi level from various GGA calculations. Top to bottom: CoPc (MPc), CoN_4 (G-MNC), and Au(111) (TM).

The shortcoming of the HMN model in describing the adsorbate binding on MNCs (relative to its success in describing TMs) should not serve as a deterrent towards further theoretical forays into the systematic and comprehensive modelling thereof. One factor contributing to the poor description of the MNCs by *d*-band methods may be how discrete their states are. From Figure 29 we see that the *d*-states of the Co in both extended and molecular MNCs are quite disjoint compared with the *d*-band of a TM surface . The narrowness of the *d*-states, while noted to be a boon for the adsorbate dipole,[1] sets the MNCs far enough apart to resist treatment by the usual tools of surface science; these materials may be better described by other models like the two-state Hamiltonian.

Outlook

Having presented the work we have done on studying the trends and reasons behind the catalytic activities of MNC systems, I would also like to take the time to present some ongoing, planned, and attempted work.

I. Electrochemical modelling of MNCs

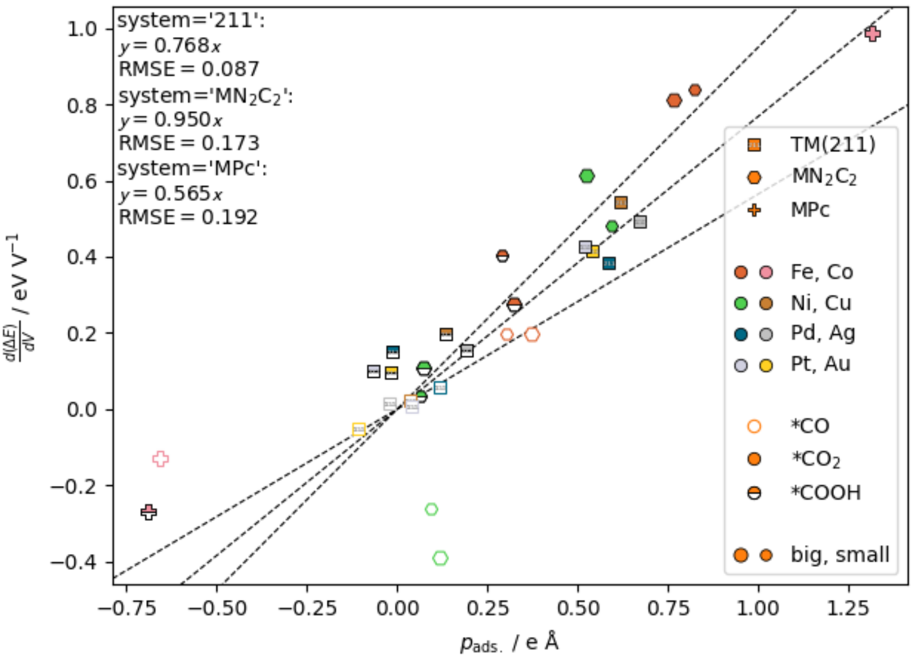

Figure 30. Plot of the potential dependence of $\Delta E_{ads.}$ against the adsorbate-induced dipole moment in vacuum for several MNCs and TM(211) facets. Calculations shown are non-spin-polarized. For the "big" and "small" MN_2C_2 calculations, see the discussion at "Computational details § VI".

As is evident from the literature, much of the current focus of research in MNCs is its use in electrocatalytic processes – specifically in CO_2RR[1,2,64,71,78,183] and NRR.[66,172,184] As such, it is of utmost importance to properly model the electrochemical interface. Following the capacitive model of charging as described in Refs.,[135,145] we have plotted in Figure 30 the potential dependence of adsorbate formation energy against the induced dipole on various MNC and TM surfaces.

As expected from the capacitor model, the relation between the DFT energies and the added charge is quadratic. However, the extraction of the dependence from referenced energetics[*] can be subtle, in that accumulative errors add up quickly while the leading terms in the E_{DFT} expression cancel out significantly, leading to huge uncertainties in the fitted parameters. Here, the quadratic fit is thus done before the slab-and-adsorbate referencing at each level of excess charge. Noting that the quadratic term is quantitatively similar for all adsorbates (and the clean-slab state) on each surface, a constrained least-squares fitting is then used to retrieve the linear coefficients ($\frac{d(\Delta E)}{dV}$) based on the assumption that the quadratic coefficients are indeed identical. Following this analysis, we see that the linear correlation between the two quantities is recovered also for the MNCs. Indeed, it is a fine balance to tread how much is to be abstracted away in order to recover the big picture while keeping as much detail as possible.

In dealing with electrostatics, especially with charging behaviors, it is instructive to have schemes qualifying and quantifying charge transfers – for this purpose, Bader partition can be used (see "Computational details § V"). While not presented elsewhere in the thesis, we are using the method to comparatively evaluate the (de-)localization of surface excess charge around the MNC centers, which may lead to a Frumkin-like[185] discrepancy between the field at the adsorption site and the potential drop into the electrolyte bulk.

While largely absent from the current state of our research (as was noted in "Computational details § VI"), it is noted that solvation effects can significantly impact the energetics and transport properties on the active sites,[186,187] perhaps steering the course of the reaction more than the intrinsic energetics. It will be instructive to later benchmark, investigate, and fine-tune the various approaches to potential and charge manipulation and examine their effects on the MNC center.[188]

---

[*] I.e. the adsorbate formation energies; see "Computational details § II".

II. ML-boosted thermodynamic surface simulations

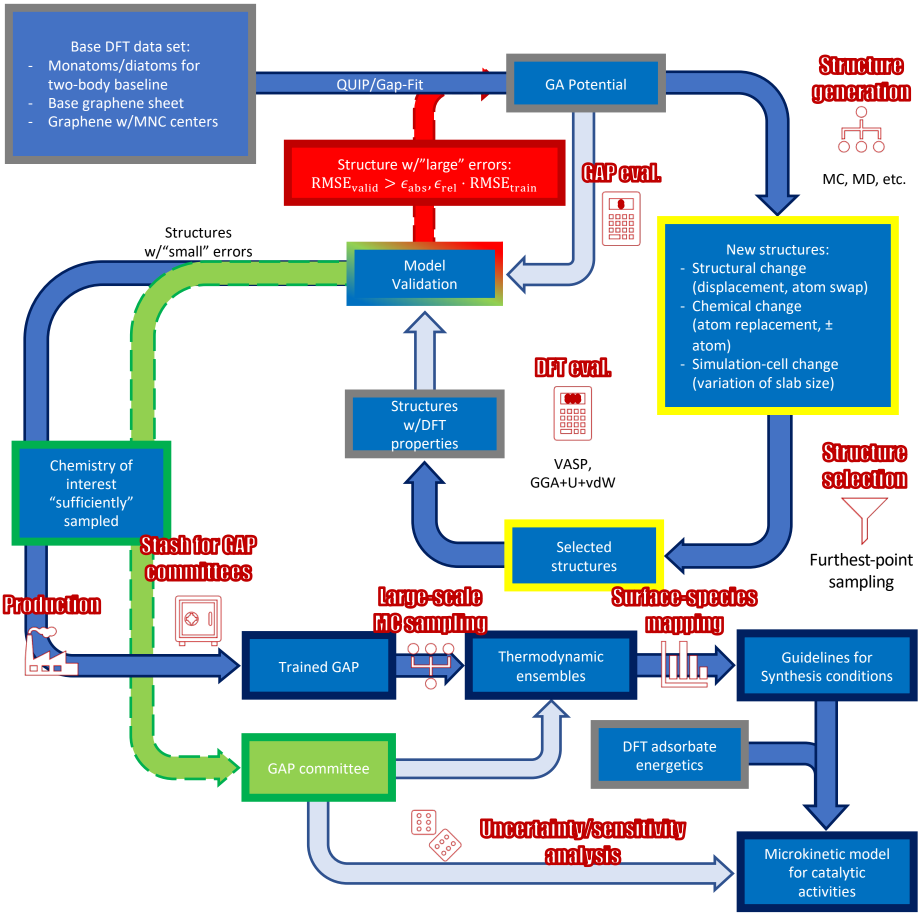
Base DFT data set:
- Monatoms/diatoms for two-body baseline
- Base graphene sheet
- Graphene w/MNC centers
QUIP/Gap-Fit
GA Potential
Structure generation
MC, MD, etc.
Structure w/"large" errors: $\mathrm{RMSE_{valid}} > \epsilon_{abs}, \epsilon_{rel} \cdot \mathrm{RMSE_{train}}$
GAP eval.
Structures w/"small" errors
Model Validation
New structures:
- Structural change (displacement, atom swap)
- Chemical change (atom replacement, ± atom)
- Simulation-cell change (variation of slab size)
DFT eval.
Structures w/DFT properties
VASP, GGA+U+vdW
Chemistry of interest "sufficiently" sampled
Structure selection
Selected structures
Furthest-point sampling
Stash for GAP committees
Production
Large-scale MC sampling
Surface-species mapping
Trained GAP
Thermodynamic ensembles
Guidelines for Synthesis conditions
DFT adsorbate energetics
GAP committee
Uncertainty/sensitivity analysis
Microkinetic model for catalytic activities

Schematic 3. Proposed iterative workflow for the GAP-aided simulation of MNC surfaces.

As briefly mentioned in "Metal–nitrogen–carbon single-atom catalysts § II" (and demonstrated in "Reaching down to the fundamentals: an exercise in atomic precision"), the MN_4 site is thought to be the active site for many kinds of reactions on MNC. It is then imperative for the optimal catalyst to be wholly covered thereby, without the formation of other metal-containing surface sites. Indeed, the value of a synthesis pathway is sometimes evaluated by its ability to uniquely yield these sites.[34,52,154]

It is true that the low cost of the catalytic species is one of the draws of MNCs (so that experiments are not limited by material availability), and years of experimental research has already resulted in much knowledge and belief regarding the optimal synthetic procedure and conditions; however, theory can still contribute as to the "whys" and "hows" about the mechanisms behind the changing of the catalyst surface during the different stages of synthesis (and even use) – and of course, what actions are advisable in view of that, to ensure the maximal coverage and quality of the desired site motif.

To this purpose, DFT-based tools like ab-initio molecule dynamics (AIMD) are invaluable, being the key towards electronically-informed thermodynamics. However, the full-scale simulation of a catalytic surface with AIMD is prohibitively expensive,[*] and the sampling of rare events like surface reconstructions and site deterioration may not be realistic. At the typical cell size accessible to AIMD it may also be difficult to model the interactions between sites or the effects of adsorbate coverage.

In recent years, machine-learning- (ML-) boosted material modeling has garnered great interest.[†] Though DFT is already one of the less expensive "workhorse" methods, especially when compared to higher levels of theory, it is still not very scalable to the same scale at which classical (force-field-based) simulation can be done. However, machine-learning methods promise a mix of the best of both worlds – to offer electronically-informed materials simulation at a fraction of the current cost. In view of this, during my external stay in the Fritz–Haber–Institut, Berlin, we began work on carrying out ML-boosted thermodynamic modelling on these MNC systems; Schematic 3 represents a design of the framework/workflow, encompassing (1) the iterative training of a ML potential capable of replacing DFT on the system of interest, and (2) the use of said potential for the scalable thermodynamic simulation of the catalyst surface.

The iterative training loop is central to the workflow: once set up, it is to continue automatically in (1) the evaluation of the performance of an ML potential (MLP), (2) the identification of the area in the chemical space in interest in which it underperforms, (3) the systematic and selective acquisition of new DFT data therefrom, and (4) the use thereof in refining (training) the MLP. While (1) is intuitive, consisting merely of the comparing of the DFT ground truth and the ML predictions, each of the other areas come with its own subtleties:

---

[*] We do note the existence of AIMD literature on MNCs;[200,201] however, such is understandably not the norm in the stability analysis of these materials.[127,167,202,203]

[†] Even some predominantly DFT codes like VASP are already starting to incorporate machine-learning algorithms into their own software.

- **Featurization of the atomic structures.** For the loop to be able to discern (the atomic structures representing) the chemistry it performs the worst on, there must exist a mapping from said structures to numbers, quantifying the chemistry. Such falls under the purview of descriptor functions, which map atomic structures of any given size, composition, and geometry into a vector space of fixed dimensions. In this project, the Smooth Overlay of Atomic Positions (SOAP)[189–192] descriptor is used.
- **Generation of new configuration.** The loop also needs to be able to generate new structures to be evaluated by DFT, so that it has new materials to train and evaluate itself on; usually it involves using the potential itself to generate random candidates, which is then followed by a selection process based on the descriptor discussed just now. In this project, a Monte-Carlo (MC) sampling scheme based on the MLP energies is to be implemented, and the generated structures are selected by dissimilarity (defined by the descriptor) with the existing training set.
- **Training and choice of ML method.** Last but not least, there is the question of the MLP to use. For this project, the Gaussian Approximation Potential[193] is employed, which uses Gaussian-process regression (GPR) to learn the input-structure energy and stress and the atomic forces.[194] While treasured for its transparency, error prediction, and ability to extrapolate from a small initial pool of data, it is noted that as the data set grows GPR (at least in its original form) may suffer from scalability issues; and at that point other ML models may be more suitable.

After the MLP is sufficiently trained, it can then be used in the force and energy evaluation on the type of materials its training has covered (in our case MNCs). Due to the low cost of evaluation, the potential can be applied to the large-scale simulation of thermodynamic ensembles (e.g. via MD or the implemented MC) representing the MNC surface at reaction conditions. Such methods will allow us to directly simulate the interface at system sizes and on timescales inaccessible to basic DFT.

Conclusions

Throughout the course of the research in the application of MNC systems towards CO_2 reduction, they have constantly shown themselves to be rather malleable and adaptable.

In the first paper,[1][*] by consideration of the electronic structure, we have justified the use of commonplace DFT methods for the analysis of CO_2RR on MNC. Individual MNC motifs have shown great variation in catalytic activity in both theoretical and experimental analysis, where the adsorbate-induced electric dipole of $^*CO_2$ is demonstrated to be instrumental in determining the reaction rate and its dependence on the catalytic conditions.

In the second paper,[2][†] we have again demonstrated the value of ab-initio modelling in enabling the interpretation of experimental results: where through the simulation of the catalytic activities of NiNC motifs, the trends exhibited in the prepared samples can be unambiguously attributed to the NiN_4, bolstering the deconvolution of the intrinsic (turnover frequency) and extrinsic (site density) facets of sample activity.

In the remainder of the thesis,[3] we have compared the electronic and energetic properties of assorted MNC systems, showing consistency and correspondence between molecular and surface-embedded MNC centers. In stark contrast to TM facets, they show deviation from established scaling relations in CO_2RR; still, the separation of the electronic–electrostatic and magnetic components of the energetics improves correlation, leaving open the possibility of a more descriptive and predictive model in the future.

With their manifold synthesis pathways and morphologies, experimentally-verified high catalytic activity, and the non-trivial theoretical properties, we foresee that they will remain a mainstay in catalysis for years to come – just like how they always have been[‡] since time immemorial.

---

[*] Chapter "Bridging the metal–SAC gap: one picture to rule them all"

[†] Chapter "Reaching down to the fundamentals: an exercise in atomic precision"

[‡] See Chapter "Metal–nitrogen–carbon single-atom catalysts"

References

(1) Vijay, S.; Ju, W.; Brückner, S.; Tsang, S.-C.; Strasser, P.; Chan, K. Unified Mechanistic Understanding of CO_2 Reduction to CO on Transition Metal and Single Atom Catalysts. *Nat Catal* **2021**, *4* (12), 1024–1031. https://doi.org/10.1038/s41929-021-00705-y.

(2) Li, C.; Ju, W.; Vijay, S.; Timoshenko, J.; Mou, K.; Cullen, D. A.; Yang, J.; Wang, X.; Pachfule, P.; Brückner, S.; Jeon, H. S.; Haase, F. T.; Tsang, S.-C.; Rettenmaier, C.; Chan, K.; Cuenya, B. R.; Thomas, A.; Strasser, P. Covalent Organic Framework (COF) Derived Ni-N-C Catalysts for Electrochemical CO_2 Reduction: Unraveling Fundamental Kinetic and Structural Parameters of the Active Sites. *Angewandte Chemie International Edition* **2022**, *61* (15), e202114707. https://doi.org/10.1002/anie.202114707.

(3) Tsang, S.-C.; Karmodak, N.; Liu, S.; Kastlunger, G. *Rationalization and Deconvolution of Trends in Adsorption Energetics on Metal–Nitrogen–Carbon Single-Atom Centers*; 2023.

(4) Foote, E. On the Heat in the Sun's Rays. *The American Journal of Science and Arts* **1856**, *22*, 382–383.

(5) Ortiz, J. D.; Jackson, R. Understanding Eunice Foote's 1856 Experiments: Heat Absorption by Atmospheric Gases. *Notes and Records: the Royal Society Journal of the History of Science* **2022**, *76* (1), 67–84. https://doi.org/10.1098/rsnr.2020.0031.

(6) Arrhenius, S. XXXI. *On the influence of carbonic acid in the air upon the temperature of the ground*. *The London, Edinburgh, and Dublin Philosophical Magazine and Journal of Science* **1896**, *41* (251), 237–276. https://doi.org/10.1080/14786449608620846.

(7) Gardiner, B. How an Early Oil Industry Study Became Key in Climate Lawsuits. *Yale Environment 360*. New Haven, CT November 2022. https://e360.yale.edu/features/climate-lawsuits-oil-industry-research.

(8) Calvin, K.; Dasgupta, D.; Krinner, G.; Mukherji, A.; Thorne, P. W.; Trisos, C.; Romero, J.; Aldunce, P.; Barrett, K.; Blanco, G.; Cheung, W. W. L.; Connors, S.; Denton, F.; Diongue-Niang, A.; Dodman, D.;

Garschagen, M.; Geden, O.; Hayward, B.; Jones, C.; Jotzo, F.; Krug, T.; Lasco, R.; Lee, Y.-Y.; Masson-Delmotte, V.; Meinshausen, M.; Mintenbeck, K.; Mokssit, A.; Otto, F. E. L.; Pathak, M.; Pirani, A.; Poloczanska, E.; Pörtner, H.-O.; Revi, A.; Roberts, D. C.; Roy, J.; Ruane, A. C.; Skea, J.; Shukla, P. R.; Slade, R.; Slangen, A.; Sokona, Y.; Sörensson, A. A.; Tignor, M.; van Vuuren, D.; Wei, Y.-M.; Winkler, H.; Zhai, P.; Zommers, Z.; Hourcade, J.-C.; Johnson, F. X.; Pachauri, S.; Simpson, N. P.; Singh, C.; Thomas, A.; Totin, E.; Alegría, A.; Armour, K.; Bednar-Friedl, B.; Blok, K.; Cissé, G.; Dentener, F.; Eriksen, S.; Fischer, E.; Garner, G.; Guivarch, C.; Haasnoot, M.; Hansen, G.; Hauser, M.; Hawkins, E.; Hermans, T.; Kopp, R.; Leprince-Ringuet, N.; Lewis, J.; Ley, D.; Ludden, C.; Niamir, L.; Nicholls, Z.; Some, S.; Szopa, S.; Trewin, B.; van der Wijst, K.-I.; Winter, G.; Witting, M.; Birt, A.; Ha, M. *IPCC, 2023: Climate Change 2023: Synthesis Report. Contribution of Working Groups I, II and III to the Sixth Assessment Report of the Intergovernmental Panel on Climate Change [Core Writing Team, H. Lee and J. Romero (Eds.)]. IPCC, Geneva, Switzerland.*; Geneva, 2023. https://doi.org/10.59327/IPCC/AR6-9789291691647.

(9) IEA. *Energy Statistics Data Browser.* https://www.iea.org/data-and-statistics/data-tools/energy-statistics-data-browser.

(10) BP p.l.c. *How energy is used.* https://www.bp.com/en/global/corporate/energy-economics/energy-outlook/how-energy-is-used.html.

(11) Haber, F. *Thermodynamik Technischer Gasreaktionen: Sieben Vorlesungen*; R. Oldenbourg: Munich & Berlin, 1905.

(12) Bosch, C. Process of Producing Ammonia. 957843, 1908. https://patents.google.com/patent/US957843 (accessed 2023-09-06).

(13) Hager, T. *The Alchemy of Air*, 1st ed.; Crown, 2009.

(14) Gibson, T.; Capestany, C.; Gillett, N. How Earth's Population Exploded, 2019. https://www.youtube.com/watch?v=U7l8imwtMkY.

(15) Boerner, L. K. Industrial Ammonia Production Emits More CO_2 than Any Other Chemical-Making Reaction. Chemists Want to Change That. *Chemical & Engineering News*. June 15, 2019. https://cen.acs.org/environment/green-chemistry/Industrial-ammonia-production-emits-CO2/97/i24.

(16) Song, Y.; Johnson, D.; Peng, R.; Hensley, D. K.; Bonnesen, P. V.; Liang, L.; Huang, J.; Yang, F.; Zhang, F.; Qiao, R.; Baddorf, A. P.; Tschaplinski, T. J.; Engle, N. L.; Hatzell, M. C.; Wu, Z.; Cullen, D. A.; Meyer, H. M.; Sumpter, B. G.; Rondinone, A. J. A Physical Catalyst for the Electrolysis of Nitrogen to Ammonia. *Sci Adv* **2018**, *4* (4). https://doi.org/10.1126/sciadv.1700336.

(17) Hess, J.; Bednarz, D.; Bae, J.; Pierce, J. Petroleum and Health Care: Evaluating and Managing Health Care's Vulnerability to Petroleum Supply Shifts. *Am J Public Health* **2011**, *101* (9), 1568–1579. https://doi.org/10.2105/AJPH.2011.300233.

(18) Nitopi, S.; Bertheussen, E.; Scott, S. B.; Liu, X.; Engstfeld, A. K.; Horch, S.; Seger, B.; Stephens, I. E. L.; Chan, K.; Hahn, C.; Nørskov, J. K.; Jaramillo, T. F.; Chorkendorff, I. Progress and Perspectives of Electrochemical CO_2 Reduction on Copper in Aqueous Electrolyte. *Chem Rev* **2019**, *119* (12), 7610–7672. https://doi.org/10.1021/acs.chemrev.8b00705.

(19) Rommens, K. T.; Saeys, M. Molecular Views on Fischer–Tropsch Synthesis. *Chem Rev* **2023**, *123* (9), 5798–5858. https://doi.org/10.1021/acs.chemrev.2c00508.

(20) Max Roser. *Why did renewables become so cheap so fast?*. Our World in Data. https://ourworldindata.org/cheap-renewables-growth.

(21) IRENA. *Renewable Power Generation Costs in 2019*; Abu Dhabi, 2020.

(22) Lazard. *Levelized Cost of Energy and Levelized Cost of Storage 2019*; New York, 2019. https://www.lazard.com/research-insights/levelized-cost-of-energy-and-levelized-cost-of-storage-2019/.

(23) IAEA. *Nuclear Power Capacity Trend.* Power Reactor Information System, IAEA.

https://pris.iaea.org/PRIS/WorldStatistics/WorldTrendNuclearPowerCapacity.aspx.

(24) Global Energy Monitor. *Global Coal Terminals Tracker*; Covina, CA, 2020. https://globalenergymonitor.org/projects/global-coal-terminals-tracker/.

(25) Hori, Y.; Murata, A.; Takahashi, R. Formation of Hydrocarbons in the Electrochemical Reduction of Carbon Dioxide at a Copper Electrode in Aqueous Solution. *Journal of the Chemical Society, Faraday Transactions 1: Physical Chemistry in Condensed Phases* **1989**, *85* (8), 2309. https://doi.org/10.1039/f19898502309.

(26) Jouny, M.; Luc, W.; Jiao, F. High-Rate Electroreduction of Carbon Monoxide to Multi-Carbon Products. *Nat Catal* **2018**, *1* (10), 748–755. https://doi.org/10.1038/s41929-018-0133-2.

(27) Hori, Y.; Wakebe, H.; Tsukamoto, T.; Koga, O. Electrocatalytic Process of CO Selectivity in Electrochemical Reduction of CO_2 at Metal Electrodes in Aqueous Media. *Electrochim Acta* **1994**, *39* (11–12), 1833–1839. https://doi.org/10.1016/0013-4686(94)85172-7.

(28) Hori, Y. Electrochemical CO_2 Reduction on Metal Electrodes. In *Modern Aspects of Electrochemistry*; Vayenas, C. G., White, R. E., Gamboa-Aldeco, M. E., Eds.; Springer New York: New York, NY, 2008; pp 89–189. https://doi.org/10.1007/978-0-387-49489-0_3.

(29) Möller, T.; Ju, W.; Bagger, A.; Wang, X.; Luo, F.; Ngo Thanh, T.; Varela, A. S.; Rossmeisl, J.; Strasser, P. Efficient CO_2 to CO Electrolysis on Solid Ni–N–C Catalysts at Industrial Current Densities. *Energy Environ Sci* **2019**, *12* (2), 640–647. https://doi.org/10.1039/C8EE02662A.

(30) Bagger, A.; Ju, W.; Varela, A. S.; Strasser, P.; Rossmeisl, J. Single Site Porphyrine-like Structures Advantages over Metals for Selective Electrochemical CO_2 Reduction. *Catal Today* **2017**, *288*, 74–78. https://doi.org/10.1016/j.cattod.2017.02.028.

(31) Varela, A. S.; Kroschel, M.; Leonard, N. D.; Ju, W.; Steinberg, J.; Bagger, A.; Rossmeisl, J.; Strasser, P. PH Effects on the Selectivity of the Electrocatalytic CO_2 Reduction on Graphene-Embedded Fe–N–

C Motifs: Bridging Concepts between Molecular Homogeneous and Solid-State Heterogeneous Catalysis. *ACS Energy Lett* **2018**, *3* (4), 812–817. https://doi.org/10.1021/acsenergylett.8b00273.

(32) Ivanov, A. S.; Boldyrev, A. I. Deciphering Aromaticity in Porphyrinoids via Adaptive Natural Density Partitioning. *Org Biomol Chem* **2014**, *12* (32), 6145–6150. https://doi.org/10.1039/C4OB01018C.

(33) Kramm, U. I.; Abs-Wurmbach, I.; Herrmann-Geppert, I.; Radnik, J.; Fiechter, S.; Bogdanoff, P. Influence of the Electron-Density of FeN_4-Centers Towards the Catalytic Activity of Pyrolyzed FeTMPPCl-Based ORR-Electrocatalysts. *J Electrochem Soc* **2011**, *158* (1), B69. https://doi.org/10.1149/1.3499621.

(34) Kramm, U. I.; Herrmann-Geppert, I.; Behrends, J.; Lips, K.; Fiechter, S.; Bogdanoff, P. On an Easy Way To Prepare Metal–Nitrogen Doped Carbon with Exclusive Presence of MeN_4-Type Sites Active for the ORR. *J Am Chem Soc* **2016**, *138* (2), 635–640. https://doi.org/10.1021/jacs.5b11015.

(35) Zhang, X.; Wang, Y.; Gu, M.; Wang, M.; Zhang, Z.; Pan, W.; Jiang, Z.; Zheng, H.; Lucero, M.; Wang, H.; Sterbinsky, G. E.; Ma, Q.; Wang, Y.-G.; Feng, Z.; Li, J.; Dai, H.; Liang, Y. Molecular Engineering of Dispersed Nickel Phthalocyanines on Carbon Nanotubes for Selective CO_2 Reduction. *Nat Energy* **2020**, *5* (9), 684–692. https://doi.org/10.1038/s41560-020-0667-9.

(36) Orellana, W.; Loyola, C. Z.; Marco, J. F.; Tasca, F. Evidence of Carbon-Supported Porphyrins Pyrolyzed for the Oxygen Reduction Reaction Keeping Integrity. *Sci Rep* **2022**, *12* (1), 8072. https://doi.org/10.1038/s41598-022-11820-6.

(37) Gottfried, J. M. Surface Chemistry of Porphyrins and Phthalocyanines. *Surf Sci Rep* **2015**, *70* (3), 259–379. https://doi.org/https://doi.org/10.1016/j.surfrep.2015.04.001.

(38) Cheng, Y.; Veder, J.-P.; Thomsen, L.; Zhao, S.; Saunders, M.; Demichelis, R.; Liu, C.; De Marco, R.; Jiang, S. P. Electrochemically Substituted Metal Phthalocyanines, e-MPc (M = Co, Ni), as Highly

Active and Selective Catalysts for CO_2 Reduction. *J Mater Chem A Mater* **2018**, *6* (4), 1370–1375. https://doi.org/10.1039/C7TA09208C.

(39) Lin, L.; Li, M.; Jiang, L.; Li, Y.; Liu, D.; He, X.; Cui, L. A Novel Iron (Ⅱ) Polyphthalocyanine Catalyst Assembled on Graphene with Significantly Enhanced Performance for Oxygen Reduction Reaction in Alkaline Medium. *J Power Sources* **2014**, *268*, 269–278. https://doi.org/https://doi.org/10.1016/j.jpowsour.2014.06.062.

(40) Zhong, H.; Ly, K. H.; Wang, M.; Krupskaya, Y.; Han, X.; Zhang, J.; Zhang, J.; Kataev, V.; Büchner, B.; Weidinger, I. M.; Kaskel, S.; Liu, P.; Chen, M.; Dong, R.; Feng, X. A Phthalocyanine-Based Layered Two-Dimensional Conjugated Metal–Organic Framework as a Highly Efficient Electrocatalyst for the Oxygen Reduction Reaction. *Angewandte Chemie* **2019**, *131* (31), 10787–10792. https://doi.org/10.1002/ange.201907002.

(41) Zhu, H.-J.; Lu, M.; Wang, Y.-R.; Yao, S.-J.; Zhang, M.; Kan, Y.-H.; Liu, J.; Chen, Y.; Li, S.-L.; Lan, Y.-Q. Efficient Electron Transmission in Covalent Organic Framework Nanosheets for Highly Active Electrocatalytic Carbon Dioxide Reduction. *Nat Commun* **2020**, *11* (1), 497. https://doi.org/10.1038/s41467-019-14237-4.

(42) Diercks, C. S.; Lin, S.; Kornienko, N.; Kapustin, E. A.; Nichols, E. M.; Zhu, C.; Zhao, Y.; Chang, C. J.; Yaghi, O. M. Reticular Electronic Tuning of Porphyrin Active Sites in Covalent Organic Frameworks for Electrocatalytic Carbon Dioxide Reduction. *J Am Chem Soc* **2018**, *140* (3), 1116–1122. https://doi.org/10.1021/jacs.7b11940.

(43) Yang, X.; Cheng, J.; Xuan, X.; Liu, N.; Liu, J. Boosting Defective Carbon by Anchoring Well-Defined Atomically Dispersed Ni–N_4 Sites for Electrocatalytic CO_2 Reduction. *ACS Sustain Chem Eng* **2020**, *8* (28), 10536–10543. https://doi.org/10.1021/acssuschemeng.0c03222.

(44) Kumar, P.; Kumar, A.; Sreedhar, B.; Sain, B.; Ray, S. S.; Jain, S. L. Cobalt Phthalocyanine Immobilized on Graphene Oxide: An Efficient Visible-Active Catalyst for the Photoreduction of Carbon Dioxide.

Chemistry – A European Journal **2014**, *20* (20), 6154–6161. https://doi.org/https://doi.org/10.1002/chem.201304189.

(45) Sengupta, K.; Chatterjee, S.; Dey, A. Catalytic H_2O_2 Disproportionation and Electrocatalytic O_2 Reduction by a Functional Mimic of Heme Catalase: Direct Observation of Compound 0 and Compound I in Situ. *ACS Catal* **2016**, *6* (3), 1382–1388. https://doi.org/10.1021/acscatal.5b02668.

(46) Kaminsky, C. J.; Wright, J.; Surendranath, Y. Graphite-Conjugation Enhances Porphyrin Electrocatalysis. *ACS Catal* **2019**, *9* (4), 3667–3671. https://doi.org/10.1021/acscatal.9b00404.

(47) Furuta, H.; Asano, T.; Ogawa, T. "N-Confused Porphyrin": A New Isomer of Tetraphenylporphyrin. *J Am Chem Soc* **1994**, *116* (2), 767–768. https://doi.org/10.1021/ja00081a047.

(48) Furuta, H.; Maeda, H.; Osuka, A. Doubly N-Confused Porphyrin: A New Complexing Agent Capable of Stabilizing Higher Oxidation States. *J Am Chem Soc* **2000**, *122* (5), 803–807. https://doi.org/10.1021/ja992679g.

(49) Toganoh, M.; Furuta, H. Creation from Confusion and Fusion in the Porphyrin World─The Last Three Decades of N-Confused Porphyrinoid Chemistry. *Chem Rev* **2022**, *122* (9), 8313–8437. https://doi.org/10.1021/acs.chemrev.1c00065.

(50) Cook, A. H. 325. Catalytic Properties of the Phthalocyanines. Part I. Catalase Properties. *Journal of the Chemical Society (Resumed)* **1938**, No. 0, 1761–1768. https://doi.org/10.1039/JR9380001761.

(51) Varela, A. S.; Ranjbar Sahraie, N.; Steinberg, J.; Ju, W.; Oh, H.-S.; Strasser, P. Metal-Doped Nitrogenated Carbon as an Efficient Catalyst for Direct CO_2 Electroreduction to CO and Hydrocarbons. *Angewandte Chemie International Edition* **2015**, *54* (37), 10758–10762. https://doi.org/10.1002/anie.201502099.

(52) Menga, D.; Low, J. L.; Li, Y.-S.; Arčon, I.; Koyutürk, B.; Wagner, F.; Ruiz-Zepeda, F.; Gaberšček, M.; Paulus, B.; Fellinger, T.-P. Resolving the Dilemma of Fe–N–C Catalysts by the Selective Synthesis of

Tetrapyrrolic Active Sites via an Imprinting Strategy. *J Am Chem Soc* **2021**, *143* (43), 18010–18019. https://doi.org/10.1021/jacs.1c04884.

(53) Liao, M.-S.; Scheiner, S. Comparative Study of Metal-Porphyrins, -Porphyrazines, and -Phthalocyanines. *J Comput Chem* **2002**, *23* (15), 1391–1403. https://doi.org/https://doi.org/10.1002/jcc.10142.

(54) Wang, M.; Torbensen, K.; Salvatore, D.; Ren, S.; Joulié, D.; Dumoulin, F.; Mendoza, D.; Lassalle-Kaiser, B.; Işci, U.; Berlinguette, C. P.; Robert, M. CO_2 Electrochemical Catalytic Reduction with a Highly Active Cobalt Phthalocyanine. *Nat Commun* **2019**, *10* (1), 3602. https://doi.org/10.1038/s41467-019-11542-w.

(55) Wu, Q.; Xie, R.-K.; Mao, M.-J.; Chai, G.-L.; Yi, J.-D.; Zhao, S.-S.; Huang, Y.-B.; Cao, R. Integration of Strong Electron Transporter Tetrathiafulvalene into Metalloporphyrin-Based Covalent Organic Framework for Highly Efficient Electroreduction of CO_2. *ACS Energy Lett* **2020**, *5* (3), 1005–1012. https://doi.org/10.1021/acsenergylett.9b02756.

(56) Zhang, H.; Hwang, S.; Wang, M.; Feng, Z.; Karakalos, S.; Luo, L.; Qiao, Z.; Xie, X.; Wang, C.; Su, D.; Shao, Y.; Wu, G. Single Atomic Iron Catalysts for Oxygen Reduction in Acidic Media: Particle Size Control and Thermal Activation. *J Am Chem Soc* **2017**, *139* (40), 14143–14149. https://doi.org/10.1021/jacs.7b06514.

(57) Huan, T. N.; Ranjbar, N.; Rousse, G.; Sougrati, M.; Zitolo, A.; Mougel, V.; Jaouen, F.; Fontecave, M. Electrochemical Reduction of CO_2 Catalyzed by Fe-N-C Materials: A Structure–Selectivity Study. *ACS Catal* **2017**, *7* (3), 1520–1525. https://doi.org/10.1021/acscatal.6b03353.

(58) Yan, C.; Li, H.; Ye, Y.; Wu, H.; Cai, F.; Si, R.; Xiao, J.; Miao, S.; Xie, S.; Yang, F.; Li, Y.; Wang, G.; Bao, X. Coordinatively Unsaturated Nickel–Nitrogen Sites towards Selective and High-Rate CO_2 Electroreduction. *Energy Environ Sci* **2018**, *11* (5), 1204–1210. https://doi.org/10.1039/C8EE00133B.

(59) Su, P.; Iwase, K.; Harada, T.; Kamiya, K.; Nakanishi, S. Covalent Triazine Framework Modified with Coordinatively-Unsaturated Co or

Ni Atoms for CO_2 Electrochemical Reduction. *Chem Sci* **2018**, *9* (16), 3941–3947. https://doi.org/10.1039/C8SC00604K.

(60) Day, H. W. A Revised Diamond-Graphite Transition Curve. *American Mineralogist* **2012**, *97* (1), 52–62. https://doi.org/10.2138/am.2011.3763.

(61) Yang, L.; Cheng, D.; Xu, H.; Zeng, X.; Wan, X.; Shui, J.; Xiang, Z.; Cao, D. Unveiling the High-Activity Origin of Single-Atom Iron Catalysts for Oxygen Reduction Reaction. *Proceedings of the National Academy of Sciences* **2018**, *115* (26), 6626–6631. https://doi.org/10.1073/pnas.1800771115.

(62) He, Y.; Liu, S.; Priest, C.; Shi, Q.; Wu, G. Atomically Dispersed Metal–Nitrogen–Carbon Catalysts for Fuel Cells: Advances in Catalyst Design, Electrode Performance, and Durability Improvement. *Chem Soc Rev* **2020**, *49* (11), 3484–3524. https://doi.org/10.1039/C9CS00903E.

(63) Ju, W.; Bagger, A.; Hao, G.-P.; Varela, A. S.; Sinev, I.; Bon, V.; Roldan Cuenya, B.; Kaskel, S.; Rossmeisl, J.; Strasser, P. Understanding Activity and Selectivity of Metal-Nitrogen-Doped Carbon Catalysts for Electrochemical Reduction of CO_2. *Nat Commun* **2017**, *8* (1), 944. https://doi.org/10.1038/s41467-017-01035-z.

(64) Wei, K.; Pan, K.; Qu, G.; Zhou, J. Customization from Single to Dual Atomic Sites for Efficient Electrocatalytic CO_2 Reduction to Value-Added Chemicals. *Chem Asian J* **2023**, *18* (17), e202300498. https://doi.org/https://doi.org/10.1002/asia.202300498.

(65) Sarma, S. C.; Barrio, J.; Bagger, A.; Pedersen, A.; Gong, M.; Luo, H.; Wang, M.; Favero, S.; Zhao, C.-X.; Zhang, Q.; Kucernak, A.; Titirici, M.-M.; Stephens, I. E. L. Reaching the Fundamental Limitation in CO_2 Reduction to CO with Single Atom Catalysts. *Adv Funct Mater* **2023**, *n/a* (n/a), 2302468. https://doi.org/https://doi.org/10.1002/adfm.202302468.

(66) Wu, T.; Melander, M. M.; Honkala, K. Coadsorption of NRR and HER Intermediates Determines the Performance of Ru-N_4 toward

Electrocatalytic N_2 Reduction. *ACS Catal* **2022**, *12* (4), 2505–2512. https://doi.org/10.1021/acscatal.1c05820.

(67) Zitolo, A.; Goellner, V.; Armel, V.; Sougrati, M.-T.; Mineva, T.; Stievano, L.; Fonda, E.; Jaouen, F. Identification of Catalytic Sites for Oxygen Reduction in Iron- and Nitrogen-Doped Graphene Materials. *Nat Mater* **2015**, *14* (9), 937–942. https://doi.org/10.1038/nmat4367.

(68) Zhou, D.; Zhang, L.; Liu, X.; Qi, H.; Liu, Q.; Yang, J.; Su, Y.; Ma, J.; Yin, J.; Wang, A. Tuning the Coordination Environment of Single-Atom Catalyst M-N-C towards Selective Hydrogenation of Functionalized Nitroarenes. *Nano Res* **2022**, *15* (1), 519–527. https://doi.org/10.1007/s12274-021-3511-z.

(69) Huang, Y.; Chen, Y.; Xu, M.; Asset, T.; Tieu, P.; Gili, A.; Kulkarni, D.; De Andrade, V.; De Carlo, F.; Barnard, H. S.; Doran, A.; Parkinson, D. Y.; Pan, X.; Atanassov, P.; Zenyuk, I. V. Catalysts by Pyrolysis: Direct Observation of Chemical and Morphological Transformations Leading to Transition Metal-Nitrogen-Carbon Materials. *Materials Today* **2021**, *47*, 53–68. https://doi.org/10.1016/j.mattod.2021.02.006.

(70) Zhou, Y.; Abazari, R.; Chen, J.; Tahir, M.; Kumar, A.; Ikreedeegh, R. R.; Rani, E.; Singh, H.; Kirillov, A. M. Bimetallic Metal–Organic Frameworks and MOF-Derived Composites: Recent Progress on Electro- and Photoelectrocatalytic Applications. *Coord Chem Rev* **2022**, *451*, 214264. https://doi.org/https://doi.org/10.1016/j.ccr.2021.214264.

(71) Karmodak, N.; Vijay, S.; Kastlunger, G.; Chan, K. Computational Screening of Single and Di-Atom Catalysts for Electrochemical CO_2 Reduction. *ACS Catal* **2022**, *12* (9), 4818–4824. https://doi.org/10.1021/acscatal.1c05750.

(72) Rai, R. K.; Tyagi, D.; Gupta, K.; Singh, S. K. Activated Nanostructured Bimetallic Catalysts for C–C Coupling Reactions: Recent Progress. *Catal Sci Technol* **2016**, *6* (10), 3341–3361. https://doi.org/10.1039/C5CY02225H.

(73) Kastlunger, G.; Heenen, H. H.; Govindarajan, N. Combining First-Principles Kinetics and Experimental Data to Establish Guidelines for

Product Selectivity in Electrochemical CO_2 Reduction. *ACS Catal* **2023**, *13* (7), 5062–5072. https://doi.org/10.1021/acscatal.3c00228.

(74) Nakata, K.; Ozaki, T.; Terashima, C.; Fujishima, A.; Einaga, Y. High-Yield Electrochemical Production of Formaldehyde from CO_2' and Seawater. *Angewandte Chemie International Edition* **2014**, *53* (3), 871–874. https://doi.org/10.1002/anie.201308657.

(75) Bagger, A.; Ju, W.; Varela, A. S.; Strasser, P.; Rossmeisl, J. Electrochemical CO_2 Reduction: A Classification Problem. *ChemPhysChem* **2017**, *18* (22), 3266–3273. https://doi.org/10.1002/cphc.201700736.

(76) Chan, K. A Few Basic Concepts in Electrochemical Carbon Dioxide Reduction. *Nat Commun* **2020**, *11* (1), 5954. https://doi.org/10.1038/s41467-020-19369-6.

(77) Govindarajan, N.; Kastlunger, G.; Heenen, H. H.; Chan, K. Improving the Intrinsic Activity of Electrocatalysts for Sustainable Energy Conversion: Where Are We and Where Can We Go? *Chem Sci* **2022**, *13* (1), 14–26. https://doi.org/10.1039/D1SC04775B.

(78) Verma, A. M.; Honkala, K.; Melander, M. M. Computational Screening of Doped Graphene Electrodes for Alkaline CO_2 Reduction. *Front Energy Res* **2021**, *8*. https://doi.org/10.3389/fenrg.2020.606742.

(79) Abild-Pedersen, F.; Greeley, J.; Studt, F.; Rossmeisl, J.; Munter, T. R.; Moses, P. G.; Skúlason, E.; Bligaard, T.; Nørskov, J. K. Scaling Properties of Adsorption Energies for Hydrogen-Containing Molecules on Transition-Metal Surfaces. *Phys Rev Lett* **2007**, *99* (1), 016105. https://doi.org/10.1103/PhysRevLett.99.016105.

(80) Schrödinger, E. An Undulatory Theory of the Mechanics of Atoms and Molecules. *Physical Review* **1926**, *28* (6), 1049–1070. https://doi.org/10.1103/PhysRev.28.1049.

(81) Hohenberg, P.; Kohn, W. Inhomogeneous Electron Gas. *Physical Review* **1964**, *136* (3B), B864–B871. https://doi.org/10.1103/PhysRev.136.B864.

(82) Kohn, W.; Sham, L. J. Self-Consistent Equations Including Exchange and Correlation Effects. *Physical Review* **1965**, *140* (4A), A1133–A1138. https://doi.org/10.1103/PhysRev.140.A1133.

(83) Perdew, J. P.; Burke, K. Comparison Shopping for a Gradient-Corrected Density Functional. *Int J Quantum Chem* **1996**, *57* (3), 309–319.

(84) Born, M.; Oppenheimer, R. Zur Quantentheorie Der Molekeln. *Ann Phys* **1927**, *389* (20), 457–484. https://doi.org/10.1002/andp.19273892002.

(85) Vanderbilt, D. Optimally Smooth Norm-Conserving Pseudopotentials. *Phys Rev B* **1985**, *32* (12), 8412–8415. https://doi.org/10.1103/PhysRevB.32.8412.

(86) Vanderbilt, D. Soft Self-Consistent Pseudopotentials in a Generalized Eigenvalue Formalism. *Phys Rev B* **1990**, *41* (11), 7892–7895. https://doi.org/10.1103/PhysRevB.41.7892.

(87) Blöchl, P. E. Generalized Separable Potentials for Electronic-Structure Calculations. *Phys Rev B* **1990**, *41* (8), 5414–5416. https://doi.org/10.1103/PhysRevB.41.5414.

(88) Blöchl, P. E. Projector Augmented-Wave Method. *Phys Rev B* **1994**, *50* (24), 17953–17979. https://doi.org/10.1103/PhysRevB.50.17953.

(89) Kresse, G.; Joubert, D. From Ultrasoft Pseudopotentials to the Projector Augmented-Wave Method. *Phys Rev B* **1999**, *59* (3), 1758–1775. https://doi.org/10.1103/PhysRevB.59.1758.

(90) Larsen, A. H.; Mortensen, J. J.; Blomqvist, J.; Castelli, I. E.; Christensen, R.; Dułak, M.; Friis, J.; Groves, M. N.; Hammer, B.; Hargus, C.; Hermes, E. D.; Jennings, P. C.; Bjerre Jensen, P.; Kermode, J.; Kitchin, J. R.; Leonhard Kolsbjerg, E.; Kubal, J.; Kaasbjerg, K.; Lysgaard, S.; Bergmann Maronsson, J.; Maxson, T.; Olsen, T.; Pastewka, L.; Peterson, A.; Rostgaard, C.; Schiøtz, J.; Schütt, O.; Strange, M.; Thygesen, K. S.; Vegge, T.; Vilhelmsen, L.; Walter, M.; Zeng, Z.; Jacobsen, K. W. The Atomic Simulation Environment—a Python Library for Working with Atoms. *Journal of Physics: Condensed*

Matter **2017**, *29* (27), 273002. https://doi.org/10.1088/1361-648X/aa680e.

(91) Kresse, G.; Furthmüller, J. Efficiency of Ab-Initio Total Energy Calculations for Metals and Semiconductors Using a Plane-Wave Basis Set. *Comput Mater Sci* **1996**, *6* (1), 15–50. https://doi.org/10.1016/0927-0256(96)00008-0.

(92) Kresse, G.; Furthmüller, J. Efficient Iterative Schemes for *ab initio* Total-Energy Calculations Using a Plane-Wave Basis Set. *Phys Rev B* **1996**, *54* (16), 11169–11186. https://doi.org/10.1103/PhysRevB.54.11169.

(93) Perdew, J. P.; Burke, K.; Ernzerhof, M. Generalized Gradient Approximation Made Simple. *Phys Rev Lett* **1996**, *77* (18), 3865–3868. https://doi.org/10.1103/PhysRevLett.77.3865.

(94) Perdew, J. P.; Burke, K.; Ernzerhof, M. Generalized Gradient Approximation Made Simple [Phys. Rev. Lett. **77**, 3865 (1996)]. *Phys Rev Lett* **1997**, *78* (7), 1396–1396. https://doi.org/10.1103/PhysRevLett.78.1396.

(95) Hammer, B.; Hansen, L. B.; Nørskov, J. K. Improved Adsorption Energetics within Density-Functional Theory Using Revised Perdew-Burke-Ernzerhof Functionals. *Phys Rev B* **1999**, *59* (11), 7413–7421. https://doi.org/10.1103/PhysRevB.59.7413.

(96) Monkhorst, H. J.; Pack, J. D. Special Points for Brillouin-Zone Integrations. *Phys Rev B* **1976**, *13* (12), 5188–5192. https://doi.org/10.1103/PhysRevB.13.5188.

(97) Pack, J. D.; Monkhorst, H. J. “Special Points for Brillouin-Zone Integrations”—a Reply. *Phys Rev B* **1977**, *16* (4), 1748–1749. https://doi.org/10.1103/PhysRevB.16.1748.

(98) Štich, I.; Car, R.; Parrinello, M.; Baroni, S. Conjugate Gradient Minimization of the Energy Functional: A New Method for Electronic Structure Calculation. *Phys Rev B* **1989**, *39* (8), 4997–5004. https://doi.org/10.1103/PhysRevB.39.4997.

(99) Gillan, M. J. Calculation of the Vacancy Formation Energy in Aluminium. *Journal of Physics: Condensed Matter* **1989**, *1* (4), 689–711. https://doi.org/10.1088/0953-8984/1/4/005.

(100) Arias, T. A.; Payne, M. C.; Joannopoulos, J. D. *Ab initio* Molecular Dynamics: Analytically Continued Energy Functionals and Insights into Iterative Solutions. *Phys Rev Lett* **1992**, *69* (7), 1077–1080. https://doi.org/10.1103/PhysRevLett.69.1077.

(101) Heyd, J.; Scuseria, G. E.; Ernzerhof, M. Hybrid Functionals Based on a Screened Coulomb Potential. *J Chem Phys* **2003**, *118* (18), 8207–8215. https://doi.org/10.1063/1.1564060.

(102) Heyd, J.; Scuseria, G. E.; Ernzerhof, M. Erratum: "Hybrid Functionals Based on a Screened Coulomb Potential" [J. Chem. Phys. 118, 8207 (2003)]. *J Chem Phys* **2006**, *124* (21). https://doi.org/10.1063/1.2204597.

(103) Krukau, A. V.; Vydrov, O. A.; Izmaylov, A. F.; Scuseria, G. E. Influence of the Exchange Screening Parameter on the Performance of Screened Hybrid Functionals. *J Chem Phys* **2006**, *125* (22). https://doi.org/10.1063/1.2404663.

(104) Grimme, S.; Antony, J.; Ehrlich, S.; Krieg, H. A Consistent and Accurate *ab initio* Parametrization of Density Functional Dispersion Correction (DFT-D) for the 94 Elements H-Pu. *J Chem Phys* **2010**, *132* (15). https://doi.org/10.1063/1.3382344.

(105) Makov, G.; Payne, M. C. Periodic Boundary Conditions in *ab initio* Calculations. *Phys Rev B* **1995**, *51* (7), 4014–4022. https://doi.org/10.1103/PhysRevB.51.4014.

(106) Venezuela, P.; Muniz, R. B.; Costa, A. T.; Edwards, D. M.; Power, S. R.; Ferreira, M. S. Emergence of Local Magnetic Moments in Doped Graphene-Related Materials. *Phys Rev B* **2009**, *80* (24), 241413. https://doi.org/10.1103/PhysRevB.80.241413.

(107) Hartree, D. R. The Wave Mechanics of an Atom with a Non-Coulomb Central Field. Part II. Some Results and Discussion. *Mathematical Proceedings of the Cambridge Philosophical Society* **1928**, *24* (1), 111–132. https://doi.org/10.1017/S0305004100011920.

(108) Fock, V. Näherungsmethode Zur Lösung Des Quantenmechanischen Mehrkörperproblems. *Zeitschrift für Physik* **1930**, *61* (1–2), 126–148. https://doi.org/10.1007/BF01340294.

(109) Fock, V. „Selfconsistent Field“ Mit Austausch Für Natrium. *Zeitschrift für Physik* **1930**, *62* (11–12), 795–805. https://doi.org/10.1007/BF01330439.

(110) Hartree, D. R.; Hartree, W. Self-Consistent Field, with Exchange, for Beryllium. *Proc R Soc Lond A Math Phys Sci* **1935**, *150* (869), 9–33. https://doi.org/10.1098/rspa.1935.0085.

(111) Perdew, J. P.; Schmidt, K. Jacob's Ladder of Density Functional Approximations for the Exchange-Correlation Energy. In *AIP Conference Proceedings*; AIP, 2001; Vol. 577, pp 1–20. https://doi.org/10.1063/1.1390175.

(112) Janthon, P.; Luo, S. (Andy); Kozlov, S. M.; Viñes, F.; Limtrakul, J.; Truhlar, D. G.; Illas, F. Bulk Properties of Transition Metals: A Challenge for the Design of Universal Density Functionals. *J Chem Theory Comput* **2014**, *10* (9), 3832–3839. https://doi.org/10.1021/ct500532v.

(113) Perdew, J. P.; Yang, W.; Burke, K.; Yang, Z.; Gross, E. K. U.; Scheffler, M.; Scuseria, G. E.; Henderson, T. M.; Zhang, I. Y.; Ruzsinszky, A.; Peng, H.; Sun, J.; Trushin, E.; Görling, A. Understanding Band Gaps of Solids in Generalized Kohn–Sham Theory. *Proceedings of the National Academy of Sciences* **2017**, *114* (11), 2801–2806. https://doi.org/10.1073/pnas.1621352114.

(114) Bader, R. F. W. *Atoms in Molecules : A Quantum Theory*; Clarendon Press, 1990; Vol. 22.

(115) Bader, R. F. W. A Quantum Theory of Molecular Structure and Its Applications. *Chem Rev* **1991**, *91* (5), 893–928. https://doi.org/10.1021/cr00005a013.

(116) Henkelman, G.; Arnaldsson, A.; Jónsson, H. A Fast and Robust Algorithm for Bader Decomposition of Charge Density. *Comput Mater Sci* **2006**, *36* (3), 354–360. https://doi.org/10.1016/j.commatsci.2005.04.010.

(117) Sanville, E.; Kenny, S. D.; Smith, R.; Henkelman, G. Improved Grid-Based Algorithm for Bader Charge Allocation. *J Comput Chem* **2007**, *28* (5), 899–908. https://doi.org/10.1002/jcc.20575.

(118) Tang, W.; Sanville, E.; Henkelman, G. A Grid-Based Bader Analysis Algorithm without Lattice Bias. *Journal of Physics: Condensed Matter* **2009**, *21* (8), 084204. https://doi.org/10.1088/0953-8984/21/8/084204.

(119) Yu, M.; Trinkle, D. R. Accurate and Efficient Algorithm for Bader Charge Integration. *J Chem Phys* **2011**, *134* (6). https://doi.org/10.1063/1.3553716.

(120) Mathew, K.; Sundararaman, R.; Letchworth-Weaver, K.; Arias, T. A.; Hennig, R. G. Implicit Solvation Model for Density-Functional Study of Nanocrystal Surfaces and Reaction Pathways. *J Chem Phys* **2014**, *140* (8). https://doi.org/10.1063/1.4865107.

(121) Mathew, K.; Kolluru, V. S. C.; Mula, S.; Steinmann, S. N.; Hennig, R. G. Implicit Self-Consistent Electrolyte Model in Plane-Wave Density-Functional Theory. *J Chem Phys* **2019**, *151* (23). https://doi.org/10.1063/1.5132354.

(122) Jouny, M.; Luc, W.; Jiao, F. General Techno-Economic Analysis of CO_2 Electrolysis Systems. *Ind Eng Chem Res* **2018**, *57* (6), 2165–2177. https://doi.org/10.1021/acs.iecr.7b03514.

(123) Seh, Z. W.; Kibsgaard, J.; Dickens, C. F.; Chorkendorff, I.; Nørskov, J. K.; Jaramillo, T. F. Combining Theory and Experiment in Electrocatalysis: Insights into Materials Design. *Science (1979)* **2017**, *355* (6321). https://doi.org/10.1126/science.aad4998.

(124) Anastasiadou, D.; Hensen, E. J. M.; Figueiredo, M. C. Electrocatalytic Synthesis of Organic Carbonates. *Chemical Communications* **2020**, *56* (86), 13082–13092. https://doi.org/10.1039/D0CC04231E.

(125) Wuttig, A.; Yaguchi, M.; Motobayashi, K.; Osawa, M.; Surendranath, Y. Inhibited Proton Transfer Enhances Au-Catalyzed CO_2-to-Fuels Selectivity. *Proceedings of the National Academy of Sciences* **2016**, *113* (32). https://doi.org/10.1073/pnas.1602984113.

(126) Verma, S.; Hamasaki, Y.; Kim, C.; Huang, W.; Lu, S.; Jhong, H.-R. M.; Gewirth, A. A.; Fujigaya, T.; Nakashima, N.; Kenis, P. J. A. Insights into the Low Overpotential Electroreduction of CO_2 to CO on a Supported Gold Catalyst in an Alkaline Flow Electrolyzer. *ACS Energy Lett* **2018**, *3* (1), 193–198. https://doi.org/10.1021/acsenergylett.7b01096.

(127) Prslja, P.; López, N. Stability and Redispersion of Ni Nanoparticles Supported on N-Doped Carbons for the CO_2 Electrochemical Reduction. *ACS Catal* **2021**, *11* (1), 88–94. https://doi.org/10.1021/acscatal.0c01909.

(128) Dunwell, M.; Lu, Q.; Heyes, J. M.; Rosen, J.; Chen, J. G.; Yan, Y.; Jiao, F.; Xu, B. The Central Role of Bicarbonate in the Electrochemical Reduction of Carbon Dioxide on Gold. *J Am Chem Soc* **2017**, *139* (10), 3774–3783. https://doi.org/10.1021/jacs.6b13287.

(129) Hansen, H. A.; Varley, J. B.; Peterson, A. A.; Nørskov, J. K. Understanding Trends in the Electrocatalytic Activity of Metals and Enzymes for CO_2 Reduction to CO. *J Phys Chem Lett* **2013**, *4* (3), 388–392. https://doi.org/10.1021/jz3021155.

(130) Chen, L. D.; Urushihara, M.; Chan, K.; Nørskov, J. K. Electric Field Effects in Electrochemical CO_2 Reduction. *ACS Catal* **2016**, *6* (10), 7133–7139. https://doi.org/10.1021/acscatal.6b02299.

(131) Ringe, S.; Morales-Guio, C. G.; Chen, L. D.; Fields, M.; Jaramillo, T. F.; Hahn, C.; Chan, K. Double Layer Charging Driven Carbon Dioxide Adsorption Limits the Rate of Electrochemical Carbon Dioxide Reduction on Gold. *Nat Commun* **2020**, *11* (1), 33. https://doi.org/10.1038/s41467-019-13777-z.

(132) Vijay, S.; Gauthier, J. A.; Heenen, H. H.; Bukas, V. J.; Kristoffersen, H. H.; Chan, K. Dipole-Field Interactions Determine the CO_2 Reduction Activity of 2D Fe–N–C Single-Atom Catalysts. *ACS Catal* **2020**, *10* (14), 7826–7835. https://doi.org/10.1021/acscatal.0c01375.

(133) Brown, S. M.; Orella, M.; Hsiao, Y. W.; Román-Leshkov, Y.; Surendranath, Y.; Bazant, M. Z.; Brushett, F. Electron Transfer Limitation in Carbon Dioxide Reduction Revealed by Data-Driven

Tafel Analysis. *ChemRxiv* **2020**. https://doi.org/10.26434/chemrxiv.13244906.v1.

(134) Ju, W.; Bagger, A.; Wang, X.; Tsai, Y.; Luo, F.; Möller, T.; Wang, H.; Rossmeisl, J.; Varela, A. S.; Strasser, P. Unraveling Mechanistic Reaction Pathways of the Electrochemical CO_2 Reduction on Fe–N–C Single-Site Catalysts. *ACS Energy Lett* **2019**, *4* (7), 1663–1671. https://doi.org/10.1021/acsenergylett.9b01049.

(135) Gauthier, J. A.; Ringe, S.; Dickens, C. F.; Garza, A. J.; Bell, A. T.; Head-Gordon, M.; Nørskov, J. K.; Chan, K. Challenges in Modeling Electrochemical Reaction Energetics with Polarizable Continuum Models. *ACS Catal* **2019**, *9* (2), 920–931. https://doi.org/10.1021/acscatal.8b02793.

(136) Anderson, P. W. Localized Magnetic States in Metals. *Physical Review* **1961**, *124* (1), 41–53. https://doi.org/10.1103/PhysRev.124.41.

(137) Newns, D. M. Self-Consistent Model of Hydrogen Chemisorption. *Physical Review* **1969**, *178* (3), 1123–1135. https://doi.org/10.1103/PhysRev.178.1123.

(138) Grimley, T. B. Overlap Effects in the Theory of Adsorption Using Anderson's Hamiltonian. *Journal of Physics C: Solid State Physics* **1970**, *3* (9), 1934–1942. https://doi.org/10.1088/0022-3719/3/9/012.

(139) Mills, G.; Jónsson, H. Quantum and Thermal Effects in H_2 Dissociative Adsorption: Evaluation of Free Energy Barriers in Multidimensional Quantum Systems. *Phys Rev Lett* **1994**, *72* (7), 1124–1127. https://doi.org/10.1103/PhysRevLett.72.1124.

(140) Henkelman, G.; Uberuaga, B. P.; Jónsson, H. A Climbing Image Nudged Elastic Band Method for Finding Saddle Points and Minimum Energy Paths. *J Chem Phys* **2000**, *113* (22), 9901–9904. https://doi.org/10.1063/1.1329672.

(141) Mehdipour, H.; Smith, B. A.; Rezakhani, A. T.; Tafreshi, S. S.; de Leeuw, N. H.; Prezhdo, O. V.; Moshfegh, A. Z.; Akimov, A. V. Dependence of Electron Transfer Dynamics on the Number of Graphene Layers in π-Stacked 2D Materials: Insights from *ab initio*

Nonadiabatic Molecular Dynamics. *Physical Chemistry Chemical Physics* **2019**, *21* (41), 23198–23208. https://doi.org/10.1039/C9CP04100A.

(142) Liu, K.; Wu, G.; Wang, G. Role of Local Carbon Structure Surrounding FeN_4 Sites in Boosting the Catalytic Activity for Oxygen Reduction. *The Journal of Physical Chemistry C* **2017**, *121* (21), 11319–11324. https://doi.org/10.1021/acs.jpcc.7b00913.

(143) Cheng, W.; Yuan, P.; Lv, Z.; Guo, Y.; Qiao, Y.; Xue, X.; Liu, X.; Bai, W.; Wang, K.; Xu, Q.; Zhang, J. Boosting Defective Carbon by Anchoring Well-Defined Atomically Dispersed Metal-N_4 Sites for ORR, OER, and Zn-Air Batteries. *Appl Catal B* **2020**, *260*, 118198. https://doi.org/10.1016/j.apcatb.2019.118198.

(144) Luo, F.; Roy, A.; Silvioli, L.; Cullen, D. A.; Zitolo, A.; Sougrati, M. T.; Oguz, I. C.; Mineva, T.; Teschner, D.; Wagner, S.; Wen, J.; Dionigi, F.; Kramm, U. I.; Rossmeisl, J.; Jaouen, F.; Strasser, P. P-Block Single-Metal-Site Tin/Nitrogen-Doped Carbon Fuel Cell Cathode Catalyst for Oxygen Reduction Reaction. *Nat Mater* **2020**, *19* (11), 1215–1223. https://doi.org/10.1038/s41563-020-0717-5.

(145) Gauthier, J. A.; Dickens, C. F.; Heenen, H. H.; Vijay, S.; Ringe, S.; Chan, K. Unified Approach to Implicit and Explicit Solvent Simulations of Electrochemical Reaction Energetics. *J Chem Theory Comput* **2019**, *15* (12), 6895–6906. https://doi.org/10.1021/acs.jctc.9b00717.

(146) Vijay, S.; Kastlunger, G.; Gauthier, J. A.; Patel, A.; Chan, K. Force-Based Method to Determine the Potential Dependence in Electrochemical Barriers. *J Phys Chem Lett* **2022**, *13* (25), 5719–5725. https://doi.org/10.1021/acs.jpclett.2c01367.

(147) Mortensen, J. J.; Hammer, B.; Nørskov, J. K. Alkali Promotion of N_2 Dissociation over Ru(0001). *Phys Rev Lett* **1998**, *80* (19), 4333–4336. https://doi.org/10.1103/PhysRevLett.80.4333.

(148) Muscat, J. P.; Newns, D. M. The Interpretation of Work-Function Variation in Alkali Chemisorption from the Atomic Viewpoint. *Journal of Physics C: Solid State Physics* **1974**, *7* (15), 2630–2644. https://doi.org/10.1088/0022-3719/7/15/012.

(149) Medford, A. J.; Shi, C.; Hoffmann, M. J.; Lausche, A. C.; Fitzgibbon, S. R.; Bligaard, T.; Nørskov, J. K. CatMAP: A Software Package for Descriptor-Based Microkinetic Mapping of Catalytic Trends. *Catal Letters* **2015**, *145* (3), 794–807. https://doi.org/10.1007/s10562-015-1495-6.

(150) Jiang, K.; Siahrostami, S.; Zheng, T.; Hu, Y.; Hwang, S.; Stavitski, E.; Peng, Y.; Dynes, J.; Gangisetty, M.; Su, D.; Attenkofer, K.; Wang, H. Isolated Ni Single Atoms in Graphene Nanosheets for High-Performance CO_2 Reduction. *Energy Environ Sci* **2018**, *11* (4), 893–903. https://doi.org/10.1039/C7EE03245E.

(151) Leonard, N.; Ju, W.; Sinev, I.; Steinberg, J.; Luo, F.; Varela, A. S.; Roldan Cuenya, B.; Strasser, P. The Chemical Identity, State and Structure of Catalytically Active Centers during the Electrochemical CO_2 Reduction on Porous Fe–Nitrogen–Carbon (Fe–N–C) Materials. *Chem Sci* **2018**, *9* (22), 5064–5073. https://doi.org/10.1039/C8SC00491A.

(152) Jiang, K.; Siahrostami, S.; Akey, A. J.; Li, Y.; Lu, Z.; Lattimer, J.; Hu, Y.; Stokes, C.; Gangishetty, M.; Chen, G.; Zhou, Y.; Hill, W.; Cai, W.-B.; Bell, D.; Chan, K.; Nørskov, J. K.; Cui, Y.; Wang, H. Transition-Metal Single Atoms in a Graphene Shell as Active Centers for Highly Efficient Artificial Photosynthesis. *Chem* **2017**, *3* (6), 950–960. https://doi.org/10.1016/j.chempr.2017.09.014.

(153) Yang, H. Bin; Hung, S.-F.; Liu, S.; Yuan, K.; Miao, S.; Zhang, L.; Huang, X.; Wang, H.-Y.; Cai, W.; Chen, R.; Gao, J.; Yang, X.; Chen, W.; Huang, Y.; Chen, H. M.; Li, C. M.; Zhang, T.; Liu, B. Atomically Dispersed Ni(i) as the Active Site for Electrochemical CO_2 Reduction. *Nat Energy* **2018**, *3* (2), 140–147. https://doi.org/10.1038/s41560-017-0078-8.

(154) Li, X.; Bi, W.; Chen, M.; Sun, Y.; Ju, H.; Yan, W.; Zhu, J.; Wu, X.; Chu, W.; Wu, C.; Xie, Y. Exclusive Ni–N_4 Sites Realize Near-Unity CO Selectivity for Electrochemical CO_2 Reduction. *J Am Chem Soc* **2017**, *139* (42), 14889–14892. https://doi.org/10.1021/jacs.7b09074.

(155) Liu, S.; Yang, H. Bin; Hung, S.; Ding, J.; Cai, W.; Liu, L.; Gao, J.; Li, X.; Ren, X.; Kuang, Z.; Huang, Y.; Zhang, T.; Liu, B. Elucidating the Electrocatalytic CO_2 Reduction Reaction over a Model Single-Atom Nickel Catalyst. *Angewandte Chemie International Edition* **2020**, *59* (2), 798–803. https://doi.org/10.1002/anie.201911995.

(156) Haldar, S.; Roy, K.; Nandi, S.; Chakraborty, D.; Puthusseri, D.; Gawli, Y.; Ogale, S.; Vaidhyanathan, R. High and Reversible Lithium Ion Storage in Self-Exfoliated Triazole-Triformyl Phloroglucinol-Based Covalent Organic Nanosheets. *Adv Energy Mater* **2018**, *8* (8), 1702170. https://doi.org/10.1002/aenm.201702170.

(157) Zhang, H.; Chung, H. T.; Cullen, D. A.; Wagner, S.; Kramm, U. I.; More, K. L.; Zelenay, P.; Wu, G. High-Performance Fuel Cell Cathodes Exclusively Containing Atomically Dispersed Iron Active Sites. *Energy Environ Sci* **2019**, *12* (8), 2548–2558. https://doi.org/10.1039/C9EE00877B.

(158) Koshy, D. M.; Chen, S.; Lee, D. U.; Stevens, M. B.; Abdellah, A. M.; Dull, S. M.; Chen, G.; Nordlund, D.; Gallo, A.; Hahn, C.; Higgins, D. C.; Bao, Z.; Jaramillo, T. F. Understanding the Origin of Highly Selective CO_2 Electroreduction to CO on Ni,N-doped Carbon Catalysts. *Angewandte Chemie International Edition* **2020**, *59* (10), 4043–4050. https://doi.org/10.1002/anie.201912857.

(159) Brunauer, S.; Emmett, P. H.; Teller, E. Adsorption of Gases in Multimolecular Layers. *J Am Chem Soc* **1938**, *60* (2), 309–319. https://doi.org/10.1021/ja01269a023.

(160) Hou, Y.; Liang, Y.-L.; Shi, P.-C.; Huang, Y.-B.; Cao, R. Atomically Dispersed Ni Species on N-Doped Carbon Nanotubes for Electroreduction of CO_2 with Nearly 100% CO Selectivity. *Appl Catal B* **2020**, *271*, 118929. https://doi.org/10.1016/j.apcatb.2020.118929.

(161) Allen, J. P.; Watson, G. W. Occupation Matrix Control of D- and f-Electron Localisations Using DFT + U. *Physical Chemistry Chemical Physics* **2014**, *16* (39), 21016–21031. https://doi.org/10.1039/C4CP01083C.

(162) Gu, J.; Hsu, C.-S.; Bai, L.; Chen, H. M.; Hu, X. Atomically Dispersed Fe^{3+} Sites Catalyze Efficient CO_2 Electroreduction to CO. *Science (1979)* **2019**, *364* (6445), 1091–1094. https://doi.org/10.1126/science.aaw7515.

(163) Shi, C.; Hansen, H. A.; Lausche, A. C.; Nørskov, J. K. Trends in Electrochemical CO_2 Reduction Activity for Open and Close-Packed Metal Surfaces. *Physical Chemistry Chemical Physics* **2014**, *16* (10), 4720–4727. https://doi.org/10.1039/C3CP54822H.

(164) Xin, H.; Vojvodic, A.; Voss, J.; Nørskov, J. K.; Abild-Pedersen, F. Effects of d-Band Shape on the Surface Reactivity of Transition-Metal Alloys. *Phys Rev B* **2014**, *89* (11), 115114. https://doi.org/10.1103/PhysRevB.89.115114.

(165) Hammer, B.; Morikawa, Y.; Nørskov, J. K. CO Chemisorption at Metal Surfaces and Overlayers. *Phys Rev Lett* **1996**, *76* (12), 2141–2144. https://doi.org/10.1103/PhysRevLett.76.2141.

(166) Réocreux, R.; Sykes, E. C. H.; Michaelides, A.; Stamatakis, M. Stick or Spill? Scaling Relationships for the Binding Energies of Adsorbates on Single-Atom Alloy Catalysts. *J Phys Chem Lett* **2022**, *13* (31), 7314–7319. https://doi.org/10.1021/acs.jpclett.2c01519.

(167) Su, Y.-Q.; Zhang, L.; Wang, Y.; Liu, J.-X.; Muravev, V.; Alexopoulos, K.; Filot, I. A. W.; Vlachos, D. G.; Hensen, E. J. M. Stability of Heterogeneous Single-Atom Catalysts: A Scaling Law Mapping Thermodynamics to Kinetics. *NPJ Comput Mater* **2020**, *6* (1), 144. https://doi.org/10.1038/s41524-020-00411-6.

(168) Anand, M.; Rohr, B.; Statt, M. J.; Nørskov, J. K. Scaling Relationships and Volcano Plots in Homogeneous Catalysis. *J Phys Chem Lett* **2020**, *11* (20), 8518–8526. https://doi.org/10.1021/acs.jpclett.0c01991.

(169) Anand, M.; Nørskov, J. K. Scaling Relations in Homogeneous Catalysis: Analyzing the Buchwald–Hartwig Amination Reaction. *ACS Catal* **2020**, *10* (1), 336–345. https://doi.org/10.1021/acscatal.9b04323.

(170) Choi, C.; Yoon, S.; Jung, Y. Shifting the Scaling Relations of Single-Atom Catalysts for Facile Methane Activation by Tuning the

Coordination Number. *Chem Sci* **2021**, *12* (10), 3551–3557. https://doi.org/10.1039/D0SC05632D.

(171) Cao, H.; Zhang, Z.; Chen, J.-W.; Wang, Y.-G. Potential-Dependent Free Energy Relationship in Interpreting the Electrochemical Performance of CO_2 Reduction on Single Atom Catalysts. *ACS Catal* **2022**, *12* (11), 6606–6617. https://doi.org/10.1021/acscatal.2c01470.

(172) Guo, Y.; Wang, G.; Shen, S.; Wei, G.; Xia, G.; Zhang, J. On Scaling Relations of Single Atom Catalysts for Electrochemical Ammonia Synthesis. *Appl Surf Sci* **2021**, *550*, 149283. https://doi.org/10.1016/j.apsusc.2021.149283.

(173) Li, Y.; Su, H.; Chan, S. H.; Sun, Q. CO_2 Electroreduction Performance of Transition Metal Dimers Supported on Graphene: A Theoretical Study. *ACS Catal* **2015**, *5* (11), 6658–6664. https://doi.org/10.1021/acscatal.5b01165.

(174) Vojvodic, A.; Nørskov, J. K.; Abild-Pedersen, F. Electronic Structure Effects in Transition Metal Surface Chemistry. *Top Catal* **2014**, *57* (1–4), 25–32. https://doi.org/10.1007/s11244-013-0159-2.

(175) Hammer, B.; Nørskov, J. K. Electronic Factors Determining the Reactivity of Metal Surfaces. *Surf Sci* **1995**, *343* (3), 211–220. https://doi.org/10.1016/0039-6028(96)80007-0.

(176) Ruban, A.; Hammer, B.; Stoltze, P.; Skriver, H. L.; Nørskov, J. K. Surface Electronic Structure and Reactivity of Transition and Noble Metals. *J Mol Catal A Chem* **1997**, *115* (3), 421–429. https://doi.org/10.1016/S1381-1169(96)00348-2.

(177) Zheng, H.; Li, H.; Luo, L.; Zhao, Z.; Henkelman, G. Factors That Influence Hydrogen Binding at Metal-atop Sites. *J Chem Phys* **2021**, *155* (2). https://doi.org/10.1063/5.0056774.

(178) Vijay, S.; Kastlunger, G.; Chan, K.; Nørskov, J. K. Limits to Scaling Relations between Adsorption Energies? *J Chem Phys* **2022**, *156* (23). https://doi.org/10.1063/5.0096625.

(179) Li, Y.; Sun, Q. Recent Advances in Breaking Scaling Relations for Effective Electrochemical Conversion of CO_2. *Adv Energy Mater* **2016**, *6* (17), 1600463. https://doi.org/10.1002/aenm.201600463.

(180) Sours, T.; Patel, A.; Nørskov, J.; Siahrostami, S.; Kulkarni, A. Circumventing Scaling Relations in Oxygen Electrochemistry Using Metal–Organic Frameworks. *J Phys Chem Lett* **2020**, *11* (23), 10029–10036. https://doi.org/10.1021/acs.jpclett.0c02889.

(181) Cao, A.; Bukas, V. J.; Shadravan, V.; Wang, Z.; Li, H.; Kibsgaard, J.; Chorkendorff, I.; Nørskov, J. K. A Spin Promotion Effect in Catalytic Ammonia Synthesis. *Nat Commun* **2022**, *13* (1), 2382. https://doi.org/10.1038/s41467-022-30034-y.

(182) Logadottir, A.; Nørskov, J. K. The Effect of Strain for N_2 Dissociation on Fe Surfaces. *Surf Sci* **2001**, *489* (1–3), 135–143. https://doi.org/10.1016/S0039-6028(01)01171-2.

(183) Gong, S.; Wang, W.; Xiao, X.; Liu, J.; Wu, C.; Lv, X. Elucidating Influence of the Existence Formation of Anchored Cobalt Phthalocyanine on Electrocatalytic CO_2-to-CO Conversion. *Nano Energy* **2021**, *84*, 105904. https://doi.org/10.1016/j.nanoen.2021.105904.

(184) Zhang, Y.; Yu, Z.; She, F.; Wei, L.; Zeng, Z.; Li, H. Design of Molecular M–N–C Dual-Atom Catalysts for Nitrogen Reduction Starting from Surface State Analysis. *J Colloid Interface Sci* **2023**, *640*, 983–989. https://doi.org/10.1016/j.jcis.2023.03.033.

(185) Frumkin, A. N.; Nikolaeva-Fedorovich, N. V.; Berezina, N. P.; Keis, Kh. E. The Electroreduction of the $S_2O_8^{2-}$ Anion. *J Electroanal Chem Interfacial Electrochem* **1975**, *58* (1), 189–201. https://doi.org/10.1016/S0022-0728(75)80352-4.

(186) Huang, B.; Myint, K. H.; Wang, Y.; Zhang, Y.; Rao, R. R.; Sun, J.; Muy, S.; Katayama, Y.; Corchado Garcia, J.; Fraggedakis, D.; Grossman, J. C.; Bazant, M. Z.; Xu, K.; Willard, A. P.; Shao-Horn, Y. Cation-Dependent Interfacial Structures and Kinetics for Outer-Sphere Electron-Transfer Reactions. *The Journal of Physical Chemistry C* **2021**, *125* (8), 4397–4411. https://doi.org/10.1021/acs.jpcc.0c10492.

(187) Favero, S.; Stephens, I. E. L.; Titirici, M.-M. Deconvoluting Kinetics and Transport Effects of Ionic Liquid Layers on FeN_4-Based Oxygen Reduction Catalysts. *EES Catalysis* **2023**, (advance article). https://doi.org/10.1039/D3EY00166K.

(188) Melander, M. M.; Kuisma, M. J.; Christensen, T. E. K.; Honkala, K. Grand-Canonical Approach to Density Functional Theory of Electrocatalytic Systems: Thermodynamics of Solid-Liquid Interfaces at Constant Ion and Electrode Potentials. *J Chem Phys* **2019**, *150* (4), 041706. https://doi.org/10.1063/1.5047829.

(189) De, S.; Bartók, A. P.; Csányi, G.; Ceriotti, M. Comparing Molecules and Solids across Structural and Alchemical Space. *Physical Chemistry Chemical Physics* **2016**, *18* (20), 13754–13769. https://doi.org/10.1039/C6CP00415F.

(190) Bartók, A. P.; Kondor, R.; Csányi, G. On Representing Chemical Environments. *Phys Rev B* **2013**, *87* (18), 184115. https://doi.org/10.1103/PhysRevB.87.184115.

(191) Bartók, A. P.; Kondor, R.; Csányi, G. Publisher's Note: On Representing Chemical Environments [Phys. Rev. B **87** , 184115 (2013)]. *Phys Rev B* **2013**, *87* (21), 219902. https://doi.org/10.1103/PhysRevB.87.219902.

(192) Bartók, A. P.; Kondor, R.; Csányi, G. Erratum: On Representing Chemical Environments [Phys. Rev. B **87**, 184115 (2013)]. *Phys Rev B* **2017**, *96* (1), 019902. https://doi.org/10.1103/PhysRevB.96.019902.

(193) Bartók, A. P.; Payne, M. C.; Kondor, R.; Csányi, G. Gaussian Approximation Potentials: The Accuracy of Quantum Mechanics, without the Electrons. *Phys Rev Lett* **2010**, *104* (13), 136403. https://doi.org/10.1103/PhysRevLett.104.136403.

(194) Deringer, V. L.; Bartók, A. P.; Bernstein, N.; Wilkins, D. M.; Ceriotti, M.; Csányi, G. Gaussian Process Regression for Materials and Molecules. *Chem Rev* **2021**, *121* (16), 10073–10141. https://doi.org/10.1021/acs.chemrev.1c00022.

(195) Creutz, C.; Schwarz, H. A.; Wishart, J. F.; Fujita, E.; Sutin, N. A Dissociative Pathway for Equilibration of a Hydrido $CoL(H)^{2+}$

Complex with Carbon Dioxide and Carbon Monoxide. Ligand Binding Constants in the Macrocyclic [14]-Dienecobalt(I) System. *J Am Chem Soc* **1989**, *111* (3), 1153–1154. https://doi.org/10.1021/ja00185a069.

(196) Donnelly, M. A.; Zimmer, M. Structural Analysis of All the Nickel 14-Membered Tetraaza Macrocycles in the Cambridge Structural Database. *Inorg Chem* **1999**, *38* (8), 1650–1658. https://doi.org/10.1021/ic980918f.

(197) Peterson, A. A.; Abild-Pedersen, F.; Studt, F.; Rossmeisl, J.; Nørskov, J. K. How Copper Catalyzes the Electroreduction of Carbon Dioxide into Hydrocarbon Fuels. *Energy Environ Sci* **2010**, *3* (9), 1311. https://doi.org/10.1039/c0ee00071j.

(198) Islam, S. M. R.; Khezeli, F.; Ringe, S.; Plaisance, C. *Development and Implementation of a Nonlocal and Nonlinear Implicit Electrolyte Model*; 2023.

(199) Peterson, A. A.; Abild-Pedersen, F.; Studt, F.; Rossmeisl, J.; Nørskov, J. K. How Copper Catalyzes the Electroreduction of Carbon Dioxide into Hydrocarbon Fuels. *Energy Environ Sci* **2010**, *3* (9), 1311. https://doi.org/10.1039/c0ee00071j.

(200) Huang, Z.-Q.; Chen, Y.-T.; Chang, C.-R.; Li, J. Theoretical Insights into Dual-Metal-Site Catalysts for the Nonoxidative Coupling of Methane. *ACS Catal* **2021**, *11* (21), 13149–13159. https://doi.org/10.1021/acscatal.1c02597.

(201) Zhao, H.; Cao, H.; Zhang, Z.; Wang, Y.-G. Modeling the Potential-Dependent Kinetics of CO_2 Electroreduction on Single-Nickel Atom Catalysts with Explicit Solvation. *ACS Catal* **2022**, *12* (18), 11380–11390. https://doi.org/10.1021/acscatal.2c02383.

(202) Li, J.; Sougrati, M. T.; Zitolo, A.; Ablett, J. M.; Oğuz, I. C.; Mineva, T.; Matanovic, I.; Atanassov, P.; Huang, Y.; Zenyuk, I.; Di Cicco, A.; Kumar, K.; Dubau, L.; Maillard, F.; Dražić, G.; Jaouen, F. Identification of Durable and Non-Durable FeN_x Sites in Fe–N–C Materials for Proton Exchange Membrane Fuel Cells. *Nat Catal* **2020**, *4* (1), 10–19. https://doi.org/10.1038/s41929-020-00545-2.

(203) Patniboon, T.; Hansen, H. A. Acid-Stable and Active M–N–C Catalysts for the Oxygen Reduction Reaction: The Role of Local Structure. *ACS Catal* **2021**, *11* (21), 13102–13118. https://doi.org/10.1021/acscatal.1c02941.

Appendices

I. Additional figures

In this Section, we present some of the Figures taken out of the main text for brevity and/or cohesion, and yet are deemed worthy of inclusion for completeness.

Most figures found in this Appendix are 1-to-1 re-plots of the main-text Figures, just with the GGA data instead of the hybrid data. However, there are also exceptions:

- App. Figure 6 pertains to a different adsorbate altogether compared to Figure 18.
- While App. Figure 7 is the GGA version of Figure 19, App. Figure 9 and App. Figure 8 are likewise their respective non-spin-polarized versions.
- Likewise, App. Figure 11 is the GGA version of Figure 27, and App. Figure 13 and App. Figure 12 are their respective counterparts calculated with idealized instead of actual *d*-state fillings.
- App. Figure 14 and App. Figure 15 are fits akin to the aforementioned ones but with all five parameters open for optimization.

It is seen that in most cases the scientific conclusion is not dependent on the choice of the functionals, save for the noted over-binding of *CO on FeNC and CoNC (see “Comparative characterization of MNCs”), and the quality of the fits.

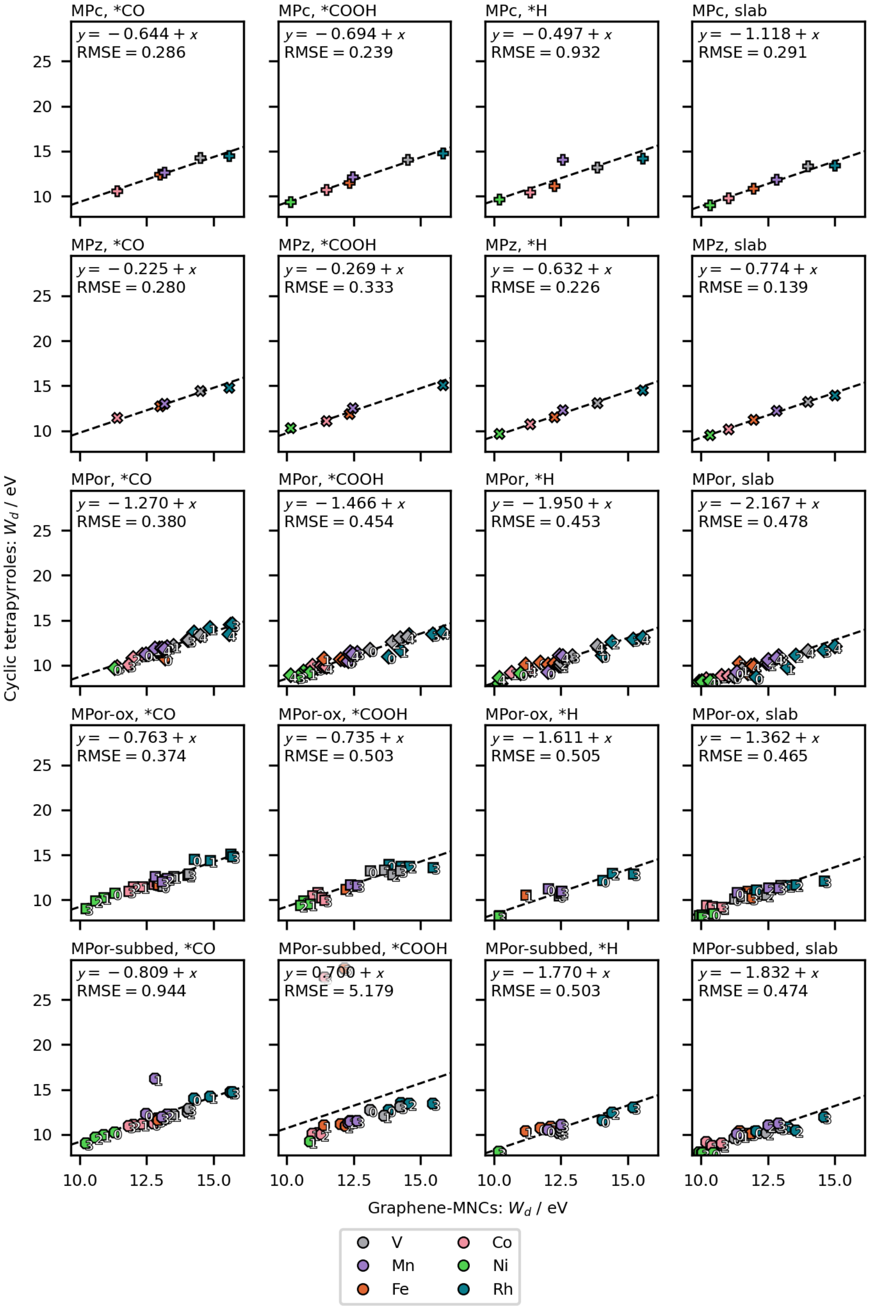

App. Figure 1. Plot of the GGA *d*-band widths of the metal CTPs, against those of the G-MNCs of corresponding local stoichiometry. The dashed lines are fitting lines with a fixed slope of unity. Data points are split between subplots by the family of the CTP, and the adsorbate on the metal (if any); the numeric subscripts indicate the number of chelating N atoms in porphyrin derivatives and G-MNCs.

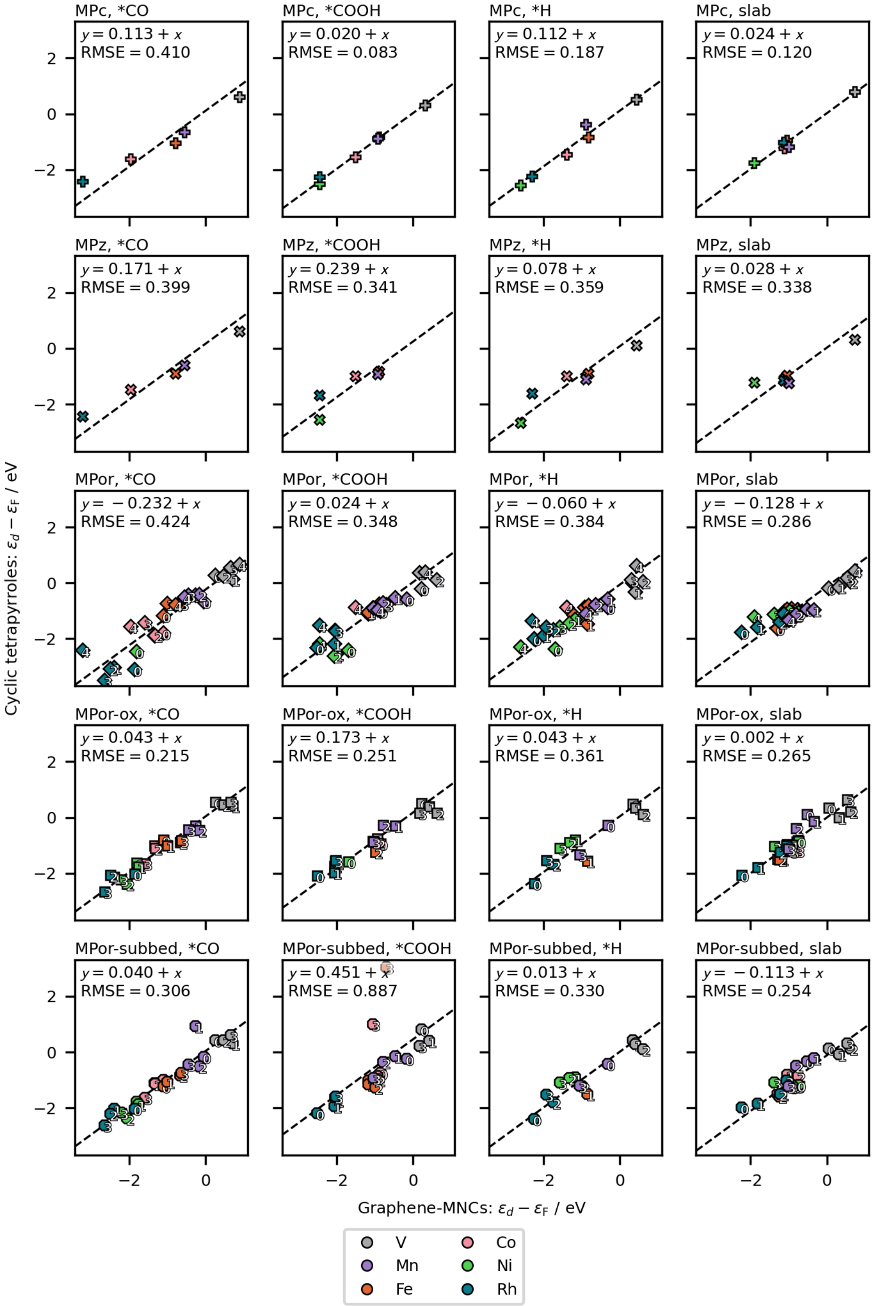

App. Figure 2. Plot of the GGA *d*-band centers of the metal CTPs against those of the G-MNCs of corresponding local stoichiometry. The dashed lines are fitting lines with a fixed slope of unity. Data points are split between subplots by the family of the CTP, and the adsorbate on the metal (if any); the numeric subscripts indicate the number of chelating N atoms in porphyrin derivatives and G-MNCs.

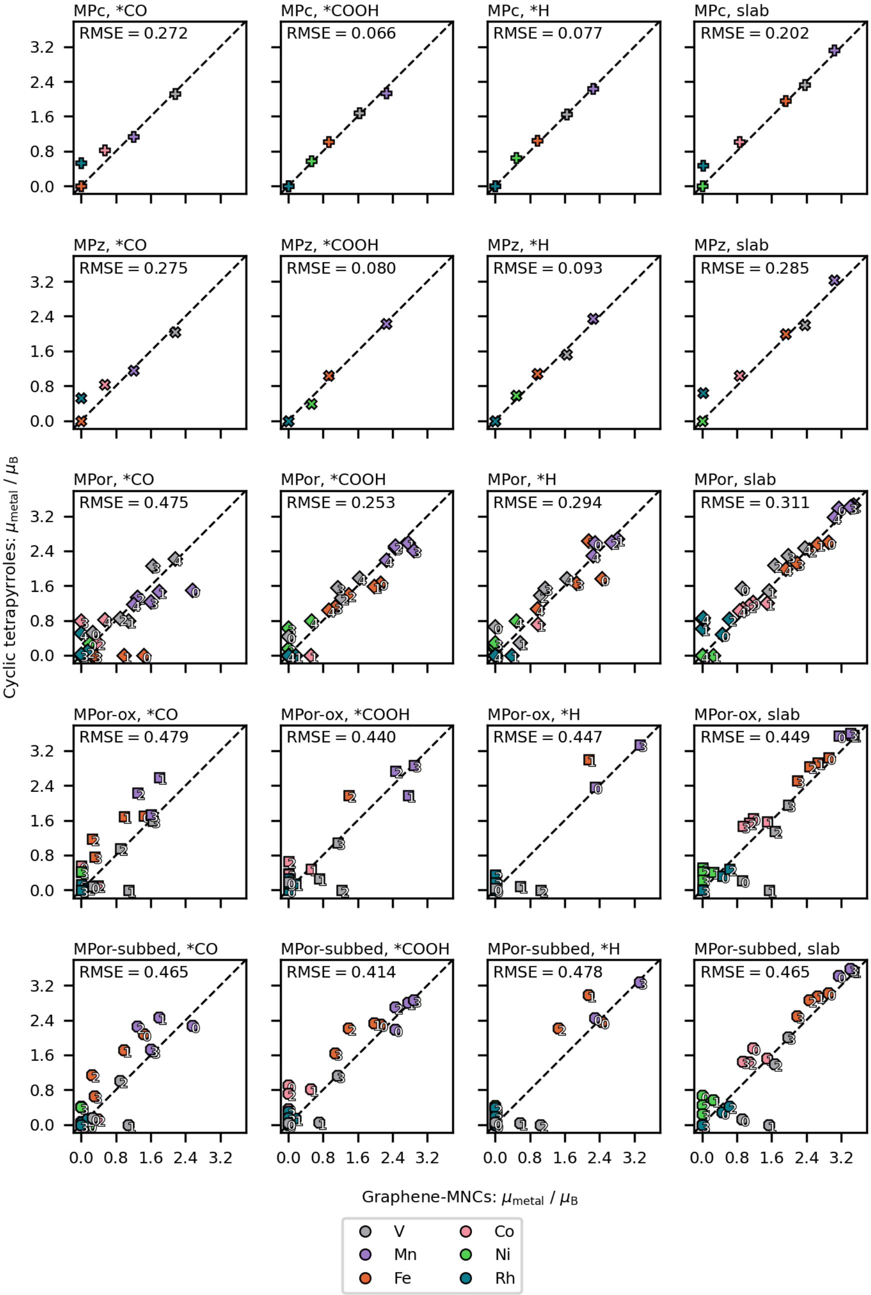

App. Figure 3. Plot of the GGA metal magnetic moments of the metal CTPs against those of the G-MNCs of corresponding local stoichiometry. The dashed lines are parity lines. Data points are split between subplots by the family of the CTP, and the adsorbate on the metal (if any); the numeric subscripts indicate the number of chelating N atoms in porphyrin derivatives and G-MNCs.

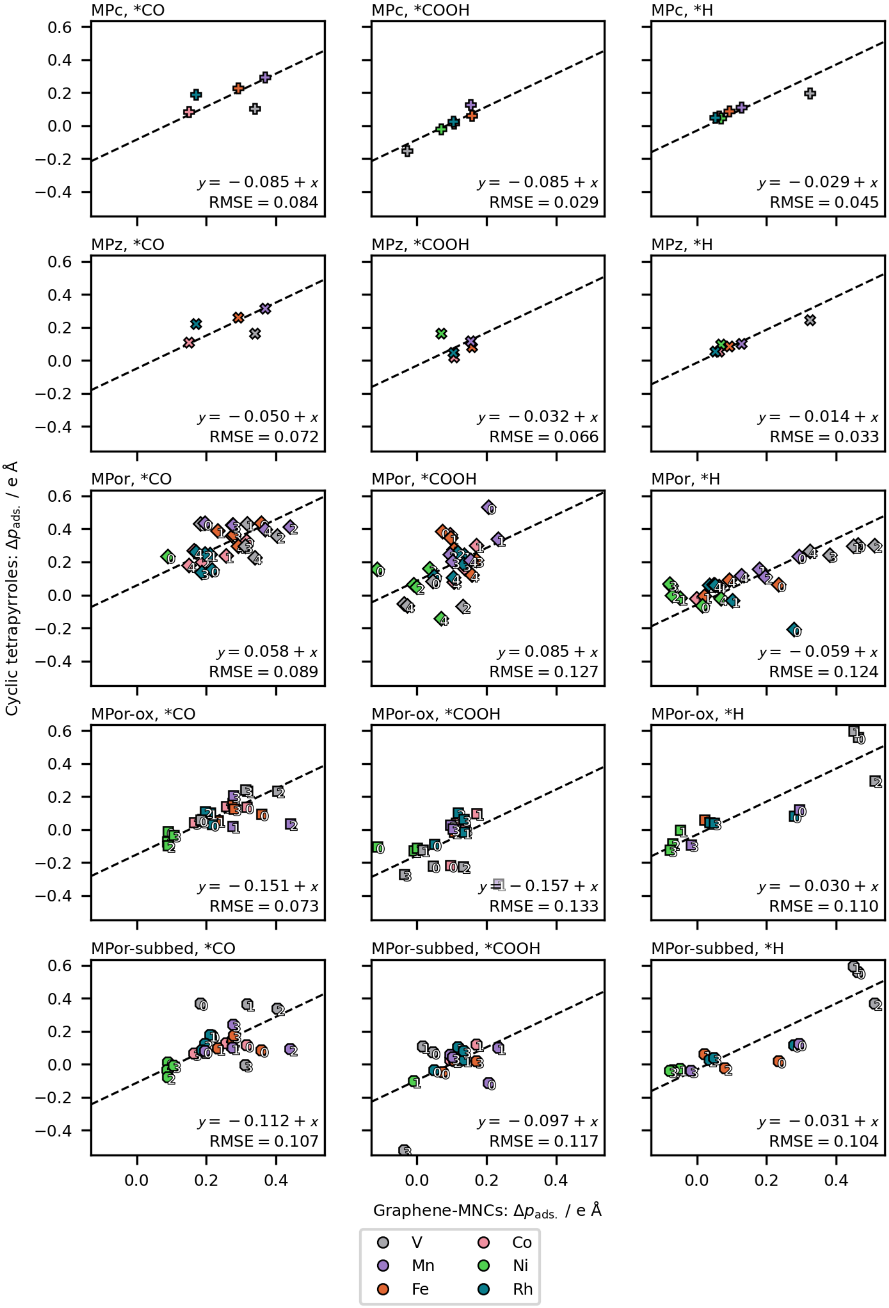

App. Figure 4. Plot of the GGA adsorbate-induced dipole moments, on metal CTPs against those on the G-MNCs of corresponding local stoichiometry. The dashed lines are fitting lines with a fixed slope of unity. Data points are split between subplots by the family of the CTP, and the adsorbate on the metal; the numeric subscripts indicate the number of chelating N atoms in porphyrin derivatives and G-MNCs.

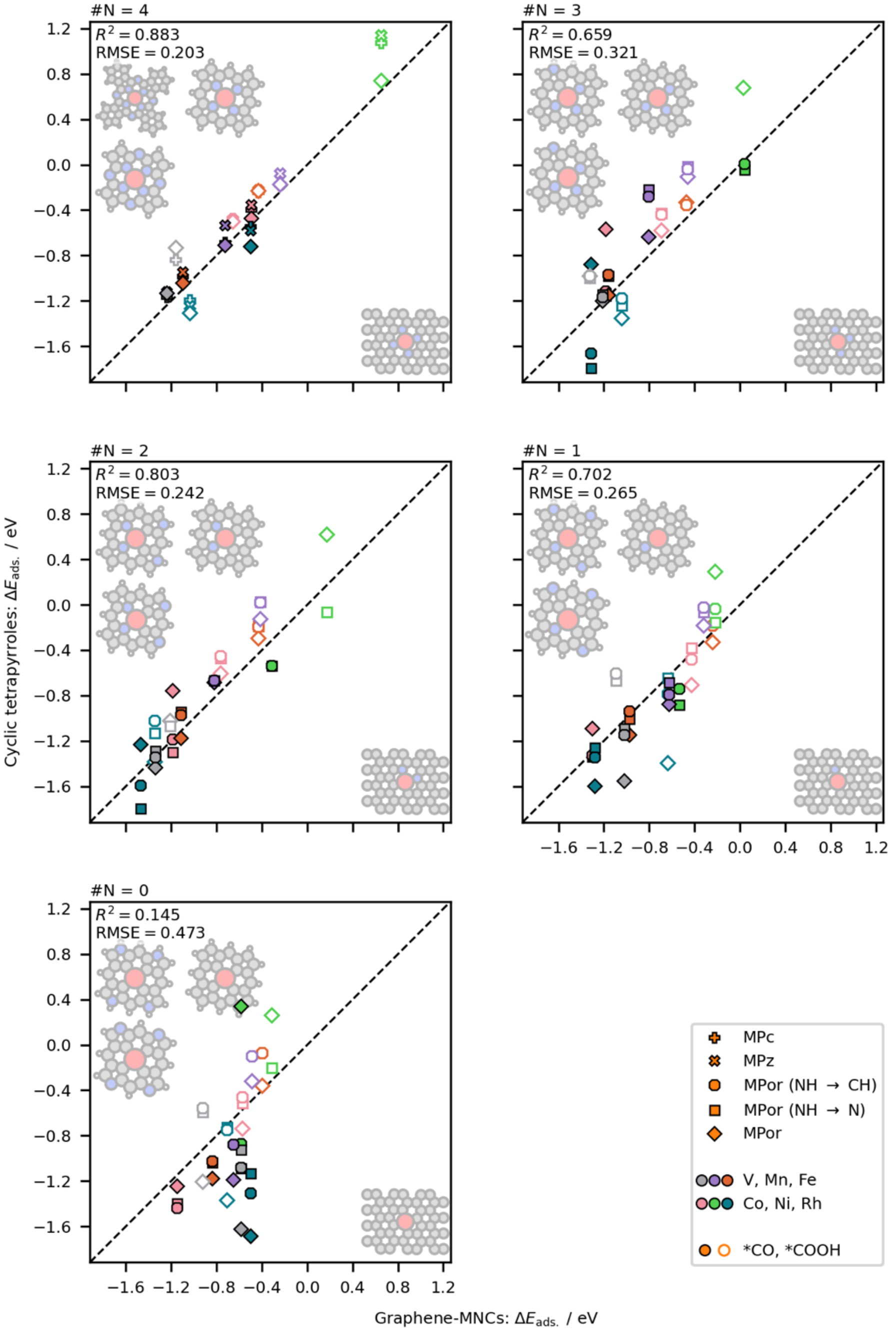

App. Figure 5. Plot of the GGA formation energies of the *CO and *COOH adsorbate states on metal CTPs against the same quantities on G-MNCs of corresponding local stoichiometry. The dashed lines are parity lines. Data points are split between subplots by the number of N atoms chelating the metal center.

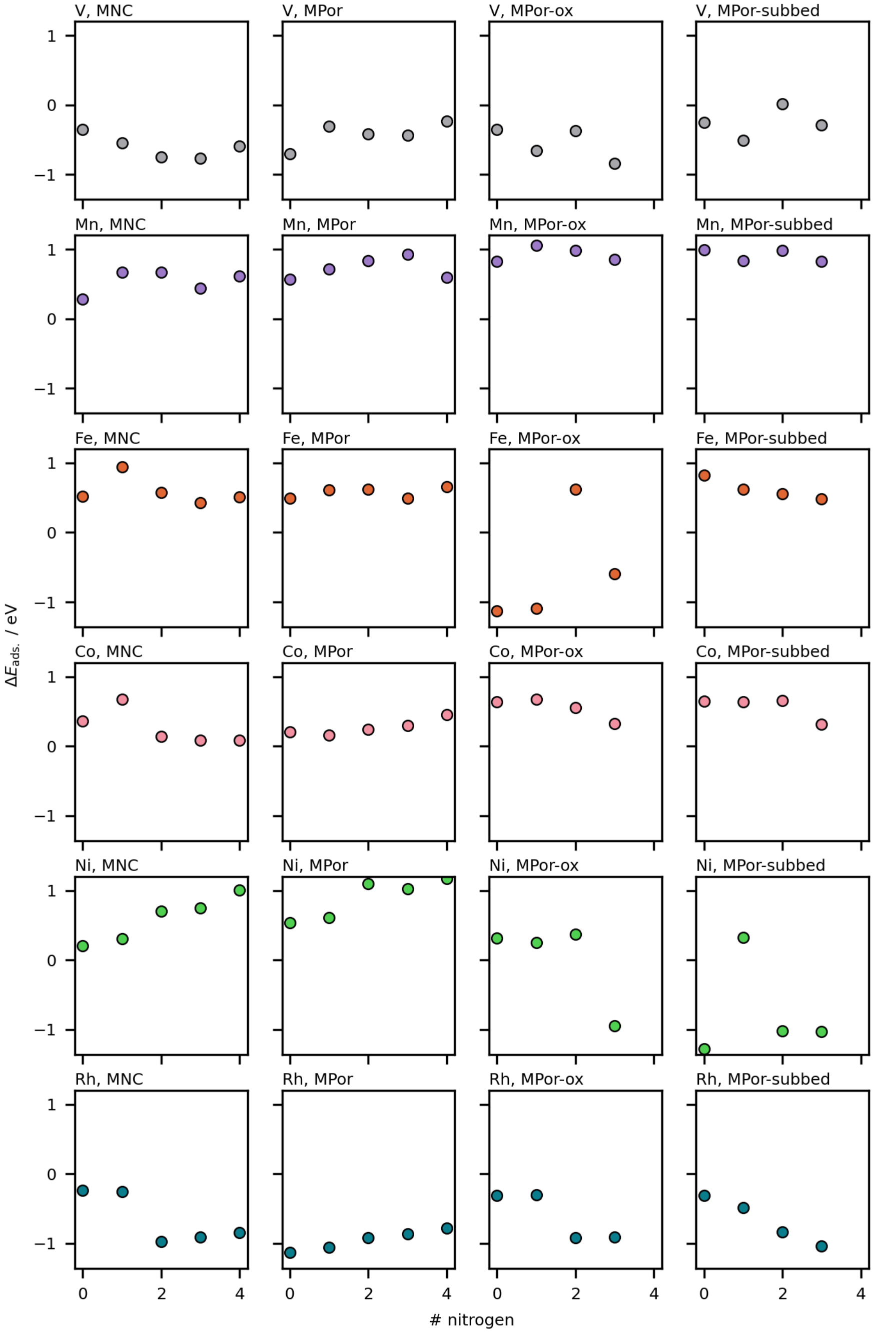

App. Figure 6. Plot of the hybrid formation energies of the *COOH adsorbate state on various MNCs against the number of N atoms chelating the metal. Data points are split between subplots by the metal species and the family of MNC structures. Note that "MNC" here is to be understood as "G-MNC".

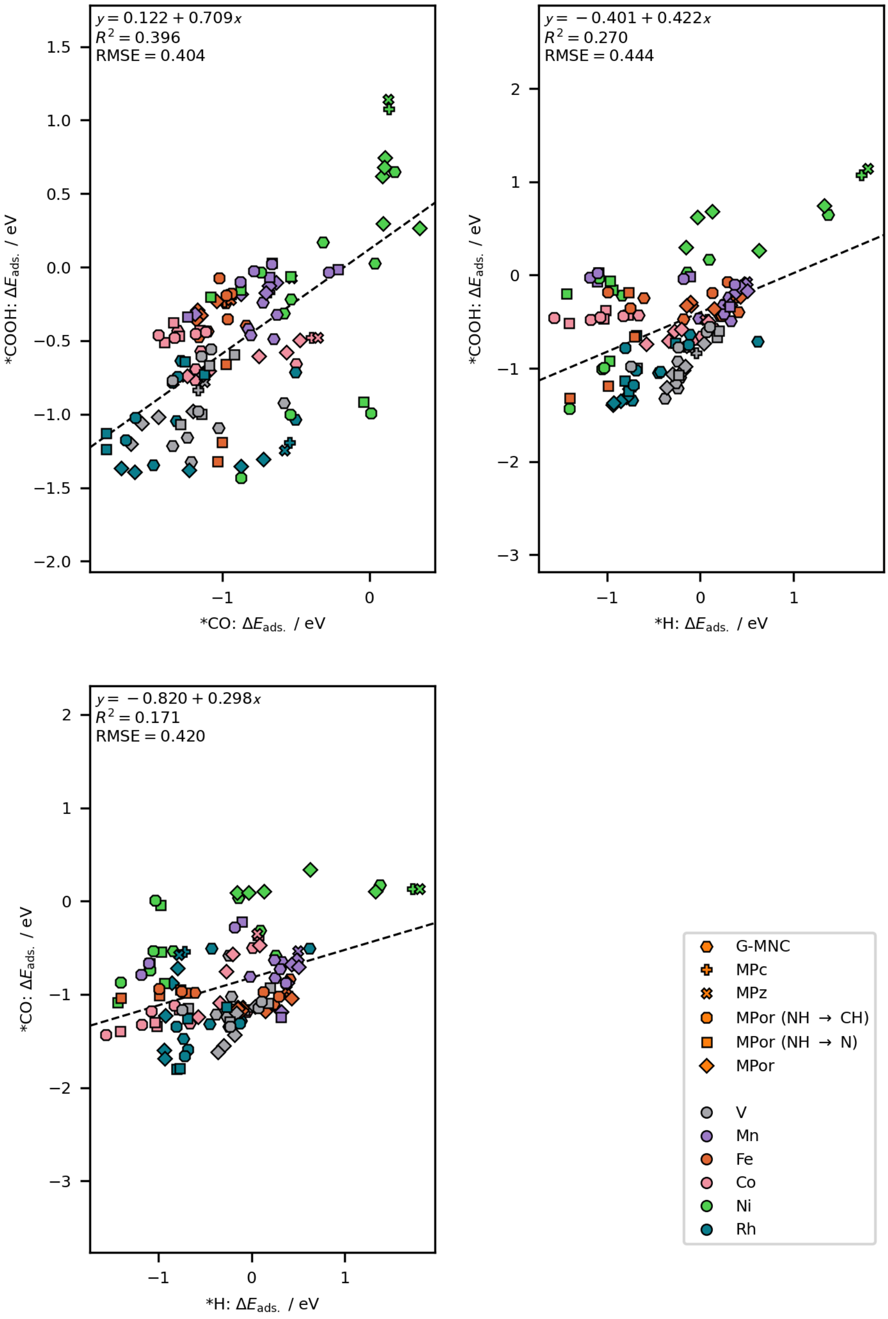

App. Figure 7. Inter-adsorbate "scaling lines" of their formation energies (spin-polarized GGA calculations).

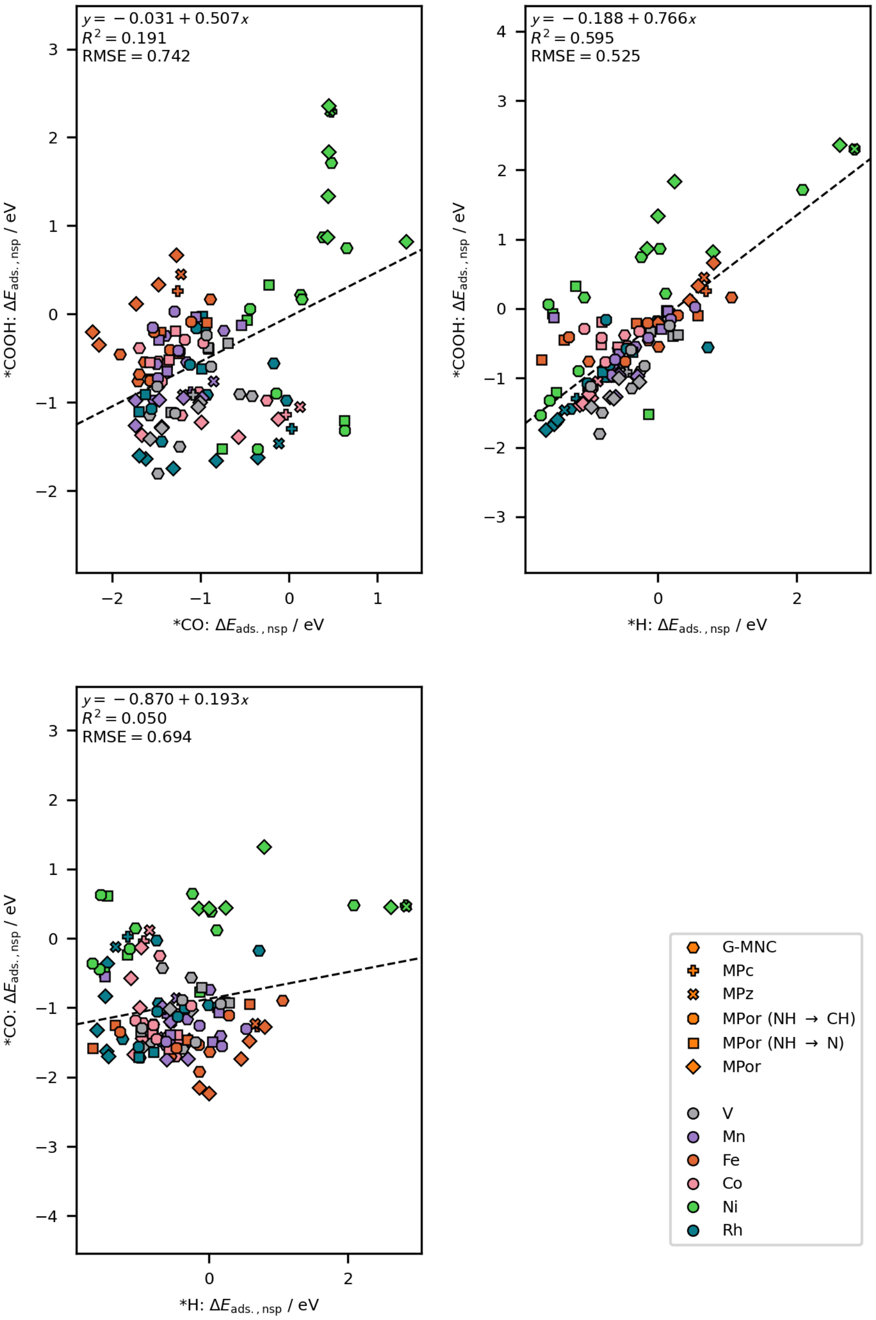

App. Figure 8. Inter-adsorbate “scaling lines” of their formation energies (non-spin-polarized hybrid calculations).

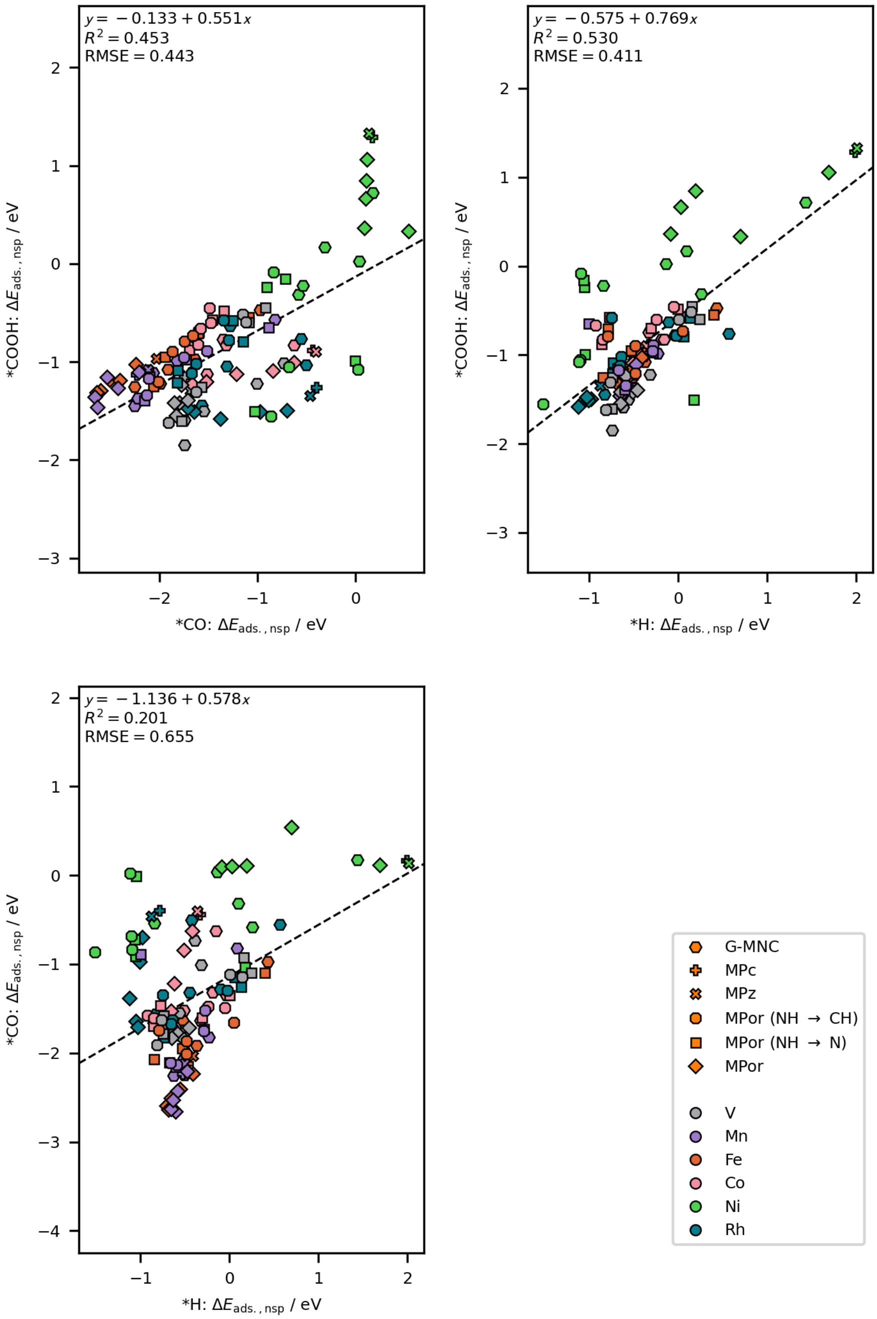

App. Figure 9. Inter-adsorbate "scaling lines" of their formation energies (non-spin-polarized GGA calculations).

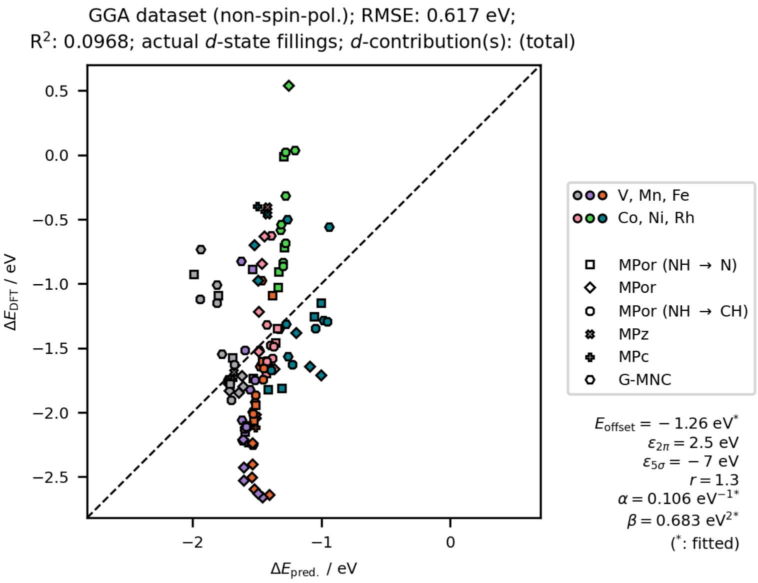

App. Figure 10. Parity plot of the GGA non-spin-polarized $\Delta E_{*\mathrm{CO}}$ against the HMN predictions fitted on all data. The total d-band projection and its actual filling are used and the parameters α and β are fitted.

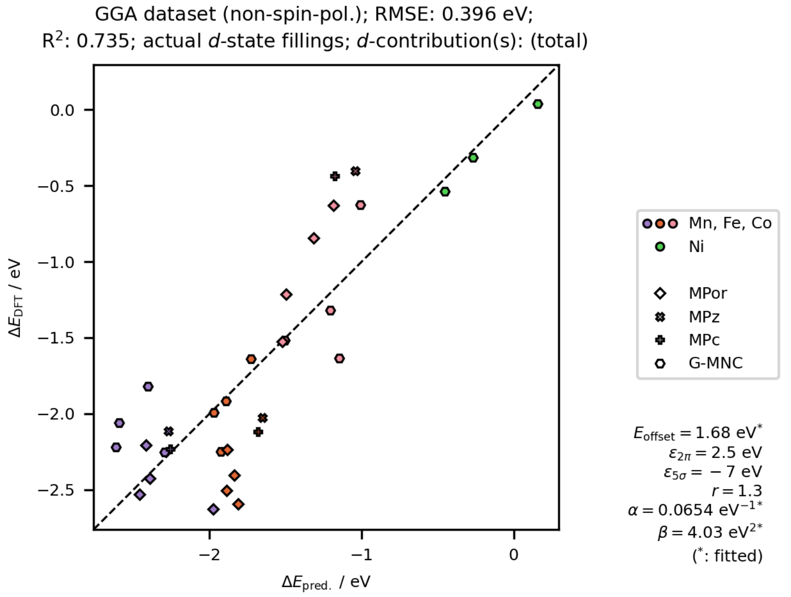

App. Figure 11. Parity plot of the GGA non-spin-polarized $\Delta E_{*\mathrm{CO}}$ against the HMN predictions fitted on the reduced set of data. The total d-band projection and its actual filling are used and the parameters α and β are fitted.

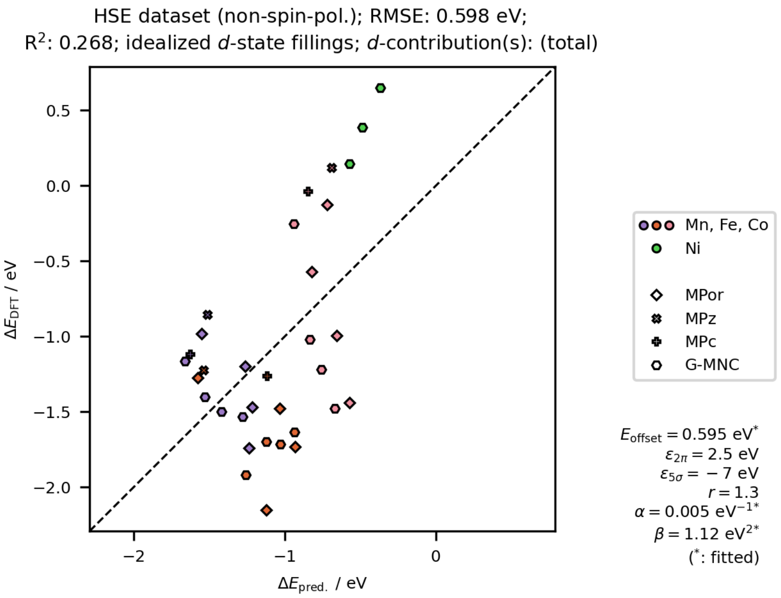

App. Figure 12. Parity plot of the hybrid non-spin-polarized ΔE_{*CO} against the HMN predictions fitted on the reduced set of data. The total d-band projection and the idealized filling are used, and the parameters α and β are fitted.

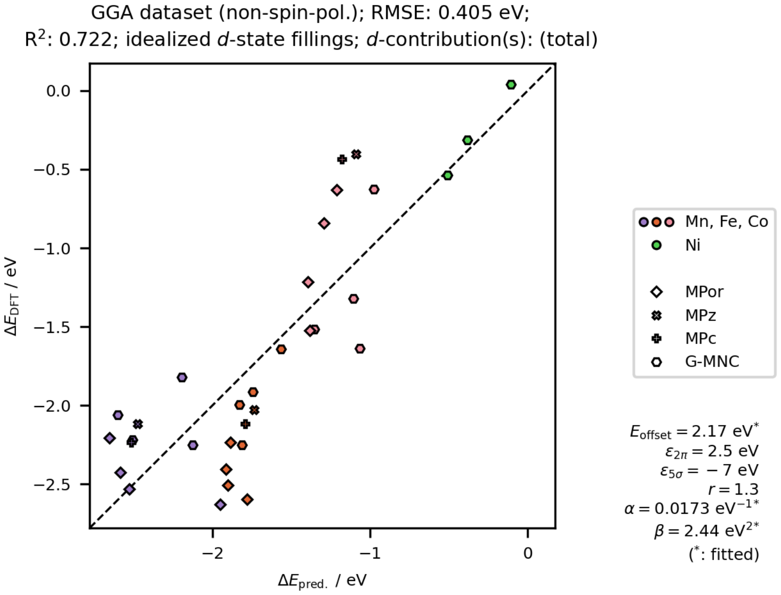

App. Figure 13. Parity plot of the GGA non-spin-polarized ΔE_{*CO} against the HMN predictions fitted on the reduced set of data. The total d-band projection and the idealized filling are used, and the parameters α and β are fitted.

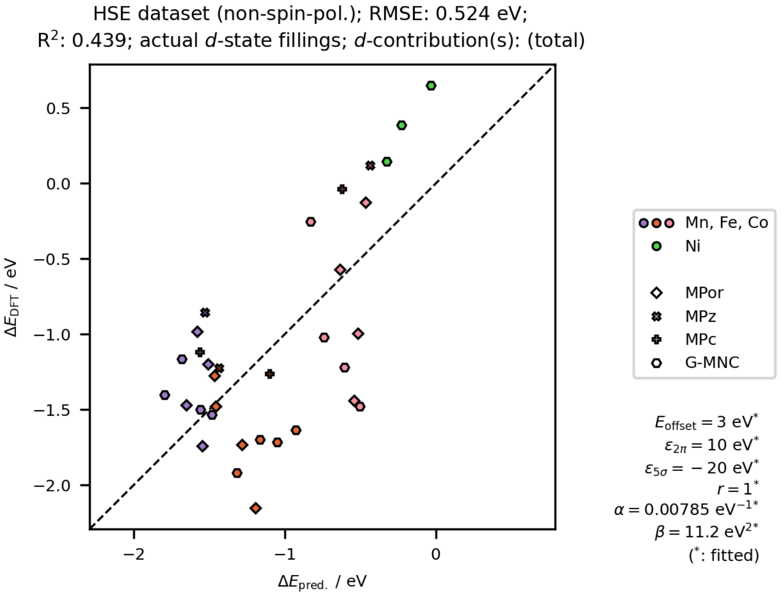
HSE dataset (non-spin-pol.); RMSE: 0.524 eV;
R^2: 0.439; actual d-state fillings; d-contribution(s): (total)

$E_{\mathrm{offset}} = 3$ eV*
$\varepsilon_{2\pi} = 10$ eV*
$\varepsilon_{5\sigma} = -20$ eV*
$r = 1^*$
$\alpha = 0.00785$ eV^{-1*}
$\beta = 11.2$ eV^{2*}
(*: fitted)

App. Figure 14. Parity plot of the hybrid non-spin-polarized ΔE_{*CO} against the HMN predictions fitted on the reduced set of data. The total d-band projection and its actual filling are used, and the parameters α, β, r, $\varepsilon_{2\pi}$, and $\varepsilon_{5\sigma}$ are fitted.

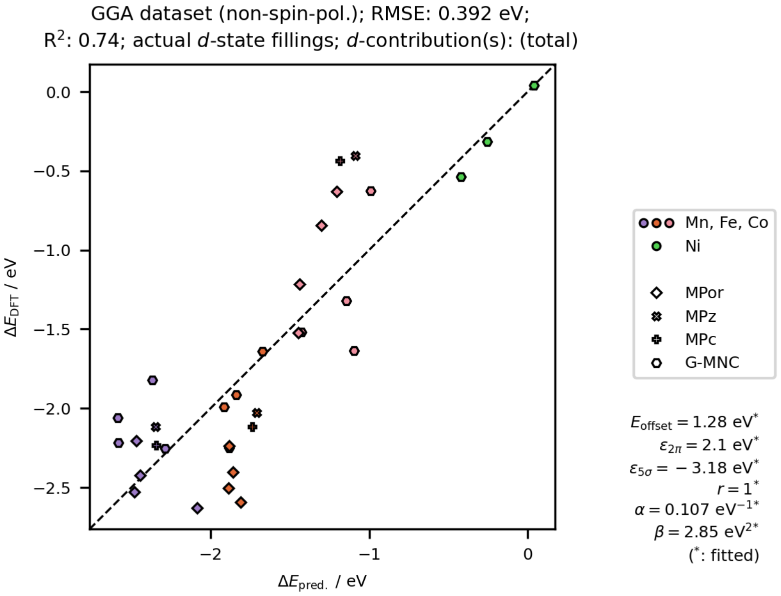
GGA dataset (non-spin-pol.); RMSE: 0.392 eV;
R^2: 0.74; actual d-state fillings; d-contribution(s): (total)

$E_{\mathrm{offset}} = 1.28$ eV*
$\varepsilon_{2\pi} = 2.1$ eV*
$\varepsilon_{5\sigma} = -3.18$ eV*
$r = 1^*$
$\alpha = 0.107$ eV^{-1*}
$\beta = 2.85$ eV^{2*}
(*: fitted)

App. Figure 15. Parity plot of the GGA non-spin-polarized ΔE_{*CO} against the HMN predictions fitted on the reduced set of data. The total d-band projection and its actual idealized filling are used, and the parameters α, β, r, $\varepsilon_{2\pi}$, and $\varepsilon_{5\sigma}$ are fitted.

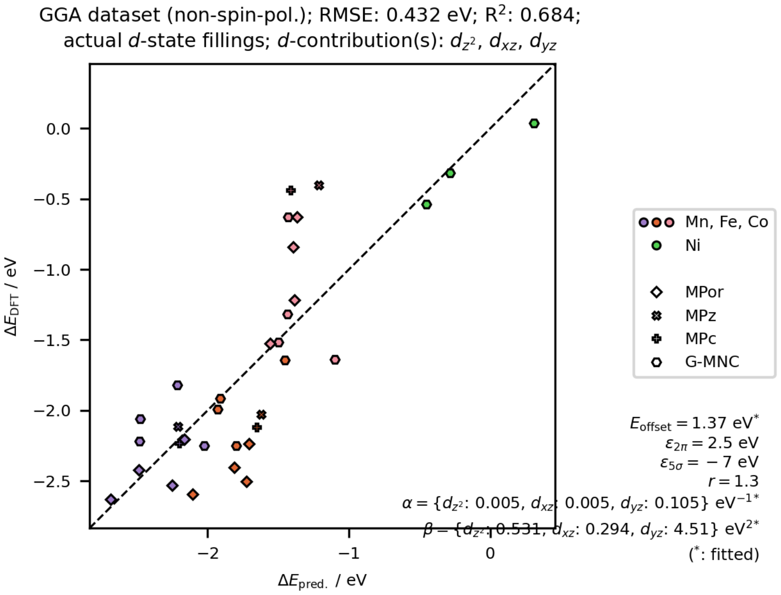

App. Figure 16. Parity plot of the GGA non-spin-polarized $\Delta E_{*\mathrm{CO}}$ against the HMN predictions fitted on the reduced set of data. The d_{z^2}, d_{xy}, and d_{xy} projections and their actual fillings are used, and the parameters α and β are fitted separately for each thereof.

II. Included publications

1. Ref.[1]: “Unified mechanistic understanding of CO_2 reduction to CO on transition metal and single atom catalysts”
2. Ref.[2]: “Covalent organic framework (COF) derived Ni-N-C catalysts for electrochemical CO2 reduction: unraveling fundamental kinetic and structural parameters of the active sites”

ARTICLES
https://doi.org/10.1038/s41929-021-00705-y
nature catalysis

Check for updates

Unified mechanistic understanding of CO_2 reduction to CO on transition metal and single atom catalysts

Sudarshan Vijay[1,3], Wen Ju[2,3], Sven Brückner[2], Sze-Chun Tsang[1], Peter Strasser[2,4] ✉ and Karen Chan[1,4] ✉

CO is the simplest product from CO_2 electroreduction (CO_2R), but the identity and nature of its rate-limiting step remain controversial. Here we investigate the activity of transition metals (TMs), metal–nitrogen-doped carbon catalysts (MNCs) and a supported phthalocyanine, and present a unified mechanistic picture of the CO_2R to CO for these catalysts. Applying the Newns–Andersen model, we find that on MNCs, like TMs, electron transfer to CO_2 is facile. We find CO_2* adsorption to generally be limiting on TMs, whereas MNCs can be limited by either CO_2* adsorption or by the proton–electron transfer reaction to form COOH*. We evaluate these computed mechanisms against pH-dependent experimental activity measurements on the CO_2R to CO activity. We present a unified activity volcano that includes the decisive CO_2* and COOH* binding strengths. We show that the increased activity of MNC catalysts is due to the stabilization of larger adsorbate dipoles, which results from their discrete and narrow *d* states.

The electrochemical reduction of CO_2 (CO_2R) has the potential to store renewable energy in the form of high-value chemicals[1–3]. The simplest product obtained during the reduction of CO_2 is CO, which can be used as a renewable feedstock for the Fischer–Tropsch reaction[4]. This process is also the first CO_2R reaction to be realized commercially, with Ag gas-diffusion electrodes that yield up to 300 mA cm^{-2} CO towards the production of polymers[5]. Nanostructured forms of gold and silver are currently the state-of-the-art catalysts for this reaction. Aside from their cost, these transition metal (TM) catalysts also catalyse the competing hydrogen evolution reaction, which reduces the selectivity for CO. A recently proposed alternative for CO_2R to CO is metal–nitrogen-doped carbon (MNC), which is low cost and Earth abundant[6]. These catalysts also have the advantage that they are less selective towards the hydrogen evolution reaction than are TM catalysts, with Faradaic efficiencies of H_2 of less than 20% under typical operating conditions of −0.6 V versus the reversible hydrogen electrode[7,8], which is consistent with the scaling of the H* and CO* binding energies on these materials[6].

CO_2R to CO requires two proton–electron transfers. In acid:

$$CO_2(g) + 2H^+ + e^- \rightarrow CO(g) + H_2O(l) \qquad (1)$$

Despite its apparent simplicity, its mechanism remains debated in recent work. First, the rate-limiting step has been proposed to be CO_2 adsorption on Au (refs. [9,10]), Fe- and Ni-doped MNC catalysts (FeNC and NiNC)[8,11], COOH* formation on noble metals[12,13] or COOH* to CO(g) on Ag from C–O bond breaking[14]. Tafel slopes of 60 or 120 mV dec^{-1} are sometimes taken as indicators of certain rate-limiting steps[9,12]; however, a recent comprehensive analysis of existing data showed silver, gold, copper, zinc and tin catalysts to have no intrinsic preference for such cardinal values, consistent with models of electron transfer in electrochemistry[15].

Furthermore, the nature of the CO_2 adsorption step is a source of some controversy. CO_2 adsorption was suggested to give rise to a unit-charged CO_2^- species on both Au (refs. [16,17]) and FeNC catalysts, which is untreatable with ground-state density functional theory (DFT) methods[18]. This hypothesis may originate from the reduction process of CO_2(aq) to CO_2^-(aq), which occurs at extremely negative potentials of −1.9 V versus the standard hydrogen electrode (SHE)[19], or from homogeneous catalysis[20,21]. Solvent reorganization, as first considered through Marcus theory, has also been hypothesized to be a major contributor to the energetics of CO_2 adsorption[17,22]. Alternatively, it has been proposed that CO_2* adsorption is driven by the interaction of the dipole of CO_2* with the interfacial electric field[23,24]; given the facile electron transfer on metals, there is no distinct, extra-charged CO_2^- species versus a polarized CO_2* adsorbate, no different from any other surface adsorbate, such as CO* and OH* (ref. [25]). The CO_2* dipole has similarly been described in terms of a partial charge transfer from the metal to adsorbate[11,26].

In this work, we present a unified mechanistic picture of CO_2R to CO on both these classes of catalysts. By consideration of the width of adsorbate-induced density of states, we found that on MNCs, as for TMs, electron transfer to CO_2 is extremely facile, such that a field-driven CO_2 adsorption step is treatable with standard ground state DFT methods. Using DFT with an explicit consideration of adsorbate–field interactions, we found CO_2* formation to generally be limiting on TMs, whereas MNCs could be limited by either CO_2* adsorption or COOH* formation. We evaluated these computed mechanisms against pH-dependent activity measurements on the CO_2R to CO activity for Au, FeNC, NiNC and supported cobalt phthalocyanine (CoPc). We present a unified kinetic activity volcano with CO_2* and COOH* binding strengths as the descriptors, which reflects how the formation of either can be rate limiting, and with consideration of the decisive adsorbate–dipole interactions.

---

[1]CatTheory, Department of Physics, Technical University of Denmark, Lyngby, Denmark. [2]Department of Chemistry, Chemical Engineering Division, Technical University Berlin, Berlin, Germany. [3]These authors contributed equally: Sudarshan Vijay and Wen Ju. [4]These authors jointly supervised: Peter Strasser and Karen Chan. ✉e-mail: pstrasser@tu-berlin.de; kchan@fysik.dtu.dk

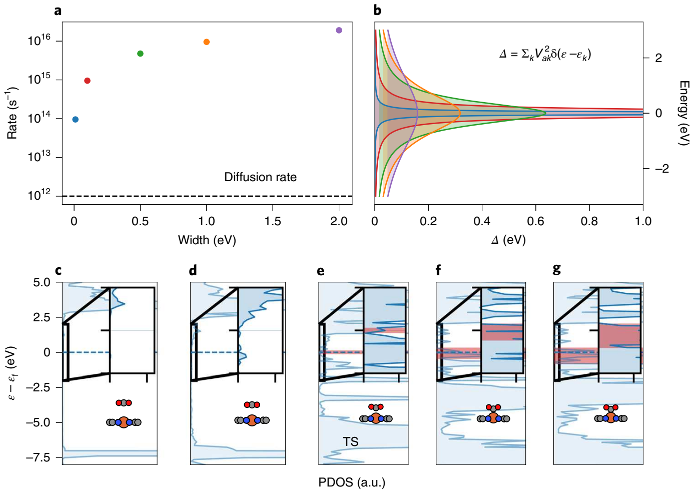

Fig. 1 | Rate of electron transfer on MNC ≈ 10^{14} s^{-1}. a,b, Rate of electron hopping (**a**) for the different idealized Lorentzian peaks shown in **b**. **c–g**, Densities of states projected onto CO_2 *s* and/or *p*-states for selected images of a CO_2 adsorption climbing image nudged elastic band run on FeNC show a short timescale of electron transfer. Insets: zoomed-in parts of the highlighted region; red bands indicate the estimated width of the states at the Fermi level, ε_f. a.u., arbitrary units.

We furthermore showed that MNC catalysts are tunable towards a higher activity away from TM scaling, due to the stabilization of larger CO_2* dipoles that result from narrower metal *d* states. We discuss the implications of these findings for catalyst design, namely that the optimization of the CO_2* dipole is a critical descriptor in addition to the adsorption energies of key intermediates.

Results

Electron transfer is not rate-limiting on MNC catalysts. Previous reports proposed the formation of a CO_2^- state as the rate-limiting step for CO_2R to CO. This step has been suggested to be limited by solvent reorganization[17,22] or by electron transfer to an uncharged CO_2* state to give an excited, charged CO_2^- state, which cannot be modelled with workhorse, ground-state periodic DFT methods[18]. Here we show that electron transfer to adsorbates is not limiting (and therefore adiabatic) on MNC catalysts, which allows us to determine the CO_2R energetics by computing the one and only CO_2* state using conventional, periodic DFT, along with the application of a stabilizing surface charge.

As in Gauthier et al.[25] for an Au surface, we determined the rate of electron hopping between the *s* and *p* states of the adsorbate and the states of the surface, *k*. We compared this rate against concurrent processes, such as the adsorbate diffusion to the surface. If the timescale for the electron transfer is very small in comparison, it will not be rate-limiting to species such as CO_2*, and we would only need to consider the adiabatic pathway for CO_2 adsorption. In the Newns–Anderson[27–29] model of chemisorption, the width of the adsorbate-induced states is $\Delta = \Sigma_k \left|V_{ak}\right|^2 \delta\left(\epsilon - \epsilon_k\right)$, where V_{ak} is the coupling matrix element between *k* and individual *s* and *p* states, ϵ is the single particle energy of the adsorbate *s* and *p* states and ε_k is the energy of the surface states. Δ can be determined from the projected density of states (PDOS) onto the *s* and *p* states of CO_2 through the width of the peak at the Fermi level[25]. We obtained the rate of electron transfer from Fermi's Golden Rule, $\frac{2\pi}{\hbar}\Delta$. To illustrate this idea, Fig. 1a shows the rates of electron transfer associated with a range of idealized peaks of different width, shown in Fig. 1b. For a very small width of 0.1 eV, the rate of electron hopping is extremely fast, greater than 10^{14} s^{-1}, and is larger with increased broadening. For comparison, an estimate for the diffusion rate of ions in solution is of the order 10^{12} s^{-1}, shown by the dashed line in Fig. 1a[30].

We then applied this methodology to PDOS obtained from DFT computations. Figure 1c–g shows the PDOS for the reaction path of CO_2 adsorption on FeN_4 (a prototype for MNC). The *s* and *p* states of CO_2 broaden as it approaches the surface, which is expected for adsorption processes in general[31]. At the transition state (TS) and further along the reaction pathway, the peaks at the Fermi level are greater than 0.1 eV. The corresponding rate of electron transfer is approximately 10^{14} s^{-1}, which implies a timescale of 10^{-14} s. This rate is, in turn, two orders of magnitude greater than that of competing processes, which implies that it will not be rate limiting on FeN_4. As the states at the Fermi level on MNC catalysts are typically the *s* and *p* states of graphene at reducing potentials, at which oxide species are absent (Supplementary Note 2), we expect this analysis to hold for all MNC catalysts considered in this work[32]. Thus, only the adiabatic pathway for CO_2 adsorption needs to be calculated to obtain the energetics for all the elementary steps on the MNC and TM catalysts. Non-adiabatic behaviour might be present in molecules such as CoPc adsorbed on a support, with rates of electron transfer on the order of the magnitude of diffusion as shown in Fig. 1[33]. In Supplementary Note 2 we show that with even a slight increase in doping concentration on the graphene sheet, hybridization between all the components of the system (CO_2, CoPc and *n*-doped graphene) improves, which would lead to an increase in the rate of electron transfer through a larger value of Δ.

We do not exclude the possibility here that solvent reorganization could contribute to the energetics of the CO_2 adsorption step, as has been considered in Brown et al.[17]. The magnitude of this contribution, however, has been estimated to be only ~0.2 eV from the

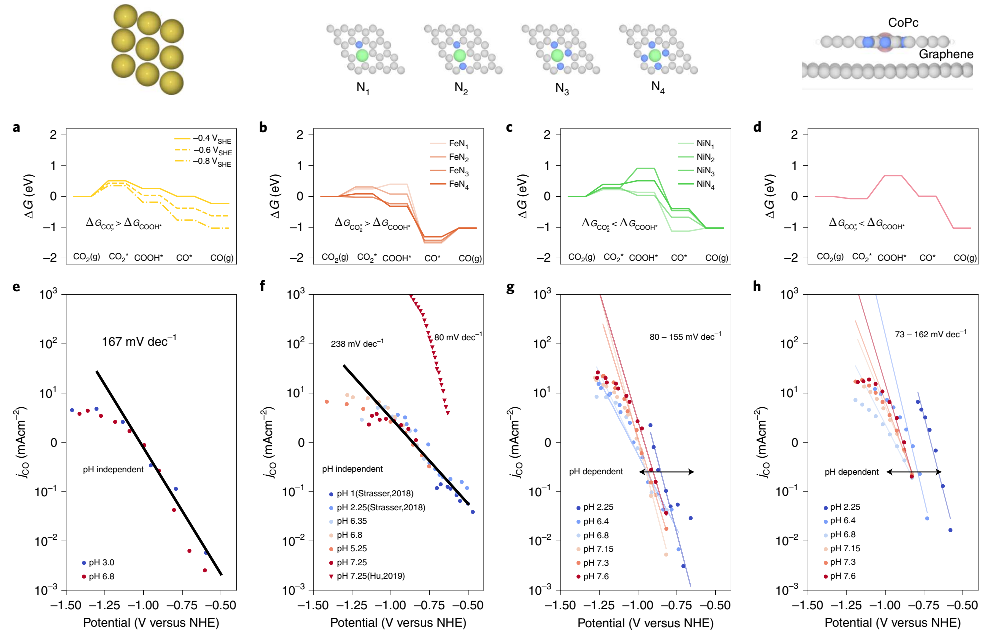

Fig. 2 | Both CO_2* adsorption and COOH* formation can be rate limiting. a–c, Free energy diagram of CO_2 to CO for Au(211) at U = −0.6, −0.8 and −1.0 V_{SHE} (**a**), FeNC (**b**), NiNC (**c**) and CoPc adsorbed on graphene (**d**) at U = −0.8 V_{SHE} and pH = 2. The schematics of the calculated surfaces are shown above their respective free energy diagrams, with the four double-vacancy MNCs. **e–h**, Experimental current densities plotted against NHE potential for polycrystalline Au (from Ringe et al.[23]) (**e**), FeNC (from Varela et al.[8] and Gu et al.[74] (reversed triangles)) (**f**), NiNC (this work) (**g**) and CoPc on CNT (this work) (**h**).

timescale of reorganization[34,35]. Recent investigations based on the Marcus–Hush–Chidsey model suggest that it can be up to 0.6 eV in the presence of certain electrolytes[36].

Both CO_2* adsorption and COOH* formation can be rate limiting. We now present the mechanism and rate-limiting step for Au, FeNC, NiNC and carbon nanotube (CNT)-supported CoPc determined from potential-dependent DFT calculations and evaluate them against pH-dependent activity measurements. We considered the following reaction pathway (written for acidic solutions):

$$CO_2(g) + * \rightarrow CO_2^* \tag{2}$$

$$CO_2^* + H^+ + e^- \rightarrow COOH^* \tag{3}$$

$$COOH^* + H^+ + e^- \rightarrow CO^* + H_2O\,(g) \tag{4}$$

$$CO^* \rightarrow CO\,(g) + * \tag{5}$$

We assumed that the barriers associated with all steps are small. As evaluated in Vijay et al.[24] for FeN_2 and FeN_4, the CO_2 adsorption barrier is well approximated by the adsorption energy (differences between barrier and reaction energies of at most 0.2 eV); the protonation of CO_2* is facile, in line with general trends in electrochemical barriers for the protonation of oxygen[37], and the COOH* to CO* step for CO-producing catalysts is generally so downhill under reducing potentials that the corresponding barriers are unlikely to be limiting (Fig. 2b–d). This reduction of the barrier for COOH* protonation is due to the two preceding potential-dependent steps and the reducing potentials at which CO_2R occurs. The rate-limiting step at a given potential is, in this case, determined by the state with the highest free energy, ΔG. Each ΔG derives its potential dependence either from the presence of a proton–electron pair as the reactants and/or from the interaction between the dipoles of participating reaction intermediates with the interfacial field. The energetic stabilisation caused by the interaction of a dipole μ with an interfacial field ξ is $\mu\xi$ (ref. [38]). At reducing potentials, fields set up by the double layer can be as large as 10^{10} V m^{-1}, which gives rise to a large stabilization of CO_2* on MNCs of 0.75–1 eV on MNCs (see Supplementary Note 1 for detailed information about the methodology used). Figure 2a shows the free energy diagram for Au(211) at −0.6, −0.8 and −1 V_{SHE} at a pH of 2. At −0.6 V_{SHE}, COOH* is the intermediate with the highest ΔG, whereas at −0.8 V_{SHE} and −1 V_{SHE}, it is CO_2*. Thus, the computations predicted a change in rate-limiting step from COOH* formation to CO_2* adsorption when the overpotential is increased, in line with previous work[23]. We note that this change in rate-limiting step occurs at −0.7 V versus SHE.

We evaluated the rate-limiting step with pH-dependent measurements. The activity was pH dependent on an absolute scale (for example, versus the SHE or normal hydrogen electrode (NHE)) when COOH* formation was rate-limiting, as a proton–electron transfer was involved. CO_2* adsorption, however, did not involve a proton–electron transfer, so when it was rate limiting, the activity

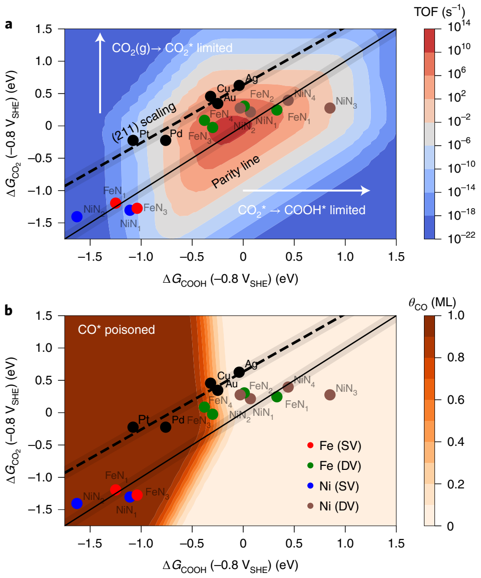

Fig. 3 | General activity volcano for CO_2R to CO. a, Rate map at −0.8 V_{SHE} and pH 2 for CO_2R to CO obtained from the (211) TM scaling line. The annotated points show MNCs either at SVs or DVs. The (211) scaling line has the best fit. $\Delta G_{CO_2} = 0.94\Delta G_{COOH} + 0.51$. **b**, Coverage map θ, in monolayers (ML) with the same points showing which surfaces are poisoned by CO.

was pH independent on an absolute scale. Figure 2e shows the measured current densities versus potential on a NHE scale. The current densities show no pH dependence at high potentials (greater than −0.8 V_{SHE}). At lower overpotentials, the scatter in the points could be indicative of COOH* formation being the rate-limiting step.

With the same arguments, we show that the FeNC catalysts were limited by the energetics of CO_2* adsorption, whereas the NiNC catalysts and supported CoPc catalysts were limited by the CO_0* → COOH* step. Figure 2b shows the free energy diagram for FeNC catalysts computed at −0.8 V_{SHE} and a pH of 2 for various nitrogen coordinations around the metal centre for double vacancies (DVs) (metals on single vacancies (SVs) tend to overbind CO*, see below). For FeN_2, FeN_3 and FeN_4, the computations predict CO_2* adsorption to be rate limiting for potentials more cathodic than −0.8 V_{SHE}, which is in line with the completely pH-independent experimental rates (Fig. 2f, Strasser data[8]). The FeN_4 vacancy configuration has also been stipulated to be the active site for CO_2R based on a comparison of the cyclic voltammograms and X-ray spectral features with those of molecular analogues[39]. In contrast, FeN_1 was limited by COOH* formation at this potential, and the lack of pH dependence in the experiments suggests that its population on the catalyst surface was small. All the NiNC catalysts investigated (Fig. 2c), except for NiN_2, were limited by COOH* formation, consistent with the pH dependence of experimental rates, as shown in Fig. 2g (see Supplementary Note 3 for the total currents and Faradaic efficiencies). Recent works[40,41] also reported large COOH* free energies for NiN_4, in line with the results shown in Fig. 2c. Molecular NiN_4 analogues also showed large COOH* free energies in comparison with that of CO_2* (ref. [42]). Similarly, supported CoPc catalysts also had COOH* formation as the rate-limiting step, as shown in Fig. 2d, which were realized in the pH-dependent experiments shown in Fig. 2h. Thus, the combination of simple field-dependent thermodynamic computations and pH-dependent measurements suggests that CO_2* adsorption is rate limiting at higher overpotentials on Au and for all potentials on FeNC, and that CO_2* → COOH* is rate limiting on NiNC and supported CoPc catalysts.

The adsorbate binding strengths would shift in more detailed models of the electrochemical interface, but the electrostatic effects are in line with experimentally observed pH dependencies for the systems considered here, which suggests they are the predominant factor in the energetics. In Supplementary Note 6, we show, with an ab initio molecular dynamics simulation of explicit water on FeNC, an explicit solvation energy of ~0.3 eV for CO* versus the solvation energy self-consistently determined through an implicit solvent model in this work; in contrast, the 0.75 eÅ dipole moment of CO_2* gives rise to a much larger −0.75 eV change in its adsorption energy over a 1 V range.

Finally, the experimental Tafel slopes in Fig. 2e–h do not show the cardinal values of 60 or 120 mV dec^{-1}, which echoes a comprehensive study of the recent literature of TM catalysts for CO_2R[15]. These slopes reflect the magnitude of the dipole ($\text{slope}^{-1} \approx \frac{C}{\epsilon}\mu$, where C is the capacitance)[23,24] and/or the symmetry factor ($0 < \alpha < 1$) of the associated proton–electron transfer and therefore are not constrained to these values. The slopes may also be affected by mass transport and buffer equilibria[23,43]. Furthermore, the fitted value depends on the number of points used to make the fit. For example, by changing the number of fitted points in Fig. 2a by two, we would obtain a value different from the Tafel slope of 167 mV dec^{-1}. We therefore considered mechanistic interpretations of the experiments only on the basis of the pH dependence, and not the specific Tafel slopes obtained.

Activity volcano determined by both COOH* and CO_2* free energies. In this section we consolidate the mechanistic insights into a general kinetic activity volcano for CO_2R to CO determined by two activity descriptors, the free energy of adsorption of CO_2, ΔG_{CO_2}, and that of COOH, ΔG_{COOH}. Figure 3a shows this unified activity volcano for the CO production for both TM and MNC catalysts, and corresponds to the energetics in Fig. 2. The theoretical maximum in activity (represented by the turnover frequency (TOF)) occurs at intermediate ΔG_{CO_2} values and at $\Delta G_{COOH} \approx 0$, that is, where both the CO_2 and COOH formation steps are facile. The parity line corresponds to the case in which the free energies of COOH* and CO_2* are equal, $\Delta G_{CO_2} = \Delta G_{COOH}$. The CO adsorption energy generally scales with those of the other two intermediates[13]; thus, its energetics are included in the volcano through the calculated scaling relationships in the kinetic model (Supplementary Note 4).

Figure 3a shows several trends in the binding of CO_2R intermediates for TMs and MNCs. First, the TMs show a scaling line (the dashed black line) between ΔG_{CO_2} and ΔG_{COOH}, whereas the MNCs show more scatter. Furthermore, metals doped into SVs tend to bind reaction intermediates more strongly than those in DVs, and are poisoned by CO. Fig. 3a,b also allows us to determine which step is rate limiting in CO_2R to CO at any given potential, using computed CO_2*, COOH* and CO* free energies. In Fig. 3a, if the point lies below the parity line, then $CO_2^* \rightarrow COOH^*$ is the rate-limiting step. Meanwhile, if it is above the parity line, CO_2 adsorption is rate limiting. At very negative adsorption energies, the surface is poisoned by CO, as shown in Fig. 3b, which leads to CO* desorption being rate limiting on TMs, such as Pd and Pt. All the TM (211) facets lie above the parity line, which indicates that CO_2 adsorption or CO desorption is rate limiting at the studied potentials. Some NiNC catalysts lie below the parity line, which shows that CO_2* → COOH*

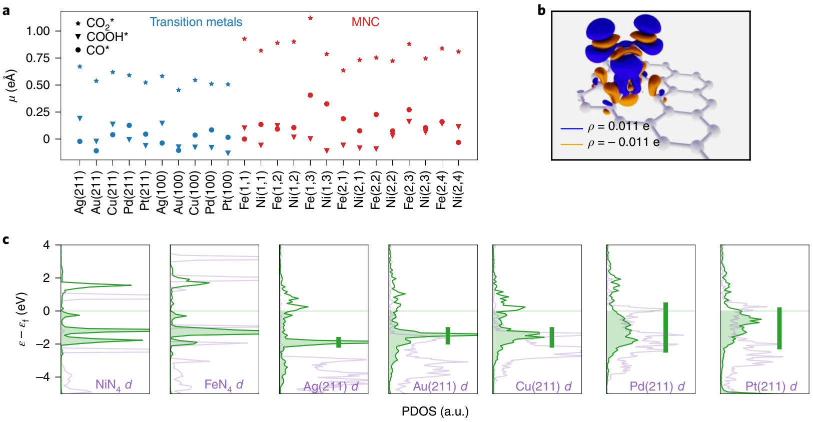

Fig. 4 | Narrow *d* states stabilize larger dipoles. a, Vacuum dipole moments for (211) and (100) TM surfaces (blue) and Fe and Ni MNCs (red). The MNCs (first index indicates the type of vacancy, 1 for single and 2 for double; second index indicates the number of substituting N atoms) have larger dipole moments as compared with those of the TMs. **b**, Charge density difference plot for CO_2 adsorbed on NiN_4C. **c**, Density of states projected onto the *s* and *p* states of CO_2* (green) and the *d* states of TMs (purple) show that the adsorbate states are much narrower on MNCs than they are on TMs.

is rate-limiting, in line with the experimental finding in Fig. 3f. Note that our approach, in contrast to that of Hansen et al.[13], includes the effects of the adsorbate–field interactions for all the intermediates (Supplementary Note 1) and the consideration of CO_2 adsorption as an elementary step, these effects that are critical to determining the activity trends. Supplementary Note 4 also shows the potential dependence versus SHE of the rate map shown in Fig. 3a.

We generally do not expect there to be only a single site motif present after the synthesis procedure for these materials[44–47]. Temperature-programmed desorption experiments (Supplementary Fig. 12 and Supplementary Note 5) show that FeNC, but not NiNC, have a peak above 300 K. This result suggests strong binding sites, such as those from SVs to be present on FeNC to a greater extent than on NiNC (ref. [48]). Note that doped SV sites, or other binding sites of similar binding strength that we have not considered, are not active sites for CO_2R, as they would be poisoned by CO.

MNCs have a higher activity because they stabilize larger dipoles. We now show that MNCs deviate from TM scaling because they stabilize large dipole moments on CO_2*. Figure 4b shows charge density difference isosurfaces for CO_2* on NiN_4C, which shows a perturbation of the electron density near the surface on adsorption. This change in electron density is captured by the dipole moment, given by $\mu = \int \rho \mathrm{d}z$, where ρ is the charge density and z is the axis of integration, and is shown in Fig. 4a for (211) and (100) TM surfaces, as well as Fe- and Ni-doped MNC catalysts in both SVs and DVs of various N concentrations. The figure shows that the dipole moments for CO_2* are larger than those for other adsorbates, such as CO* and COOH*. Furthermore, the CO_2* dipoles are significantly higher on MNCs than on TMs. MNCs therefore have CO_2* adsorption energies that are stabilized more at reducing potentials, at which the surface is generally negatively charged. This electrostatic stabilization caused by the dipole-field interaction gives rise to the offset of MNCs from the TM scaling line shown in Fig. 3.

We rationalize the differences in dipole moments with the PDOS on the *s* and *p* states of CO_2*. The strength of the adsorbate–surface interaction is determined by both the position and shape of the *d* states, and is reflected in the width of the *s* and/or *p* adsorbate states[49]. As shown in Fig. 4c for a selected set of surfaces (in green), the width of the *s* and *p* states increases in the order FeN_4, NiN_4, Ag, Au, Pd and Pt.

In FeN_4 and NiN_4 catalysts, the sharp *s* and/or *p* states of CO_2* mean they resemble those of their molecular counterpart, which indicates a weak interaction (poor hybridization) with the surface. A poor overlap between the *s* or *p* states close to the Fermi level (±1 eV in either direction) of CO_2 and the *d* states of the surface means that CO_2* retains a greater charge polarization between its two poles, that is a larger dipole (see Supplementary Note 7 for an explanation of this effect through the Newns–Muscat model). The same effect is present to a lesser extent on the weakly binding metals, Ag and Au, which, in comparison with the strongly binding ones, have slightly narrower *d* states and correspondingly slightly larger dipoles. In the strongly binding Pt and Pd catalysts, the broadened states indicate a large interaction[27], and a lower charge polarization results from the mixing of adsorbate states with those of the surface and a lower resultant surface dipole. Overall, the trends in the width of the *s* and/or *p* PDOS of CO_2* are consistent with the larger dipole moments of MNC catalysts.

TM alloys, in contrast to MNC catalysts, generally have wide *d* states, as with pure TMs[50]. In view of the results, improvements in activity through alloying can be attributed not to the stabilization of larger dipoles, but to the tuning of the CO_2* binding strengths through the degree of hybridization with the surface.

The activity volcano of Fig. 3 and electronic structure arguments of Fig. 4 give two simple design principles. As shown in the TOF of Fig. 3, the ideal CO_2R catalyst has moderate ΔG_{CO_2} and ΔG_{COOH} of 0.25–0.5 eV and $\Delta G_{CO} > 0$ eV (to prevent CO* poisoning). It must, additionally, be able to stabilize a large dipole moment of CO_2*, such that CO_2 adsorption does not require a significant overpotential (and thereby deviate from the scaling of TMs in the direction of a higher activity, shown in Fig. 3). These larger dipole moments are stabilized for MNC catalyst materials through their narrow *d* states. We suggest that other materials that have similar discrete and narrow *d* states, such as supported single atoms[51,52], molecules and clusters[53,54], as well as two-dimensional materials and ionic compounds[32,55,56], could also be active CO_2R catalysts, provided that hydrogen evolution is not competitive or suppressed through a decrease in water activity[57]. This principle could also be relevant for other processes in which dipole -field interactions are decisive, such as in C_2 product formation[4,58].

Conclusions

In summary, we present a unified picture of CO_2R to CO on both TM and MNC catalysts that resolves the existing controversies on the identity and nature of the rate-limiting step. Considering the widths of the projected densities of states of an adsorbing CO_2, we showed that, as for TMs, the electron transfer to CO_2 is not limiting in MNCs, and that CO_2 adsorption is driven by adsorbate dipole-field interactions. With a combination of field-dependent DFT and pH-dependent activity measurements, we showed that CO_2* adsorption is limiting on TMs over relevant potentials, whereas either CO_2* adsorption or COOH* formation is rate limiting on MNCs. We present a unified kinetic activity volcano, based on critical COOH* and CO_2* binding as the descriptors, that accounts for the decisive adsorbate dipole-field interactions. The volcano shows that ideal catalysts should have both a moderate binding strength of COOH* and CO_2*, as well as large adsorbate dipoles on CO_2*. We furthermore showed that MNCs deviate favourably from TM scaling through the stabilization of large CO_2* dipoles, due to the localized narrow *d* states of these materials.

These results suggest that MNCs or other materials with similarly narrow *d* states, such as supported single atoms, molecules and clusters, as well as two-dimensional materials and ionic compounds, can be optimized for large dipoles and correspondingly higher catalytic activity beyond TM scaling. This principle can be relevant for other processes in which adsorbate–field interactions are decisive. The presented kinetic activity volcano and catalyst design rules should be used as the basis for computation-guided catalyst development of CO_2R to CO catalysts.

Methods

Computational methods. DFT calculations were carried out using the Vienna Ab Initio Software Package (VASP)[59]. Core electrons were described using projector augmented wave potentials[60]. Valence electrons were described with plane waves with a kinetic energy up to 500 eV. Gaussian smearing with a width of 0.1 eV was used. In the case of density of states plots, smearing was reduced to 0.05 eV. For relaxations, we applied the RPBE[61] functional. Hybrid calculations with the HSE06[62,63] were performed for the density of states calculations in Fig. 1. In the case of FeNC calculations, a Hubbard-U[64] parameter of $U=2$ eV was added to the *d* orbitals of iron, in line with previous benchmark calculations[24].

TMs were modelled using a 3 × 3 × 3 slab, with the bottom two layers fixed. MNC systems were modelled using a 3 × 3 graphene layer. All the structures were prepared using the Atomic Simulation Environment[65]. The lattice for all the TM and MNC catalysts were relaxed using a 12 × 12 × 1 Monkhorst–Pack[66] *k*-point mesh. All the supercells were treated with a 4 × 4 × 1 Monkhorst–Pack *k*-point mesh. All the geometries were optimized until the forces were lower than 0.025 eV Å^{-1}. TS geometries and energies were obtained using the climbing image nudged elastic band[67] implemented within VASP. All the density of states plots used twice the *k*-point sampling used in the relaxation and/or TS calculations. DFT energies were converted into free energies at 298.15 K using vibrations obtained from VASP calculations using IBRION = 5. The ASE[65] Thermochemistry class was used to determine the Helmholtz free energy from harmonic thermochemistry and the Gibbs free energy from ideal gas thermochemistry.

Implicit solvation and continuum charge were added using VASPsol[68]. A Debye screening length of 3 Å was chosen, as it corresponds to a bulk ion concentration of 1 M. The non-electrostatic parameter, TAU, was set to zero for purposes of convergence[30]. Continuum charge was varied in increments of 0.25 e.

The computational hydrogen electrode[69] was used to determine the reaction energetics as a function of the potential with a proton–electron pair was in the reactant. The chemical potential of the proton can be related to that of H_2 at 0 V versus the reversible hydrogen electrode:

$$\mu_{\mathrm{H}^+} + \mu_{\mathrm{e}^-} = \frac{1}{2}\mu_{\mathrm{H}_2(\mathrm{g})} \qquad (6)$$

The incorporation of the dipole-field interactions is described in detail in Supplementary Note 1.

Microkinetic modelling was performed using CatMAP[70]. The rate of a given elementary step was

rate $= k_+ \Pi\theta_i \Pi p_j - k_- \Pi\theta_i \Pi p_j$, where '+' indicates the forward reaction and '−' the reverse reaction. The rate constants are $k_+ = \exp\left(-\frac{G_{a,+}}{k_\mathrm{B}T}\right)$ and $k_- = \exp\left(-\frac{G_{a,-}}{k_\mathrm{B}T}\right)$, where $G_{a,+}$ and $G_{a,-}$ are the free energy barriers. In the absence of electrochemical barriers, the free energy is used, which is given as $\Delta G = \Delta G^\circ + neU + \Delta G_\mathrm{field}$, where ΔG° is the free energy for the reaction at the potential of zero charge, *n* is the number of proton–electron pairs transferred and ΔG_field is the dipole-field contribution.

A multiprecision Newton root-finding algorithm was used to determine the steady-state rates and coverages. A decimal precision of 100 along with a convergence tolerance value of 10^{-25} were used.

Synthesis. The polyaniline-derived NiNC catalyst is identical to that reported in our previous studies[71,72]. Aniline (3 ml), $NiCl_2 \cdot 6H_2O$ (5 g) and ammonium persulfate (5 g) were added to 0.5 l of 1 M HCl and stirred for 1 h. This suspension was then mixed with 0.4 g of a dispersed activated Ketjen 600 carbon black support (washed in HCl for purification and HNO_3 for oxygen doping), stirred for 48 h and then dried in the air at 95 °C for 24 h. The residual solid-state mixture was ball milled with Zr_2O_3 balls for 20 min. We conducted the pyrolysis protocol in a furnace at 900 °C (ramp of 30 °C min^{-1}) for 1 h under N_2 conditions, followed by acid washing steps (2 M H_2SO_4 at 90 °C overnight) to remove the excessive Ni particles. We performed heat treatment four times and acid washing three times and the catalyst was obtained after the fourth pyrolysis.

Synthesis of CoPc/CNT. CoPc/CNT was synthesized following an analogous protocol reported in the literature[73]. CoPc (1 mg) was mixed with 30 mg of a multiwall CNT in 30 ml dimethylformamide solution and stirred for 24 h. The suspension became transparent. The final suspension was washed using EtOH and H_2O within a centrifuge to remove the dimethylformamide, and after that was freeze-dried to give the final catalyst.

Electrode preparation. Carbon paper (1 cm × 2.5 cm, Freudenberg C2H23) was sonicated in ethanol and deionized water for 15 min and dried as the electrode substrate. The catalyst ink was prepared using 4.0 mg of catalyst mixed with 60 µl of Nafion solution (5% in ethanol, Sigma-Aldrich), 200 µl of isopropanol and 200 µl of deionized water. After 15 min of sonification, the ink was deposited on the microporous layer of carbon paper to achieve an area of 1 cm^2 with catalyst loading of 1 mg cm^{-2}.

Electrochemical measurement. The electrochemical CO_2R performance was measured in a regular three-electrode H-cell divided by a Nafion N117 membrane. The working electrode was the catalyst-coated carbon paper mentioned above, and a Pt mesh was deployed as the counter electrodes. A leak-free Ag/AgCl electrode was used as the reference. The current density was normalized to the working electrode's geometrical area (1 cm^2). All the electrochemical experiments were performed in a CO_2-purged electrolyte (CO_2 flow rate, 30 ml min^{-1}). The pH value of each is presented in Supplementary Table 1.

Product analysis. A Shimadzu 2014 on-line gas chromatograph was utilized for product quantification. The gas stream was separated by Hayesep Q + R columns and then analysed by a thermoconductivity detector and flame ionization detector. The thermoconductivity detector detects the volume percentage of the H_2 product, and the flame ionization detector measures the CO after methanization. On all the NiNC type catalysts, no liquid product was found after the electrolysis. Calculations of the production rate, partial current density and Faradaic efficiency are given in the Supplementary Methods.

Data availability

All computational data, which include the adsorption energies of CO_2, COOH and CO, optimized atomic coordinates, data for plotting density of states and microkinetic analysis are available at https://doi.org/10.24435/materialscloud:ws-7t.

Code availability

Python analysis scripts to reproduce all the figures in the manuscript are available at https://github.com/CatTheoryDTU/kinetic-modelling-CO2R.

Received: 16 April 2021; Accepted: 13 October 2021;
Published online: 25 November 2021

References

1. Jouny, M., Luc, W. & Jiao, F. General techno-economic analysis of CO_2 electrolysis systems. *Ind. Eng. Chem. Res.* **57**, 2165–2177 (2018).
2. Seh, Z. W. Combining theory and experiment in electrocatalysis: insights into materials design. *Science* **355**, aad4998 (2017).

3. Anastasiadou, D., Hensen, E. J. M. & Figueiredo, M. C. Electrocatalytic synthesis of organic carbonates. *Chem. Commun.* **56**, 13082–13092 (2020).
4. Nitopi, S. et al. Progress and perspectives of electrochemical CO_2 reduction on copper in aqueous electrolyte. *Chem. Rev.* **119**, 7610–7672 (2019).
5. Haas, T., Krause, R., Weber, R., Demler, M. & Schmid, G. Technical photosynthesis involving CO_2 electrolysis and fermentation. *Nat. Catal.* **1**, 32–39 (2018).
6. Bagger, A., Ju, W., Varela, A. S., Strasser, P. & Rossmeisl, J. Single site porphyrine-like structures advantages over metals for selective electrochemical CO_2 reduction. *Catal. Today* **288**, 74–78 (2017).
7. Clark, E. L. et al. Influence of atomic surface structure on the activity of Ag for the electrochemical reduction of CO_2 to CO. *ACS Catal.* **9**, 4006–4014 (2019).
8. Varela, A. S. et al. pH effects on the selectivity of the electrocatalytic CO_2 reduction on graphene-embedded Fe–N–C motifs: bridging concepts between molecular homogeneous and solid-state heterogeneous catalysis. *ACS Energy Lett.* **3**, 812–817 (2018).
9. Wuttig, A., Yaguchi, M., Motobayashi, K., Osawa, M. & Surendranath, Y. Inhibited proton transfer enhances Au-catalyzed CO_2 -to-fuels selectivity. *Proc. Natl Acad. Sci. USA* **113**, E4585–E4593 (2016).
10. Verma, S. et al. Insights into the low overpotential electroreduction of CO_2 to CO on a supported gold catalyst in an alkaline flow electrolyzer. *ACS Energy Lett.* **3**, 193–198 (2018).
11. Prslja, P. & López, N. Stability and redispersion of Ni nanoparticles supported on N-doped carbons for the CO_2 electrochemical reduction. *ACS Catal.* **11**, 88–94 (2021).
12. Dunwell, M. et al. The central role of bicarbonate in the electrochemical reduction of carbon dioxide on gold. *J. Am. Chem. Soc.* **139**, 3774–3783 (2017).
13. Hansen, H. A., Varley, J. B., Peterson, A. A. & Nørskov, J. K. Understanding trends in the electrocatalytic activity of metals and enzymes for CO_2 reduction to CO. *J. Phys. Chem. Lett.* **4**, 388–392 (2013).
14. Chen, L. D., Urushihara, M., Chan, K. & Nørskov, J. K. Electric field effects in electrochemical CO_2 reduction. *ACS Catal.* **6**, 7133–7139 (2016).
15. Limaye, A. M., Zeng, J. S., Willard, A. P. & Manthiram, K. Bayesian data analysis reveals no preference for cardinal Tafel slopes in CO_2 reduction electrocatalysis. *Nat. Commun.* **12**, 703 (2021).
16. Hori, Y., Wakebe, H., Tsukamoto, T. & Koga, O. Electrocatalytic process of CO selectivity in electrochemical reduction of CO_2 at metal electrodes in aqueous media. *Electrochim. Acta* **39**, 1833–1839 (1994).
17. Brown, S. M. et al. Electron transfer limitation in carbon dioxide reduction revealed by data-driven Tafel analysis. Preprint at *ChemRxiv* https://doi.org/10.26434/chemrxiv.13244906.v1 (2020).
18. Ju, W. et al. Unraveling mechanistic reaction pathways of the electrochemical CO_2 reduction on Fe–N–C single-site catalysts. *ACS Energy Lett.* **4**, 1663–1671 (2019).
19. Benson, E. E., Kubiak, C. P., Sathrum, A. J. & Smieja, J. M. Electrocatalytic and homogeneous approaches to conversion of CO_2 to liquid fuels. *Chem. Soc. Rev.* **38**, 89–99 (2009).
20. Göttle, A. J. & Koper, M. T. M. Proton-coupled electron transfer in the electrocatalysis of CO_2 reduction: prediction of sequential vs. concerted pathways using DFT. *Chem. Sci.* **8**, 458–465 (2016).
21. Gennaro, A. et al. Mechanism of the electrochemical reduction of carbon dioxide at inert electrodes in media of low proton availability. *J. Chem. Soc. Faraday Trans.* **92**, 3963–3968 (1996).
22. Zhang, B. A., Costentin, C. & Nocera, D. G. Driving force dependence of inner-sphere electron transfer for the reduction of CO_2 on a gold electrode. *J. Chem. Phys.* **153**, 094701 (2020).
23. Ringe, S. et al. Double layer charging driven carbon dioxide adsorption limits the rate of electrochemical carbon dioxide reduction on gold. *Nat. Commun.* **11**, 33 (2020).
24. Vijay, S. et al. Dipole-field interactions determine the CO_2 reduction activity of 2D Fe–N–C single atom catalysts. *ACS Catal.* **10**, 7826–7835 (2020).
25. Gauthier, J. A. et al. Facile electron transfer to CO_2 during adsorption at the metal|solution interface. *J. Phys. Chem. C* **123**, 29278–29283 (2019).
26. Verma, A. M., Honkala, K. & Melander, M. M. Computational screening of doped graphene electrodes for alkaline CO_2 reduction. *Front. Energy Res.* **8**, 388 (2021).
27. Newns, D. M. Self-consistent model of hydrogen chemisorption. *Phys. Rev.* **178**, 1123–1135 (1969).
28. Anderson, P. W. Localized magnetic states in metals. *Phys. Rev.* **124**, 41–53 (1961).
29. Grimley, T. B. Overlap effects in the theory of adsorption using Anderson's Hamiltonian. *J. Phys. C* **3**, 1934–1942 (1970).
30. Gauthier, J. A. et al. Challenges in modeling electrochemical reaction energetics with polarizable continuum models. *ACS Catal.* **9**, 920–931 (2019).
31. Nørskov, J. K., Studt, F., Abild-Pedersen, F. & Bligaard, T. *Fundamental Concepts in Heterogeneous Catalysis* (Wiley, 2014).
32. Kim, D., Shi, J. & Liu, Y. Substantial impact of charge on electrochemical reactions of two-dimensional materials. *J. Am. Chem. Soc.* **140**, 9127–9131 (2018).
33. Mehdipour, H. et al. Dependence of electron transfer dynamics on the number of graphene layers in π-stacked 2*d* materials: insights from ab initio nonadiabatic molecular dynamics. *Phys. Chem. Chem. Phys.* **21**, 23198–23208 (2019).
34. Hansen, H. A., Viswanathan, V. & Nørskov, J. K. Unifying kinetic and thermodynamic analysis of 2 e^- and 4 e^- reduction of oxygen on metal surfaces. *J. Phys. Chem. C* **118**, 6706–6718 (2014).
35. Limmer, D. T., Willard, A. P., Madden, P. & Chandler, D. Hydration of metal surfaces can be dynamically heterogeneous and hydrophobic. *Proc. Natl Acad. Sci. USA* **110**, 4200–4205 (2013).
36. Huang, B. et al. Cation-dependent interfacial structures and kinetics for outer-sphere electron-transfer reactions. *J. Phys. Chem. C* **125**, 4397–4411 (2021).
37. Patel, A. M. et al. Theoretical approaches to describing the oxygen reduction reaction activity of single-atom catalysts. *J. Phys. Chem. C* **122**, 29307–29318 (2018).
38. Mortensen, J. J., Hammer, B. & Nørskov, J. K. Alkali promotion of N_2 dissociation over Ru(0001). *Phys. Rev. Lett.* **80**, 4333–4336 (1998).
39. Marshall-Roth, T. et al. A pyridinic Fe–N_4 macrocycle models the active sites in Fe/N-doped carbon electrocatalysts. *Nat. Commun.* **11**, 5283 (2020).
40. Sa, Y. J. et al. Thermal transformation of molecular Ni^{2+}–N_4 sites for enhanced CO_2 electroreduction activity. *ACS Catal.* **10**, 10920–10931 (2020).
41. Hossain, M. D., Huang, Y., Yu, T. H., Goddard, W. A. & Luo, Z. Reaction mechanism and kinetics for CO_2 reduction on nickel single atom catalysts from quantum mechanics. *Nat. Commun.* **11**, 2256 (2020).
42. Kim, H. et al. Identification of single-atom Ni site active toward electrochemical CO_2 conversion to CO. *J. Am. Chem. Soc.* **143**, 925–933 (2021).
43. Marcandalli, G., Villalba, M. & Koper, M. T. M. The importance of acid–base equilibria in bicarbonate electrolytes for CO_2 electrochemical reduction and CO reoxidation studied on Au(*hkl*) electrodes. *Langmuir* **37**, 5707–5716 (2021).
44. Luo, F. et al. Accurate evaluation of active-site density (SD) and turnover frequency (TOF) of PGM-free metal–nitrogen-doped carbon (MNC) electrocatalysts using CO cryo adsorption. *ACS Catal.* **9**, 4841–4852 (2019).
45. Kramm, U. I. et al. Structure of the catalytic sites in Fe/N/C-catalysts for O_2-reduction in PEM fuel cells. *Phys. Chem. Chem. Phys.* **14**, 11673–11688 (2012).
46. Jiang, K. et al. Transition-metal single atoms in a graphene shell as active centers for highly efficient artificial photosynthesis. *Chem* **3**, 950–960 (2017).
47. Jiang, K. et al. Isolated Ni single atoms in graphene nanosheets for high-performance CO_2 reduction. *Energy Environ. Sci.* **11**, 893–903 (2018).
48. Luo, F. et al. Surface site density and utilization of platinum group metal (PGM)-free Fe–NC and FeNi–NC electrocatalysts for the oxygen reduction reaction. *Chem. Sci.* **12**, 384–396 (2021).
49. Vojvodic, A., Nørskov, J. K. & Abild-Pedersen, F. Electronic structure effects in transition metal surface chemistry. *Top. Catal.* **57**, 25–32 (2014).
50. Xin, H., Vojvodic, A., Voss, J., Nørskov, J. K. & Abild-Pedersen, F. Effects of *d*-band shape on the surface reactivity of transition-metal alloys. *Phys. Rev. B* **89**, 115114 (2014).
51. Greiner, M. T. et al. Free-atom-like *d* states in single-atom alloy catalysts. *Nat. Chem.* **10**, 1008–1015 (2018).
52. Thirumalai, H. & Kitchin, J. R. Investigating the reactivity of single atom alloys using density functional theory. *Top. Catal.* **61**, 462–474 (2018).
53. Larsen, A. H., Kleis, J., Thygesen, K. S., Nørskov, J. K. & Jacobsen, K. W. Electronic shell structure and chemisorption on gold nanoparticles. *Phys. Rev. B* **84**, 245429 (2011).
54. Li, L. et al. Investigation of catalytic finite-size-effects of platinum metal clusters. *J. Phys. Chem. Lett.* **4**, 222–226 (2013).
55. Ji, Y., Nørskov, J. K. & Chan, K. Scaling relations on basal plane vacancies of transition metal dichalcogenides for CO_2 reduction. *J. Phys. Chem. C* **123**, 4256–4261 (2019).
56. Zhao, X. & Liu, Y. Unveiling the active structure of single nickel atom catalysis: critical roles of charge capacity and hydrogen bonding. *J. Am. Chem. Soc.* **142**, 5773–5777 (2020).
57. Singh, A. R. et al. Computational design of active site structures with improved transition-state scaling for ammonia synthesis. *ACS Catal.* **8**, 4017–4024 (2018).
58. Birdja, Y. Y. et al. Advances and challenges in understanding the electrocatalytic conversion of carbon dioxide to fuels. *Nat. Energy* **4**, 732–745 (2019).
59. Kresse, G. & Furthmüller, J. Efficient iterative schemes for ab initio total-energy calculations using a plane-wave basis set. *Phys. Rev. B* **54**, 11169–11186 (1996).
60. Joubert, D. From ultrasoft pseudopotentials to the projector augmented-wave method. *Phys. Rev. B* **59**, 1758–1775 (1999).
61. Hammer, B., Hansen, L. B. & Nørskov, J. K. Improved adsorption energetics within density-functional theory using revised Perdew–Burke–Ernzerhof functionals. *Phys. Rev. B* **59**, 7413–7421 (1999).
62. Heyd, J., Scuseria, G. E. & Ernzerhof, M. Hybrid functionals based on a screened Coulomb potential. *J. Chem. Phys.* **118**, 8207–8215 (2003).
63. Heyd, J., Scuseria, G. E. & Ernzerhof, M. Erratum: hybrid functionals based on a screened Coulomb potential. *J. Chem. Phys.* **124**, 219906 (2006).

64. Dudarev, S. & Botton, G. Electron-energy-loss spectra and the structural stability of nickel oxide: an LSDA+U study. *Phys. Rev. B* **57**, 1505–1509 (1998).
65. Hjorth Larsen, A. et al. The atomic simulation environment—a Python library for working with atoms. *J. Phys. Condens. Matter* **29**, 273002 (2017).
66. Monkhorst, H. J. & Pack, J. D. Special points for Brillouin-zone integrations. *Phys. Rev. B* **13**, 5188–5192 (1976).
67. Henkelman, G., Uberuaga, B. P. & Jónsson, H. Climbing image nudged elastic band method for finding saddle points and minimum energy paths. *J. Chem. Phys.* **113**, 9901–9904 (2000).
68. Mathew, K., Kolluru, V. S. C., Mula, S., Steinmann, S. N. & Hennig, R. G. Implicit self-consistent electrolyte model in plane-wave density-functional theory. *J. Chem. Phys.* **151**, 234101 (2019).
69. Nørskov, J. K. et al. Origin of the overpotential for oxygen reduction at a fuel-cell cathode. *J. Phys. Chem. B* **108**, 17886–17892 (2004).
70. Medford, A. J. et al. CatMAP: a software package for descriptor-based microkinetic mapping of catalytic trends. *Catal. Letters* **145**, 794–807 (2015).
71. Luo, F. et al. P-block single-metal-site tin/nitrogen-doped carbon fuel cell cathode catalyst for oxygen reduction reaction. *Nat. Mater.* **19**, 1215–1223 (2020).
72. Möller, T. et al. Efficient CO_2 to CO electrolysis on solid Ni–N–C catalysts at industrial current densities. *Energy Environ. Sci.* **12**, 640–647 (2019).
73. Zhang, X. et al. Molecular engineering of dispersed nickel phthalocyanines on carbon nanotubes for selective CO_2 reduction. *Nat. Energy* **5**, 684–692 (2020).
74. Gu, J., Hsu, C. S., Bai, L., Chen, H. M. & Hu, X. Atomically dispersed Fe^{3+} sites catalyze efficient CO_2 electroreduction to CO. *Science* **364**, 1091–1094 (2019).

Acknowledgements

The research leading to these results received funding from the European Union's Horizon 2020 research and innovation program under grant agreement no. 851441, SELECTCO2, and from the VILLUM Centre for the Science of Sustainable Fuels and Chemicals (no. 9455) from VILLUM FONDEN. Research leading to some of these results received funding from the Fuel Cells and Hydrogen 2 Joint Undertaking under grant agreement no. 779366, CRESCENDO. The authors acknowledge computational resource from PRACE (project ID: prpa85) and the Juelich Supercomputing Centre. We thank G. Kastlunger for helpful discussions.

Author contributions

S.V. and K.C. designed the computational study and wrote the first draft of the paper. S.V. and S.-C.T. performed the DFT calculations and the data analysis. P.S. designed the experiments, and W.J. and S.B. performed them. All the authors contributed to revising the manuscript.

Competing interests

The authors declare no competing interests.

Additional information

Supplementary information The online version contains supplementary material available at https://doi.org/10.1038/s41929-021-00705-y.

Correspondence and requests for materials should be addressed to Peter Strasser or Karen Chan.

Peer review information *Nature Catalysis* thanks Yang Hou, Hyungjun Kim and the other, anonymous, reviewer(s) for their contribution to the peer review of this work.

Reprints and permissions information is available at www.nature.com/reprints.

Publisher's note Springer Nature remains neutral with regard to jurisdictional claims in published maps and institutional affiliations.

© The Author(s), under exclusive licence to Springer Nature Limited 2021

nature portfolio

https://doi.org/10.1038/s41929-021-00705-y

Supplementary information

Unified mechanistic understanding of CO_2 reduction to CO on transition metal and single atom catalysts

In the format provided by the
authors and unedited

Supplementary Information

Unified mechanistic understanding of CO_2 reduction to CO on transition metal and single atom catalysts

Sudarshan Vijay[1⊥], Wen Ju [2⊥], Sven Brückner[2], Sze-Chun Tsang[1], Peter Strasser[2], Karen Chan[1]**

AUTHOR ADDRESS

1. *CatTheory, Department of Physics, Technical University of Denmark, 2800 Kgs. Lyngby, Denmark*
2. *Department of Chemistry, Chemical Engineering Division, Technical University Berlin, Berlin 10623, Germany*

*⊥ Contributed equally to this work * Corresponding authors*

**kchan@fysik.dtu.dk*

**pstrasser@tu-berlin.de*

Supplementary Methods

Details about the pH and electrolyte are given in **Supplementary Table 1.**

Electrolyte	pH
CO_2 saturated 0.1 M $KHCO_3$	6.8
CO_2 saturated 0.3 M $KHCO_3$	7.15
CO_2 saturated 0.5 M $KHCO_3$	7.3
CO_2 saturated 1.0 M $KHCO_3$	7.6
CO_2 saturated 0.05 M K_3PO_4 + 0.05 M H_3PO_4	6.4
CO_2 saturated 0.05 M KH_2PO_4 + 0.05 M H_3PO_4	2.25
N_2 saturated 0.05 M KH_2PO_4 + 0.05 M H_3PO_4	2.25
N_2 saturated 0.05 M K_3PO_4 + 0.05 M H_3PO_4	6.9
N_2 saturated 0.05 M K_3PO_4 + 0.05 M K_2HPO_4	11.8

Supplementary Table 1: Electrolyte and pH used in this work

Cathode potential

The working potential is controlled by the Biologic SP-300 potentiostat against the Ag/AgCl reference electrode. 50% of the ohmic drop was automatically corrected, and the other half was corrected manually. All potentials were rescaled to the reversible hydrogen electrode (RHE) and the normal hydrogen electrode (NHE).

$$E_{IR-free/RHE} = E_{vs.\ Ref} + E_{Ref\ vs.\ NHE} + 0.059 * pH + I * R * 50\% \quad (1)$$

$E_{IR-free/RHE}$: IR correct cathode potential against RHE / V_{RHE}
$E_{vs.\ Ref}$: Applied potential against the reference electrode / V
$E_{Ref\ vs.\ RHE}$: Reference electrode potential measured against NHE / V
pH: pH-value of the electrolyte
I: Total current of the experiment (absolute value) / A
R: Ohmic resistance between cathode and reference electrode / Ω

$$E_{IR-free/NHE} = E_{vs.\ Ref} + E_{Ref\ vs.\ NHE} + I * R * 50\%$$

$E_{IR-free/NHE}$: IR correct cathode potential against NHE / V_{NHE}

$E_{vs.\ Ref}$:	Applied potential against the reference electrode	/ V
$E_{Ref\ vs.\ RHE}$:	Reference electrode potential measured against NHE	/ V
I:	Total current of the experiment (absolute value)	/ A
R:	Ohmic resistance between cathode and reference electrode	/ Ω

Product analysis

$$\dot{n}_{Product} = \frac{\dot{V}_{Total} \times C_{Product}}{A \times V_{MOL}} \ (2)$$

$\dot{n}_{Product}$:	geometric reaction rate of each product	/ mol cm^{-2} s^{-1}
$\dot{V}_{Total}$:	CO_2 purging flow rate	/ mL s^{-1}
$C_{Product}$:	product concentration (volumetric ratio) from GC	/ $\%_{VOL}$
A:	geometric area of the electrode	/ cm^2
V_{MOL}:	volume of gas per mole at ATM	/ mL mol^{-1}

$$j_{Product} = \dot{n}_{Product} \times F \times z \ (3)$$

$j_{Product}$:	partial current density of each product	/ mA cm^{-2}
F:	faradaic constant	/ C mol^{-1}
z:	charge transfer per mole of product	

$$FE_{Product} = \frac{j_{Product}}{j_{Total}} \times 100\% \ (4)$$

$FE_{Product}$:	faradaic efficiency of each product	/ %
j_{Total}:	total current density	/ mA cm^{-2}

Supplementary Note 1: Methodology used to calculate potential dependent energetics

We use the method of Ref[1] to determine the potential dependence of polar intermediate $\mathrm{CO_2}$. We briefly describe the methodology here below, along with a method to determine the contribution of the polarized adsorbate to the charge separation at the interface.

When an intermediate such as $\mathrm{CO_2}$ adsorbs in a finite-sized unit cell, it changes the workfunction dramatically, as large as 1–2 eV in small unit cells. This alteration of the workfunction is problematic because it prevents the computation from being done at a constant driving force. To alleviate this problem, constant workfunction methods have been developed,[2,3] which introduces excess electrons into a DFT calculation, while preserving charge neutrality by adding positive charge into a continuum placed a suitable height above the adsorbate. However, the mis-match in capacitances of the different charging components give rise to variations in energies amongst different calculation setups or cell sizes, which are sometimes as large as 1 eV.[1] One way to solve this problem is to use the *effective* surface charge as the descriptor of the driving force, instead of the workfunction, since it reflects the local interfacial field and potential drop[1]. Here we describe these terms mathematically as well as illustrate how they are used to describe $\mathrm{CO_2}$ adsorption.

We employ two parallel plate capacitors to describe the charge separation arising from adsorbed $\mathrm{CO_2}$ and from the excess continuum charge, as shown in **Supplementary Figure 1.** The *integral* energy, E, for this system is

$$E = E_0 + q_c\, {E'}_{q_c} + q_i\, {E'}_{q_i} + \frac{q_c^2}{2} E''_{q_c} + \frac{q_i^2}{2}\, E''_{q_i} + q_e\, q_i\, E''_{q_i, q_c} \quad (5)$$

Where, q_c is the charge stored in the CO_2 capacitor, q_i is the charge stored in the implicit capacitor and the number of primes denote the number of derivatives with respect to the quantit(ies) in the subscript.

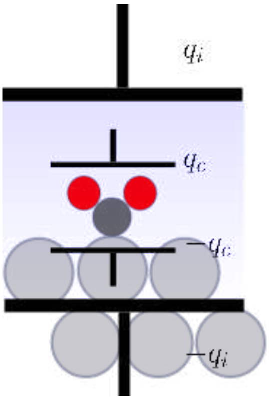

Supplementary Figure 1: Schematic showing the multiple capacitances that have been used in this work; q_c denotes the charge for the capacitance for CO_2 adsorption, while q_i denotes the charge for the capacitance from continuum charging.

The resultant differential energy, between two states CO_2(g) and CO_2*, ΔE is

$$\Delta E = \Delta E_0 + q_c \left(\phi_0 + \frac{q_c + q_i}{2AC_c} \right) \quad (6)$$

Where ΔE_0 is the energy of a hypothetical reference state, with a workfunction of ϕ_0. q_c is the "charge" on the bent CO_2 capacitor (we assume that CO_2(g) is the uncharged parallel plate capacitor) and q_i is the amount of continuum charge added. A is the surface area of the cell and C_c is the capacitance of the CO_2 capacitor. In order to perform the calculations as per Ref[1], we would need multiple unit-cells to determine q_c before we can plot ΔE vs. σ, where σ is the *effective* surface charge given by $\frac{q_c+q_i}{A}$. Here we detail a simple way to approximate q_c without having to increase the cell size.

We assume here that q_c varies linearly with the reaction path, ω. This relationship is shown schematically in **Supplementary Figure 2**.

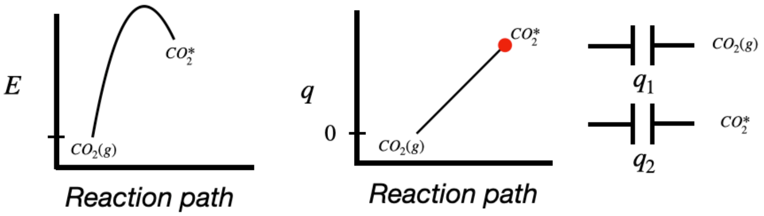

Supplementary Figure 2: Assumed ideal pathway for CO_2 adsorption from $CO_2(g)$, where the energy varies with reaction path ω as per a second order polynomial and so the charge varies linearly with ω.

We write this linear variation of charge against the ω as

$$q = \frac{\partial q}{\partial \omega}|_{\omega=0} \cdot \omega + O(\omega^2) \quad (7)$$

We relate the first derivative of q to the change in dipole moment along the reaction coordinate. This quantity cannot be determined in practice because dipole moments are usually computed in cartesian coordinates. We take the dot product between the change in the dipole moment along cartesian coordinates, μ , with the normal mode corresponding to the reaction coordinate, ω to get the following expression for q:

$$q = \frac{d}{d\omega}\frac{d\mu}{dR} \cdot \omega|_{\omega=0} \cdot \omega = \frac{d\mu}{dR}|_{\omega=0} \cdot \omega \ (8)$$

The quantity $\frac{d\mu}{dR}$ can be determined through the use of finite differences using either the dipole moment in the unit cell, or the atom centered forces from a DFT simulation. For a small displacement dz:

$$\frac{d\mu}{dR} = \frac{\mu^{i+1} - \mu^{i-1}}{2dz} \quad (9)$$

To determine ω we use a simple approximation based on the atomic positions of CO_2(g) and CO_2*,

$$\omega \approx \frac{\mathrm{pos}(\mathrm{CO}_{2(g)}) - \mathrm{pos}(\mathrm{CO}_2^*)}{\mathrm{norm}\left(\mathrm{pos}(\mathrm{CO}_{2(g)}) - \mathrm{pos}(\mathrm{CO}_2^*)\right)}, \quad (10)$$

Where pos denotes the atomic positions of the representative species. For MNC catalysts, the metal atom was also included due to its noticeable motion upon an adsorption.

Transition metal	*q* (e)	Metal-Nitrogen Carbon	*q* (e)
Ag(100)	0.37	Fe(1,1)	0.35
Au(100)	0.21	Ni(1,1)	0.21
Cu(100)	0.25	Ni(1,2)	0.31
Pd(100)	0.14	Fe(1,3)	0.10
Pt(100)	0.13	Fe(2,1)	0.38
Ag(211)	0.35	Ni(2,1)	0.42
Au(211)	0.30	Fe(2,2)	0.49
Cu(211)	0.22	Ni(2,2)	0.47
Pd(211)	0.13	Fe(2,3)	0.1
Pt(211)	0.09	Ni(2,3)	0.49
		Fe(2,4)	0.29
		Ni(2,4)	0.49

Supplemntary Table 2: Charges for the CO_2 capacitor determined by using the methodology detailed in this section; note that on average the MNC charges are larger than TM ones, which is similar to the idea presented in Figure 3 with vacuum dipole moments.

Having determined the charge stored in the CO_2 capacitor, we plot the energy against σ. We repeat this procedure for other less polar adsorbates, but neglect the contribution to the capacitance arising from the polarization of charge from the adsorbate, i.e. we set $q = 0$.

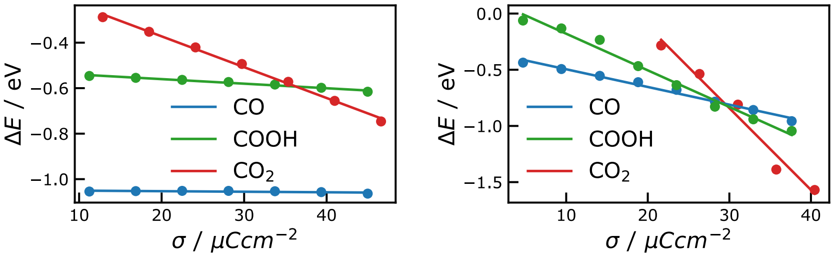

Supplementary Figure 3: Energy as a function of the effective surface charge for Pd(100) and Fe(2,4) MNC catalyst; best line fits are shown for each adsorbate

Having accounted for the CO_2* dipoles in this manner, we convert the surface charge relationship to one against potential. We use the following capacitor relationship to relate σ to an absolute potential ϕ,

$$\sigma = C_{\mathrm{exp}} \left(\phi - \phi_0 \right)$$

Where C_{exp} is the experimental capacitance, assumed here to be $25\mu F cm^{-2}$. ϕ_o is assumed to be the workfunction of the bare metal slab, as an approximation for the potential of zero charge, which might lead to a constant offset on the potential scale.[4] While this can cause issues for materials such as Pt and Pd, due to the adsorption of water,[5,6] we anticipate it works well for the weak binding materials which are the main focus of this study. In line with previous experimental work, we use $\phi_0 = -0.05$ eV for graphene.[7]

Supplementary Note 2: Additional results for electron transfer rates and extrapolation

Previous reports have suggested that the density of states at the Fermi level changes dramatically with excess continuum charge (and hence a change in workfunction) for graphene-like systems. This change in density of states can cause an additional "quantum" capacitance to form at lower overpotentials.[8,9] To determine if the effect is seen in the potentials considered in the main text (about −0.6 V vs. SHE), we alter the workfunction in our simulation cells using the addition of protons (**Supplementary Figure 4**), and through continuum charge (**Supplementary Figure 5**). We find that the bands stay relatively constant in the potential range of interest, thus allowing us to apply our assumption of a constant capacitance in our extrapolation scheme. We note that there are always states present at the Fermi level at all the potentials we have consider.

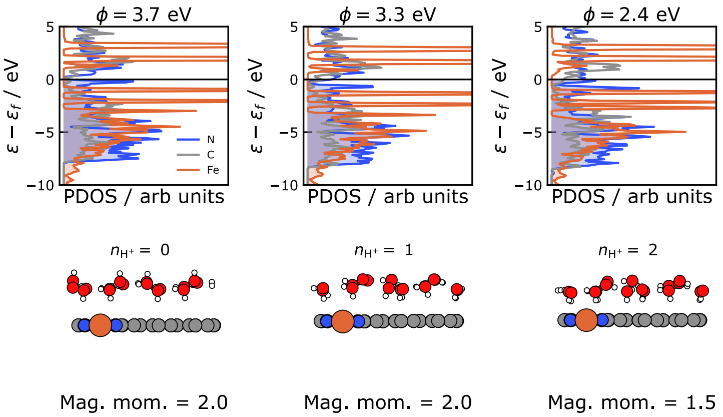

Supplementary Figure 4: Projected density of states onto Fe, C and N at different workfunctions generated by changing the coverage of protons in the water layer, showing that the states do not change drastically with potential

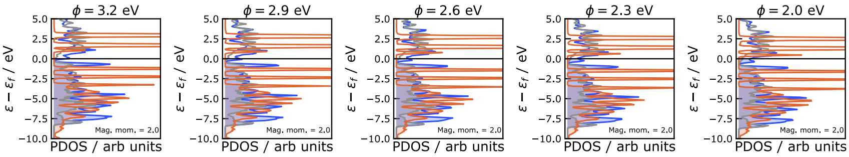

Supplementary Figure 5: Projected density of states onto Fe, C and N at different workfunctions generated by different continuum charge, showing that the states do not change drastically with potential

Electron transfer on CoPc adsorbed on *n*-doped graphene: Previous studies have shown that CoPc adsorbed on graphene[10] can have electron transfer rates as low as 810 fs, which might lead to electron transfer being rate limiting. **Supplementary Figure 6** show that with even a small amount of *n*-doping on graphene, the CO_2* states move below the Fermi level. This change indicates that all components of the system - CO_2*, CoPc and *n*-doped graphene - are hybridized and electron hopping from any of these entities is likely to be fast as compared to diffusion.

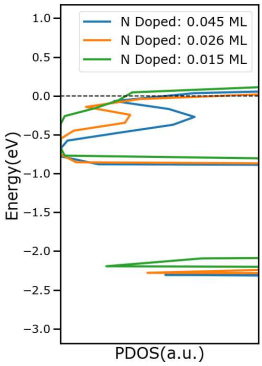

Supplementary Figure 6: Change in the density of states projected onto the *s,p* states of CO2*, adsorbed on CoPc, supported on graphene with different *n*-doping concentrations

Supplementary Note 3: Further experimental data

Supplementary Figure 7-8 show the total current densities, partial current densities towards H_2 and Fradaic efficiencies (FE) of the main products of the reaction. The major product of the reaction is CO at cathodic potentials.

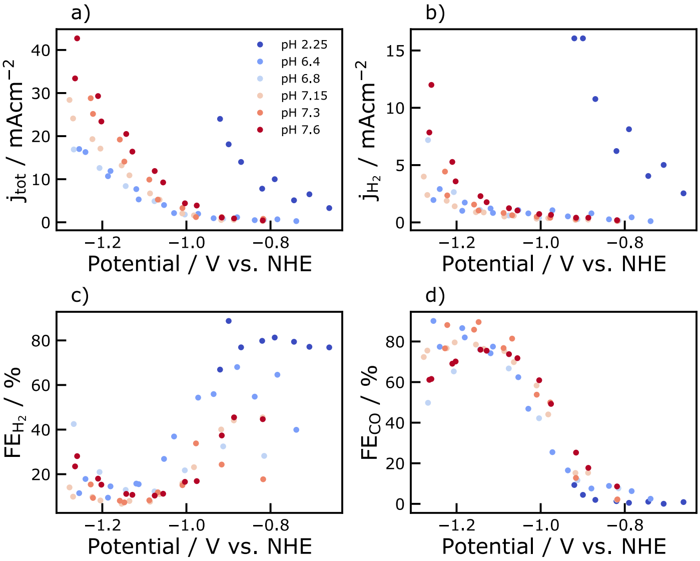

Supplementary Figure 7: a) Total current densities for NiNC at different pH values b) partial current densities towards H_2; Fradaic efficiencies towards c) H_2 d) CO

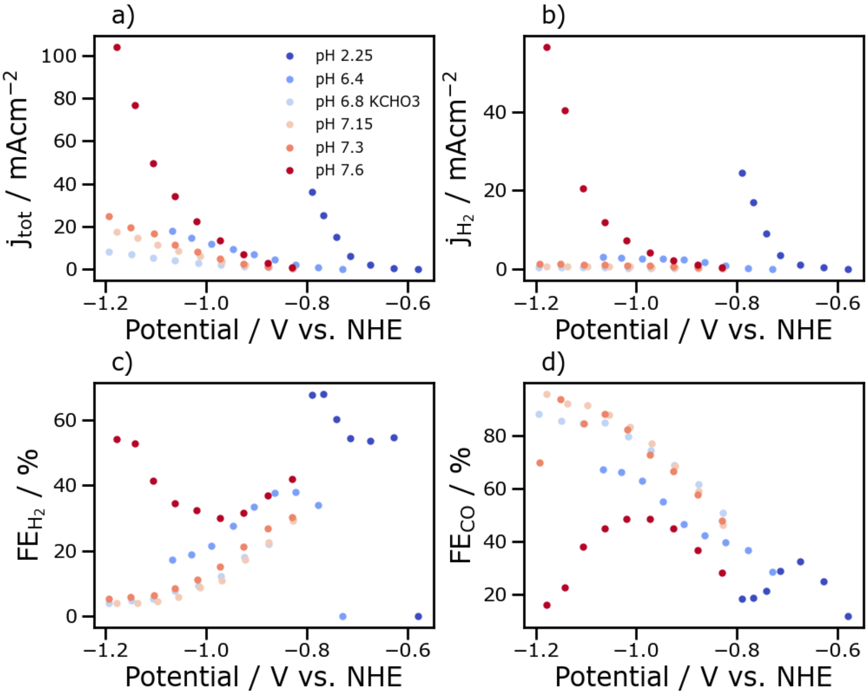

Supplementary Figure 8: a) Total current densities for CoPc at different pH values b) partial current densities towards H_2; Fradaic efficiencies towards c) H_2 d) CO

Cyclic Voltammograms (CV): Supplementary Figure 9 shows CVs that were performed in the presence and absence of CO_2 for CoPc on CNT (see **Figure 2h**). We observe a peak at potentials between 0 − 0.4 V vs. RHE, which is reversible in N_2 environments, but irreversible in CO_2 environments. Since the peaks show a pH dependence on the potential vs. RHE, they should arise from adsorbates other than hydrogen or oxygen species. While we have not identified the adsorbate species involved, we suggest they do not influence the pH dependence shown in **Figure 2h**, since the onset potentials for CO2R occur at more reducing potentials < −0.6 V vs. SHE.

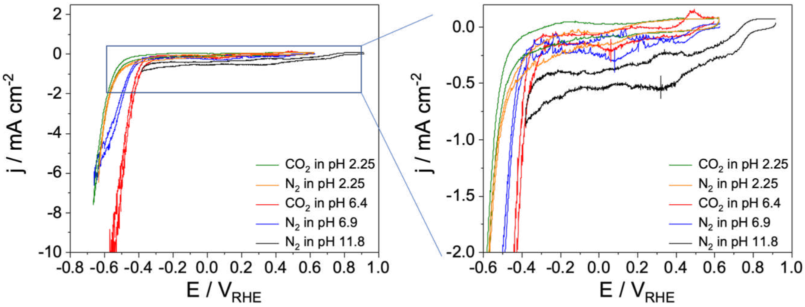

Supplementary Figure 9: Cyclic voltammograms of CoPc on CNT in phosphate buffer solution, under various conditions.

Supplementary Note 4: Further kinetic analysis: COOH vs. CO scaling and different potentials CO_2 vs. COOH scaling

In line with Ref.[11], we show that COOH* and CO* adsorption energies scale with each other. This scaling allows us to consider the activity as a function of CO_2* vs COOH* binding in **Figure 3** while also implicitly including CO* energies.

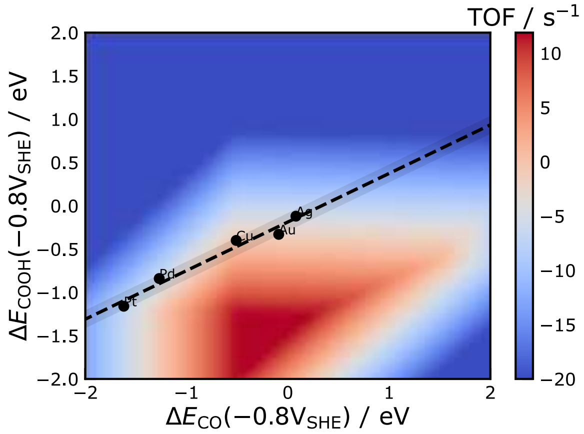

Supplementary Figure 10: Rate map for transition metals including COOH* vs. CO* scaling. Note that this scaling implicitly includes the adsorption energy of CO* in the volcano shown in **Figure 3**.

The kinetic rate map for different potentials is shown in **Supplementary Figure 11**. At lower overpotentials, we can see that most TMs and MNCs are limited by COOH * formation. As the overpotential is increased, the rate limiting step becomes CO_2* adsorption.

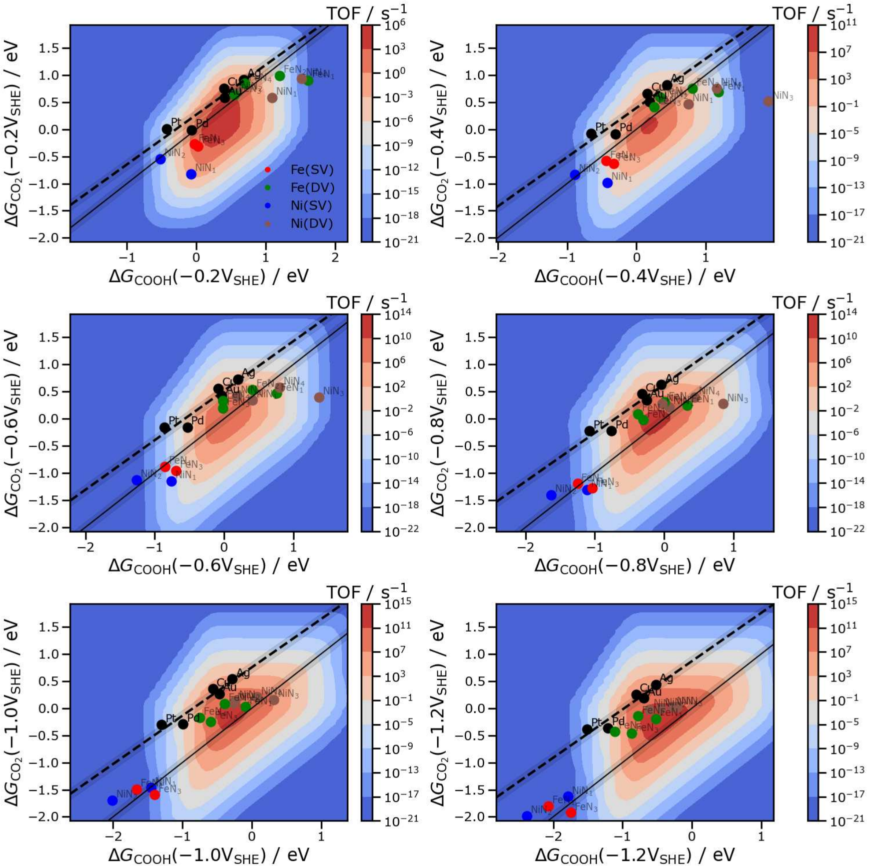

Supplementary Figure 11: Kinetic rate map at different SHE potentials at pH = 2 show that the TM metals go from COOH* limited to CO_2* limited at relatively low overpotentials, while NiNC stays COOH* limited until very reducing potentials of -1.0 V vs SHE.

Supplementary Note 5: Presence of multiple sites on FeNC and NiNC

The TPD protocol is performed after a pre-He-purging at 600 °C for surface cleaning, and six CO -pluses at – 80 °C for CO uptake. The helium purging involves heating the Fe0.5NC sample from room temperature with a ramping of 10 °C min^{-1} under 20 sccm He flow, and keeping at 600 °C for 15 mins. After being spontaneiosuly cooled to room temperature, the sample loop is located in dry ice and acetone mixture for −80 °C environment. While keeping 20 sccm He flow, six CO pulses (0.338 mL for each), dosed at 25 min intervals, were passed through the samples for CO chemisorption. Subsequently, a temperature-programmed CO desorption (TPD) was performed by ramping from −80 °C to 600 °C (+10 °C min^{-1}). The gas flow/emission is analyzed by a thermo conductivity detector. The measurement protocol, the FeNC, and the NC catalysts are analogous with those reported in our previous study.[12]

Supplementary Figure 12 shows the Temperature Programmed Desorption (TPD) spectra for FeNC, NiNC and NC. FeNC shows a clear signal between 300 – 425 K, indicating the presence of strong binding CO sites, while NiNC and NC show no signal. We determine a rough estimate of the adsorption energy of CO through the Redhead equation, $E_{\mathrm{CO}} = k_B T_p \ln\left(\frac{\nu T_p}{\beta} - 3.64\right)$,[13] to which we add free energy contributions of 0.6 eV (procedure detailed in the methods section) to obtain G_{CO}. Assuming that a distribution of sites shows a signal between 300 – 425 K, we obtain $\Delta G_{\mathrm{CO}} \approx -0.15 \text{ to } -0.5$ eV < 0, which would imply saturation of CO on the sites probed with TPD. As **Figure 3**b shows, sites that are saturated with CO^* (like the SV ones) are not active for $\mathrm{CO_2}$R.

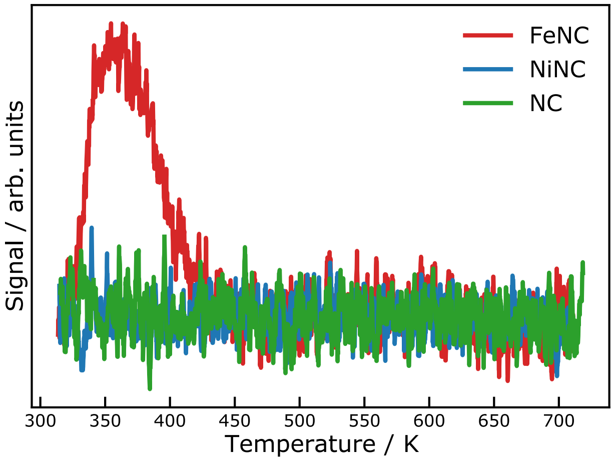

Supplementary Figure 12: Temperature programmed desorption (TPD) on FeNC, NiNC and NC (no CO uptake, reference) show the presence of strong binding CO sites only on FeNC.

Supplementary Note 6: Solvation energies

In this section we perform a preliminary assessment of the solvation energies with Born–Oppenheimer *ab initio* molecular dynamics (AIMD). We use a Nose–Hoover[14] thermostat set to 300 K. The calculations were performed with the BEEF-vdW functional (to ensure water stays near the surface), were spin polarized, and had otherwize identical computational settings to all calculations done in the manuscript. **Supplementary Figure 13** shows the representative images of the trajectories during the AIMD. The internal energies for CO adsorption as determined from the AIMD is −0.12 eV, which leads to a solvation energy of 0.33 eV.

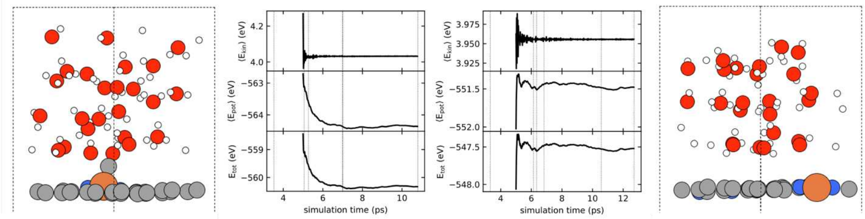

Supplementary Figure 13: Representative images of two AIMD trajectories along with convergence of kinetic, potential and total energies

Supplementary Note 7: Dipole moments and the width of states

In order to describe the dependence of surface dipole moments on the underlying electronic structure of the material, we turn to a simple analytical model proposed for the deposition of cations on metallic surfaces in Ref.[15] Within this model, two states *s* and *p* have a certain occupancy based on their position with respect to the Fermi level. They have a dipole moment defined as the interaction between the two states (cf. Equation 8 within Ref[15]). For a fixed set of states at a fixed energy level, the only free parameter in the determination of the dipole moment is Δ, the width of the state. As the width is reduced (making it narrower), the dipole moment is increased. This behavior is identical to that seen in **Figure 4** of this manuscript, where the dipole moments of CO_2* are large in the case of MNCs (which have narrow states) as compared to TMs (which have broader states).

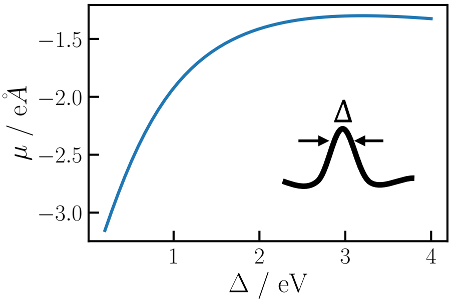

Supplementary Figure 14: Variation of the dipole moment with the width of the states

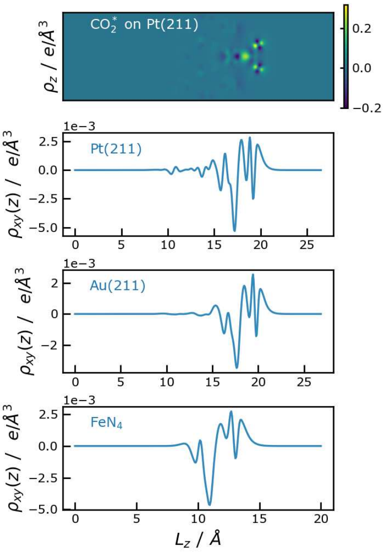

Supplementary Figure 15: Charge density differences averaged along *z* for CO_2* on Pt(211), followed by the *xy* averaged charge density.

We now visualize the states in real space in order to gain a greater understanding of the role of the metal – CO_2* interaction in the surface dipole moment. **Supplementary Figure 15** shows the charge density differences on a plane passing through the centers of the O-C-O atoms, given by

ρ_z. We see the characteristic O *p*-states and a hybridized C-Metal bond. We also plot the *xy*-averaged density for Pt(211), Au(211) and FeN$_4$ MNC. We find that the distributions of charge density look similar, implying that it is the interaction of the same single particle state, the HOMO of the bent diabatic CO$_2$, that is likely to be responsible for the different dipole moments.

Supplementary Note 8: Solution of Newns–Muscat model (Appendix A)

In the low coverage regime, the dipole moment and occupancy n of an adsorbed molecule on the surface can be related to the workfunction (ϕ) and field (in the direction of surface normal) to a first order as

$$\mathrm{Field} = \frac{\mathrm{d}\phi}{\mathrm{dz}} = \theta\ (\mu + \mathrm{edn}\ )$$

Where d is the image plane distance (a constant), θ is the coverage.

Meanwhile both and n can be written as functions of Green operators of *ss*, *sp* and *pp* states, as written

$$n = -\frac{1}{\pi} Im \int_{-\infty}^{\epsilon_f} G_{ss}(\epsilon) d\epsilon - \frac{1}{\pi} Im \int_{-\infty}^{\epsilon_f} G_{pp}(\epsilon) d\,\epsilon$$

$$\mu = -2\lambda \frac{1}{\pi} Im \int_{-\infty}^{\epsilon_f} G_{sp}(\epsilon) d$$

Which in turn are related to the field and workfunction through their energies ϵ in the definition of their respective Green functions.

$$(\epsilon - \hat{H} + i\alpha)G = I$$

Thus, this becomes a self-consistent problem, which we can be solved for a chosen set of parameters. The parameter that we choose to plot is against Δ, the width of the states, keeping all other parameters constant.

Supplementary References

1. Gauthier, J., Dickens, C., Heenen, H., Ringe, S. & Chan, K. Unified Approach to Implicit and Explicit Solvent Simulations of Electrochemical Reaction Energetics. *J. Chem. Theory Comput.* (2019) doi:10.26434/chemrxiv.8396954.v1.
2. Kastlunger, G., Lindgren, P. & Peterson, A. A. Controlled-Potential Simulation of Elementary Electrochemical Reactions: Proton Discharge on Metal Surfaces. *J. Phys. Chem. C* **122**, 12771–12781 (2018).
3. Hörmann, N. G., Marzari, N. & Reuter, K. Electrosorption at metal surfaces from first principles. *npj Comput. Mater.* **6**, (2020).
4. Trasatti, S. Structure of the metal/electrolyte solution interface: new data for theory. *Electrochim. Acta* **36**, 1659–1667 (1991).
5. Heenen, H. H., Gauthier, J. A., Kristoffersen, H. H., Ludwig, T. & Chan, K. Solvation at metal/water interfaces: An *ab initio* molecular dynamics benchmark of common computational approaches. *J. Chem. Phys.* **152**, 144703 (2020).
6. Hörmann, N. G., Andreussi, O. & Marzari, N. Grand canonical simulations of electrochemical interfaces in implicit solvation models. *J. Chem. Phys.* **150**, 41730 (2019).
7. Choi, C. H. *et al.* The Achilles' Heel of Iron-based Catalysts during Oxygen Reduction in an Acidic Medium. *Energy Environ. Sci.* **11**, 3176–3182 (2018).

8. Kim, D., Shi, J. & Liu, Y. Substantial Impact of Charge on Electrochemical Reactions of Two-Dimensional Materials. *J. Am. Chem. Soc.* **140**, 9127–9131 (2018).
9. Radin, M. D., Ogitsu, T., Biener, J., Otani, M. & Wood, B. C. Capacitive charge storage at an electrified interface investigated via direct first-principles simulations. *Phys. Rev. B - Condens. Matter Mater. Phys.* **91**, 125415 (2015).
10. Mehdipour, H. *et al.* Dependence of electron transfer dynamics on the number of graphene layers in π-stacked 2d materials: Insights from: Ab initio nonadiabatic molecular dynamics. *Phys. Chem. Chem. Phys.* **21**, 23198–23208 (2019).
11. Hansen, H. A., Varley, J. B., Peterson, A. A. & Nørskov, J. K. Understanding trends in the electrocatalytic activity of metals and enzymes for CO2 reduction to CO. *J. Phys. Chem. Lett.* **4**, 388–392 (2013).
12. Luo, F. *et al.* Accurate Evaluation of Active-Site Density (SD) and Turnover Frequency (TOF) of PGM-Free Metal-Nitrogen-Doped Carbon (MNC) Electrocatalysts using CO Cryo Adsorption. *ACS Catal.* **9**, 4841–4852 (2019).
13. Redhead, P. A. Thermal desorption of gases. *Vacuum* **12**, 274 (1962).
14. Nosé, S. A unified formulation of the constant temperature molecular dynamics methods. *J. Chem. Phys.* **81**, 511–519 (1984).
15. Muscat, J. P. & Newns, D. M. The interpretation of work-function variation in alkali chemisorption from the atomic viewpoint. *J. Phys. C Solid State Phys.* **7**, 2630–2644 (1974).

Check for updates

GDCh

Research Articles

Angewandte Chemie
International Edition
www.angewandte.org

How to cite: *Angew. Chem. Int. Ed.* **2022,** *61,* e202114707
International Edition: doi.org/10.1002/anie.202114707
German Edition: doi.org/10.1002/ange.202114707

Electrocatalysis *Very Important Paper*

Covalent Organic Framework (COF) Derived Ni-N-C Catalysts for Electrochemical CO_2 Reduction: Unraveling Fundamental Kinetic and Structural Parameters of the Active Sites

Changxia Li$^+$, Wen Ju$^+$, Sudarshan Vijay, Janis Timoshenko, Kaiwen Mou, David A. Cullen, Jin Yang, Xingli Wang, Pradip Pachfule, Sven Brückner, Hyo Sang Jeon, Felix T. Haase, Sze-Chun Tsang, Clara Rettenmaier, Karen Chan, Beatriz Roldan Cuenya, Arne Thomas,* and Peter Strasser**

Abstract: Electrochemical CO_2 reduction is a potential approach to convert CO_2 into valuable chemicals using electricity as feedstock. Abundant and affordable catalyst materials are needed to upscale this process in a sustainable manner. Nickel-nitrogen-doped carbon (Ni-N-C) is an efficient catalyst for CO_2 reduction to CO, and the single-site Ni–N_x motif is believed to be the active site. However, critical metrics for its catalytic activity, such as active site density and intrinsic turnover frequency, so far lack systematic discussion. In this work, we prepared a set of covalent organic framework (COF)-derived Ni-N-C catalysts, for which the Ni–N_x content could be adjusted by the pyrolysis temperature. The combination of high-angle annular dark-field scanning transmission electron microscopy and extended X-ray absorption fine structure evidenced the presence of Ni single-sites, and quantitative X-ray photoemission addressed the relation between active site density and turnover frequency.

Introduction

The direct electrochemical CO_2 reduction reaction (CO_2RR) to value-added chemicals and fuels is a potential pathway to reduce CO_2 emissions.[1] However, the CO_2RR is commonly accompanied by water splitting; hence, the hydrogen evolution reaction (HER) is strongly competing.[2] Moreover, the CO_2RR process yields a wide range of carbon-based products as CO, formate, hydrocarbons, and oxygenates,[3] which require additional product separation in the practical implementation. Therefore, an affordable and selective catalyst is urgently needed to drive this electrochemical conversion efficiently.

In previous investigations, a great variety of catalysts have been studied for CO_2RR.[2a,4] Among them, the class of non-precious metal-nitrogen doped carbon (M-N-C) catalysts has received particular attention.[5] These catalysts feature graphene-embedded, single-site M–N_x structural motifs, which allow efficient CO_2 to CO conversion.[6] Unlike extended metal surfaces, the single-site M–N_x moieties in the M-N-C catalysts enable the suppression of the HER side reaction, yielding highly selective catalysis and high purity CO streams.[2b,6c,7] The Ni-functionalized versions (Ni-N-Cs) attracted attention due to their exceptional performance and selectivity to CO. Over 90 % CO selectivity could be achieved on these Ni-N-C catalysts, even at industry-relevant currents.[6a–e,g,8] Our current understanding of this catalytic reaction attributes this unique reactivity to the chemical nature of the embedded Ni–N_x motifs. A key hypothesis to explain the reactivity states that under CO_2RR conditions, the Ni–N_x site binds weakly to *H (diminished proton uptake competition) and *CO (minor CO poisoning issue), enabling the CO_2-to-CO cascade at

---

[*] C. Li,$^+$ J. Yang, P. Pachfule, A. Thomas
Department of Chemistry, Division of Functional Materials,
Technical University Berlin
Berlin 10623 (Germany)
E-mail: arne.thomas@tu-berlin.de

W. Ju,$^+$ K. Mou, X. Wang, S. Brückner, P. Strasser
Department of Chemistry, Chemical Engineering Division,
Technical University Berlin
Berlin 10623 (Germany)
E-mail: ju@tu-berlin.de
pstrasser@tu-berlin.de

S. Vijay, S.-C. Tsang, K. Chan
CatTheory, Department of Physics, Technical University of Denmark
2800 Kongens Lyngby (Denmark)

J. Timoshenko, H. S. Jeon, F. T. Haase, C. Rettenmaier, B. R. Cuenya
Interface Science Department, Fritz-Haber Institute of Max-Planck Society
Berlin 14195 (Germany)

D. A. Cullen
Center for Nanophase Materials Sciences, Oak Ridge National Laboratory
Oak Ridge, TN (USA)

[+] These authors contributed equally to this work.

© 2022 The Authors. Angewandte Chemie International Edition published by Wiley-VCH GmbH. This is an open access article under the terms of the Creative Commons Attribution License, which permits use, distribution and reproduction in any medium, provided the original work is properly cited.

15213773, 2022, 15, Downloaded from https://onlinelibrary.wiley.com/doi/10.1002/anie.202114707 by Danish Technical Knowledge, Wiley Online Library on [30/08/2023]. See the Terms and Conditions (https://onlinelibrary.wiley.com/terms-and-conditions) on Wiley Online Library for rules of use; OA articles are governed by the applicable Creative Commons License

reduced kinetic barriers. Therefore, a reasonable turnover frequency (TOF) could be realized at sufficiently applied cathode potentials.[6a,g] However, this hypothesis about the origin of the high catalytic reactivity still awaits experimental verification at the molecular level, nor has the Ni-N-C CO_2 to CO catalytic reactivity ever been fundamentally deconvoluted into the two basic kinetic descriptors of surface active site density (SD) and intrinsic TOF. This contribution will address these points.

In M-N-C single metal atom site electrocatalysts, carbon is the main constituent element. Its porous structure provides a large electrochemical surface area and tunable chemical composition, benefiting the loading of active M–N_x moieties. To date, a number of distinct synthesis strategies have been established to generate M-N-C catalysts. These strategies involve catalyst precursors as diverse as supported macrocyclic compounds,[6e,9] polymers,[7a] zeolitic imidazolate frameworks (ZIF),[10] or covalent and metal organic frameworks (COFs and MOFs, respectively).[6d,11]

Generally, the catalyst's apparent catalytic mass activity (MA) is contingent on two basic descriptors: the intrinsic catalytic TOF and the active SD. The MA is linked according to $MA = TOF \times SD$.[6f,12] To effectively improve the CO_2RR performance of M-N-C catalysts, one approach is to select the active site and a suitable potential window for an optimal TOF, while the other is to increase the effective SD. In previous studies on pyrolyzed M-N-C CO_2RR catalysts, only the active sites' nature (i.e., TOF-related) has been addressed, whereas the SD descriptor still lacks systematic exploration and discussion.

Herein, we study and unravel the molecular structure, composition, and CO_2 reduction reaction mechanism of new COF-derived Ni-N-Cs. The experimental MA of the Ni-N-C catalysts has been deconvoluted into SD and TOF of the surface-active Ni–N_x sites. Finally, these fundamental experimental descriptors have been correlated to corresponding computational results derived from first principle density functional theory (DFT). Through the first principle calculations and comparisons of intrinsic TOF and Tafel slopes, we were able to attribute the mean N coordination of the Ni–N_x motifs and conclude on the chemical structure of the active sites.

The COF precursor material in focus is a nitrogen-rich triazole-based COF (named TpDt-COF and TpDt-COF-Ni after Ni loading). In general, COFs are ideal materials to anchor coordinative metal sites precisely due to their ordered porous structure and tunable composition.[13] The structural features can be partially preserved when the metal-coordinated COF is heated to higher temperatures and carbonized.[13d] The COF-derived Ni-N-C catalysts are referred to as C-TpDt-Ni. After pyrolysis and acid washing, the catalyst C-TpDt-Ni-900 (treated at 900 °C) shows above 90 % faradaic CO efficiency at approximately 25 $mA\,cm^{-2}$ current density, measured in the regular liquid H-cell. High angle annular dark-field scanning transmission electron microscopy (HAADF-STEM) and extended X-ray absorption fine structure (EXAFS) were performed to evidence the single-atom nature of the Ni active sites. X-ray photoemission (XPS) analysis was carried out and yielded quantitative catalyst SD for the Ni-N-C catalysts. Linking the quantitative experimental fittings to DFT calculations and micro-kinetic modelling, a mechanistic relationship between the synthesis condition, SD, TOF, and their apparent MA for CO_2RR could be provided.

Synthesis and Characterization

Synthesis of the TpDt-COF-Ni Precursor

A triazole-based COF (TpDt-COF) was selected as the catalyst precursor because of its high nitrogen content.[14] The detailed synthesis route is given in the Supporting Information. In brief, the TpDt-framework was prepared by the condensation polymerization of 1,3,5-tri-formyl-phloroglucinol (Tp) and 3,5-diamino-1,2,4-triazole (Dt) via a solvothermal method (Figure 1a and Figure S1), delivering a nitrogen-rich COF backbone with high porosity. Ni impregnation was performed by dispersing the TpDt-COF in a $Ni(NO_3)_2 \cdot 6H_2O$ aqueous solution. The Ni ions can coordinate to the heteroatoms of the backbone and are thus uniformly dispersed in the COF. After removing excess Ni ions with distilled water, the TpDt-COF-Ni precursor was obtained.

TpDt-COF before Ni immobilization was characterized by several techniques (Figure S2 to S5). The specific N_2 sorption isotherms and the pore size distribution are presented in Figure S2a, b. The specific surface area (derived from the Brunnauer–Emmett–Teller theory, BET) reached 253 $m^2\,g^{-1}$, with a pore size of about 1.2 nm, which is close to the theoretical one. The successful synthesis allowed the facile incorporation and immobilization of Ni ions into the backbone. The scanning electron microscopy (SEM) image and the X-ray diffraction (XRD) pattern (Figure S2c, d) of TpDt-COF indicate a flake-like morphology and low crystallinity, consistent with the earlier reported COF.[14] From the Fourier transform infrared (FT-IR) spectra, the absence of aldehyde and amine groups stretching vibration in TpDt-COF implies a complete condensation (Figure S3).[14,15] As shown in the ^{13}C solid-state nuclear magnetic resonance (NMR) profile, the characteristic signals of C–N bond at ≈149 ppm, C=C bond at ≈108 ppm, and carbonyl carbon (C=O) at ≈184 ppm corroborated the formation of β-ketone-amine structure (Figure S4). The thermogravimetric analysis (TGA) showed the gradual decomposition of TpDt-COF after 400 °C (Figure S5).

Synthesis of the C-TpDt-Ni Catalyst

TpDt-COF provides a unique structure to immobilize Ni–N_x functionalities; however, COFs notoriously suffer from low electric conductivity. Therefore, thermal annealing was used to carbonize the framework. The heat treatment of the TpDt-Ni was conducted under inert gas (N_2) and followed by an acid washing protocol (to remove formed exposed Ni particles). The pyrolysis temperature was changed from 800 °C, 900 °C, to 1000 °C to obtain a series of distinct

© 2022 The Authors. Angewandte Chemie International Edition published by Wiley-VCH GmbH

15213773, 2022, 15, Downloaded from https://onlinelibrary.wiley.com/doi/10.1002/anie.202114707 by Danish Technical Knowledge, Wiley Online Library on [30/08/2023]. See the Terms and Conditions (https://onlinelibrary.wiley.com/terms-and-conditions) on Wiley Online Library for rules of use; OA articles are governed by the applicable Creative Commons License

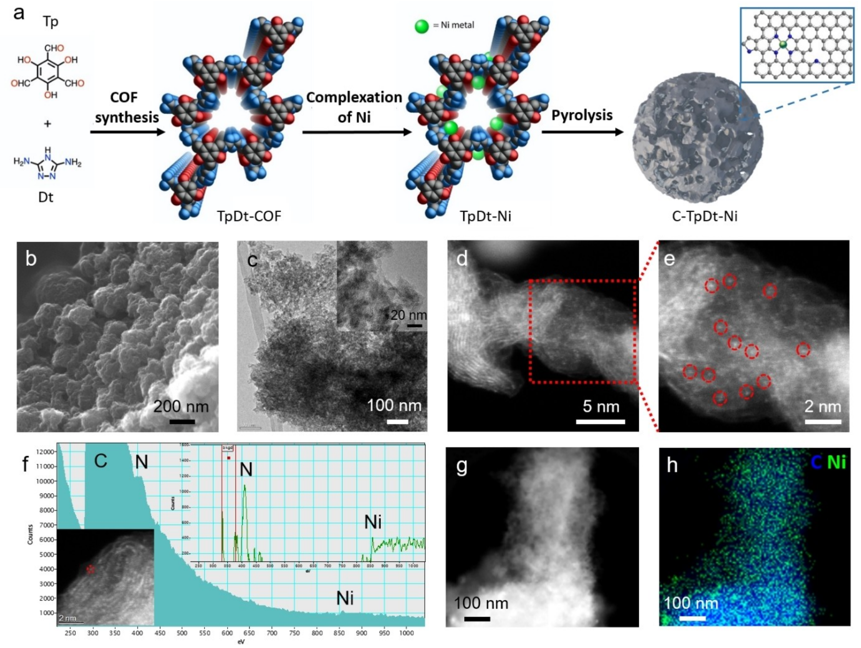

Figure 1. a) Scheme for the synthesis of C-TpDt-Ni (carbon atoms are shown in grey, nitrogen in blue, oxygen in red, Ni in green; hydrogen atoms are not shown). b) SEM image and c) TEM image of C-TpDt-Ni-900. d, e) High-resolution HAADF-STEM image of C-TpDt-Ni-900. f) EELS spectrum acquired at Ni single-atom region circled in red. g, h) HAADF-STEM image and corresponding EDS mapping image of C-TpDt-Ni-900.

carbonized C-TpDt-Ni as CO_2RR catalysts. The synthesis protocol is shown in Figure 1a.

Synthesis of Additional Reference Catalysts

Besides the C-TpDt-Ni catalysts, additional Ni-N-C materials were prepared as references. An additional COF-derived catalyst was synthesized via an analogous protocol but using a different linker, para-phenylene-diamine (Pa, instead of Dt, see Figure S6a). Identical post-treatments were done on this TpPa-COF, and the pyrolysis temperature was selected to be 900 °C for the final catalyst, named C-TpPa-Ni-900. The unpyrolyzed TpPa-COF framework shows a surface area of 571 $m^2 g^{-1}$ and also high crystallinity. However, the BET surface area drops to 135 $m^2 g^{-1}$ after pyrolysis and acid washing (Figure S6, Table S1). Furthermore, a carbon nanotube supported Ni-phthalocyanine (NiPc/CNT), and our previously studied polyaniline derived PANI-Ni-900 were involved in our experimental comparison (synthesis details are represented in the Supporting Information).

Characterization

The morphology of the pyrolyzed C-TpDt-Ni was investigated using scanning electron microscopy (SEM) and transmission electron microscopy (TEM). As shown in Figure 1b, c and Figure S7, the nanosheets of TpDt-COF fused to form porous particles, showing the co-existence of micropores and mesopores. In addition, a small amount of Ni metal particles was observed in C-TpDt-Ni by low magnification TEM measurement (Figure S8). Considering those particles are encapsulated in an approximately 3 nm carbon shell (Figure S8b, unreachable in acid washing), they would only play a minor role during the electrolysis.[10b,16] The BET surface area of the C-TpDt-Ni samples decreased to ≈190 $m^2 g^{-1}$ after pyrolysis/acid-washing, caused by the structural changes during carbonization (pore-collapse or sheet-distortion, details are given in Figure S9 and Table S1).

HAADF-STEM was applied to analyze the structure and surface composition of C-TpDt-Ni-800 and C-TpDt-Ni-900 samples. The STEM (Figure 1d, e and Figure S10a–c) images evidence graphitized carbon layers and directly proved the existence of atomically dispersed Ni sites (highlighted by red dashed circles) in both pyrolyzed samples.

© 2022 The Authors. Angewandte Chemie International Edition published by Wiley-VCH GmbH

15213773, 2022, 15, Downloaded from https://onlinelibrary.wiley.com/doi/10.1002/anie.202114707 by Danish Technical Knowledge, Wiley Online Library on [30/08/2023]. See the Terms and Conditions (https://onlinelibrary.wiley.com/terms-and-conditions) on Wiley Online Library for rules of use; OA articles are governed by the applicable Creative Commons License

For the sample treated at 900 °C, the electron energy loss spectrum (EELS) was measured at one single Ni atom location, and a Ni-N_4-C matrix-like surrounding could be observed (Figure 1f).[17] HAADF-STEM images with other scale and corresponding energy-dispersive X-ray spectroscopy (EDS) mapping are shown in Figure 1g,h, proving Ni and N elements′ homogeneous distribution.

The XRD patterns of the catalysts are summarized in Figure S11. All samples exhibited a pronounced Bragg peak at around 26°, assigned to the (002) plane of graphitic carbon. For the C-TpDt-Ni samples, the peak at 26° became sharper with increasing pyrolysis temperature, suggesting an increasing graphitization degree. A weak diffraction peak at 44° is observed in the catalysts obtained at 900 and 1000 °C (C-TpDt-Ni-900 and C-TpDt-Ni-1000), which can be assigned to the (111) plane of Ni metal species. This stands in line with the TEM images of the samples (Figure S8a). As expected, the electronic conductivity of TpDt-derived catalysts, measured using a 4-probe sensing, increased with increasing temperature (Table S2). The chemical state and elemental composition of the catalyst surface were analyzed using X-ray photoelectron spectroscopy (XPS), and the profiles are plotted in Figure S12 (Table S3–S5). The analysis of carbon 1s, nitrogen 1s spectra are given in the Supporting Information. In Figure S12c, the XPS profiles of the Ni2$p_{3/2}$ core level range are presented, which indicate the chemical state and amount of Ni at the surface. Different groups were assigned according to their central 2$p_{3/2}$ photoemission peak positions (Group 0: 852.6 ± 0.2 eV, Ni^0; Group I: 854.4 ± 0.2 eV, Ni^+-like; Group II: 855.3 ± 0.2 eV, Ni^{2+}; and the satellite region: > 856.5 eV).[7b,8,18] In the pristine TpDt-Ni sample, the apparent satellite intensity suggests the prevalence of Ni in its +2 state.[19] After pyrolysis, the intensity of Ni^0 species slightly increased (see 900 °C), which can be attributed to the formed carbon-encapsulated Ni nanoparticles (Figure S8). However, in all pyrolyzed samples, Ni^{2+} and Ni^+-like remained the dominant species. Due to the removal of all unencapsulated metallic Ni species by acid washing, we conclude that both the Ni^{2+} and Ni^+-like states in the pyrolyzed samples indicate the presence of single metal atom site Ni–N_x moieties, which are believed to serve as catalytic active sites. Accordingly, we estimate the Ni–N_x sites ratios ($\%_{\mathrm{at.}}$) on the surface via Equation (1) (Figure S13c) and extract the exposed SDs in combination with BET area-weight surface [Eq. (2) and Figure S13d].

$$x_{\mathrm{Ni-N}_x}\%_{at.} = x_{\mathrm{Ni}^{+}}\%_{\mathrm{at.}} + x_{\mathrm{Ni}^{2+}}\%_{\mathrm{at.}} \tag{1}$$

$$\mathrm{SD}_{\mathrm{Ni-N}_x} = x_{\mathrm{Ni-N}_x}\%_{\mathrm{at.}} \times A_{\mathrm{BET}} \tag{2}$$

Furthermore, the bulk Ni content of the catalysts was determined by inductively coupled plasma mass spectroscopy (ICP-MS), and yielded 5.0 wt%, 7.6 wt%, and 0.8 wt % for C-TpDt-Ni-800, C-TpDt-Ni-900, and C-TpDt-Ni-1000, respectively. Altogether, the TpDt-Ni-900 sample provides a higher SD than other carbonized COF counterparts (Figure S13).

X-ray Absorption Spectra

To explore the local molecular structure of the Ni–N_x motif, the catalysts were investigated using X-ray absorption near-edge structure (XANES) and extended X-ray absorption fine structure (EXAFS) spectroscopies at Ni K-edge coupled to a wavelet transformed EXAFS analysis. For reference, the measurements were carried out also on Ni foil, NiO, and NiPc.

The collected normalized Ni K-edge XANES spectra are compared in Figure 2a. The significant difference between the spectra for unpyrolyzed (TpDt-Ni) and pyrolyzed (C-TpDt-Ni-800 and C-TpDt-Ni-900) samples is evident immediately. The spectrum of the unpyrolyzed sample resembles that of rocksalt-type NiO, suggesting a +2-oxidation state and an octahedral coordination of Ni in this sample. On the other hand, the spectra for the pyrolyzed samples are more similar to the spectrum of the NiPc reference sample. In particular, the prominent feature at ca. 8337 eV is a fingerprint of a square-planar Ni–N_4 configuration with $D4_h$ symmetry in porphyrin-like structures located in di-vacancy (DV).[16,20] In the Ni-based catalysts, this feature is also clearly present even though is reduced in intensity in comparison to NiPc. This is in agreement with previous reports in the literature,[16,21] suggesting that the structure of the pyrolyzed catalysts is significantly disordered. The XANES spectra for samples pyrolyzed at 800 and 900 °C, respectively are quite similar. Still, one can note that for the sample pyrolyzed at 900 °C, the XANES spectrum is shifted slightly towards lower energies, e.g., closer to the metallic Ni spectrum, which could be an indication of the formation of metallic Ni clusters. All these findings are in line with the above-described TEM and XPS analyses.

We performed linear combination fitting of the XANES spectra to quantify this trend by using spectra for metallic Ni foil and NiPc as references (Figure S14). Due to the significant differences between the local Ni structures in the catalyst samples and the reference samples, the linear combinations of reference spectra do not describe the XANES spectra for the catalysts perfectly. Still, one can estimate from such a fitting that the contribution of metallic Ni increases from ca. 15 % in the sample pyrolyzed at 800 °C to ca. 28 % in the sample pyrolyzed at 900 °C.

Fourier transforms (FT) of extracted EXAFS spectra (Figure S15) for Ni catalysts and the reference samples are shown in Figure 2b. For all catalyst samples, the EXAFS signal is dominated by the first coordination shell contribution (peak in FT-EXAFS between 1 and 2 Å (phase-uncorrected)), corresponding to the Ni bonding to low Z elements (e.g., oxygen, carbon, or nitrogen). However, one can note a difference in the main FT-EXAFS peak position for the pyrolyzed and unpyrolyzed samples. In the former case, the maximum peak is located at lower R values, and it aligns well with the first shell peak (corresponding to Ni–N bond) in the reference spectrum for NiPc. For the unpyrolyzed sample, the maximum of the main FT-EXAFS peak is shifted to slightly larger R values. This peak position and intensity are thus comparable to that of Ni–O contribution in the NiO spectrum.

© 2022 The Authors. Angewandte Chemie International Edition published by Wiley-VCH GmbH

15213773, 2022, 15, Downloaded from https://onlinelibrary.wiley.com/doi/10.1002/anie.202114707 by Danish Technical Knowledge, Wiley Online Library on [30/08/2023]. See the Terms and Conditions (https://onlinelibrary.wiley.com/terms-and-conditions) on Wiley Online Library for rules of use; OA articles are governed by the applicable Creative Commons License

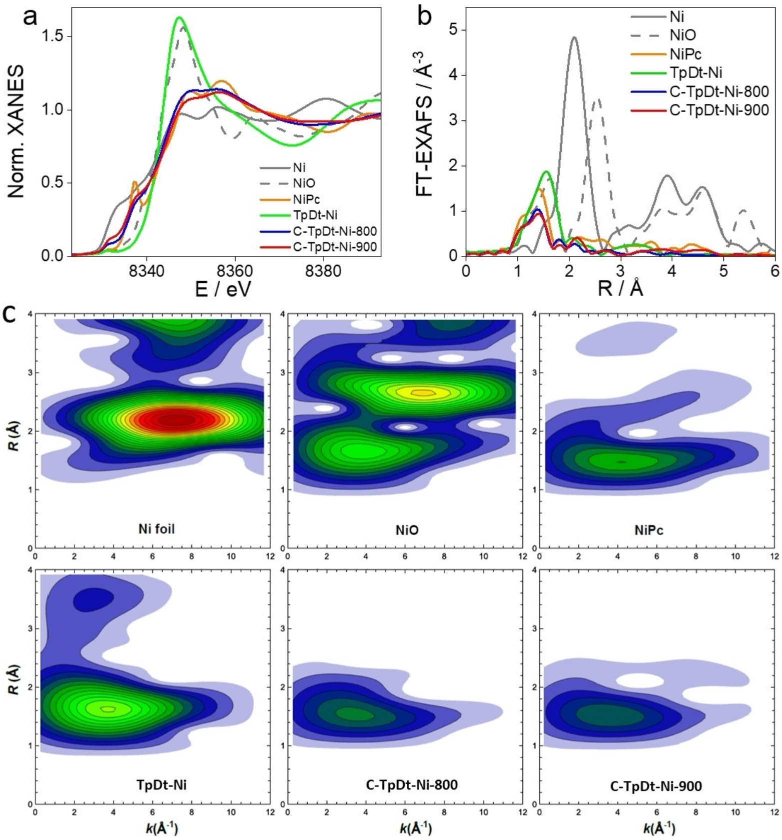

Figure 2. a) Normalized Ni K-edge XANES spectra, b) absolute values of Fourier-transformed (FT)-EXAFS spectra, and c) absolute values of wavelet transformed (WT)-EXAFS spectra for Ni foil, NiO, NiPc, TpDt-Ni, C-TpDt-Ni-800 and C-TpDt-Ni-900. The structure parameters obtained from EXAFS data fitting are presented in Table S6.

In all FT-EXAFS spectra, the weaker peaks at R values between ca. 2 and 4 Å are also observed. For visualization and interpretation of these contributions, it is convenient to use the Morlet wavelet transform (WT).[22] WT-EXAFS spectra for Ni catalysts and reference samples are shown in Figure 2c. First, for the unpyrolyzed TpDt-Ni, it can be observed that the position of the main maximum in the WT-EXAFS map (corresponding to the 1st coordination shell), not only in R-space but also in k-space matches well to that of Ni–O contribution in the NiO reference spectrum, which are seen at a R-value of ca. 1.6 Å, and k value of ca. 3.5 Å^{-1}. Furthermore, the second WT-EXAFS peak at a R-value of ca. 3.4 Å has a maximum at a similar k value. From this, we conclude that this contribution at higher R-values is also associated with photoelectron interactions with low Z elements (N, C, or O) and maybe even a result of multiple scattering events within the first coordination shell. The low amplitude of this feature and the absence of peaks at higher R-values suggest a lack of long-range order and a disordered local environment around Ni in the unpyrolyzed sample. Lack of contributions at higher k-values confirms the absence of a significant amount of metallic Ni clusters in this sample. Nevertheless, one should note that caution is needed when interpreting the lack of distant coordination contribution as evidence for the single-atom nature of the catalyst, and the presence of small amounts of disordered larger clusters cannot be completely ruled out.[23]

For the pyrolyzed C-TpDt-Ni samples, WT-EXAFS is dominated by the maximum at k-value ca. 3.5–4 Å^{-1} and R-value ca. 1.5 Å, which aligns well with that of Ni–N

© 2022 The Authors. Angewandte Chemie International Edition published by Wiley-VCH GmbH

15213773, 2022, 15, Downloaded from https://onlinelibrary.wiley.com/doi/10.1002/anie.202114707 by Danish Technical Knowledge, Wiley Online Library on [30/08/2023]. See the Terms and Conditions (https://onlinelibrary.wiley.com/terms-and-conditions) on Wiley Online Library for rules of use; OA articles are governed by the applicable Creative Commons License

contribution in NiPc. Significantly, upon increasing pyrolysis temperature, a second feature is gradually developed at *k* value ca. 8 Å^{-1} and *R*-value ca. 2.2 Å, which strongly resembles the Ni–Ni contribution in metallic Ni. The WT-EXAFS spectra thus reveal the formation of metallic clusters at higher pyrolysis temperatures.

Electrochemical CO_2RR Activity Evaluation: TOF vs. SD

The CO_2RR performance of our studied COF-derived Ni-N-C catalysts was assessed in a liquid phase three-electrode H-cell. The testing potential varied from $-0.4\ V_{RHE}$ to $-0.9\ V_{RHE}$, and each electrolysis condition was kept stationary for 15 min for gas analysis. CO and H_2 contribute as the main products during the bulk reaction. No liquid products were detected after the bulk electrolysis. Overall, all our tested Ni-based (together with all references) catalysts show their dominant selectivity to CO; however, they deliver deviated mass-based activity.

The unpyrolyzed TpDt-Ni shows negligible CO_2RR reactivity, while the thermal treatment switches on the CO_2 conversion to CO. The C-TpDt-Ni-900 (pyrolyzed at 900 °C) sample reached over 90 % FE_{CO} at $-0.7\ V_{RHE}$, delivering about 22 mA cm^{-2} CO partial current density. The sample treated at 800 °C shows comparable but slightly lower performance. By contrast, the C-TpDt-Ni-1000 delivers only 2/3 of the HER and CO_2RR activity as the catalysts pyrolyzed at lower temperatures. All those outperform the C-TpPa-Ni-900 one, prepared using the precursor with less nitrogen content (Figure 3).

The distinct CO_2RR reactivity and selectivity values of the individual Ni-N-C catalysts are a sensitive function of, on the one hand, their molecular nature and intrinsic reactivity (TOF) and, on the other hand, their surface SD of catalytic active $Ni–N_x$ moieties on the catalyst surface. In previous works, individual TOF and SD values remained convoluted and have not been properly disentangled, which is one reason why their accurate correlation to theoretical reactivity data has remained challenging and elusive. Here, we normalized the apparent CO activity to the SD values [from Eq. (2)] and obtained intrinsic kinetic TOF values [Eq. (S5)].

The extracted experimental intrinsic CO-specific TOFs of the various Ni-N-C catalysts from -0.4 to $-0.85\ V_{RHE}$ (kinetic region) are displayed in Figure 4a. Although this set of Ni-N-C catalysts were pyrolyzed at different temperatures during their preparation and displayed dissimilar FE values and partial current densities, after normalization of the apparent current densities using the extracted SD values, very similar intrinsic TOF trends ensued within. Furthermore, very similar TOF is observed on the molecular-derived NiPc/CNT and the solid-state PANI-Ni reference catalysts. This finding suggests that the intrinsic catalytic behavior may be controlled by one dominant common site motif present in all materials.

To understand the TOF trends on the molecular scale, we separated the potential dependent TOF into two regions. From -0.4 to $-0.75\ V_{RHE}$, the CO production is primarily

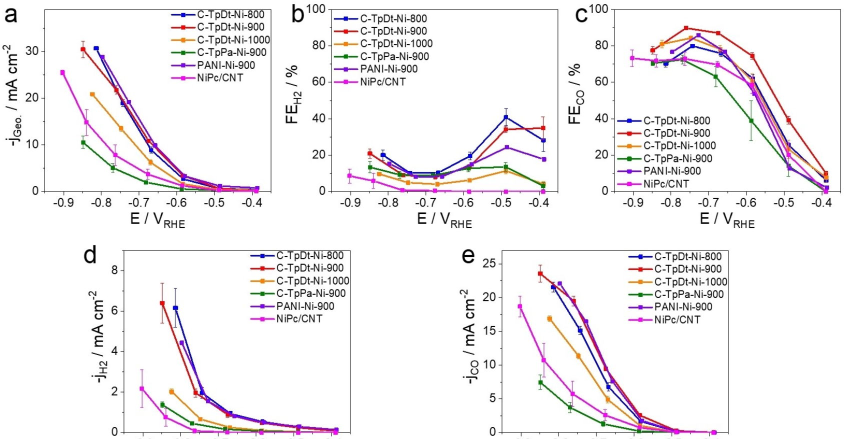

Figure 3. The electrochemical performance of various COF-derived Ni-N-C and reference catalysts. a) Geometric current densities, b) Faradaic efficiency of H_2, c) Faradaic efficiency of CO, d) geometric H_2 partial current densities, and e) geometric CO partial current densities as functions of IR-corrected potential. Calculations are described in Supporting Information (Eq S1–S4). The catalyst loading is 1 mg cm^{-2} on Freudenberg C2H23 carbon paper. The electrolyte is CO_2-saturated 0.5 M $KHCO_3$ solution (pH 7.3). The product analysis is done after 15 min of each bulk electrolysis. Presented data is standard mean and deviation from 3 measurements.

© 2022 The Authors. Angewandte Chemie International Edition published by Wiley-VCH GmbH

15213773, 2022, 15, Downloaded from https://onlinelibrary.wiley.com/doi/10.1002/anie.202114707 by Danish Technical Knowledge, Wiley Online Library on [30/08/2023]. See the Terms and Conditions (https://onlinelibrary.wiley.com/terms-and-conditions) on Wiley Online Library for rules of use; OA articles are governed by the applicable Creative Commons License

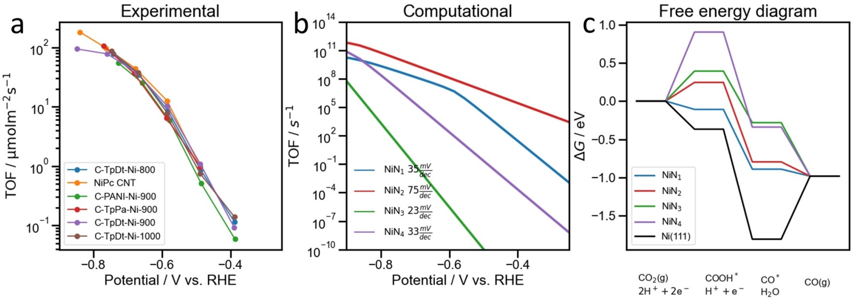

Figure 4. a) The experimentally derived CO turnover frequency (TOF) from −0.4 to −0.85 V_{RHE}, normalized by Ni–N$_x$ site density (SD). Apparent Tafel slopes are approximately 100 mV dec.$^{-1}$ b) Theoretical TOF obtained from a micro-kinetic model of the CO_2(g) to CO(g) electro-reduction process (calculation detailed in Supporting Information). c) The free energy diagram of CO_2RR from CO_2(g) to CO(g) on various DV-Ni–N$_x$ ($x=1$, 2, 3, 4) motifs and Ni(111) facet at −0.8 V_{SHE} in pH 4. The projected density of state (PDOS) plots of all studied Ni–N$_x$ motifs are displayed in Figure S16.

controlled by the applied electrode potential. Here, the nearly overlapping TOF-potential trends of the tested catalysts imply a similar kinetic reaction barrier: the binding energy to the COOH* intermediate.[24] DFT calculations show the trends on various simplified DV Ni–N$_x$ ($x=1$, 2, 3, 4) motifs, and the Ni(111) facet. Displayed in Figure 4c, the nitrogen coordination number significantly affects the COOH* binding and leads to distinct theoretical TOF-potential trend lines (Figure 4b). Instead, in experiments, all TOF values followed a similar trend as the CNT-supported molecular NiPc (Figure 4a). Therefore, the experimentally observed TOF trends seem to originate predominantly from the fully embedded Ni–N$_4$ coordination.

Furthermore, looking at larger cathodic potentials (beyond −0.7 V_{RHE}, shown in Figure 3e) the C-TpDt-Ni-900 electrocatalyst was the first to enter a CO_2 mass transport-limited reaction regime. By plotting the faradaic CO efficiency as a function of the current strength, the FE_{CO} of all catalysts appears to reach or pass through a plateau beyond 20 mA cm^{-2} (Figure S17a). We attribute this to in-pore CO_2 transfer limitations, where densely spaced active sites generate a high local pH. The in-pores OH^- convert CO_2 in equilibrium reactions to bicarbonate, causing rapid locally non-electrochemical (acid-base) CO_2 depletion (scheme displayed in Figure S17b).

Conclusion

In this contribution, we synthesized a set of novel TpDt-COF-derived Ni-N-C single metal atom site catalysts. Even though harsh synthetic steps such as pyrolysis and acid washing were performed, the Ni-N-Cs derived from TpDT-COF at different temperatures exhibit similar surface areas, microporous structures, and comparable surface chemical composition, while their Ni–N$_x$ site densities are largely different. This provides reliable materials basis to study the mass activity of catalysts regarding the two descriptors, intrinsic active site activity vs. number of active sites (TOF vs. SD).

Based on this family of Ni-N-C catalysts, we investigated reactivity trends and provided a new molecular understanding of the CO_2 to CO reduction reactivity. What sets this work apart from earlier ones is that we deconvolute the usually reported apparent experimental CO_2-to-CO geometric- or else mass-based catalyst activity into two relevant descriptors, SD and TOF. Moreover, we correlated synthesis conditions with TOF values and compared experimental trends with computational DFT-derived ones. Various characterization techniques (TEM, HAADF-STEM, BET, XPS, XAS) identified and quantified the active Ni–N$_x$ sites, while, in parallel, DFT-derived Gibbs free energy diagram guided our understanding of the reaction kinetics from the atomic level.

We found that the apparent CO_2-to-CO mass activities were highly dependent on the SD values, dominated by the synthesis details (i.e., annealing temperatures). By contrast, TOF was affected by synthesis conditions to a much lesser degree. When aiming at high apparent CO_2-to-CO activities, it can be thus suggested to apply sp^2-N rich precursors, as seen for the used COF precursor, as this can largely enhance the amount of Ni ion coordinated in the final N-doped carbon, thus increasing the SD. Later, the annealing temperature plays multiple roles. On the one hand, higher temperature improves the catalyst conductivity and accelerates the Ni–N$_x$ moieties formation, showing to be positive for the catalytic performance. On the other hand, higher temperatures also reduce the amount of nitrogen within the carbon framework, resulting in a lower amount of formed Ni–N$_x$ species. For the present materials, 900 °C turned out to be ideal pyrolysis temperature for optimizing the SD and conductivity of the catalysts. Further towards their intrinsic activity, the Tafel slope comparisons between experiment and theory suggested the presence and the predominant catalytic contribution of the DV Ni–N$_4$ sites, evidenced in our absorption and photoemission studies.

© 2022 The Authors. Angewandte Chemie International Edition published by Wiley-VCH GmbH

15213773, 2022, 15, Downloaded from https://onlinelibrary.wiley.com/doi/10.1002/anie.202114707 by Danish Technical Knowledge, Wiley Online Library on [30/08/2023]. See the Terms and Conditions (https://onlinelibrary.wiley.com/terms-and-conditions) on Wiley Online Library for rules of use; OA articles are governed by the applicable Creative Commons License

In the high current density region, the TOF values saturated for the high-SD catalysts, which is attributed to the local CO_2 concentration depletion due to the high local OH^- concentration. As reported recently, using a rotating electrode or more acidic media could neutralize the surface pH, ensuring the CO_2 transfer to the catalyst surface.[25] Moreover, controlling the inner-particle pore size (of the catalyst) and inter-particle pore size (of the manufactured catalyst layer) tends to be a practical approach. To our hypothesis, the broader interfacial pores may accelerate the OH^- removal, maintaining the CO_2 incoming at high current densities.

Acknowledgements

The research leading to these results has received funding from the European Union's Horizon 2020 research and innovation program under grant agreement No 851441, SELECTCO2. Partial funding by the Deutsche Forschungsgemeinschaft (DFG, German Research Foundation) under Germany's Excellence Strategy—EXC 2008/1 (UniSysCat)—390540038 is acknowledged. We also acknowledge the financial support from the China Scholarship Council (CSC). We thank VILLUM Centre for the Science of Sustainable Fuels and Chemicals (no. 9455) from VILLUM FONDEN. We thank Christina Eichenauer for assisting in N_2 sorption and TGA measurements and Maria Unterweger for conducting XRD measurements. A portion of this research was conducted at ORNL's Center for Nanophase Materials Sciences, a DOE Office of Science User Facility. We acknowledge DESY (Hamburg, Germany), a member of the Helmholtz Association HGF, for the provision of experimental facilities. Parts of this research were carried out at PETRA-III and we would like to thank Dr. Vadin Murzin and Dr. Wolfgang Caliebe for assistance in using P64 beamline. Open Access funding enabled and organized by Projekt DEAL.

Conflict of Interest

The authors declare no competing financial interest.

Data Availability Statement

The data that support the findings of this study are available from the corresponding author upon reasonable request.

Keywords: Active Site Density · CO2 Reduction · Covalent Organic Framework · Single-Site Ni-N-C · Turnover Frequency

---

[1] D. T. Whipple, P. J. A. Kenis, *J. Phys. Chem. Lett.* **2010**, *1*, 3451–3458.

[2] a) Y. Hori in *Modern Aspects of Electrochemistry* (Eds.: C. G. Vayenas, R. E. White, M. E. Gamboa-Aldeco), Springer New York, New York, **2008**, pp. 89–189; b) A. Bagger, W. Ju, A. S. Varela, P. Strasser, J. Rossmeisl, *Catal. Today* **2017**, *288*, 74–78.

[3] Y. Hori, A. Murata, R. Takahashi, *J. Chem. Soc. Faraday Trans. 1* **1989**, *85*, 2309–2326.

[4] a) A. S. Varela, W. Ju, P. Strasser, *Adv. Energy Mater.* **2018**, *8*, 1703614; b) H. Mistry, A. S. Varela, S. Kühl, P. Strasser, B. R. Cuenya, *Nat. Rev. Mater.* **2016**, *1*, 16009; c) W. Ju, A. Bagger, N. Leonard, X. Wang, J. Rossmeisl, P. Strasser in *Carbon Dioxide Electrochemistry: Homogeneous and Heterogeneous Catalysis*, The Royal Society of Chemistry, London, **2021**, pp. 151–196.

[5] A. S. Varela, N. Ranjbar Sahraie, J. Steinberg, W. Ju, H.-S. Oh, P. Strasser, *Angew. Chem. Int. Ed.* **2015**, *54*, 10758–10762; *Angew. Chem.* **2015**, *127*, 10908–10912.

[6] a) W. Ju, A. Bagger, G.-P. Hao, A. S. Varela, I. Sinev, V. Bon, B. Roldan Cuenya, S. Kaskel, J. Rossmeisl, P. Strasser, *Nat. Commun.* **2017**, *8*, 944; b) X. Li, W. Bi, M. Chen, Y. Sun, H. Ju, W. Yan, J. Zhu, X. Wu, W. Chu, C. Wu, Y. Xie, *J. Am. Chem. Soc.* **2017**, *139*, 14889–14892; c) K. Jiang, S. Siahrostami, T. Zheng, Y. Hu, S. Hwang, E. Stavitski, Y. Peng, J. Dynes, M. Gangisetty, D. Su, K. Attenkofer, H. Wang, *Energy Environ. Sci.* **2018**, *11*, 893–903; d) P. Su, K. Iwase, T. Harada, K. Kamiya, S. Nakanishi, *Chem. Sci.* **2018**, *9*, 3941–3947; e) M. Wang, K. Torbensen, D. Salvatore, S. Ren, D. Joulié, F. Dumoulin, D. Mendoza, B. Lassalle-Kaiser, U. Işci, C. P. Berlinguette, M. Robert, *Nat. Commun.* **2019**, *10*, 3602; f) N. Leonard, W. Ju, I. Sinev, J. Steinberg, F. Luo, A. S. Varela, B. Roldan Cuenya, P. Strasser, *Chem. Sci.* **2018**, *9*, 5064–5073; g) K. Jiang, S. Siahrostami, A. J. Akey, Y. Li, Z. Lu, J. Lattimer, Y. Hu, C. Stokes, M. Gangishetty, G. Chen, Y. Zhou, W. Hill, W.-B. Cai, D. Bell, K. Chan, J. K. Nørskov, Y. Cui, H. Wang, *Chem* **2017**, *3*, 950–960.

[7] a) T. Möller, W. Ju, A. Bagger, X. Wang, F. Luo, T. Ngo Thanh, A. S. Varela, J. Rossmeisl, P. Strasser, *Energy Environ. Sci.* **2019**, *12*, 640–647; b) H. B. Yang, S.-F. Hung, S. Liu, K. Yuan, S. Miao, L. Zhang, X. Huang, H.-Y. Wang, W. Cai, R. Chen, J. Gao, X. Yang, W. Chen, Y. Huang, H. M. Chen, C. M. Li, T. Zhang, B. Liu, *Nat. Energy* **2018**, *3*, 140–147; c) W. Ju, A. Bagger, X. Wang, Y. Tsai, F. Luo, T. Möller, H. Wang, J. Rossmeisl, A. S. Varela, P. Strasser, *ACS Energy Lett.* **2019**, *4*, 1663–1671.

[8] S. Liu, H. B. Yang, S.-F. Hung, J. Ding, W. Cai, L. Liu, J. Gao, X. Li, X. Ren, Z. Kuang, Y. Huang, T. Zhang, B. Liu, *Angew. Chem. Int. Ed.* **2020**, *59*, 798–803; *Angew. Chem.* **2020**, *132*, 808–813.

[9] a) Q. Wu, R.-K. Xie, M.-J. Mao, G.-L. Chai, J.-D. Yi, S.-S. Zhao, Y.-B. Huang, R. Cao, *ACS Energy Lett.* **2020**, *5*, 1005–1012; b) X. Zhang, Y. Wang, M. Gu, M. Wang, Z. Zhang, W. Pan, Z. Jiang, H. Zheng, M. Lucero, H. Wang, G. E. Sterbinsky, Q. Ma, Y.-G. Wang, Z. Feng, J. Li, H. Dai, Y. Liang, *Nat. Energy* **2020**, *5*, 684–692.

[10] a) H. Zhang, S. Hwang, M. Wang, Z. Feng, S. Karakalos, L. Luo, Z. Qiao, X. Xie, C. Wang, D. Su, Y. Shao, G. Wu, *J. Am. Chem. Soc.* **2017**, *139*, 14143–14149; b) H. Zhang, H. T. Chung, D. A. Cullen, S. Wagner, U. I. Kramm, K. L. More, P. Zelenay, G. Wu, *Energy Environ. Sci.* **2019**, *12*, 2548–2558; c) S. Mukherjee, X. Yang, W. Shan, W. Samarakoon, S. Karakalos, D. A. Cullen, K. More, M. Wang, Z. Feng, G. Wang, G. Wu, *Small Methods* **2020**, *4*, 1900821; d) T. N. Huan, N. Ranjbar, G. Rousse, M. Sougrati, A. Zitolo, V. Mougel, F. Jaouen, M. Fontecave, *ACS Catal.* **2017**, *7*, 1520–1525.

[11] C. Yan, H. Li, Y. Ye, H. Wu, F. Cai, R. Si, J. Xiao, S. Miao, S. Xie, F. Yang, Y. Li, G. Wang, X. Bao, *Energy Environ. Sci.* **2018**, *11*, 1204–1210.

[12] a) N. D. Leonard, S. Wagner, F. Luo, J. Steinberg, W. Ju, N. Weidler, H. Wang, U. I. Kramm, P. Strasser, *ACS Catal.* **2018**, *8*, 1640–1647; b) F. Luo, S. Wagner, I. Onishi, S. Selve, S. Li,

15213773, 2022, 15, Downloaded from https://onlinelibrary.wiley.com/doi/10.1002/anie.202114707 by Danish Technical Knowledge, Wiley Online Library on [30/08/2023]. See the Terms and Conditions (https://onlinelibrary.wiley.com/terms-and-conditions) on Wiley Online Library for rules of use; OA articles are governed by the applicable Creative Commons License

W. Ju, H. Wang, J. Steinberg, A. Thomas, U. I. Kramm, P. Strasser, *Chem. Sci.* **2021**, *12*, 384–396; c) M. Primbs, Y. Sun, A. Roy, D. Malko, A. Mehmood, M.-T. Sougrati, P.-Y. Blanchard, G. Granozzi, T. Kosmala, G. Daniel, P. Atanassov, J. Sharman, C. Durante, A. Kucernak, D. Jones, F. Jaouen, P. Strasser, *Energy Environ. Sci.* **2020**, *13*, 2480–2500.

[13] a) S. Lin, C. S. Diercks, Y.-B. Zhang, N. Kornienko, E. M. Nichols, Y. Zhao, A. R. Paris, D. Kim, P. Yang, O. M. Yaghi, C. J. Chang, *Science* **2015**, *349*, 1208–1213; b) C. S. Diercks, S. Lin, N. Kornienko, E. A. Kapustin, E. M. Nichols, C. Zhu, Y. Zhao, C. J. Chang, O. M. Yaghi, *J. Am. Chem. Soc.* **2018**, *140*, 1116–1122; c) X. Zhao, P. Pachfule, S. Li, T. Langenhahn, M. Ye, C. Schlesiger, S. Praetz, J. Schmidt, A. Thomas, *J. Am. Chem. Soc.* **2019**, *141*, 6623–6630; d) X. Zhao, P. Pachfule, S. Li, T. Langenhahn, M. Ye, G. Tian, J. Schmidt, A. Thomas, *Chem. Mater.* **2019**, *31*, 3274–3280; e) H.-J. Zhu, M. Lu, Y.-R. Wang, S.-J. Yao, M. Zhang, Y.-H. Kan, J. Liu, Y. Chen, S.-L. Li, Y.-Q. Lan, *Nat. Commun.* **2020**, *11*, 497.

[14] S. Haldar, K. Roy, S. Nandi, D. Chakraborty, D. Puthusseri, Y. Gawli, S. Ogale, R. Vaidhyanathan, *Adv. Energy Mater.* **2018**, *8*, 1702170.

[15] a) P. Pachfule, A. Acharjya, J. Roeser, T. Langenhahn, M. Schwarze, R. Schomäcker, A. Thomas, J. Schmidt, *J. Am. Chem. Soc.* **2018**, *140*, 1423–1427; b) C. Li, J. Yang, P. Pachfule, S. Li, M.-Y. Ye, J. Schmidt, A. Thomas, *Nat. Commun.* **2020**, *11*, 4712.

[16] D. M. Koshy, S. Chen, D. U. Lee, M. B. Stevens, A. M. Abdellah, S. M. Dull, G. Chen, D. Nordlund, A. Gallo, C. Hahn, D. C. Higgins, Z. Bao, T. F. Jaramillo, *Angew. Chem. Int. Ed.* **2020**, *59*, 4043–4050; *Angew. Chem.* **2020**, *132*, 4072–4079.

[17] W. Zheng, J. Yang, H. Chen, Y. Hou, Q. Wang, M. Gu, F. He, Y. Xia, Z. Xia, Z. Li, B. Yang, L. Lei, C. Yuan, Q. He, M. Qiu, X. Feng, *Adv. Funct. Mater.* **2020**, *30*, 1907658.

[18] a) Z. Jakub, J. Hulva, F. Mirabella, F. Kraushofer, M. Meier, R. Bliem, U. Diebold, G. S. Parkinson, *J. Phys. Chem. C* **2019**, *123*, 15038–15045; b) L. Soriano, I. Preda, A. Gutiérrez, S. Palacín, M. Abbate, A. Vollmer, *Phys. Rev. B* **2007**, *75*, 233417.

[19] A. P. Grosvenor, M. C. Biesinger, R. S. C. Smart, N. S. McIntyre, *Surf. Sci.* **2006**, *600*, 1771–1779.

[20] Y. Hou, Y.-L. Liang, P.-C. Shi, Y.-B. Huang, R. Cao, *Appl. Catal. B* **2020**, *271*, 118929.

[21] C. F. Wen, F. Mao, Y. Liu, X. Y. Zhang, H. Q. Fu, L. R. Zheng, P. F. Liu, H. G. Yang, *ACS Catal.* **2020**, *10*, 1086–1093.

[22] J. Timoshenko, A. Kuzmin, *Comput. Phys. Commun.* **2009**, *180*, 920–925.

[23] J. Resasco, L. DeRita, S. Dai, J. P. Chada, M. Xu, X. Yan, J. Finzel, S. Hanukovich, A. S. Hoffman, G. W. Graham, S. R. Bare, X. Pan, P. Christopher, *J. Am. Chem. Soc.* **2020**, *142*, 169–184.

[24] S. Vijay, W. Ju, S. Brückner, S.-C. Tsang, P. Strasser, K. Chan, *Nat. Catal.* **2021**, *4*, 1024–1031.

[25] A. Goyal, G. Marcandalli, V. A. Mints, M. T. M. Koper, *J. Am. Chem. Soc.* **2020**, *142*, 4154–4161.

Manuscript received: October 30, 2021
Accepted manuscript online: January 31, 2022
Version of record online: February 16, 2022

© 2022 The Authors. Angewandte Chemie International Edition published by Wiley-VCH GmbH

Angewandte Chemie
Eine Zeitschrift der Gesellschaft Deutscher Chemiker

Supporting Information

Covalent Organic Framework (COF) Derived Ni-N-C Catalysts for Electrochemical CO_2 Reduction: Unraveling Fundamental Kinetic and Structural Parameters of the Active Sites

C. Li, W. Ju, S. Vijay, J. Timoshenko, K. Mou, D. A. Cullen, J. Yang, X. Wang, P. Pachfule, S. Brückner, H. S. Jeon, F. T. Haase, S.-C. Tsang, C. Rettenmaier, K. Chan, B. R. Cuenya, A. Thomas*, P. Strasser**

Supporting Information

Covalent Organic Framework (COF) derived Ni-N-C Catalysts for Electrochemical CO_2 Reduction:

Unraveling Fundamental Kinetic and Structural Parameters of the Active Sites

Changxia Li+ [a], Wen Ju+* [b], Sudarshan Vijay [c], Janis Timoshenko [d], Kaiwen Mou [b], David A. Cullen [e], Jin Yang [a], Xingli Wang [b], Pradip Pachfule [a], Sven Brückner [b], Hyo Sang Jeon [d], Felix T. Haase [d], Sze-Chun Tsang [C], Clara Rettenmaier [d], Karen Chan [c], Beatriz Roldan Cuenya [d], Arne Thomas* [a], Peter Strasser* [b]

[+] These authors contributed equally to this work.

Affiliation

[a] *Department of Chemistry, Division of Functional Materials, Technical University Berlin, Berlin 10623, Germany*

[b] *Department of Chemistry, Chemical Engineering Division, Technical University Berlin, Berlin 10623, Germany*

[c] *CatTheory, Department of Physics, Technical University of Denmark, 2800 Kongens Lyngby, Denmark*

[d] *Interface Science Department, Fritz-Haber Institute of Max-Planck Society, Berlin 14195, Germany*

[e] *Center for Nanophase Materials Sciences, Oak Ridge National Laboratory, Oak Ridge, TN, USA*

Contents

Synthesis protocol of the C-TpDt-Ni- family catalysts 3

Synthesis of TpDt-COF 3

Synthesis of TpDt-Ni 3

Synthesis of pyrolyzed C-TpDt-Ni 4

Synthesis of reference Ni-N-C catalysts 5

Synthesis of C-TpPa-COF-900 5

Synthesis of NiPc/CNT 5

Synthesis of PANI-Ni-900 6

Characterization details 7

XRD, TGA, BET, ICP-OES, FT-IR, SEM, TEM, and HAADT-STEM 7

X-ray Photoelectron Spectra 7

X-ray absorption Spectra 8

Electrochemical performance screening 9

Electrode preparation 9

Electrochemical measurement 9

Cathode potential 10

Product analysis 11

Computational methods 13

Supplementary figures and tables 14

Characterization of TpDt-COF 14

Synthesis and characterization of TpPa-COF 17

Characterization of C-TpDt-Ni-family candidates 18

XRD patterns of all CO_2RR catalysts 21

XPS analysis 22

XAS analysis 27

Reference 33

Synthesis protocol of the C-TpDt-Ni- family catalysts

Chemicals

All the chemicals were used without further purification. The 3,5-diamino-1,2,4-triazole (Dt), paraphenylenediamine (Pa), mesitylene (1,3,5-trimethylbenzene, > 98%), Ni phthalocyanine (NiPc, > 95%) and $Ni(NO_3)_2$ $6H_2O$ were purchased from Sigma Aldrich Chemicals. 1,4-dioxane (99.9 %), methanol (Carl Roth, ≥ 99%), acetone (≥ 99.5%), N,N-dimethylacetamide (DMA) and N,N-dimethylformamide (DMF) (≥ 99.9%) were purchased from Carl Roth.

Protocol

Synthesis of Tp

Tp was synthesized following our previous literature approach.[1] 15.1 g hexamethylenetetramine, 6.0 g phloroglucinol, and 90 mL trifluoroacetic acid were refluxed under N_2 at 100 °C for 2.5 h. 150 mL of 3M HCl was added slowly and the solution was heated at 100 °C for another 1 h. After cooling down, the solution was filtered through Celite and extracted with 350 mL dichloromethane. Then, the solution was evaporated under reduced pressure to afford 2.4 g of an off-white powder. Purification was carried out by sublimation.

Synthesis of TpDt-COF

1,3,5-triformylphloroglucinol (90 mg, 0.42 mmol), 3,5-diamino-1,2,4-triazole (45 mg, 0.45 mmol) and 1.5 mL dioxane were put into a Pyrex tube and the mixture was sonicated for 5 min. 0.5 mL DMA and 1.5 mL mesitylene were added to the above solution and sonicated for 5 min. Following this, 0.5 mL of 6 M aqueous acetic acid was added. This mixture was sonicated for another 10 minutes to yield a homogenous dispersion. The tube was then flash frozen in a liquid nitrogen bath and degassed by three freeze-pump-thaw cycles. The tube was sealed and then placed in an oven at 120 °C for 3 days. After the mixture was cooled to room temperature, the reddish brown precipitate was collected and washed with hot DMF, methanol and acetone. The powder collected was then dried at 80 °C under vacuum for 12 hours to obtain a deep red colored powder (81%, isolated yield).

Synthesis of TpDt-Ni

100 mg TpDt-COF was dispersed in 20 mL of $Ni(NO_3)_2$ $6H_2O$ (2M) aqueous solution and sonicated for 30 min and stirred for 10 h. The impregnated TpDt-COF was then separated by vacuum filtration and washed

with distilled water four times to remove weakly adsorbed ions. After drying at 80 °C, the TpDt-Ni was obtained.

Synthesis of pyrolyzed C-TpDt-Ni

The TpDt-Ni was placed in a tube furnace and annealed at 900 °C (800 and 1000 °C) for 2 h under N_2 atmosphere (80 sccm) at a heating rate of 5.0 °C min^{-1}. The carbonized COF was dispersed in aqueous HCl (ca. 1 M) and stirred for 1 day. The leached sample was collected and washed with DI water until the pH value was close to neutral. The obtained materials were denoted as C-TpDt-Ni-T (where T represents the temperature).

Synthesis of reference Ni-N-C catalysts

Synthesis of C-TpPa-COF-900

Synthesis of TpPa-COF

1,3,5-triformylphloroglucinol (63 mg, 0.3 mmol), paraphenylenediamine (48 mg, 0.45 mmol), 1.5 mL of mesitylene, 1.5 mL of 1,4-dioxane, 0.5 mL of 3 M aqueous acetic acid were placed into a Pyrex tube and the mixture was sonicated for 20 min to obtain a homogenous dispersion. The tube was then flash frozen in a liquid nitrogen bath and degassed by three freeze-pump-thaw cycles. The tube was sealed off and then placed in an oven at 120 °C for 3 days. After the mixture was cooled to room temperature, the red precipitate was collected and washed with THF and acetone. The powder collected was then dried at 80 °C under vacuum for 12 hours.

Synthesis of C-TpPa-Ni-900

100 mg TpPa-COF was dispersed in 20 mL of $Ni(NO_3)_2$ $6H_2O$ (2M) aqueous solution and sonicated for 30 min and stirred for 10 h. The impregnated TpPa-COF was then separated by vacuum filtration and washed with distilled water four times to remove weakly adsorbed ions. After drying at 80 °C, the TpPa-Ni was obtained. The TpPa-Ni was then placed in tube furnace and annealed at 900 °C for 2 h under N_2 atmosphere (80 sccm) at a heating rate of 5.0 °C min^{-1}. The carbonized COF was dispersed in aqueous HCl (ca. 1 M) and stirred for 1 day. The leached sample was collected and washed with DI water until a pH value close to neutral.

Synthesis of NiPc/CNT

NiPc/CNT was synthesized following the analogous protocol reported in the literature.[2] 1 mg NiPc was mixed with 30 mg MWCNTs (multi wall carbon nanotubes) in 30 mL DMF solution and kept stirred for 24 hours. The suspension color turned from the initial violet to transparent. The final suspension was dried to obtain the NiPc/CNT catalyst.

Synthesis of PANI-Ni-900

PANI-Ni-900 was synthesized following our previous literature approach.[3] 3 ml of aniline, 5 g $NiCl_2\cdot 6H_2O$ and 5 g ammonium persulfate (APS, $(NH_4)_2S_2O_8$) was added to 0.5 L of 1 M HCl and stirred for 1 hour. Then, the suspension was stirred for 48 hours along with 0.4 g of dispersed activated Ketjen 600 carbon black support (washed in HCl for purification and HNO_3 for oxygen doping). Afterwards, the suspension was dried at 95 °C for 24 hours. After drying, the solid mixture was ball-milled with ZrO_2 balls for 20 min. The pyrolysis is carried in a furnace with a ramp of 30°C min^{-1} to 900 °C and kept at this temperature for 1 hour, in N_2 condition, and followed by acid washing steps (2M H_2SO_4 at 90 °C for overnight) to remove the excess Ni particles. In our synthesis, 4 times heat treatment (HT) and 3 times acid washing was performed by turn, and the catalyst is obtained after the 4th pyrolysis.

Characterization details

XRD, TGA, BET, ICP-OES, FT-IR, SEM, TEM, and HAADT-STEM

X-ray powder diffraction (XRD) patterns were performed on a Bruker D8 Advance instrument with Cu Kα radiation (λ=1.54 Å) operating at 40 kV and 40 mA. XRD patterns were collected in the range of 2°–60° at a scanning speed of 2° min^{-1}. Thermo-gravimetric analyses (TGA) were conducted using a Mettler Toledo TGA/DSC1 Star System analyzer at a heating rate of 10 °C min^{-1} under N_2 atmosphere. N_2 sorption measurements was carried out using a Quantachrome Quadrasorb SI instrument with degassing temperature of 200 °C for 6 h for carbon samples and 120 °C for 12 h for COFs samples before the measurement. The specific surface areas were calculated by using Brunauer-Emmett-Teller (BET) calculations. The pore size distributions of COF and carbon samples were obtained from the adsorption branch of isotherms by the quenched solid density functional theory (QSDFT) and non-localized density functional theory (NLDFT) model, respectively. Bulk metal contents were measured with Varian 715-ES ICP-OES. For this, the samples were previously solved in aqua-regia and treated using microwave. Fourier transform infrared spectroscopy (FT-IR) analyses were carried out on Varian 640IR spectrometer equipped with an ATR cell. Scanning electron microscope (SEM) was measured using Gemini SEM 500 low vacuum high-resolution SEM. Transmission electron microscope (TEM) was performed using FEI Tecnai G^2 20 S-TWIN electron microscope with an operating voltage of 200 kV. The conductivity was measured with Yokogawa GS610 Sourcemeter unit in galvanostatic mode between -2 mA and +2 mA in 0.2 mA steps. Aberration-corrected STEM images were recorded by using a high-angle annular dark-field (HAADF) detector equipped with a 54-200 mrad collection semi-angle at Oak Ridge National Laboratory.

X-ray Photoelectron Spectra

XPS was performed on a K-Alpha X-ray photoelectron spectrometer system (Thermo Scientific) with Hemispheric 180° dual-focus analyzer with 128-channel detector. X-ray monochromator was microfocused Al Kα radiation. The samples were pasted and pressed onto the sample holder using carbon tapes for measurement.

X-ray absorption Spectra

XAS measurements at Ni K-edge (8333 eV) were performed at P64 beamline at PETRA-III synchrotron radiation facility (Hamburg). Measurements were performed in transmission mode. Intensities of incident radiation and transmitted radiation were measured with ionization chamber detector I_0 and I_1 filled with pure N_2. For data alignment, Ni foil's XAS spectrum was acquired in transmission mode simultaneously with the spectra for Ni samples. I_2 ionization chamber used for such reference measurements was also filled with pure N_2. Si (111) monochromator was used for energy selection. All measurements were performed in air at room temperature. ATHENA software was used for data alignment, normalization, and XAS spectra extraction.

Electrochemical performance screening

Electrode preparation

Carbon paper (1 cm × 2.5 cm, Freudenberg C2H23) was sonicated in ethanol and deionized water for 15 min and dried as the electrode substrate. The catalyst ink is prepared using 4.0 mg catalyst mixed with 60 µL Nafion solution (5% in ethanol, Sigma-Aldrich), 200 µL isopropanol, and 200 µL DI water. After 15 min sonification, the ink was deposited on the micro-porous-layer side of carbon paper to achieve an area of 1 cm^2 with catalysts loading of 1 mg cm^{-2}.

Electrochemical measurement

The CO_2RR performance screening was carried out in a regular 3-electrode H-cell, divided by a Nafion N117 membrane. The working electrode was the catalysts-coated carbon paper mentioned above, and a Pt mesh was deployed as the counter electrodes. A leak-free Ag/AgCl electrode was used as the reference. Electrochemical experiments were performed in CO_2 purged 0.5 M $KHCO_3$ (CO_2 flow rate: 30 ml min^{-1}, pH: 7.3). The current density (*j*) was normalized to the working electrode's geometrical area (1 cm^2).

Cathode potential

The working potential is controlled by the Biologic SP-300 potentiostat against the Ag/AgCl reference electrode. Before the bulk electrolysis, the ohmic resistance between cathode and reference electrode was measured using PEIS (potentiostatic electrochemical impedance spectroscopy) module at -1.0 V vs. Ag/AgCl Ref, and the frequency was set from 100 k Hz to 1 Hz. Subseqently, 50% of the ohmic drop was automatically corrected, and the other half was corrected manually. All potentials were rescaled to reversible hydrogen electrode (RHE) by Eq. S1.

$$E_{IR-free} = E_{vs.\ Ref} + E_{Ref\ vs.\ NHE} + 0.059 * pH + I * R * 50\% \qquad \text{Eq. S1}$$

$E_{IR-free}$:	IR corrected cathode potential against RHE	/ V_{RHE}
$E_{vs.\ Ref}$:	Applied potential against the reference electrode	/ V
$E_{Ref\ vs.\ RHE}$:	Reference electrode potential measured against NHE	/ V
pH:	pH-value of the electrolyte	
I:	Total current of the experiment (absolute value)	/ A
R:	Ohmic resistance between cathode and reference electrode	/ Ω

Product analysis

A Shimadzu 2014 on-line GC is utilized for product quantification. The gas stream is separated by the Hayesep Q + R columns and then analyzed by the TCD (Thermo Conductivity Detector) and FID (Flame Ionization Detector). The TCD detects the volume percentage ($\%_{VOL}$) of the H_2 product, and the FID measures the CO after being methanized. On the all Ni-N-C type catalyst, no liquid product is found after the electrolysis. Calculations of the production rate (Eq. S2), partial current density (Eq. S3), and faradaic efficiency (Eq. S4) are given below. The calculation of the TOF is given in (Eq. S5).

$$\dot{n}_{Product} = \frac{\dot{V}_{Total} \times C_{Product}}{A \times V_{MOL}} \qquad \text{Eq. S2}$$

$\dot{n}_{Product}$:	geometric reaction rate of each product	/ mol cm^{-2} s^{-1}
$\dot{V}_{Total}$:	Exhaust stream flow rate	/ mL s^{-1}
$C_{Product}$:	product concentration (volumetric ratio) detected by GC	/ $\%_{VOL}$
A:	geometric area of the electrode	/ cm^2
V_{MOL}:	volume of gas per mole at ATM	/ mL mol^{-1}

$$j_{Product} = \dot{n}_{Product} \times F \times z \qquad \text{Eq. S3}$$

$j_{Product}$:	partial current density of each product	/ A cm^{-2}
F:	faradaic constant	/ C mol^{-1}
z:	charge transfer per product molecule	

$$FE_{Product} = \frac{j_{Product}}{j_{Total}} \times 100\% \qquad \text{Eq. S4}$$

$FE_{Product}$:	faradaic efficiency of each product	/ %
j_{Total}:	total current density	/ A cm^{-2}

$$TOF = \frac{\dot{n}_{CO}}{M_{loading} \times x_{Ni-Nx}\%_{at.} \times A_{BET}} \qquad \text{Eq. S5}$$

TOF:	CO Turnover Frequency normalized by active Ni-N_x area	/ mol m^{-2} s^{-1}
$\dot{n}_{CO}$:	geometric CO reaction rate	/ mol cm^{-2} s^{-1}
$M_{loading}$:	catalyst loading	/ mg cm^{-2}
A_{BET}:	specific N_2 adsorption area measured using BET	/ m^2 mg^{-1}
$x_{N-Nx}\%_{at.}$:	atomic ratio of total exposed Ni-N_x on surface	/ $\%_{at.}$

Computational methods

Density functional theory calculations were performed using Vienna Ab-initio Software Package (VASP).[4] Core electrons were described using Projector Augmented Waves (PAW) potentials.[5] Valence electrons were described using plane-waves with kinetic energy up to 500eV. Gaussian smearing with a width of 0.1eV was used. The RPBE[6] functional was used for all calculations. All calculations were run with spin-polarization.

Structures were prepared using the Atomic Simulation Environment (ASE).[7] The lattice constant of graphene was optimized using a 12x12x12 Monkhorst-Pack *k*-point mesh grid.[8] A 3×3 single-layer graphene structure was made with the obtained lattice parameter. All structures were then treated with a 4×4×1 Monkhorst–Pack k-point mesh with at least 10 Å of vacuum. Depending on the vacancy type, carbon atoms in the graphene structure were replaced by nitrogen and Nickel atoms. The structure obtained after creating vacancies and doping was subjected to an optimization of positions before adding an adsorbate to the unit cell. All geometries are optimized until forces are less than 0.025 eV Å^{-1}. The density of states were obtained by using Gaussian smearing of 0.1 eV.

The computational hydrogen electrode (CHE)[9] was used to determine reaction energies as a function of potential for reactions with an electron in the reactant or product. The chemical potential of the proton and electron is related to that of H2 at 0 V vs RHE using:

$$\mu_{\mathrm{H}^+} + \mu_{\mathrm{e}^-} = \frac{1}{2}\mu_{\mathrm{H}_2} \qquad \text{Eq. S6}$$

Microkinetic modelling was performed using CatMAP.[10] The rate of a given elementary step was:

$$\mathrm{rate} = k_+\Pi\theta_i\Pi p_j - k_-\Pi\theta_i\Pi p_j \qquad \text{Eq. S7}$$

where $+$ indicates the forward reaction and – the reverse reaction. The rate constants can be given as $k_+ = \exp\left(-\frac{G_{a,+}}{k_BT}\right)$ and $k_- = \exp\left(-\frac{G_{a,-}}{k_BT}\right)$. In the absence of electrochemical barriers, the free energy is used, which is given as $\Delta G = \Delta G^o + neU + \Delta G_{\mathrm{field}}$, where ΔG^o is the free energy for the reaction at the potential of zero charge (pzc), n is the number of proton-electron pairs transferred and $\Delta G_{\mathrm{field}}$ is the dipole-field contribution.

A multi-precision Newton root finding algorithm was used to determine the steady-staterates and coverages. A decimal precision of 100 along with a convergence tolerance value of 10^{-25} was used.

Supplementary figures and tables

Characterization of TpDt-COF

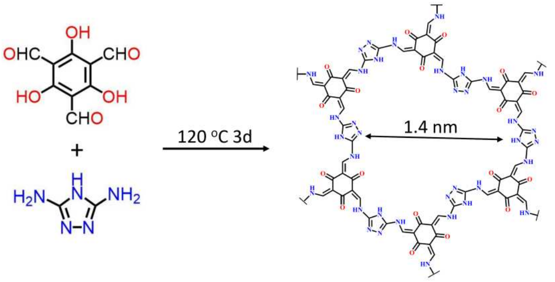
OH
OHC
CHO
HO
OH
CHO
+
H
H2N
N
NH2
N–N
120 °C 3d
1.4 nm

Figure S1. Schematic representation of the synthesis of TpDt-COF.

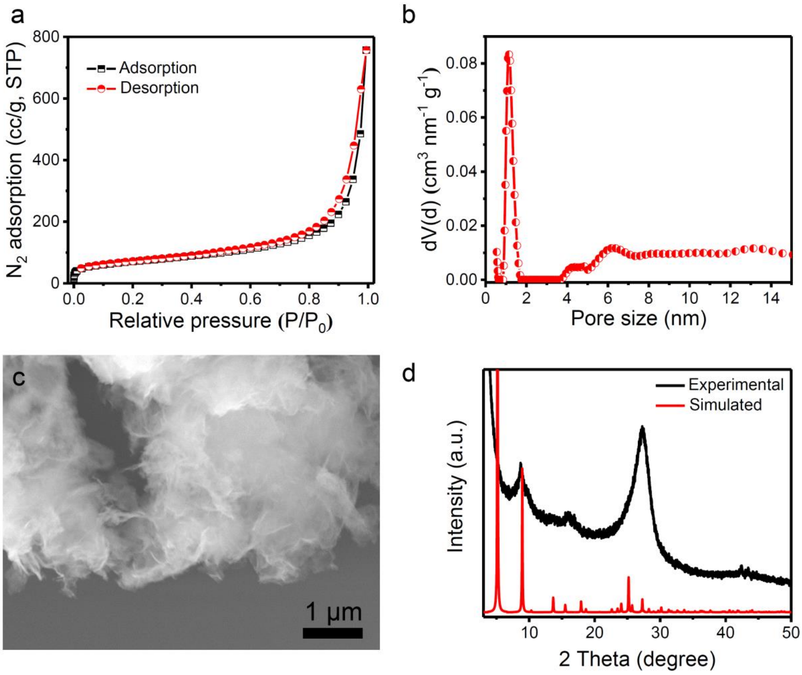

Figure S2. (a) N_2 absorption-desorption isotherms, (b) pore size distribution, (c) SEM image and (d) XRD pattern of TpDt-COF.

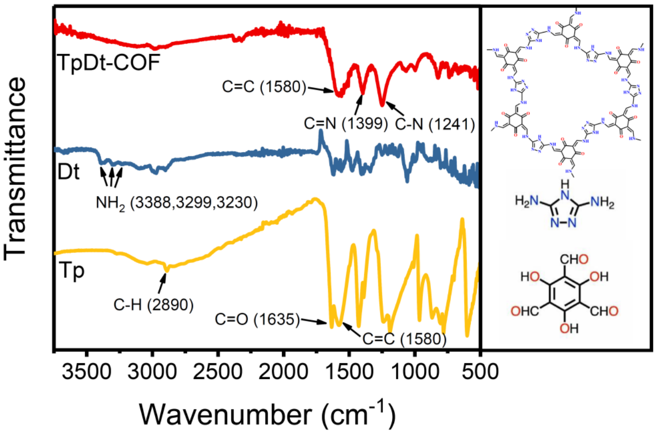

Figure S3. FT-IR spectroscopy of TpDt-COF, Tp and Dt.

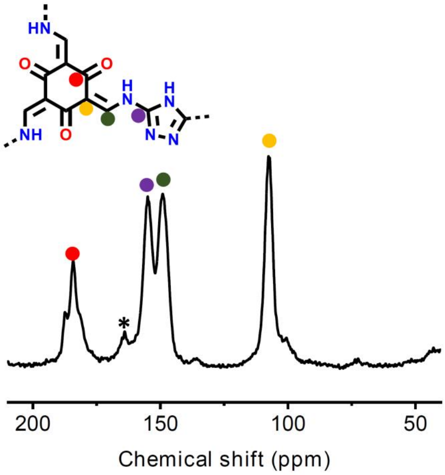

Figure S4. ^{13}C solid state NMR of TpDt-COF. *- corresponds to the solvent DMF.

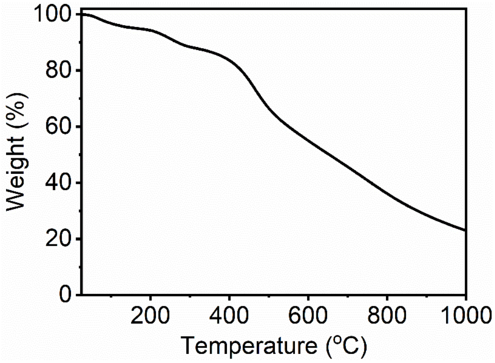

Figure S5. The TGA curve of TpDt-COF.

Synthesis and characterization of TpPa-COF

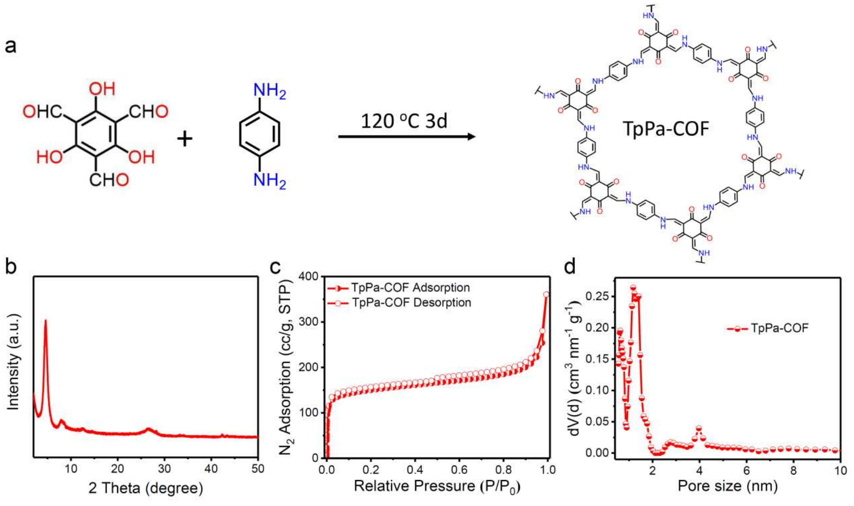

Figure S6. (a) Schematic representation of the synthesis of TpPa-COF. (b) XRD pattern, (c) N_2 absorption-desorption isotherms and (d) pore size distribution of TpPa-COF.

Characterization of C-TpDt-Ni-family candidates

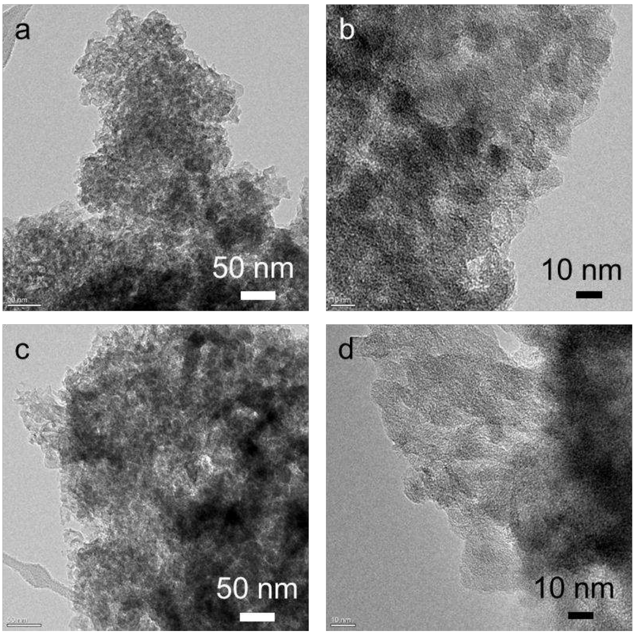

Figure S7. TEM images of (a, b) C-TpDt-Ni-800 and (c, d) C-TpDt-Ni-1000.

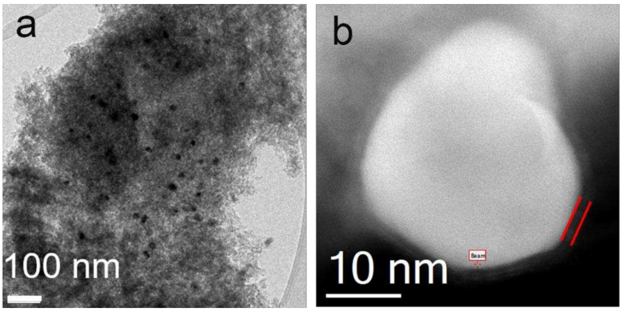

Figure S8. (a) Low magnification TEM image and (b) HAADF-STEM image of C-TpDt-Ni-900.

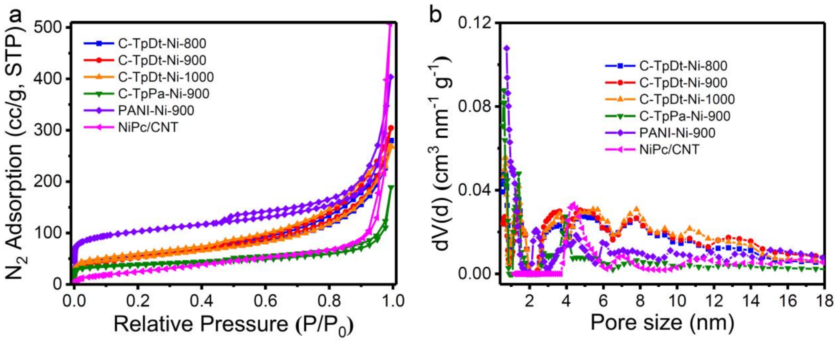

Figure S9. (a) N_2 absorption-desorption isotherms and (b) pore size distributions of C-TpDt-Ni-800, C-TpDt-Ni-900, C-TpDt-Ni-1000, C-TpPa-Ni-900, PANI-Ni-900, and NiPc/CNT.

Table S1. The BET specific surface areas and pore volume of all the samples involved.

Samples	**Specific surface area (m^2 g^{-1})**	**Pore volume (cm^3 g^{-1})**
TpDt-COF	253	0.597
TpPa-COF	571	0.369
C-TpDt-Ni-800	192	0.335
C-TpDt-Ni-900	188	0.380
C-TpDt-Ni-1000	184	0.359
C-TpPa-Ni-900	135	0.162
PANI-Ni-900	414	0.413
NiPc/CNT	85	0.296

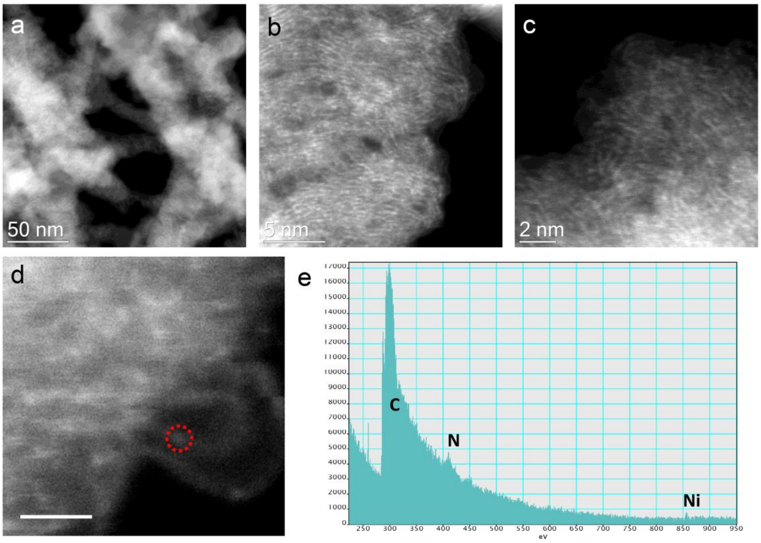
a
50 nm
b
5 nm
c
2 nm
d
e
C
N
Ni
0
1000
2000
3000
4000
5000
6000
7000
8000
9000
10000
11000
12000
13000
14000
15000
16000
17000
250
300
350
400
450
500
550
600
650
700
750
800
850
900
950
eV

Figure S10. (a-d) HAADF-STEM images of C-TpDt-Ni-800 and (e) the corresponding EELS spectrum acquired at Ni single atom region circled in red from S10d.

Table S2. Conductivity of TpDt-COF, C-TpDt-Ni-800, C-TpDt-Ni-900, C-TpDt-Ni-1000.

Samples	**Conductivity (S cm^{-1})**
TpDt-COF	*
C-TpDt-Ni-800	0.24
C-TpDt-Ni-900	1.98
C-TpDt-Ni-1000	3.45

The power samples were pressed between steel cylinders in a PE-die.

* Resistance is too high, out of measurement range.

XRD patterns of all CO_2RR catalysts

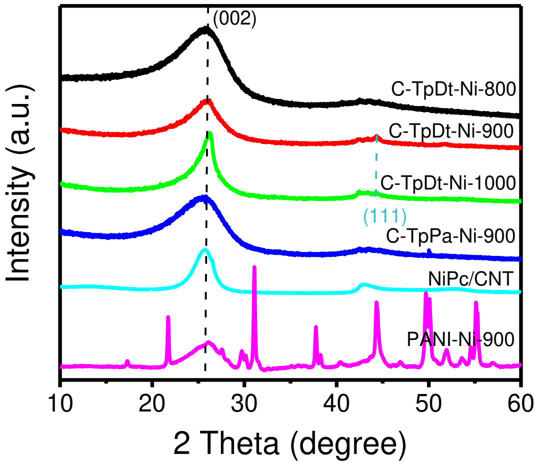

Figure S11. XRD patterns of C-TpDt-Ni-800, C-TpDt-Ni-900, C-TpDt-Ni-1000, C-TpPa-Ni-900, PANI-Ni-900, and NiPc/CNT. The profile of PANI-Ni-900 is identical with our earlier work.[3]

XPS analysis

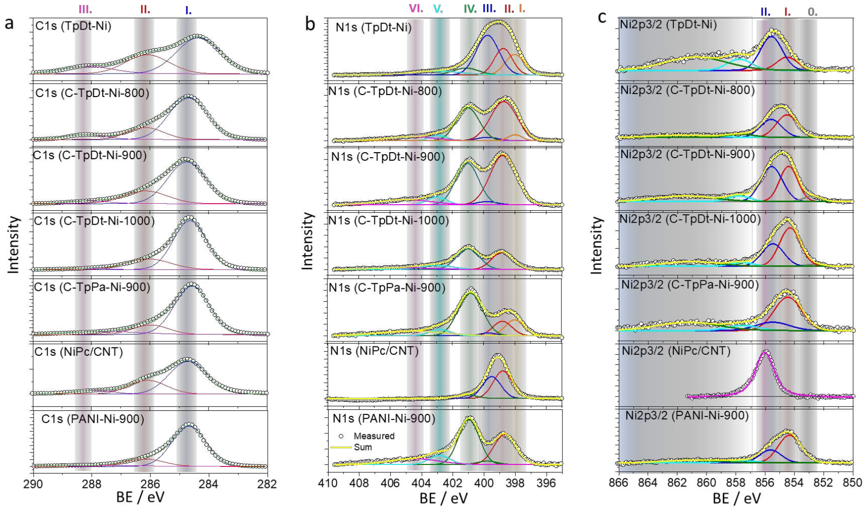

Figure S12. (a) XPS C 1s spectra, (b) XPS N 1s spectra, and (c) XPS Ni 2p spectra for TpDt-Ni, C-TpDt-Ni-800, C-TpDt-Ni-900, C-TpDt-Ni-1000, C-TpPa-Ni-900, NiPc/CNT, and PANI-Ni-900. The PANI-Ni-900 is analogous with our earlier work.[3]

Here, the fitting of the XPS profiles is according to the previous studies.

The C1s spectra are fitted as Ref[11]:

Group I:	284.4 eV to 284.8 eV;
Group II:	286.2 ± 0.2 eV, FWHM ~ 1.5 ± 0.2 eV;
Group III:	288.2 ± 0.2 eV, FWHM ~ 1.5 ± 0.2 eV;

The N1s spectra are fitted following the Ref[12]:

Group I:	398.1 ± 0.2 eV, FWHM ~ 1.5 ± 0.2 eV;
Group II:	398.7 ± 0.2 eV, FWHM ~ 1.5 ± 0.2 eV;
Group III:	399.6 ± 0.2 eV, FWHM ~ 1.5 ± 0.2 eV;
Group IV:	401 ± 0.2 eV, FWHM ~ 1.5 ± 0.2 eV;
Group V:	402.8 ± 0.2 eV, FWHM ~ 1.5 ± 0.2 eV;

Group VI: > 404 eV.

The Ni2p spectra are fitted following the Ref[13]:

Group 0:	852.6 ± 0.2 eV;
Group I:	854.4 ± 0.2 eV, FWHM ~ 1.5 ± 0.2 eV;
Group II:	855.3 ± 0.2 eV, FWHM ~ 1.5 ± 0.2 eV; *

* The chemical state of NiPc/CNT is ~0.5 eV positive than other candidates, consistent with previous studies.[13c, 14]

Note:

In the C1s spectra, it is seen that the intensities for carbon atoms bound to hetero-atoms (C=O/C=N at 288.2 ± 0.2 eV, C-O/C-N at 286.2 ± 0.2 eV, Figure S12a) drop along with increasing pyrolysis temperatures. Aromatic ring formation was revealed by the peak shift from 284.4 eV to 284.8 eV.[11]

The fitted high-resolution N 1s profiles of the pyrolyzed catalyst precursors are shown in Figure S12b (detailed fitted parameters are presented in Table S3-5). The fitted group I (398.1 ± 0.2 eV) and group II (398.7 ± 0.2eV) cover two sp2-hybridized nitrogens bound to carbons, such as imine, pyridinic, or triazinic type N. The group III (399.6 ± 0.2 eV) indicates sp2 hybridized N in Metal-N coordination (Ni-N), OC-NH-C partial double bonds, or multiple graphitic N motifs in a single aromatic ring. Group IV (401 ± 0.2 eV) and V (402.8 ± 0.2 eV) cover the in-plane N-H, graphitic N(-H), and out-of-plane N-H, such as protonated-pyridinic, pyrrolic, graphitic, and quaternary N. Species in group VI (404 eV) should be assigned to oxide N moieties.[12] Clearly, the pyrolysis temperature controls the resulting N species in all C-TpDt-Ni samples. In the unpyrolyzed TpDt-Ni sample, the group I and III signals can be assigned to imine and amine groups. The pyrolysis treatment significantly transformed those into the in-plane sp2 hybridized N moieties.

Table S3. Content (at%) of Ni, N, C and O elements for all the samples as measured by XPS.

Samples	Ni	N	C	O
TpDt-Ni	0.50	15.15	66.24	18.11
TpPa-Ni	0.35	10.09	71.81	17.74
C-TpDt-Ni-800	0.66	10.28	80.62	8.45
C-TpDt-Ni-900	0.97	11.27	82.11	5.65
C-TpDt-Ni-1000	0.48	4.63	90.85	4.04
C-TpPa-Ni-900	0.21	5.13	89.27	5.39
PANI-Ni-900	0.47	4.8	91.22	3.51
NiPc/CNT	0.36	3.65	95.44	0.55

Table S4. The atomic ratio of various N species fitted by XPS analysis.

Samples	Group I. BE~398eV	Group II. BE~398.7eV	Group III. BE~399.6eV	Group IV. BE~401eV	Group V. BE~403eV	Group VI. BE>=404
TpDt-Ni	18.32	22.14	41.75	8.23	9.56	0
TpDt-Ni-800	3.81	46.12	3.27	33.82	4.08	8.89
TpDt-Ni-900	0	47.08	2.56	34.49	5.52	10.39
TpDt-Ni-1000	0	33.06	1.06	42.50	12.59	10.79
TpPa-Ni-900	14.43	13.11	2.24	49.18	6.25	14.79
PANI-Ni-900	0	30.88	3.12	43.55	8.89	13.50
NiPc/CNT	0	52.34	40.53	7.12	0	0

Table S5. The atomic ratio of various Ni species fitted by XPS analysis.

Samples	Group 0. BE~852.6eV	Group I. BE~854.4eV	Group II. BE~855.3eV	Satellites BE > 856eV
C-TpDt-Ni-800	0	44.35	35.20	20.44
C-TpDt-Ni-900	5.10	32.32	38.66	23.93
C-TpDt-Ni-1000	2.29	47.83	29.09	20.79
C-TpPa-Ni-900	0	49.19	15.04	35.77
PANI-Ni-900	0	55.58	24.38	20.04
NiPc/CNT	0	0	100 (BE~856.1eV)	0

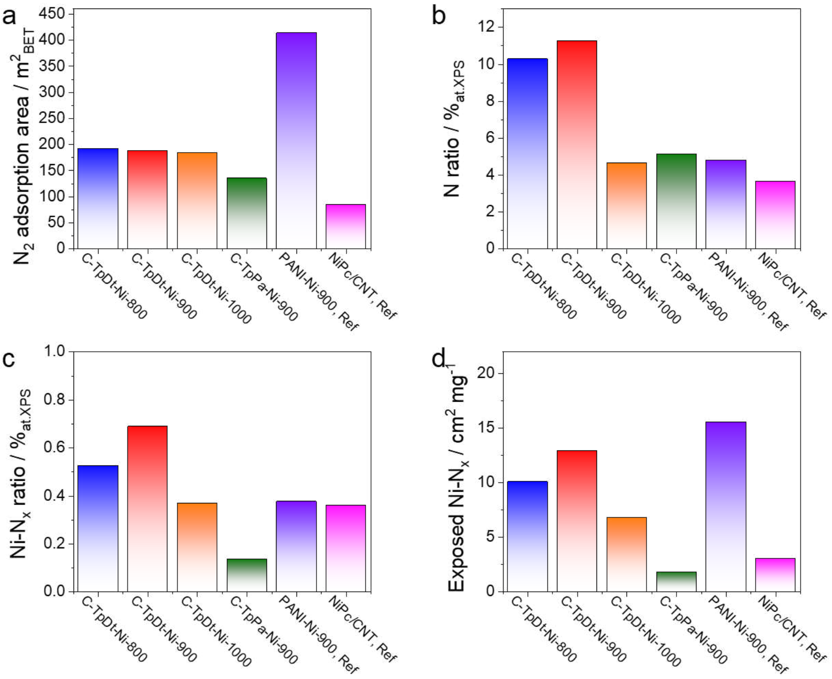

Figure S13. (a) BET derived specific N_2 adsorption area, (b) XPS derived surface nitrogen atomic ratio, (c) surface Ni-N_x atomic ratio, estimated upon XPS derived Ni^{2+} and Ni^{+} species ($x_{Ni-Nx}\%_{at.} = x_{Ni^{+}}\%_{at.} + x_{Ni^{2+}}\%_{at.}$), and (d) the surface area contributed by Ni-N_x moieties ($A_{Ni-Nx} = x_{Ni-Nx}\%_{at.} \times A_{BET}$; unit is transferred into cm^2 mg^{-1}).

XAS analysis

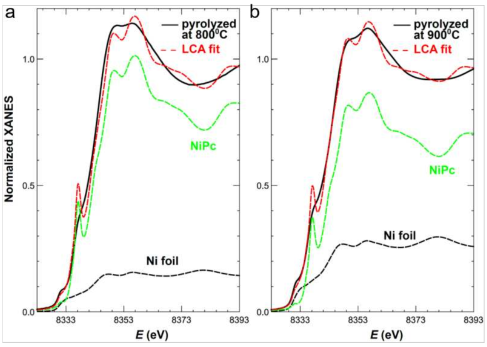

Figure S14. Results of linear combination fitting of experimental Ni K-edge XANES for sample (a) pyrolyzed at 800°C (C-TpDt-Ni-800) and (b) 900°C (C-TpDt-Ni-900). Reference spectra for Ni foil and Ni phthalocyanine used for linear combination analysis are also shown (scaled by their corresponding weight in linear combination).

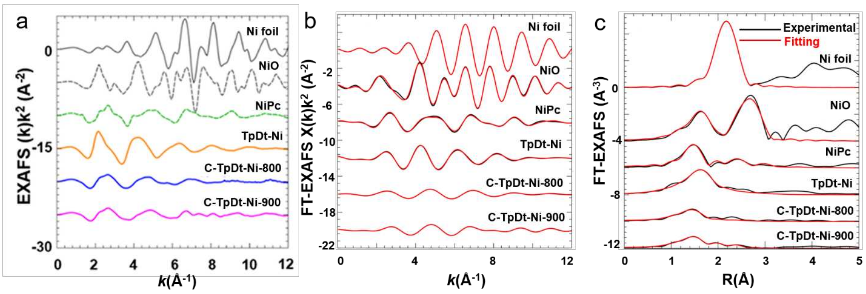

Figure S15. (a) EXAFS spectra for Ni foil, NiO, NiPc, TpDt-Ni, C-TpDt-Ni-800 and C-TpDt-Ni-900. XAFS data fitting in (b) k-space and (c) R-space.

For quantitative EXAFS analysis we perform non-linear least square fitting to theoretical standards, as implemented in FEFFIT code, see Figure S14.[15] Theoretical phases and amplitudes were obtained in self-consistent ab-initio calculations with FEFF8.5 code[16] for reference materials. The complex exchange-correlation Hedin-Lundqvist potential and default values of muffin-tin radii as provided within the FEFF8.5 code were employed.

Fitting of EXAFS spectra $\chi(k)k^2$ was carried out in R-space in the range from $R_{\min}$ = 1.0 Å up to $R_{\max}$, where $R_{\max}$ was set to 3.0 Å for NiO and NiPc and to 2.5 Å for metallic Ni, unpyrolyzed Ni COF and Ni COF pyrolyzed at 900^{0}C. For Ni COF pyrolyzed at 800^{0}C we set R_{max} to 1.8 Å to exclude from fitting the contributions beyond the first coordination shells which are too weak in this sample to be reliably identified. In all cases Fourier transform was carried out in the k range from 3.0 Å^{-1} up to 12 Å^{-1}.

Guided by the insight from WT-EXAFS analysis in Figure 2c, following paths were included in the fitting: Ni-Ni path for metallic Ni, Ni-O and Ni-Ni paths for NiO, Ni-N, Ni-C and longer Ni-N path for NiPc, Ni-O path for unpyrolyzed sample, Ni-N path for sample pyrolyzed at 800^{0}C, and Ni-N and Ni-Ni paths for sample pyrolyzed at 900^{0}C. For each path the refined parameter were coordination number N, bond-length R and disorder factor σ^2. In addition, correction to photoelectron reference energy ΔE_0 was also fitted. Amplitude reduction factors due to many-electronic processes (S_0^2 factors) were estimated based on the fitting of EXAFS samples for reference materials with known coordination numbers.

The results of such fitting are summarized in Figure S15 and Table S6. Good agreement between experimental and modeled data (Figure S15), and low values of fit R-factors (Table S6) give us confidence in the chosen fitting models.

It is challenging to distinguish between EXAFS contributions from elements that are neighbors in Periodic Table (such as N, O and C). Valuable information in this case can be obtained from interatomic distances. As evident from Table S6, significant difference between the bond-lengths in the first coordination shell can be observed for unpyrolyzed and pyrolyzed samples. In the former case, the obtained bond length (2.04 ±0.03 Å) is in a good agreement with Ni-O bond length in NiO reference sample (2.08 ±0.01 Å). In the latter case, the bond between Ni and its nearest neighbor is shorter, (1.87 ±0.01 Å), and agrees with Ni-N bond length in NiPc (1.879 ±0.009 Å). Thus one can conclude that in the pyrolyzed samples (unlike the unpyrolized one), the main Ni-containing structural motifs are Ni-N_x units, similar to those in NiPc. Moreover, for unpyrolyzed sample the 1st shell coordination number is close to 6, suggesting octahedral coordination of Ni species in this sample, in agreement with conclusions from XANES analysis. For pyrolyzed samples, the 1st shell coordination number is significantly lower, making plausible hypothesis that Ni-N_4 structural motifs are dominating moieties.

In addition to these structural motifs, the existence of metallic Ni clusters in pyrolyzed samples is confirmed by EXAFS data fitting. In particular, for sample pyrolyzed at 900 ^{0}C the inclusion of Ni-Ni scattering path was found to be necessary to obtain a good fit. The obtained value of Ni-Ni interatomic distance (2.458 ±0.006 Å) is close to Ni-Ni distance in fcc metallic nickel (2.481 ±0.001 Å). The fact that Ni-Ni distance is slightly shorter in pyrolyzed Ni COF sample in comparison to that in bulk Ni metal, may imply the small sizes of formed Ni clusters and/or their strongly disordered nature.

Due to the low contribution of Ni-Ni scattering path, the obtained Ni-Ni coordination number has large uncertainty and cannot be used for a reliable estimation of the concentration of metallic Ni clusters. However, the fraction of metallic Ni can be estimated indirectly from Ni-N coordination number. Since the measured EXAFS signal is averaged over all Ni species in the sample, in the case when Ni-N_x motifs coexist with metallic Ni, the Ni-N coordination number obtained in the EXAFS fitting N_{Ni-N} differs from the true number of N neighbors $\widetilde{N}_{Ni-N}$, and is related to the concentration of metallic Ni w as $N_{Ni-N} = (1 - w)\widetilde{N}_{Ni-N}$. Assuming that in Ni-$N_x$ motifs Ni is coordinated with 4 N atoms (i.e., $\widetilde{N}_{Ni-N} = 4$), the fraction of metallic Ni can be estimated as $1 - N_{Ni-N}/4$. As a result, we can estimate that in the sample pyrolyzed at 800^{0}C, concentration of metallic Ni is ca. 22%, while in the sample pyrolyzed at 900^{0}C concentration of metallic Ni increased to ca. 33%. These estimates are in a good agreement with the aforementioned estimates from XANES analysis. Good agreement between EXAFS and XANES results indicates the validity of our assumption that Ni-N_4 motifs are the main N-N_x species in the pyrolyzed catalysts.

Table S6. Structure parameters (coordination numbers N, interatomic distances R, disorder factors σ^2), obtained in fitting of experimental Ni K-edge EXAFS data. Uncertainties of the last digit are given in parentheses.

Sample	$\boldsymbol{N_{Ni-C/N/O}}$	$\boldsymbol{R_{Ni-C/N/O}}$ (Å)	$\boldsymbol{\sigma^2_{Ni-C/N/O}}$ (Å^2)	$\boldsymbol{N_{Ni-Ni}}$	$\boldsymbol{R_{Ni-Ni}}$ (Å)	$\boldsymbol{\sigma^2_{Ni-Ni}}$ (Å^2)	$\boldsymbol{\Delta E_0}$ (eV)	*R* factor
Ni foil	-	-	-	12	2.481(1)	0.0064(1)	2.8(1)	0.1%
NiO	6	2.08(1)	0.009(2)	12(2)	2.95(1)	0.007(2)	3.4(8)	1.3%
NiPc (1st shell, Ni-N)	4	1.879(9)	0.001(1)	-	-	-	2.1(9)	2.0%
NiPc (2nd shell, Ni-C)	8	2.95(2)	0.003(3)					
NiPc (3rd shell, Ni-N)	6	3.32(4)	0.007(7)					
TpDt-Ni	6.9(7)	2.04(3)	0.010(2)	-	-	-	1(2)	0.6%
C-TpDt-Ni-800	3.1(4)	1.87(1)	0.008(2)	-	-	-	-3(2)	0.8%
C-TpDt-Ni-900	2.8(2)	1.875(6)	0.0079(9)	1(1)	2.458(6)	0.0017(9)	-0.7(8)	0.2%

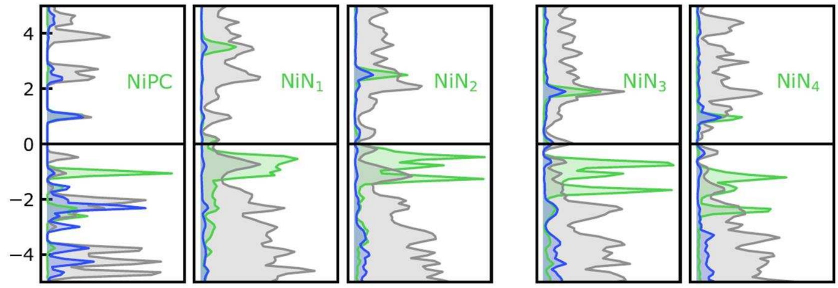

Figure S16. Projected density of state (PDOS) of our studied Ni-N-C catalysts. Those are NiPc (Phthalocyanine), DV-Ni-N1, DV-Ni-N2, DV-Ni-N3, and DV-Ni-N4.

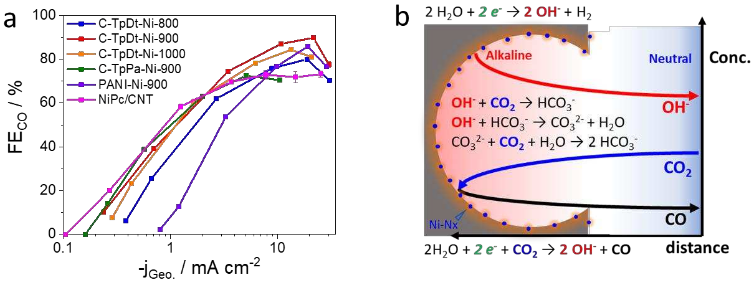

Figure S17. (a) FE_{CO} as a function of overall geometric current density on various Ni-N-C catalysts. (b) Schematic illustration of CO_2 mass transfer limitation due to in-pores OH^- formation (by electrochemical H_2 and CO evolution) and retention.

Reference

[1] C. Li, J. Yang, P. Pachfule, S. Li, M.-Y. Ye, J. Schmidt, A. Thomas, *Nature Communications* **2020**, *11*, 4712.

[2] X. Zhang, Y. Wang, M. Gu, M. Y. Wang, Z. S. Zhang, W. Y. Pan, Z. Jiang, H. Z. Zheng, M. Lucero, H. L. Wang, G. E. Sterbinsky, Q. Ma, Y. G. Wang, Z. X. Feng, J. Li, H. J. Dai, Y. Y. Liang, *Nature Energy* **2020**, *5*, 684-692.

[3] T. Möller, W. Ju, A. Bagger, X. Wang, F. Luo, T. Ngo Thanh, A. S. Varela, J. Rossmeisl, P. Strasser, *Energy & Environmental Science* **2019**.

[4] G. Kresse, J. Furthmüller, *Physical Review B* **1996**, *54*, 11169-11186.

[5] G. Kresse, D. Joubert, *Physical Review B* **1999**, *59*, 1758-1775.

[6] B. Hammer, L. B. Hansen, J. K. Nørskov, *Physical Review B* **1999**, *59*, 7413-7421.

[7] A. Hjorth Larsen, J. Jørgen Mortensen, J. Blomqvist, I. E. Castelli, R. Christensen, M. Dułak, J. Friis, M. N. Groves, B. Hammer, C. Hargus, E. D. Hermes, P. C. Jennings, P. Bjerre Jensen, J. Kermode, J. R. Kitchin, E. Leonhard Kolsbjerg, J. Kubal, K. Kaasbjerg, S. Lysgaard, J. Bergmann Maronsson, T. Maxson, T. Olsen, L. Pastewka, A. Peterson, C. Rostgaard, J. Schiøtz, O. Schütt, M. Strange, K. S. Thygesen, T. Vegge, L. Vilhelmsen, M. Walter, Z. Zeng, K. W. Jacobsen, *Journal of Physics: Condensed Matter* **2017**, *29*, 273002.

[8] H. J. Monkhorst, J. D. Pack, *Physical Review B* **1976**, *13*, 5188-5192.

[9] J. K. Nørskov, J. Rossmeisl, A. Logadottir, L. Lindqvist, J. R. Kitchin, T. Bligaard, H. Jónsson, *The Journal of Physical Chemistry B* **2004**, *108*, 17886-17892.

[10] A. J. Medford, C. Shi, M. J. Hoffmann, A. C. Lausche, S. R. Fitzgibbon, T. Bligaard, J. K. Nørskov, *Catalysis Letters* **2015**, *145*, 794-807.

[11] K. Artyushkova, *Journal of Vacuum Science & Technology A* **2020**, *38*, 031002.

[12] aK. Artyushkova, B. Kiefer, B. Halevi, A. Knop-Gericke, R. Schlogl, P. Atanassov, *Chem Commun* **2013**, *49*, 2539-2541; bK. A. S. Kabir, B. Kiefer, P. Atanassov, *Phys. Chem. Chem. Phys.* **2015**, *17*, 17785-17789; cK. Artyushkova, A. Serov, S. Rojas-Carbonell, P. Atanassov, *The Journal of Physical Chemistry C* **2015**, *119*, 25917-25928; dF. Luo, A. Roy, L. Silvioli, D. A. Cullen, A. Zitolo, M. T. Sougrati, I. C. Oguz, T. Mineva, D. Teschner, S. Wagner, J. Wen, F. Dionigi, U. I. Kramm, J. Rossmeisl, F. Jaouen, P. Strasser, *Nature Materials* **2020**, *19*, 1215-1223.

[13] aZ. Jakub, J. Hulva, F. Mirabella, F. Kraushofer, M. Meier, R. Bliem, U. Diebold, G. S. Parkinson, *The Journal of Physical Chemistry C* **2019**, *123*, 15038-15045; bS. Liu, H. B. Yang, S.-F. Hung, J. Ding, W. Cai, L. Liu, J. Gao, X. Li, X. Ren, Z. Kuang, Y. Huang, T. Zhang, B. Liu, *Angewandte Chemie International Edition* **2020**, *59*, 798-803; cH. B. Yang, S.-F. Hung, S. Liu, K. Yuan, S. Miao, L. Zhang, X. Huang, H.-Y. Wang, W. Cai, R. Chen, J. Gao, X. Yang, W. Chen, Y. Huang, H. M. Chen, C. M. Li, T. Zhang, B. Liu, *Nature Energy* **2018**, *3*, 140-147; dL. Soriano, I. Preda, A. Gutiérrez, S. Palacín, M. Abbate, A. Vollmer, *Physical Review B* **2007**, *75*, 233417.

[14] C. Yan, H. Li, Y. Ye, H. Wu, F. Cai, R. Si, J. Xiao, S. Miao, S. Xie, F. Yang, Y. Li, G. Wang, X. Bao, *Energy & Environmental Science* **2018**, *11*, 1204-1210.

[15] B. Ravel, M. Newville, *Journal of Synchrotron Radiation* **2005**, *12*, 537-541.

[16] A. L. Ankudinov, S. D. Conradson, J. Mustre de Leon, J. J. Rehr, *Physical Review B* **1998**, *57*, 7518-7525.